

https://dspace.org/

Nano-reinforced hydro-filled 3D scaffold for neural tissue engineering

Mahumane, Gillian Dumsile

2021
https://hdl.handle.net/10539/32049

Downloaded from a DSpace repository. https://dspace.org/

NANO-REINFORCED HYDRO-FILLED 3D SCAFFOLD FOR NEURAL TISSUE ENGINEERING

GILLIAN DUMSILE MAHUMANE

A thesis and original published work submitted to the Faculty of Health Sciences, University of the Witwatersrand, in fulfilment of the requirements for the degree of Doctor of Philosophy



WITS
UNIVERSITY

Supervisor:
Professor Viness Pillay

Co-Supervisors:
Professor Yahya Essop Choonara and Associate Professor Pradeep Kumar

Department of Pharmacy and Pharmacology, University of the Witwatersrand, Johannesburg
South Africa

Johannesburg
2021

DECLARATION

I, Gillian Dumsile Mahumane, declare that this Thesis is my own, unaided work. It is being submitted for the Degree of Doctor of Philosophy of Pharmacy in the Faculty of Health Sciences at the University of the Witwatersrand, Parktown, Johannesburg. It has not been submitted before for any degree or examination at any other University.

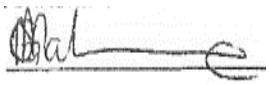

Gillian Dumsile Mahumane

Signed this 12th day of March 2021

ANIMAL ETHICS DECLARATION

I hereby confirm that the following study entitled “Nano-reinfoced hydrofilled 3D scaffold for neural tissue engineering” has received the approval from the Animal Ethics Committee of the University of the Witwatersrand with ethics clearance number 2017/8/49/D (**Appendix A**).

DEDICATION

God

And the LORD shall guide thee continually, and satisfy thy soul in drought, and make fat they bones: and thou shalt be like a watered garden, and like a spring of water whose waters fail not (Isaiah 58:11). I have the honour of presenting this truth upon every single eye that reads this work, to know that God can take a village girl to levels beyond her imagination. I thank the Lord that I came to know of God in my life and I thank God for using me in the spaces I have come to know and those that I have yet to reach. Peace and a fruitful spirit be with all mankind. Be still and know that God is.

My grandmother, Linah Mzolokoqo Shongwe (30 June 1934 - 9 August 2016)

Gogo, this is your granddaughter, JiJi. You passed away a year too soon, I wish you could've lived to see this. You gave me the greatest gift of all in this world, which is your influence on the woman my mother became. Moreover, you embodied kindness in your being that I could not ignore. If I have learnt anything from you, it is kindness. You kept telling me I was a Doctor, despite my efforts to differentiate to you between a pharmacist and a medical doctor. Little did I know…your wisdom was revealing to me a portion of me I could not see with my learnered self despite your limited education. You told me I was a Doctor, and now I am. Thank you for seeing me when I could not, and for being relentless in your vision.

My grandfather, Mr. Jacob Malisha Zulu (23 August 1925 - 23 September 2020)

Mkhul' Zulu, you left just months away from submission. I guess you were too excited to go tell Gogo that she was right all along. Thank you for being an exemplary man. I hope to make your legacy proud and honour the gentleman you were.

PRESENTATIONS ARISING FROM THIS STUDY

- G.D. Mahumane, P. Kumar, Y. E. Choonara and V. Pillay. Bio-architecture-mimicking medical materials: A hybrid NAC-loaded biomaterial scaffolding system for potential biomedical applications. 5TH BRICS Young Scientist Forum. Held 21-25 September 2020. Conference theme: BRICS Partnership of Young Scientists and Innovators for Science Progress and Innovative growth Thematic areas: (i) Ecology, (ii) Materials Science, (iii) Application of Artificial Intelligence in the areas of Ecology and Materials Science. Online meeting. Country host: Russia. (**Oral presentation** and conference abstract (**Appendix B**).

- G. Mahumane, P. Kumar, Y. Choonara, V. Pillay. Synthesis and characterization of N-acetylcysteine-loaded PLGA nanofibers as a neuro-scaffold. Held 17 -19 October 2019. Hosted by the Research Capacity Development (RCD) of the South African Medical Research Council, Cape Town. (**Oral presentation** and conference abstract (**Appendix C**).

- G. Mahumane, P. Kumar, Y. Choonara, V. Pillay. 3D scaffold for neural tissue engineering. 12th Anniversary of the Early Career Scientific Convention held 17-19 October 2018. Hosted by the Research Capacity Development (RCD) of the South African Medical Research Council, Cape Town. (Conference abstract (**Appendix D**).

- G. Mahumane, P. Kumar, Y. Choonara, V. Pillay. Fabrication and characterization of a 3D, hybrid scaffold for neural tissue engineering. 11th Anniversary of the Early Career Scientific Convention held 12-13 October 2017. Hosted by the Research Capacity Development (RCD) of the South African Medical Research Council, Cape Town. (Conference abstract (**Appendix E**).

- G. Mahumane, P. Kumar, Y. Choonara, V. Pillay. Nano-reinforced hydro-filled cryogel scaffold for neural tissue regeneration. 10th Anniversary of the Early Career Scientific Convention held 19-20 October 2016. Hosted by the Research Capacity Development (RCD) of the South African Medical Research Council, Cape Town. (Conference abstract (**Appendix F**).

PUBLICATIONS ARISING FROM THIS STUDY

Research Publications

- Mahumane Gillian Dumsile, Kumar Pradeep, Viness Pillay and Choonara Yahya Essop. (2020). Repositioning N-Acetylcysteine (NAC): NAC-loaded electrospun drug delivery scaffolding for potential neural tissue engineering application. *Pharmaceutics*, 12(10), 934; doi.org/10.3390/pharmaceutics12100934. (Publication abstract in **Appendix G**).

- Mahumane Gillian Dumsile, Kumar Pradeep, du Toit Lisa Claire, Choonara Yahya Essop and Viness Pillay. (2018). 3D scaffolds for brain tissue regeneration: architectural challenges. *Biomaterials Science*, 6: 2812-2837. doi: 10.1039/c8bm00422f. (Publication abstract in **Appendix H**).

ABSTRACT/SUMMARY

Traumatic brain injury (TBI) presents a serious challenge for modern medicine due to the poor regenerative capabilities of the brain, complex pathophysiology, and lack of effective treatment for TBI to date. Current approaches (pharmacological and non-pharmacological) are largely focused on preventing further damage and rehabilitation instead of facilitating regeneration and tissue repair. Although a decellularized brain tissue matrix would be the best choice for a neural tissue engineering scaffold, the limitation brain tissue resource is a great obstacle for the practical application of this type of scaffold (decellularised matrix). Tissue engineered three-dimensional (3D) scaffolds have shown various degrees of experimental success in augmenting cell survival, unfortunately, these biomaterial scaffolds present with various limitations that lead to a lack of successful clinical translation. Hybrid composite scaffolds hold promise for addressing some of the deficiencies of previous biomaterials scaffolds for tissue engineering application. The objective of this work was to prepare a novel neuromimetic three dimensional (3D) 3-in-1 scaffold system in the form of a nano-reinforced hydro-filled cryogel scaffold for neural tissue application. The scaffold was fabricated via a stepwise process whereby electrospun nanofibers where embedded in a polymer solution and crosslinker, incubation at sub-zero temperature (-20°C) to produce a cryogel, followed by filling of the nano-reinforced cryogel with a hydrogel. Fourier-transform infrared spectroscopy confirmed the presence of and interaction between the composite polymer materials in the scaffold. The temperature related observations from DSC and TGA analysis revealed the scaffolds thermal profile to be influenced by the combination of its composites. The degradation temperature of the scaffold was well above the physiological temperature of 37°C, indicative of stability and mechanical strength at ambient and physiological temperatures for potential application as thermostable implants/delivery devices. The hybrid scaffold presented with an interconnected porous structure. A low mass loss of 36.5% was observed after 28 days. This slow degradation is desired and supports the suitability for practical application as an implant in the highly hydrated brain tissue environment. Mechanical characterization using unconfined compression test, demonstrated the scaffold to be viscoelastic, possesses shape memory properties, and a low compression modulus 525Pa. Effect on cell viability and proliferation evaluated by MTT assay showed that the 3-in-1 scaffold was non-toxic to both PC12 and A172 cells and therefore holds promising potential to support neural cell survival.

Histological analysis revealed that the novel 3-in-1 scaffold succesffuly filled the lesion site, maintained tissue-scaffold contact, remained intact with the interconnected pores and was progressively infiltrated with cells and native tissue material throughout the residence period in the brain. Based on the observed results, the synthesized 3-in-1 scaffold properties suggest it has the potential to serve as an integrative and supportive platform for neural tissue engineering application. A 3-in-1 neuromimetic scaffold system is presented herein for application as a novel acellular implant to aid in neural tissue regeneration. This system is unique in the sense that it captures the multi-scale, multi-porous (micro/meso/macro-porous), intricate properties of native ECM (a key component of neural regeneration) in its design. Therefore, the results herein are unique to the composition and architecture of the novel 3-in-1 scaffold design, and thus contribute to potentially furthering knowledge influencing neural tissue regeneration research in comparison to any other previously reported CNS scaffolds in literature.

ACKNOWLEDGEMENTS

I would like to acknowledge the wonderful work that God has and continues to do in my life. This accomplishment is the evidence of his many works and presence in my life.

My family Georginah (mom), Elijah (dad), Pretty (older sister), Sandra (little sister) and Bridgette (niece). You are my heartbeat on earth manifest. I love you all dearly and I am grateful for all that you are. If I were given the choice, I would choose you over and over in all dimensions of my life.

Professor Viness Pillay, you are the intersection of intelligence and instinct manifest. I came to join your research unit (WADDP) after watching you present on the 10th of June 2015 - *Nano-neuro-therapeutics: Unravelling neurodegeneration*. The way you dared to challenge the complexities of neural tissue and the way you presented these complex concepts so accessibly made the lecture a prestigious intriguing event. I immediately came to ask to join you- had to do my PhD with you! I aspire to be at home in the space of innovation as you were. I want to thank you for believing in me and taking a chance on me with your work. This work is an extension of your vision and dreams. I am honoured that you trusted me and all the other students that cross your path to be part of your vision. Your kindness is remarkable, we thank you for this unique growth opportunity.

Professor Yahya Choonara, I am not sure if you intended to, but from observing you over the years, you have taught me valuable lessons about leadership. You are diplomatic and tactful. I used to jokingly describe you to my colleagues as “the technical professor” because you always had a plan, a detailed plan. You are dynamic, your interpersonal skills and emotional intelligence are unmatched, and it is a privilege to have been able to observe and learn from you. I am leaving richer in character because of all of you (my supervisors)

Professor Pradeep Kumar, there is too much to thank you for; the motivation, presence and your careful balance of care and discipline. Everytime I felt overwhelmed you would take the time to challenge my perspective using wisdom from your own experiences. Somehow your stories always helped me dust myself up and reralise that I can do it. You said to me “I believe in you” and that has made all the difference. Thank you for the human touch in your supervision.

Thank you to Phumzile, Sello Ramarumo, Kleinboi, Bafana, Tshidi, WADDP senior scientists and supervisors, postdoctoral researchers and all the other students in the Wits Advanced Drug Delivery Platform for engaging with me, you have contributed dearly to my growth and experience.

Thank you Professor Sandy van Vuuren for the etiquette, professional conduct, work ethic and discipline you taught me while doing my Masters research under your supervision. You have imprinted practical interpersonal skills I depend on grately and daily to this day.

Thank you to Professor Kennedy Erlwanger for the excellent work you have done with regards to your advice, care and excellent surgical expertise.

Thank you to the Central Animal Services (Faculty of Health Sciences, Witwatersrand University, 7 York Road, Parktown 2193, Johannesburg, South Africa) team.

The work was funded by the National Research Foundation (NRF) of South Africa; the South African Medical Research Council (SAMRC) through its Division of Research Capacity Development under the Bongani Mayosi National Health Scholars Program from funding received from the Public Health Enhancement Fund/South African National Department of Health and the SIR Grant; and the University of the Witwatersrand, Johannesburg. To the SAMRC, I believe you were truly heaven sent, a part of Gods provision for where God has guided me. Your investment in the progression of healthcare in South Africa is remarkable ad unmatched. Ngiyabonga kakhulu.

Thank you to the Wits Advanced Drug Delivery Platform, a division of the Wits Health Consortium, for the fellowship award towards this Doctor of Philosophy degree.

The authors are grateful to Evonik Nutrition & Care GmbH, Germany for the ex gratia supply of PLGA (poly(lactic-co-glycolic acid).

TABLE OF CONTENTS

DECLARATION ..... **i**

ANIMAL ETHICS DECLARATION ..... **ii**

DEDICATION ..... **iii**

PRESENTATIONS ARISING FROM THIS STUDY ..... **iv**

PUBLICATIONS ARISING FROM THIS STUDY ..... **v**

ABSTRACT/SUMMARY ..... **vi**

ACKNOWLEDGEMENTS ..... **viii**

TABLE OF CONTENTS ..... **x**

LIST OF FIGURES ..... **xix**

LIST OF TABLES ..... **xxvi**

NOMENCLATURE ..... **xxvii**

CHAPTER ONE **1**

Introduction and motivation for study **1**

1.1. Introduction 1

1.2. Rationale and motivation 3

1.3. Novelty, study aim and objectives 6

1.4. Potential therapeutic applications of the proposed novel 3-in-1 scaffold. 8

1.5. Thesis overview 9

1.5.1. Chapter one: 9

1.5.2. Chapter two:..... 9

1.5.3. Chapter three: 10

1.5.4. Chapter four: 10

1.5.5. Chapter five:.....10

1.5.6. Chapter six:.....10

1.5.7. Chapter seven:.....11

CHAPTER TWO..... 14

3D SCAFFOLDS FOR BRAIN TISSUE REGENERATION: ARCHITECTURAL CHALLENGES..... 14

2.1. Abstract.....14

2.2. Introduction 14

2.2.1. Regeneration potential of the central nervous system 14

2.2.2. Therapeutic interventions for neurotrauma 16

2.2.3. Trends in 3D scaffolding for neural tissue engineering/application.....17

2.3. Neural tissue-based critical architectural design challenges for neuromimicry in 3D scaffolds 26

2.4. Macro-architectural profile of 3D scaffolds: Biomimicry of tissue properties, and translational potential.....27

2.5. Micro-architectural profiles of 3D scaffolds: compartmentalization, multi-scaling, mechanical anisotropy 30

Neuromimetic compartmentalization and multiscale organizational architectural features 30

2.6. Influencing neural cell fate through multi-scaling features 33

Mimicking neuromechanical anisotropy through architecture....34
2.7. Engineering neuromimetic architectures....38
2.8. Biomaterials for 3D neuro-scaffolding....43
Biocompatibility....44
Biodegradability....45
Biomaterial swelling to enhance architectural performance....46
2.9. Processbility....48
2.10. *In vivo* tissue integration and performance of 3D scaffolds....48
2.11. Translational potential of 3D scaffolds with in vivo experimental models of TBI..51
2.12. Chapter two summary....52
2.11. Conflicts of interest....54
2.12. Acknowledgements....54

CHAPTER THREE.... 66

Repositioning N-acetylcysteine (NAC): NAC-loaded electrospun drug delivery scaffolding for potential neural tissue engineering application.... 66

3.2. Introduction....66
3.3. Materials and Methods....69
3.3.1. Materials....69
3.3.2. Fabrication of the NAC-loaded electrospun system....70
3.3.3. Characterization of the NAC-loaded electrospun system....70
3.3.4. NAC-loading, entrapment efficiency, and NAC release kinetics....74

3.3.5. Effect of NAC loading in electrospun nanofiber system on PC12 and A172 cell viability and proliferation *in vitro*.....74

3.4. Results and Discussion 75

3.4.1. NAC-polymer interaction analysis by fourier transform infrared spectroscopy (FTIR) 75

3.4.2. Analysis of NAC loading on thermal stability of electrospun system 76

3.4.4. Morphological analysis of electrospun nanofibers 79

3.4.5. Mechanical Characterization of NAC-Loaded Nanofibers 82

3.4.6. Analysis of NAC-loading, encapsulation, and cumulative NAC release.....83

3.4.7. Effect of NAC-loading on cell viability and proliferation 86

3.5. Conclusions 87

3.6. References 88

CHAPTER FOUR..... 93

Fabrication and characterization of a crosslinked GELATIN-ELASTIN HYDROGEL..... 93

4.1. Introduction 93

4.2. Materials and Methods.....95

4.2.2. Characterization of hydrogel 95

4.2.3. Swelling ratio 95

4.2.4. Rheological evaluation of the viscoelastic properties of the protein based hydrogel 95

4.3. Results.....96

4.3.1. Stabilizing Interactions of crosslinking: FTIR, XRD, thermal stability, thermal transitions, swelling ratio of hydrogel. 96

4.3.1.1. Fourier-transform infrared spectroscopy analysis of hydrogel 96

4.3.1.2. X-ray powder diffraction analysis of Ge-BDDE-Ela hydrogel 97

4.3.1.3. Thermogravimetric analysis 98

4.3.1.4. Differential scanning calorimetry 100

4.3.1.5. Swelling characteristics of the hydrogels....101

4.3.1.6. Mechanical analysis of Ge-BDDE-Ela hydrogel....103

4.4. Chapter four summary 105

4.5. References 106

CHAPTER FIVE....109

Fabrication and characterization of a novel hybrid 3-in-1 nano-reinforced hydrofilled cryogel scaffold....109

5.1. Introduction....109

5.2. Materials and methods....112

5.2.1. Fabrication of a novel 3-in-1 nano-reinforced, hydro-filled scaffold 112

5.2.2. Characterization of 3-in-1 scaffold 113

5.2.3. Mechanical and swelling ratio and mass loss 113

5.2.4. Cytotoxicity: PC12 and A172 cell culture and MTT assay....114

5.3. Results and discussion 115

5.3.1. FTIR: Analysis of vibrational molecular changes of the chemical constituents and 3-in-1 scaffold....115

5.3.2. Thermogravimetric analysis 118

5.3.3. XRD and Differential scanning calorimetry analysis 119

5.3.4. Morphology, swelling and morphological properties 123

5.3.4.2. Effect of freezing temperature HA-PLL cryogel structure 124

5.3.5. Biomaterial swelling and mass loss. 133

5.3.6. Biomechanical properties 136

5.3.7. Cell cytotoxicity evaluation of scaffold 140

5.8. Chapter five summary 143

5.9. References 143

CHAPTER SIX 150

***In vivo* analysis of the novel 3-in-1 scaffold implant in Sprague-Dawley rat TBI model 150**

6.1. Introduction 150

6.2. Materials and Methods 151

6.2.1. Animal procurement 151

6.2.2. Animal care/pre-surgical preparation of animals 151

6.2.3. Experimental design for an intervention study 151

6.3.4. Design of *in vivo* experimental study 152

6.3.4.1. Description of surgical procedures with recovery 152

a) Surgical preparation 152

b) Craniectomy 153

c) Corticectomy 153

d) Injury site closure and post-surgical recovery 153
e) Terminal procedure 155
6.3.5. Histomorphological analysis of brain samples 156
6.3.6. Behavioral assessment 156
6.3.6.1. The cylinder test (limb use asymmetry) 156
6.3.6.2. Adhesive removal test 156
6.3.6.3. Modified Neurological severity score (mNSS) 157
6.3.6.4. Ladder rung 159
6.3.6.5. Statistical analysis 159
6.4. Results and discussion 159
6.4.1. Animal survival, recovery and qualitative behavioral observations and study duration 159
6.4.2. *In vivo* effect of acellular 3-in-1 hybrid scaffold intervention 160
6.4.2.1. *In vivo* implantation and decreased bleeding 160
6.4.2.2. Shape of brain with or without scaffold implantation 162
6.4.2.3. Cell infiltration and tissue formation after scaffold implantation 162
6.4.2.4. In vivo 3D structural support, architectural integrity and stability 163
6.4.2.5. Scaffold intervention on lesion cavity and surrounding tissue 163
6.4.2.6. Architectural vasculature: decreased bleeding, tissue integration potential .164
6.4.3. Recovery and behavioral analysis 167
6.4.3.1. Cylinder test 167
6.4.3.2. Adhesive removal 168
6.4.3.3. Modified Neurological severity score (mNSS) and ladder rung 170

6.4.4. Chapter six summary 171

6.4.5. References 173

CHAPTER SEVEN.....177

Study conclusion, recommendations and future outlook 177

7.1. Conclusions 177

7.2. Recommendations.....179

7.3. Future Outlook.....180

APPENDIX A 183

Ethics clearance certificate.....183

APPENDIX B 184

Conference proceeding: 5th BRICS Young Scientist Forum (2020) 184

APPENDIX C 186

Conference proceedings: South African Medical Research Council (2019).....186

APPENDIX D 188

Conference proceedings: South African Medical Research Council (2018).....188

APPENDIX E.....190

Conference proceedings: South African Medical Research Council (2017).....190

APPENDIX F.....192

Conference proceedings: South African Medical Research Council (2016).....192

APPENDIX G 194

Research paper publication: doi.org/10.3390/pharmaceutics12100934.....194

APPENDIX H 195

Literature review publication: doi.org/10.1039/C8BM00422F 195

APPENDIX I……..……196

Details of drug release for Chapter 3……..196

LIST OF FIGURES

Figure 1.1. Schematic conceptualization of design for 3-in-1 nano-reinforced hydro-filled cryogel scaffold for neural regeneration following implantation into cavity site following TBI.. 6

Figure 1.2. A schematic outline of the study for the design and development of a novel 3-in-1 scaffold system for neural tissue engineering application. 8

Figure 2.1. Parameters governing recent multifunctional 3D neural scaffold designs. This figure is reused from Nanomedicine: Nanotechnology, Biology, and Medicine,11, Zhu and co-workers (Zhu et al., 2015). Highly aligned nanocomposite scaffolds by electrospinning and electrospraying for neural tissue regeneration, pp. 693-704, 2015, with permission from Elsevier. 18

Figure 2.2. Schematic outline of the review paper for the evaluation of 3D scaffolds for neural regeneration and repair. 19

Figure 2.3. Analysis of the reviewed 3D scaffold experimental studies reported in Table 2.1 25

Figure 2.4. Schematic depiction of the neural environment. (a) Spatial arrangement of the brain tissue compartments (cyan cells = neurons, purple cells = astrocytes, zoom-in subplot: ECM = a net-like cover attached to the surface of neural cells. (b) Enlarged view of the zoom-in subplot of the brain ECM in (a). The net-like cover = hyaluronic acid (HA) secreted by cells acting as a trestle for the ECM net-like structure. The penniform objects crossing the gaps between the HA chains = glycoproteins. Orange triple-circle = tenascin linking glycoproteins

up. Multi-coloured single circles = components of interstitial fluid (ISF), e.g., water molecules (H_2O), extracellular vesicles (EVs), matrix metallopeptidase (MMP), glucose (Glu), dopamine (DA), and tissue plasminogen activators (tPAs). This figure is reused and reprinted from Progress in Neurobiology, Lei and co-workers (Lei et al., 2017). The brain interstitial system: Anatomy, modelling, *in vivo* measurement, and applications, 2016, under the terms of the Creative Commons Attribution License (CC BY).....27

Figure 2.5. Scaffold architecture affects cell binding and spreading. (a and b) Cells binding to scaffolds with microscale architectures flatten and spread. (c) Scaffolds with nanoscale architectures possess larger surface areas for protein absorption, presenting many more binding sites to cell membrane receptors. Figures 2.5a-c are reused from Science, 310(5751), Stevens and George (Stevens and George, 2005). Exploring and engineering the cell surface interface, pp. 1135-1138, 2005, with permission from the American Association for the Advancement of Science.....34

Figure 2.6. Representation of substrate-directed cell fate (images not to scale). (a) Soft isotropic force resulting in a spherical cell shape and (b) spreading on stiffer substrate. (c) Random distribution of cells in isotropic conditions while (f) cell elongation is observed under anisotropic strain.(d) Cell protrusions in multiple directions is induced with biaxial strain whereas (e) uniaxial strain induces an elongated cell shape. This figure is reused and reprinted from Journal of Biomedicine and Biotechnology, Nava and co-workers (Nava et al., 2012). Controlling self-renewal and differentiation of stem cells via mechanical cues, pp. 1-12, 2012, under the terms of the Creative Commons Attribution License. 35

Figure 2.7. Examples of topographical design features incorporated into 3D scaffolds represented by (a) squares, (b) grooves, (c-d) pores in polymeric scaffolds and (e) random and (f) aligned electrospun fibrous mats. The scale bars for figures 2.7e and 7f measure 10 µm.

Figure 2.7a-d is reused and reprinted from Biotechnology Advances, 30(1), Martino and co-workers (Martino et al., 2011). Stem cell-biomaterial interactions for regenerative medicine, pp.338–351, 2011, with permission from Elsevier. Figure 2.7e-f is reused and reprinted from from Scientific Reports, 6(1), Beliveau and co-workers (Beliveau et al., 2016). Aligned nanotopography promotes a migratory state in glioblastoma multiforme tumor cells, p.26143, 2014, under the terms of the Creative Commons Attribution 4.0 International License. 37

Figure 2.8. An example of a typical 3D tissue bioprinting process. The process is simple; design of the printed tissue is guided by an image of the tissue (step 1) followed by choice of design approach (step 2). This is followed by input with suitable material and biological matter (steps 3 and 4). Feeding the instrument with the CAD and suitable materials yields a 3D printed tissue-mimetic construct (steps 5 and 6). This figure is reused and reprinted from Nature Biotechnology, 32(8), Murphy and Atala (Murphy and Atala, 2014). 3D bioprinting of tissues and organs, pp. 773-785, 2014, with permission from Nature Publishing Group.....43

Figure 3.1. Fourier transform infrared (FTIR) spectra of the native materials (NAC, PLGA), electrospun PLGA and NAC-loaded nanofiber. NAC: N-acetylcysteine, PLGA: poly(lactic-co-glycolic acid).....76

Figure 3.2. Thermogravimetric curves of PLGA (bulk), PLGA nanofibers, NAC and NAC/PLGA nanofibers. 77

Figure 3.3. (**a**) X-ray diffraction patterns of PLGA nanofibers, NAC, and NAC/PLGA nanofibers. (**b**) DSC curves of bulk PLGA, PLGA nanofibers, NAC and NAC/PLGA nanofibers. 79

Figure 3.4. Scanning electron micrograph of electrospun nanofibers. (a,b) Beaded fibers are formed at low concentrations: (a) 10% and (b) 15%. (c) Bead-less nanofibers were formed at higher concentrations 20%. (d): The critical entanglement concentration was noted at 18% PLGA. (e) The incorporation of NAC in the nanofibers did not alter nanofiber formation at 18%. 80

Figure 3.5. Equilibrium (a) adsorption/desorption isotherms and (b) pore size distribution of PLGA and NAC/PLGA nanofibers. 82

Figure 3.6. Stress–strain curves of the PLGA and NAC/PLGA nanofiber matrices obtained under a test speed of 0.167 mm/s. 83

Figure 3.7. Water contact angle images of (a) NAC-free nanofibers and (b) NAC-loaded nanofibers (c) and changes within a 5-min period. (d) *In vitro* drug release (percent cumulative drug released) profile of NAC from PLGA nanofibers in PBS at 37 °C observed over 10 days (240 h).....85

Figure 3.8. Cell viability and proliferation on control, and scaffold treatment of (a) PC12 and (b) A172 cell lines after 72 h incubation. Indirect cytotoxicity evaluation of various treatments based on the viability of PC12 and A172 cell lines that were cultured for 72 h.....87

Figure 4.1. FTIR spectra of Gelatin, Elastin, BDDE, non-crosslinked Ge-Ela gels and BDDE crosslinked hydrogels (Ge-BDDE-Ela).....97

Figure 4.2. X-ray diffraction (XRD) pattern of gelatin, elastin and Ge-BDDE-Ela hydrogel (4:1 Ge-Ela ratio).....98

Figure 4.3. Thermogravimetric analysis (TGA) thermograms of Gelatin, Elastin, Ge-Ela gel and crosslinked Ge-BDDE-Ela hydrogel. 99

Figure 4.4. Differential Scanning Calorimetry (DSC) curves of gelatin, elastin, uncrosslinked gel (Ge-El) and crosslinked hydrogel (Ge-BDDE-Ela).....101

Figure 4.5. Swelling ratios of the hydrogels in aCSF. 103

Figure 4.6. The Rheological mechanical properties of the hydrogels (a, c) dynamic moduli, G′ and G″, as function of frequency for the Ge-BDDE-Ela hydrogel at 37 °C. (b, d) Linear material functions, G* and η*, of the Ge-BDDE-Ela: a constant G* and a η* that increased with decreasing frequency. a,b =4:1 Ge-Ela ratio and c,d= 10:1 Ge-Ela ratio. 105

Figure 5.1. Schematic of the biomaterial composition and fabrication process and to achieve the proposed novel 3-in-1 scaffold.....112

Figure 5.2. Spectra showing the FTIR spectra of the native materials and scaffold. 117

Figure 5.3. Thermogravimetric analysis curves of composite materials and scaffold. 119

Figure 5.4. b) Differential Scanning Calorimetry (DSC) thermograms of native polymers gel (gelatin), Ela (elastin) and scaffold recorded at 10 °C/min between 10°C and 300°C. 122

Figure 5.5 a) Filament-like internal cryogel structure of BDDE-crosslinked HA-PLL cryogel at a 4:1 ratio. scale bar:200µm. b) Sheet-like internal cryogel structure of BDD- crosslinked HA-

PLL cryogel at a 10:1 ratio. scale bar: 320µm.c) result of cryogelation at -80°C d) result of cryogelation at -20°C. 126

Figure 5.6. a) Lyophilised cryogel b) hydrated cryogel. c) Lyophilised scaffold d) hydrated scaffold. Black arrows indicate to the nanofibers. Swelling ratios of scaffolds in aCSF. Error bars represent standard deviations for 3 parallel measurements. e) Percentage mass loss of 3-in-1 scaffolds over a 28 day period in aCSF. 136

Figure 5.7. a) Compression moduli of composite hybrid scaffold in hydrated and dry state; b) Typical compressive stress–stain curves of the dry and hydrated scaffolds; c) Compression stress-strain curve of hydrated and d) dry scaffold (=3 load cycles).....139

Figure 5.8. The Rheological mechanical properties of the scaffold (a) dynamic moduli, G′ and G″ as a function of frequency. (b) Linear material functions, G* and η*, of the scaffold at 37 °C: a constant G* and a η* that increases with decreasing frequency. 140

Figure 5.9. Cell cytotoxicity on control, and scaffold treatment of a) PC12 and b) A172 cell lines after 72 hours incubation. 142

Figure 6.1. Surgical procedures with recovery. a) The head of the rat was shaved between the ears to expose the scalp followed by sterilization with 70% ethanol. b) craniectomy, the coordinates were: coordinate A=+4,+1; coordinate B=−2,+1; and coordinate C=+4, +6. c) corticectomy. c) Corticectomy. d) Scaffold implantation. e) Scaffold in lesion cavity. f) injury site closure and post-surgical recovery.....161

Figure 6.2. (a-f) Gross brain images before preservation in formalin and sectioning illustrating the visual difference at 3, 14 and 28 days post-TBI. (a*- f*) Hematoxylin and eosin (H&E)-stained sections of brain tissue without (a*, c* and e*) and with scaffolds (b*, d* and f*) implants at 3, 14 and 28 days post-TBI. Sham brain sections postoperative 3 days Scale bar: 1mm. b) Scaffold intervention brain sections postoperative 3 days Scale bar: 1mm. c) Sham brain sections postoperative 14 days Scale bar: 1mm. d) Scaffold intervention brain sections postoperative 14 days Scale bar: 1mm. e) Sham brain sections postoperative 28 days Scale bar: 500µm. 166

Figure 6.3. Cylinder test (Limb-use asymmetry), a) Uninjured rats spontaneously use both forelimbs, while b) post TBI (sham and scaffold groups) rat's exhibit reliance on the ispilatelateral forelimb. c) Asymmetries in forelimb use in the "cylinder" task assessment. Scores above 0.5 indicate a greater reliance on the unimpaired forelimb (ipsilateral). 168

Figure 6.4. Effect of sensory experience on the recovery of tactile sensitivity. a) Adhesive tape plied on the rat paw. b) Tactile abilities post-TBI were assessed using the adhesive removal test in sham versus intervention group. Dash lines indicate time taken to notice tape while solid lines indicate time to remove tape. 170

Figure 6.5. Modified Neurological Severity Score (mNSS) observations and results. a) Progression of improvement on beam balance test, initially animals attempted to balance hugging the beam with tow limbs but failed rusting in spinning and falling off, b) progressing to hugging the bean with both limbs but the contralateral limbs slide off the beam due to weakness. c) Photograph indicating a total miss in the contralateral hind limb in the ladder rung task. Total miss (d) Modified Neurological Severity Scores. 171

LIST OF TABLES

Table 2.1. Recent 3D scaffolds and their outcomes following *in vivo* assessment investigated for the repair of brain tissue (2011-onwards) 20

Table 2.2. Macro/micro architectural profiles of acellular biomaterial scaffolds in comparison to brain tissue.....30

Table 2.3. Summary of critical architectural design parameters for 3D neural scaffolds observed in this review.....53

Table 3.1. Parameters and settings employed during degassing and analysis of the nanofibers 72

Table 3.2. Surface area and porosity criteria.....73

Table 5.1. The bulk and macro/microarchitectural properties of the scaffolds and their architectural similarity to brain ECM features. The alphabets e.g. ***a, b c…"*** in the last two columns indicate the corresponding features of the scaffold and brain ECM structure. 129

Table 6.1. Modified Neurological Severity Scores (mNSS) is reused and reprinted from PLoS ONE. Yao and co-workers (Yao et al., 2015). Transdifferentiation-Induced Neural Stem Cells Promote Recovery of Middle Cerebral Artery Stroke Rats, 2015 under the terms of the Creative commons Attribution License (CC BY). 158

NOMENCLATURE

3D	Three dimensional
2D	Two dimensional
aCSF	Articifical cerebrospinal fluid
AESC	Animal Ethics Screening Committee
BBB	Blood-Brain Barrier
BDDE	1,4-butanediol diglycidyl ether
BDNF	Brain-Derived Neurotrophic Factor
BET	Brunauer–Emmett–Teller
Biomaterial	For the purpose of the study, biomaterial shall mean the pre-processed structural materials (polymers (natural and synthetic) used to fabricate the scaffold structure.
CAS	Central Animal Services
DEE	Drug Entrapment Efficiency
DES	Donor Equine Serum
DMEM	Dulbecco's Modified Eagle Medium
DSC	Differential Scanning Calorimetry
CAS	Central Animal Services
CNS	Central nervous system (CNS)
CT	Computed tomography
ECM	Extracellular matrix
Ela	Elastin
ELISA	Enzyme linked immunosorbent assay
FBS	Foetal Bovine Serum
FTIR	Fourier Transform Infrared
Ge	Gelatin
GAG	Glycosaminoglycans
HA	Hyaluronic acid
ECM	Extracellular matrix
FBS	Foetal Bovine Serum
ISF	Interstitial fluid
MRI	Magnetic resonance imaging
MTT	3-(4,5-Dimethylthiazol-2-yl)-2,5-Diphenyltetrazolium Bromide

NAC	N-Acetylcysteine
NaOH	Sodium hydroxide
NGF	Nerve Growth Factor
P/S/AB	Penicillin/Streptomycin/Amphotericin B
PBS	Phosphate buffered saline
Scaffold	For the purpose of the study, scaffold shall mean the acellular structures (e.g. nanofibers, hydrogel, cryogel) obtained from the processing of the biomaterials.
SEM	Scanning electron microscopy
TA	Texture Analysis
TBI	Traumatic brain injury
Td	Degradation temperature
Tg	Glass transition temperature
TGA	Thermogravimentric analysis
Tm	Melting temperature
UV	Ultraviolet
XRD	X-ray Diffraction
VEGF	Vascular Endothelial Growth Factor
WHO	World Health Organization

CHAPTER ONE

INTRODUCTION AND MOTIVATION FOR STUDY

1.1. Introduction

Traumatic brain injury (TBI) is one of the greatest contributors to death and disability among all trauma-related injuries globally (Dinsmore, 2013). The global incidence of traumatic brain injury (TBI) is reported as ~200 in 100,000 with a mortality of 20 per 100,000 people (Reilly, 2007). Despite its frequency, the indices and impact of TBI are largely underestimated due in part to the variable way statistics are recorded, the lack of formal trauma registries, figures based on admission (excluding include pre-hospital deaths, which account for ≈50% of road trauma deaths) (Goldstein et al., 2017; Reilly, 2007; Rubiano et al., 2015). Therefore, traumatic brain injury is somewhat of a silent global epidemic for which interventions and surveillance are sorely lacking (formal registers, funding, therapies, dedicated research centers, and human resource). There is immense opportunity for researchers worldwide to contribute to the many problems surrounding TBI.

Traumatic brain injury is damage caused to the brain tissue as a result of an external insult (Dinsmore, 2013). The resultant lesion and severity of the injury is dependent on the type of external insult such as falls, motor vehicle accidents, assaults and gunshot wounds (Crandall, 2016). Irrespective of the external insult, the resultant internal neuronal changes in connectivity, integrity, and degeneration from the primary injury, complicated by further secondary injury are of major concern. This is because TBI often results in irreversible damage due to the limited regenerative ability of the central nervous system (CNS) and the lack of effective therapies to aid in the regeneration of neurons after injury (Conejero-García et al., 2015; He et al., 2012; Jurga et al., 2011).

There are several impediments to neural regeneration of brain tissue following TBI. One of the impediments is the formation of a cavity at the injury site, which severs connections and creates a distance between neurons (Clausen et al., 2014; Ellis-Behnke et al., 2006, p.; Struzyna et al., 2015). The second impediment is the inhibitory environment created at the injury site. In response to injury, there is the formation of a glial scar, accumulation of myelin-associated inhibitors, and the secretion of free radicals via the Blood-Brain Barrier (BBB) resulting in secondary injury (Ellis-Behnke et al., 2006; Huang et al., 2014; Silver and Miller,

2004; Subramanian et al., 2009). This is a necessary response to injury; the brain forms this glial scar in order to protect the surrounding healthy tissue from secondary damage. However, this is at the cost of regenerative function (Silver and Miller, 2004). The resulting problem is a lack of structural support to aid in axonal guidance to connect with other neurons past the cavity site and the inability of neural cells to penetrate the scar tissue in order to connect with other neurons; proliferate and remain viable in the hostile environment (inhibitory ECM molecules, inflammation, necrosis, ischemia, free radicals). In addition, TBI sites present with 'penumbra' zones; these are the areas surrounding the primary lesion prone to secondary injury if timely treatment is not administered (Wang et al., 2014). Therefore, future treatment approaches would benefit greatly, by focusing on immediate intervention strategies as to prevent glial scar formation and irreversible damage to tissue in the penumbra zones.

Current treatment and neural regeneration strategies include, autologous grafts, neural electrodes, growth factors, neuroprotective agents/pharmacological treatment, cell replacement therapy and tissue engineered scaffolds (Clausen et al., 2014; Sirivisoot et al., 2014; Subramanian et al., 2009; Thompson et al., 2015). However, these therapies fall short due to various limitations while others show great promise for future intervention studies. For example, stem cells show a low survival rate without a supportive matrix at the lesion site, while molecules (growth factors and pharmaceutical drugs) tend to show a low residence time at the site (Wong et al., 2008). On the other hand, numerous studies have shown promising results, improved survival of stem cells, and improved neural regeneration outcomes with polymeric scaffolds (e.g. hydrogels, and nanofibers, sponges) in animal models (Jurga et al., 2011, p. 200; Sun, 2016; Xiong et al., 2009). In all these previous studies, a number of architectural features have been indicated to influence neural regeneration, such as pore size, interconnected pores, permeability, and topography (two dimension (2D) or three dimension (3D). This shows that there is great potential for optimization of scaffold features for a more optimal neural tissue regeneration outcome. This is a practical, achievable outcome, given the plethora of biocompatible, biodegradable, polymeric biomaterials and fabrication techniques (e.g. 3D printing, peptide self-assembly, electrospinning, cryogelation, phase separation) available for manipulation.

Mounting literature evidence has identified the extracellular matrix (ECM) as the key structure to neural regeneration. The ECM is a unique environment that provides structural support and cues that can regulate differentiation, axonal growth and cell-cell communication (Das et al., 2016; Geckil et al., 2010; Jurga et al., 2011; Kathuria et al., 2009). Hence, the unique environment of the ECM may therefore be instrumental to informing novel approaches in the

creation/design of a pro regenerative environment to provide tissue contiguity and support of neural tissue regeneration at the cavity/injury site. In consideration of the ECM properties and influence on regeneration, scaffold architecture may well be an indispensable feature that presents opportunity for improvement for an optimal regeneration outcome. This may be the key to maximizing the neural regeneration outcome. Mimicking the multi-scale organization of brain tissue is a major challenge, considering the complex organization of the central nervous system and its ECM. In addition to innate tissue complexity, TBI lesions vary in size and also in shape. This makes it challenging to determine ideal scaffold architecture from a laboratory and clinical application perspective. The fate of the neuronal cell is largely dependent on its niche environment, which is more than just the ECM. This niche comprises cells, blood vessels, growth factors, and the ECM (Wang et al., 2014). While, scaffold design approach can be used to mimic structural cues, the therapeutic effect of scaffolds can be improved through the incorporation of biological cues. Neurotrophic factors such as Vascular Endothelial Growth Factor (VEGF) and Brain-Derived Neurotrophic Factor (BDNF), which serve as a biological stimulus through the promotion of angiogenesis and neuronal survival respectively (Liu et al., 2016; Wang et al., 2011; Zhang et al., 2016).

This study aims to bridge the gap between neural tissue engineering and neural regeneration principles, through the design of a novel nano-reinforced hydro-filled cryogel scaffold for neural tissue regeneration after TBI. This will be undertaken with the objective of creating a biomimetic implantable scaffold that will serve as a temporary framework to support the adhesion, proliferation, differentiation, and repair of native nerve cells at the TBI site. The ‘temporary’ characteristic of the framework will be achieved by the use of biodegradable polymeric biomaterials that can be absorbed by the surrounding tissue without the need for surgical removal of the neuroactive scaffold once implanted. For the purpose of this study, a scaffold refers to the 3D biomaterial prior to cell seeding, whereas tissue engineering refers to the combination of the cells, signals (e.g. growth factor) and a 3D biomaterial (O’Brien, 2011).

1.2. Rationale and motivation

As previously noted, the ECM is a key structure to understanding neural tissue regeneration. The natural ECM is an insoluble, interlaced network embedded in a hydrated gel-like substrate (Lodish et al., 2000). Therefore, the proposed 3-in-1 system presents a novel multi-scale, multi-porous design approach in an effort to closely mimic the structural features of the natural ECM. The scales have previously been categorized into macro (10^{-1} – 10^{-3} m), micro (10^{-3} – 10^{-6} m) and nano (10^{-6} – 10^{-9} m) (Lee et al., 2008). The cryogel component represents the macro-scale portion of the system analogous to the macro-scale tissue architecture of the ECM. The ‘macro’

scale affects the size and overall shape of the scaffold, which ultimately affects the ability to handle the scaffold in a laboratory or clinical setting, fill the lesion cavity, integrate with surrounding tissue and produce regenerated tissue of appropriate size (Lee et al., 2008). The hydrogel component represents the micro-scale portion of the system analogous to the micro-scale tissue architecture of the ECM. According to Lee and coworkers, cells recognize structures with comparable dimension (10 – 100 µm) (Lee et al., 2008). Therefore, the micro-scale is anticipated to have an effect on cell behavior and support cell migration and transport, while the porosity allows free flow of nutrients, gases and metabolic waste. Cell-ECM interaction is achieved by the interaction of cells with nano-scale proteins/components (e.g. collagen fibrils of 50 – 200nm diameter) (Lee et al., 2008; McMurtrey, 2015; Rivet et al., 2015). Therefore, the nano-reinforcement represents the nano-scale, portion of the system analogous to the nano-scale tissue architecture of the ECM anticipated to significantly influence cell-scaffold interaction properties such as cell adhesion.

This design strategy will be applied in the fabrication of a 3-in-1, 3D, nano-reinforced hydro-filled cryogel scaffold implant for neural regeneration following TBI. The proposed mechanism of innovation is by utilizing a 3-in-1 system wherein; nanofibers will be “in-process” embedded into a cryogel scaffold, followed by filling of the macro-microporous architecture with an ECM-mimicking hydrogel for neural tissue engineering (Figure 1.1.).

A nano-reinforced cryogel will be pre-designed into a 3D, stable macro-microporous architecture. This interconnected porous network multi-porous design is anticipated to facilitate the incorporation of multi-scaled range of tissue forming processes and structures. These include nutrient and gaseous exchange, migration of cells, and secretion of ECM by cells, axonal extension, and penetration by blood vessels at the lesion site following implantation. This highly porous interconnected structure ideal for migration and nutrient flow. However, this is at the cost of mechanical integrity as the more pores there are, the less material present and therefore the lower the overall mechanical strength of the scaffold. Therefore, nano-reinforcement (e.g. embedding nanofibers in the macro-porous cryogel matrix) will preserve the mechanical strength threatened by the high porosity of the design. The mechanical stability of the structure will ensure structural integrity of the 3D architecture and aid in the easy handling of the 3-in-1 scaffold system during implantation.

Implantation of this nano-reinforced cryogel structure at the lesion site might lead to withdrawal of fluids from the surrounding tissue leading to dehydration of surrounding tissue. Empty cryogel pores might lead to attachment of cells against the scaffold walls forming a flat

monolayer and possible 2D growth instead of a 3D arrangement as there is no support at the pore center. Looking at native brain tissue, the cells are surrounded by a hydrated matrix (ECM) which allows them to be entrapped, migrate, and interact (Gattazzo et al., 2014). Therefore, an ECM mimicking hydrogel will be incorporated into the structure to mimic this *in vivo* cell growth condition enabling 3D arrangement. Large pore size can lead to areas with poor cell seeding (Lee et al., 2008). Therefore, filling the large cryogel pores with the ECM mimicking hydrogel will facilitate migration efficiency within the entire scaffold system. The advantage of this "hydro-filled scaffold" is that the hydrogels are hydrated, 3D porous networks that will act to physically entrap the cells throughout the entire matrix. Within this hydrogel, the cells can maintain their rounded shape 3D shape as they won't be confined to attachment at the cryogel wall, proliferate within the hydrogel and increase cell density. The hydrogel, will be dispersed throughout the entire scaffold, dispersion of cells within the entire scaffold with interconnected pores for cell-cell communication.

Independently, hydrogels do not possess the mechanical strength for surgical implantation and manipulation (Gong et al., 2007). Independently the porous cryogel architecture provides the mechanical support but is missing the ECM mimicking environment that the hydrogel can provide. This 3-in-1 system construct enables utilization of the advantages of both porous scaffold architecture and ECM mimicking hydrogels, while limiting the downside of each individual component. The result is a 3-in-1 system with a 'stiffer' 3D architecture (nano-reinforced cryogel) and a 'softer' ECM-mimicking filling (hydrogel) with the following characteristics: (i) a pre-designed 3D architecture that will serve as physical cues to native 3D tissue, (ii) mechanical strength to ensure structural integrity during processing and implantation. (iii) an analogous ECM-mimicking hydrogel to ensure entrapment of cells throughout the scaffold and to keep the scaffold hydrated to avoid dehydration of surrounding tissue, (iv) a 3-in-1 scaffold system that can facilitate the potential incorporation of therapeutics within its structure in an effort to maximize regeneration outcome.

This scaffold will be used to treat penetrating TBI (< 1 cm cavity size). Stereotaxic surgery will be used to insert the implant into the brain. The highly compressible spongy scaffold will be surgically implanted into the injury cavity (Figure 1.1.). Surgical implantation will allow for targeted localized delivery of scaffold with minimal disturbance/injury to non-injured tissue. Upon implantation, the 3-in-1 scaffold system is anticipated to take the shape of and fill the cavity due to its elastic modulus and provide a hydrated environment (hydrogel component) while maintaining its 3D architecture (nano-reinforced cryogel) at the cavity site. The scaffold will create an interface with the brain parenchyma surrounding the lesion. This interface allows

the scaffold to act as a biocompatible bridge for neural extension and reorganizing neurons as they grow across the cavity. In addition, the interface will provide the mechanical and cues to guide migration of endogenous stem cells thereby augmenting endogenous neurogenesis. Finally yet importantly, the interface is anticipated to pacify triggering of secondary effects (e.g. inflammation) and gliosis in the surrounding tissue following implantation, as the implant is meant to remain in the parenchyma for several weeks while being slowly degraded by the body and being replaced by new tissue. Selected non-toxic/low toxicity biodegradable, biocompatible polymers (such as polysaccharides, proteinaceous polymers, soluble derivatives of polysaccharides, soluble derivatives of proteinaceous polymers, polypeptides, polyesters) may be used for fabrication, based on desired scaffold properties. Biodegradable materials are prioritized as they present the advantage of implantation without the need for surgical removal, thereby avoiding unnecessary surgical injury to the healing/regenerating brain tissue post implantation. Preference will be given to polymer properties in consideration of the milieu of the injury site following TBI. For example, polymer properties such as the anti-oxidant properties of polypyrrole and polyaniline which is ideal for scavenging free radicals to minimize scar formation at the lesion site *in vivo* (Subramanian et al., 2009).

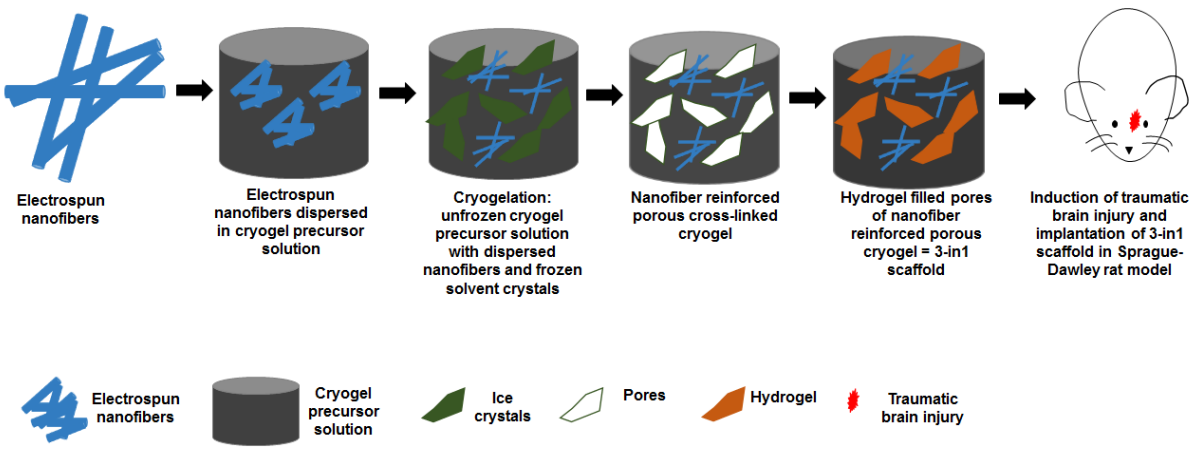

Figure 1.1. Schematic conceptualization of design for 3-in-1 nano-reinforced hydro-filled cryogel scaffold for neural regeneration following implantation into cavity site following TBI.

1.3. Novelty, study aim and objectives

The aim of the study is to design a 3-in-1 nano-reinforced hydro-filled cryogel scaffold system with properties of a neural tissue regeneration milieu following TBI. A 3-in-1 cryogel scaffold system is proposed for application as a novel acellular implant to aid in neural tissue regeneration. This system is unique in the sense that it captures the multi-scale, multi-porous (micro/meso/macro-porous), intricate properties of native ECM (a key component of neural regeneration) in its design. Therefore, it is anticipated to yield unique results that may significantly contribute to and potentially further knowledge influencing neural tissue

regeneration research in comparison to any other previously reported CNS scaffolds in literature.

Figure 1.2. Conveys a schematic outline of the study for the design and development of the novel 3-in-1 scaffold system for neural tissue engineering application. The aforementioned aim will be achieved with following objectives:

a. To identify and suitable fabrication methods and candidate polymeric and non-polymeric material to synthesize:
    a. Nanofibers
    b. Hydrogel
    c. Cryogel and
    d. Novel 3-in-1 3D cryogel scaffold to facilitate native neural tissue regeneration.
b. To perform physicochemical and physicomechanical characterisation analyses utilizing techniques such as; Fourier Transform Infrared (FTIR) spectroscopy, and X-ray diffraction (XRD), Scanning Electron Microscopy (SEM), Differential Scanning Calorimetry (DSC), Textural analysis (TA), Thermogravimetric (TGA).
c. To evaluate the effect of the proposed scaffold on the viability and proliferation of neuronal cell lines.
d. To evaluate the *in vivo* potential of the scaffold as a brain tissue implant, biocompatibility and investigating the dynamics between the scaffold and native brain tissue using histomorphology and functional recovery outcomes in a Sprague–Dawley rat TBI model for evaluation of preliminary and preclinical potential of the scaffold.

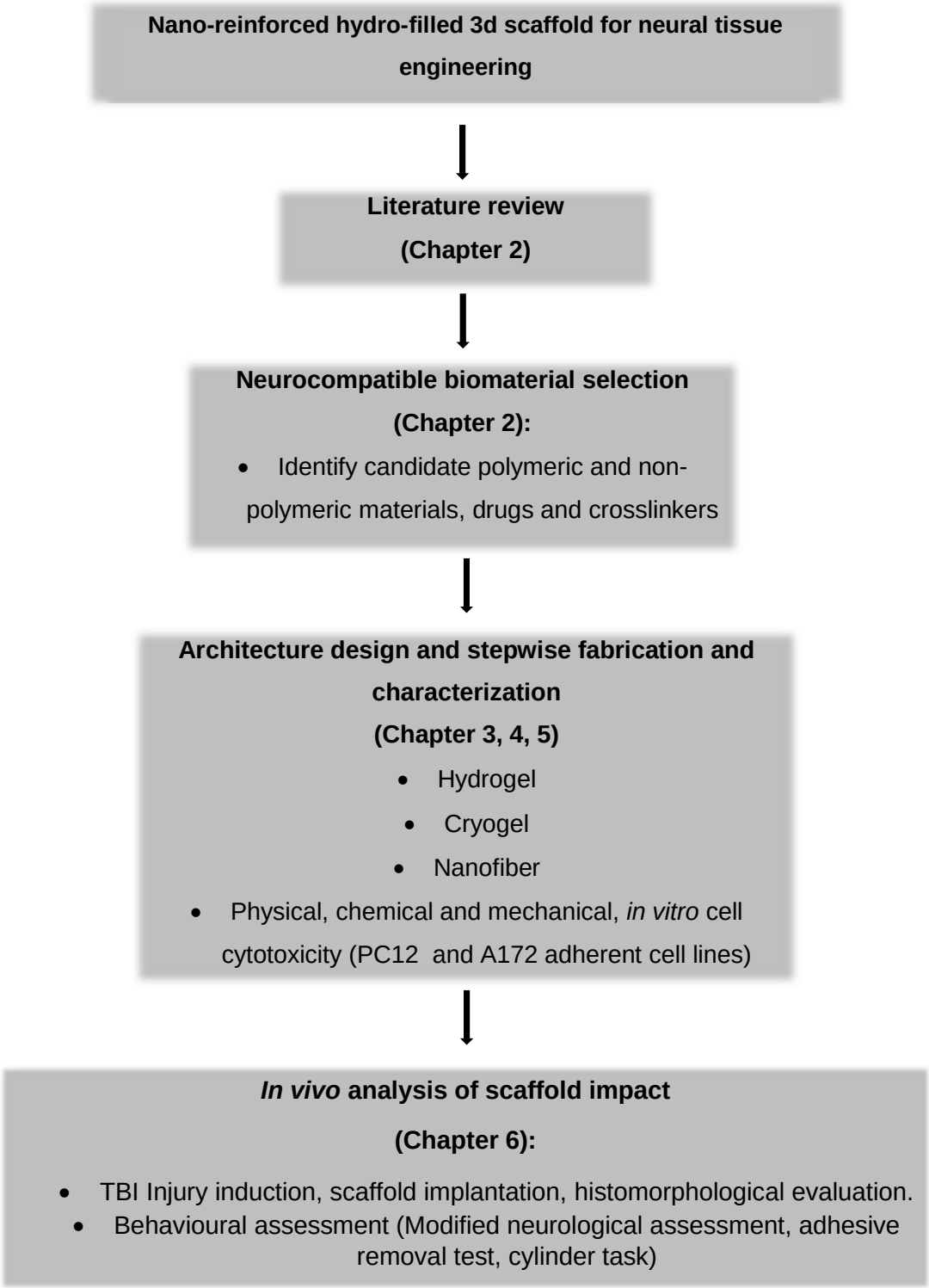

Figure 1.2. A schematic outline of the study for the design and development of a novel 3-in-1 scaffold system for neural tissue engineering application.

1.4. Potential therapeutic applications of the proposed novel 3-in-1 scaffold.

a) Function as a cell culture system
b) Development for applications towards studying cell growth behavior, development of soft tissue organoids
c) Localised delivery of drugs that otherwise have difficulty passing the blood brain barrier.
d) Incorporation of neurotrophic factors, drugs and other factors independently or in combination (as informed by the injury requirements) for delivery of bioactives for an additive or synergistic effect on the furtherance of functional tissue repair and potential regeneration.
e) Function as an encapsulating integrative tuneable supportive structure for the protection of cells from the harsh lesion environment, thus improving cell survival rates.
f) Function as a blue-print furnishing guidance for cells when re-establishing their ECM.
g) Enhanced tissue continuity, repair and potential regeneration by the provision of a pro-regenerative, platformative neuromimetic microenvironment capable of simulating the architecture of the ECM and the lesion cavity.

1.5. Thesis overview

1.5.1. Chapter one:

An introduction and background to this study. This chapter discusses the context, rationale, motivation, novelty and highlights the aim, objectives and potential benefits of this work. Traumatic brain injury can be defined as damage to the brain which can result from a range of traumatic events such as motor vehicle accidents, surgical operations and falls. These traumatic events are indiscriminate of age, gender and social standing; hence TBI is a condition that can affect all humans. Furthermore, the lack of effective treatment options and poor regenerative capacity of brain tissue often leaves victims disabled, causing a socioeconomic crisis on a larger scale. Biomaterials have shown great potential for application but there is yet to be a scaffold of consummate results. The proposed intervention is a nano-reinforced hydro-filled cryogel scaffold system for application as a novel acellular implant to aid in neural tissue regeneration. This system is unique in its design as a biomimetic 3-in-1 scaffold system. By virtue of its complex, multicomposite, hierarchical design, the scaffold is anticipated to yield unique results (in comparison previous scaffolds) that will significantly contribute to and influence the progression of neural tissue regeneration research.

1.5.2. Chapter two:

A comprehensive literature review focused on the 3D scaffolds for brain tissue regeneration and the architectural design challenges. The chapter provides a critical analysis of current 3D scaffolds for neural tissue engineering. Suitability of architectural properties (e.g.

interconnected pores, scaling, composition, swelling, and architectural influences) for designing ideal scaffold structures to better mimic the desired tissue properties (ECM) were scrutinized in this chapter which later informed the design approach, material choice and the novel 3-in-1 scaffold fabrication herein.

1.5.3. Chapter three:

This chapter focuses on the fabrication of first components of the 3-in-1 scaffold system. The development of a N-acetylcysteine (NAC)-loaded poly (lactic-co-glycolic acid) (PLGA) electrospun system for potential neural tissue application for TBI is presented herein. The chapter also highlights the dual potential application of the scaffold to not only function as a neuromimetic scaffold, but also function as a localized drug delivery system.

1.5.4. Chapter four:

This chapter focuses on the fabrication of second component of the 3-in-1 scaffold. The fabrication and characterization of a 1,4-butanediol diglycidyl ether chemically crosslinked protein-based (gelatin-elastin) hydrogel is presented herein. Characterization studies will be conducted including differential scanning calorimetry (DSC), thermogravimetric analysis (TGA), X-ray powder diffraction (XRD), Rheology.

1.5.5. Chapter five:

This chapter focuses on the fabrication of third component and the novel 3-in-1 scaffold. The third component is the cryogel which is prepared using the cryogelation method. The design of a 3-in-1 system wherein nanofibers were be “in-process” embedded into a cryogel scaffold followed by filling of the macro-microporous architecture with a hydrogel is presented in this chapter. This system is unique as it uses a combination of scaffold systems and composite biomaterials to capture the multi-scale, multi-porous (micro/meso/macro-porous), intricate hierarchical properties of native ECM (a key component of neural regeneration) in its design.

1.5.6. Chapter six:

This chapter focuses on the *in vivo* analysis experimental work. The in vivo performance of the scaffold (e.g. structural stability, filling the lesion gap, potential as an implantable scaffold, *in vivo* residence throughout healing). A survivable, reproducible, localized penetrating TBI is induced in a Sprague-Dawley rat model. The effect of the novel 3-in-1 scaffold implant in the rat brain is evaluated using histomorphology and behavioral studies (sensory, motor weakness recovery).

1.5.7. Chapter seven:

This chapter presents the conclusion of the research work, outlines the recommendations for future outlook for the novel 3-in-1 scaffold presented herein.

1.6. References

Clausen, F., Lindh, T., Salimi, S., Erlandsson, A., 2014. Combination of growth factor treatment and scaffold deposition following traumatic brain injury has only a temporary effect on regeneration. Brain Research 1588, 37–46. https://doi.org/10.1016/j.brainres.2014.08.043

Conejero-García, A., Vilariño-Feltrer, G., Martínez-Ramos, C., Monleón Pradas, M., Vallés-Lluch, A., 2015. Channeled polymeric scaffolds with polypeptide gel filling for lengthwise guidance of neural cells. European Polymer Journal 70, 331–341. https://doi.org/10.1016/j.eurpolymj.2015.07.033

Crandall, M., 2016. Epidemiology of TBI in: Manual of Traumatic Brain Injury: Assessment and Management, in: Manual of Traumatic Brain Injury: Assessment and Management. Springer Publishing Company.

Das, S., Carnicer-Lombarte, A., Fawcett, J.W., Bora, U., 2016. Bio-inspired nano tools for neuroscience. Progress in Neurobiology 142, 1–22. https://doi.org/10.1016/j.pneurobio.2016.04.008

Dinsmore, J., 2013. Traumatic brain injury: an evidence-based review of management. Continuing Education in Anaesthesia Critical Care & Pain 13, 189–195. https://doi.org/10.1093/bjaceaccp/mkt010

Ellis-Behnke, R.G., Liang, Y.-X., You, S.-W., Tay, D.K.C., Zhang, S., So, K.-F., Schneider, G.E., 2006. Nano neuro knitting: Peptide nanofiber scaffold for brain repair and axon regeneration with functional return of vision. PNAS 103, 5054–5059. https://doi.org/10.1073/pnas.0600559103

Gattazzo, F., Urciuolo, A., Bonaldo, P., 2014. Extracellular matrix: a dynamic microenvironment for stem cell niche. Biochim Biophys Acta 1840, 2506–2519. https://doi.org/10.1016/j.bbagen.2014.01.010

Geckil, H., Xu, F., Zhang, X., Moon, S., Demirci, U., 2010. Engineering hydrogels as extracellular matrix mimics. Nanomedicine (Lond) 5, 469–484. https://doi.org/10.2217/nnm.10.12

Goldstein, L.N., Beringer, C., Morrow, L., 2017. What intracranial pathologies are most likely to receive intervention? A preliminary study on referrals from an emergency centre with no on-site neurosurgical capabilities. Afr J Emerg Med 7, 100–104. https://doi.org/10.1016/j.afjem.2017.04.012

Gong, Y., He, L., Li, J., Zhou, Q., Ma, Z., Gao, C., Shen, J., 2007. Hydrogel-filled polylactide porous scaffolds for cartilage tissue engineering. J Biomed Mater Res B Appl Biomater 82, 192–204. https://doi.org/10.1002/jbm.b.30721

He, J., Wang, X., Spector, M., Cui, F., 2012. Scaffolds for central nervous system tissue engineering. Frontiers of Materials Science 6, 1–25. https://doi.org/10.1007/s11706-012-0157-5

Huang, L., Wu, Z.-B., ZhuGe, Q., Zheng, W., Shao, B., Wang, B., Sun, F., Jin, K., 2014. Glial Scar Formation Occurs in the Human Brain after Ischemic Stroke. Int J Med Sci 11, 344–348. https://doi.org/10.7150/ijms.8140

Jurga, M., Dainiak, M.B., Sarnowska, A., Jablonska, A., Tripathi, A., Plieva, F.M., Savina, I.N., Strojek, L., Jungvid, H., Kumar, A., Lukomska, B., Domanska-Janik, K., Forraz, N., McGuckin, C.P., 2011. The performance of laminin-containing cryogel scaffolds in neural tissue regeneration. Biomaterials 32, 3423–3434. https://doi.org/10.1016/j.biomaterials.2011.01.049

Kathuria, N., Tripathi, A., Kar, K.K., Kumar, A., 2009. Synthesis and characterization of elastic and macroporous chitosan–gelatin cryogels for tissue engineering. Acta Biomaterialia 5, 406–418. https://doi.org/10.1016/j.actbio.2008.07.009

Lee, J., Cuddihy, M.J., Kotov, N.A., 2008. Three-Dimensional Cell Culture Matrices: State of the Art. Tissue Engineering Part B: Reviews 14, 61–86. https://doi.org/10.1089/teb.2007.0150

Liu, Q., Huang, J., Shao, H., Song, L., Zhang, Y., 2016. Dual-factor loaded functional silk fibroin scaffolds for peripheral nerve regeneration with the aid of neovascularization. RSC Adv. 6, 7683–7691. https://doi.org/10.1039/C5RA22054H

Lodish, H., Berk, A., Zipursky, S.L., Matsudaira, P., Baltimore, D., Darnell, J., 2000. Cell-Matrix Adhesion. Molecular Cell Biology. 4th edition.

McMurtrey, R.J., 2015. Novel advancements in three- dimensional neural tissue engineering and regenerative medicine. Neural Regeneration Research 10, 352–354.

O'Brien, F.J., 2011. Biomaterials & scaffolds for tissue engineering. Materials Today 14, 88–95. https://doi.org/10.1016/S1369-7021(11)70058-X

Reilly, P., 2007. The impact of neurotrauma on society: an international perspective, in: Weber, J.T., Maas, A.I.R. (Eds.), Progress in Brain Research, Neurotrauma: New Insights into Pathology and Treatment. Elsevier, pp. 3–9. https://doi.org/10.1016/S0079-6123(06)61001-7

Rivet, C.J., Zhou, K., Gilbert, R.J., Finkelstein, D.I., Forsythe, J.S., 2015. Cell infiltration into a 3D electrospun fiber and hydrogel hybrid scaffold implanted in the brain. Biomatter 5, e1005527–e1005527. https://doi.org/10.1080/21592535.2015.1005527

Rubiano, A.M., Carney, N., Chesnut, R., Puyana, J.C., 2015. Global neurotrauma research challenges and opportunities. Nature 527, S193–S197. https://doi.org/10.1038/nature16035

Silver, J., Miller, J.H., 2004. Regeneration beyond the glial scar. Nature Reviews Neuroscience 5, 146–156. https://doi.org/10.1038/nrn1326

Sirivisoot, S., Pareta, R., Harrison, B.S., 2014. Protocol and cell responses in three-dimensional conductive collagen gel scaffolds with conductive polymer nanofibres for tissue regeneration. Interface Focus 4. https://doi.org/10.1098/rsfs.2013.0050

Struzyna, L.A., Harris, J.P., Katiyar, K.S., Chen, H.I., Cullen, D.K., 2015. Restoring nervous system structure and function using tissue engineered living scaffolds. Neural Regen Res 10, 679–685. https://doi.org/10.4103/1673-5374.156943

Subramanian, A., Krishnan, U.M., Sethuraman, S., 2009. Development of biomaterial scaffold for nerve tissue engineering: Biomaterial mediated neural regeneration. J Biomed Sci 16, 108. https://doi.org/10.1186/1423-0127-16-108

Sun, D., 2016. The potential of neural transplantation for brain repair and regeneration following traumatic brain injury. Neural Regen Res 11, 18–22. https://doi.org/10.4103/1673-5374.169605

Thompson, C.H., Zoratti, M.J., Langhals, N.B., Purcell, E.K., 2015. Regenerative Electrode Interfaces for Neural Prostheses. Tissue Engineering Part B: Reviews 22, 125–135. https://doi.org/10.1089/ten.teb.2015.0279

Wang, K., Liu, B., Ma, J., 2014. Research progress in traumatic brain penumbra. Chinese Medical Journal 127, 1964–1968. https://doi.org/10.3760/cma.j.issn.0366-6999.20120638

Wang, Y., Wei, Y.T., Zu, Z.H., Ju, R.K., Guo, M.Y., Wang, X.M., Xu, Q.Y., Cui, F.Z., 2011. Combination of Hyaluronic Acid Hydrogel Scaffold and PLGA Microspheres for Supporting Survival of Neural Stem Cells. Pharm Res 28, 1406. https://doi.org/10.1007/s11095-011-0452-3

Wong, D.Y., Krebsbach, P.H., Hollister, S.J., 2008. Brain cortex regeneration affected by scaffold architectures. Journal of Neurosurgery 109, 715–722. https://doi.org/10.3171/JNS/2008/109/10/0715

Xiong, Y., Qu, C., Mahmood, A., Liu, Z., Ning, R., Li, Y., Kaplan, D.L., Schallert, T., Chopp, M., 2009. Delayed transplantation of human marrow stromal cell-seeded scaffolds

increases transcallosal neural fiber length, angiogenesis, and hippocampal neuronal survival and improves functional outcome after traumatic brain injury in rats. Brain Research 1263, 183–191. https://doi.org/10.1016/j.brainres.2009.01.032

Zhang, Y., Huang, J., Huang, L., Liu, Q., Shao, H., Hu, X., Song, L., 2016. Silk Fibroin-Based Scaffolds with Controlled Delivery Order of VEGF and BDNF for Cavernous Nerve Regeneration. ACS Biomater. Sci. Eng. 2, 2018–2025. https://doi.org/10.1021/acsbiomaterials.6b00436

CHAPTER TWO

3D SCAFFOLDS FOR BRAIN TISSUE REGENERATION: ARCHITECTURAL CHALLENGES

Published in Biomaterials Science

Mahumane GD, Kumar P, du Toit LC, Choonara YE , Pillay V., 2018. 3D scaffolds for brain tissue regeneration: architectural challenges. *Biomaterials Science*, 2018 24;6(11):2812-2837. doi: 10.1039/c8bm00422f. PMID: 30255869.

2.1. Abstract

Biomaterials are being utilized to engender biomimetic, pro-regenerative constructs in the form of 3D scaffolds to augment functional neural tissue (brain tissue) repair and regeneration. Tissue engineered three-dimensional (3D) scaffolds have shown various degrees of experimental success, indicating great potential for development as treatment options. However, there is yet to be a 3D scaffold that exhibits consummate results of an effective clinical standard. Critical assessment of the performance of current 3D scaffolds could provide insightful feedback for tailoring future 3D scaffolds towards more promising results. This review provides a critical analysis of current 3D scaffolds for neural tissue engineering. Architectural properties, such as porosity, swelling, and architectural influences, such as design approach and polymeric material choice, were scrutinized for suitability for the desired tissue target properties. Success and shortcomings of various 3D scaffolds were evaluated through the analysis of tissue integration of the 3D scaffold ***in vivo***. Investigations focused on in this review included those: (1) reporting at an ***in vivo*** experimental level in animal models, (2) involving polymer-based (natural/synthetic) scaffolds described as possessing a '3D' architecture, (3) targeting brain tissue regeneration (4) published from 2011 onward.

2.2. Introduction

2.2.1. Regeneration potential of the central nervous system

An understanding of the regenerative potential of neural tissue is crucial to scrutinizing the current three-dimensional (3D) scaffold interventions for neural tissue regeneration. From a macro/tissue perspective, the consequence of neurotrauma is a cavitary defect/some form of tissue discontinuity at the lesion site and a disruption in the unidirectional architecture of the nerve tracts (He et al., 2012; Su et al., 2014; Tamariz and Varela-EchavarrÃ-a, 2015; Tian et al., 2015). This discontinuity results in a destruction of the neural network that transmits signals

responsible for so many body functions in the central nervous system (CNS). Neural network repair may be crucial to CNS function. This can only happen if there is functional tissue continuity at the cavitary site. Naturally, 'bridging' the lesion is the logical step. The challenge in this step from a tissue engineering perspective has been ensuring that the 'bridge' (scaffold) mimics the native tissue as closely as possible, biologically and architecturally.

From a micro/cellular perspective, nerve injury results in a loss of neurons and/or supporting cells (Tian et al., 2015). Generation of new neurons is limited to specified areas, such as the sub-ventricular zone and the dentate gyrus (Casarosa et al., 2014; Das et al., 2016; Hao et al., 2017). Mature neurons are post-mitotic, meaning they do not divide to give rise to new cells (Aurand et al., 2012b). Instead, they may be generated from neural stem cells or via *in situ* reprogramming of endogenous astrocytes to neurons (Das et al., 2016; Su et al., 2014). Neural stem cells are able to both self-renew and differentiate into neurons, astrocytes and oligodendrocytes (Casarosa et al., 2014; Tian et al., 2015). Su and co-workers (Su et al., 2014) showed that astrocytes can be converted into Doublecortin (DCX)-positive neuroblasts which could mature into synapse-forming neurons *in vivo in the spinal cord* by a single transcription factor, sex-determining region Y-box 11 (SOX11). These astrocytes can be reprogrammed in the brain as well. Provided with a *f*avourable cellular milieu, neurons can regenerate their axons post injury (Das et al., 2016). In general, the peripheral nervous system (PNS) shows better recovery in comparison to the CNS post injury. The difference in results has in part been linked to cellular composition, and the presence and absence of Schwann cells in the PNS and CNS respectively. Schwann cells guide, myelinate nerve fibres, secrete neurotrophins and produce extracellular matrix (ECM) molecules, functions which facilitate neural regeneration (Casarosa et al., 2014; Das et al., 2016; Tian et al., 2015). Whereas in the CNS, astrocytes contribute to scar formation and oligodendrocytes express inhibitory proteins in the area, functions which hinder axonal outgrowth and neural regeneration effort (Aurand et al., 2012b; Davoust et al., 2017; Tian et al., 2015). This difference in neuroglia between the PNS and the CNS is one of main differences in the regeneration potential between the two. In both instances, regeneration can occur; the requirements from a tissue perspective are slightly varied in focus keeping in mind the cell types of the PNS and CNS, respectively. With the PNS, a guidance structure is the main requirement for regeneration. Whereas for the CNS, in addition to guidance, the structure needs to be able to alter the inhibitory environment by exhibiting functions similar to the Schwann cells.

2.2.2. Therapeutic interventions for neurotrauma

Stem cell transplantation alone or in combination with neurotrophins have been introduced with the goal that they may replace lost cells in the injured area and stimulate regeneration (Casarosa et al., 2014; Heile and Brinker, 2011; Pettikiriarachchi et al., 2010; Sarnowska et al., 2013). These cells can be genetically modified to over-express neurotrophic factors such as brain-derived neurotrophic factor (BDNF), which aids in the growth of axons (Günther et al., 2015). The shortfall with the cell/neurotrophin strategy is the lack of a physical 3D construct at the lesion site to facilitate directed axonal growth of the stimulated axons. Axons tend to grow in an arbitrary orientation and thus very few reach the distal portion of the lesion for reconnection of the neural circuit (Günther et al., 2015). Years of cell transplants have shown that cells show poor survival when presented as dissociated suspensions in comparison to implantation as donor tissue or when presented within scaffolds, in part due to exposure to and lack of protection from the inhibitory environment at the lesion site (Davoust et al., 2017; Delcroix et al., 2010; Ghuman and Modo, 2016; Guan et al., 2013; Günther et al., 2015; Hwang et al., 2014; Tian et al., 2015; Wang et al., 2016). Losses as high as 90-99% of transplanted cells have been reported (Liang et al., 2013).

The alternative to the transplantation of molecules and stem cells are ‘surgical’ and ‘bridging’ treatment options. End-to-end suturing is the gold standard for surgical treatment (Daly et al., 2013; Liang et al., 2013). This treatment option is limited to ideal settings, such as: clean-cut nerve transaction, minimal tissue loss, denervation of less than 6 months, minute gaps (< 1 cm (Samer et al., 2018; Zhang et al., 2016)) and an injury zone with good blood supply surrounded by soft tissue (Daly et al., 2013; Liang et al., 2013). Unfortunately, injuries vary and ‘ideal’ lesions are not representative of the clinical reality.

For non-ideal lesions (e.g. with bigger nerve gaps ranging from 1 to 5 cm (Samer et al., 2018)), a ‘bridging’ treatment option is often required(Kuffler, 2015; Tian et al., 2015). The “gold-standard” treatment approach for nerve injuries (e.g. PNS) is an autologous nerve transplant therapy when the gap considered is ‘big’ (Daly et al., 2013; Das et al., 2016; Grinsell and Keating, 2014; Hopkins et al., 2015; Kuihua et al., 2014; Liang et al., 2013; Martino et al., 2011; Panagopoulos et al., 2016; Tian et al., 2015). Autologous nerve transplants are, however, limited by their zero-sum nature as therapeutic options (requiring sacrifice of healthy donor tissue) that does not necessarily guarantee a gain. For example, this therapy option results in donor-site morbidity, mismatched size of graft and recipient nerve further complicated by processes such as intraneural fibrosis, scar formation, and vascular complications (Das et al., 2016; Kuihua et al., 2014; Martino et al., 2011; Panagopoulos et al., 2016; Sedaghati and

Seifalian, 2015; Tian et al., 2015; Zhu et al., 2017). These all lead to narrowed chances of therapeutic success and neural regeneration. Alternate bridging material, such as allografts, present limitations such as a high risk of immune-rejection (Daly et al., 2013).

To avoid the zero-sum nature of autologous grafts and host rejection of allografts, various artificial scaffolds have been developed as alternative bridging material. Scaffolds are systems used to re-establish tissue continuity at the cavitary site (He et al., 2012). They promise a non-zero-sum therapeutic alternative (requiring no sacrifice of healthy donor tissue) by serving as a temporary stand-in structure to stimulate and support the reconstruction and repair of nerve tissue. The tissue continuity offered at the lesion site varies with each scaffold system (two-dimensional (2D) versus 3D).

A few neural scaffolds have attained Food and Drug Administration (FDA) approval (e.g. Neuragen®, Neuroflex™, NeuroMatrix™ (collagen nerve guidance conduits); NeuroTube® polyglycolic acid (PGA) nerve guidance conduit; Neurolac™ poly(D,L-lactide-epsilon-caprolactone) (PCL) nerve guidance conduit) (Sensharma et al., 2017). Even these FDA-approved scaffolds show clinical limitations in that their performance is generally limited to 3 cm gaps) and are generally inferior to the performance of autograft treatment (Daly et al., 2013; Kuihua et al., 2014; Liang et al., 2013; Martino et al., 2011; Pfister et al., 2011; Sensharma et al., 2017; Tian et al., 2015). For example, Neurolac is extremely rigid resulting in breaking of needles and nerve tearing during implantation, suturing and regeneration, respectively (Kehoe et al., 2012). The majority of these FDA-approved/commercial scaffolds are mainly for application in the PNS (Tian et al., 2015). Far less success is noted with CNS research as scaffolds for CNS repair are largely in the experimental/research phase. Furthermore, current treatment approaches for conditions of the brain such as traumatic brain injury (TBI), are largely focused on preventing further damage (pharmacological agents and rehabilitation) rather than facilitating regeneration (Pettikiriarachchi et al., 2010).

2.2.3. Trends in 3D scaffolding for neural tissue engineering/application

There has been a noteworthy growth in the design approach to 3D scaffolding. Neural tissue engineering efforts have gravitated towards a novel type of neural scaffold that addresses the shortcomings of previous scaffolds while probing at fundamental concepts behind neuro-mimicry. Kumar and co-workers (Kumar et al., 2015) suggested ‘a multifunctional combinatorial device assimilating the biomaterial, cellular, molecular, structural and functional aspects altogether is the best way forward for effective neuroregeneration post traumatic spinal cord injury’. This observation is applicable across the board for neural tissue engineering.

Figure 2.1 illustrates the new type of scaffold design approach observed in recent (from 2011 onward) literature. It is multimodal, encompassing this 'multifunctional combinatorial' nature.

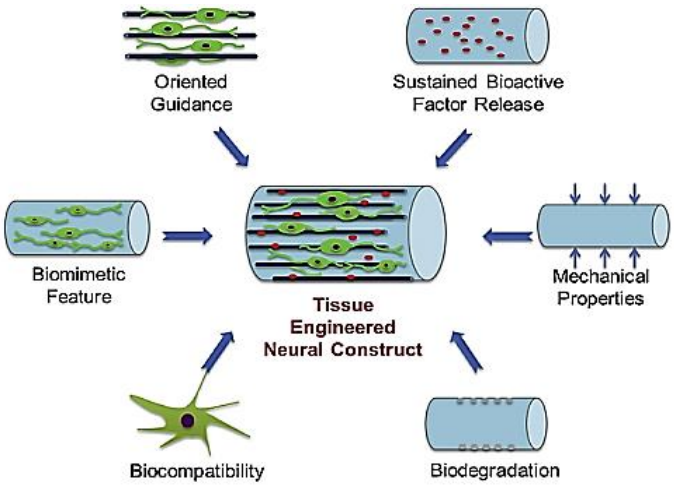

Figure 2.1. Parameters governing recent multifunctional 3D neural scaffold designs. This figure is reused from Nanomedicine: Nanotechnology, Biology, and Medicine,11, Zhu and co-workers (Zhu et al., 2015). Highly aligned nanocomposite scaffolds by electrospinning and electrospraying for neural tissue regeneration, pp. 693-704, 2015, with permission from Elsevier.

Advances in technology such as computer aided design have led to promising efforts towards specialized architecture. Accompanying these potential design approaches are the improvements in fabrication methods, such as application of 3D bioprinting. Furthermore, there have been great efforts in terms of optimizing material properties. These advances have resulted in a variety of 3D biomaterial scaffolds, with diverse architectural features for application in neural tissue regeneration (Table 2.1).

However, there are still shortfalls regarding the performance of these 3D scaffolds *in vivo*. The majority of the work is largely experimental with very little investigations performed at an *in vivo* level. Furthermore, hardly any scaffolds reach clinical testing stages, especially with regards to CNS regeneration in traumatic brain injury (Tung, 2015). Most of the scaffolds are reported as possessing 'potential' for neural tissue regeneration applications (Cholas et al., 2012; Huang et al., 2012; Tung, 2015). These observations surrounding neural tissue regeneration are an indicator of the need for a critical review of the success and shortcomings of 3D scaffolds to consolidate their true potential for the desired function (Figure 2.2).

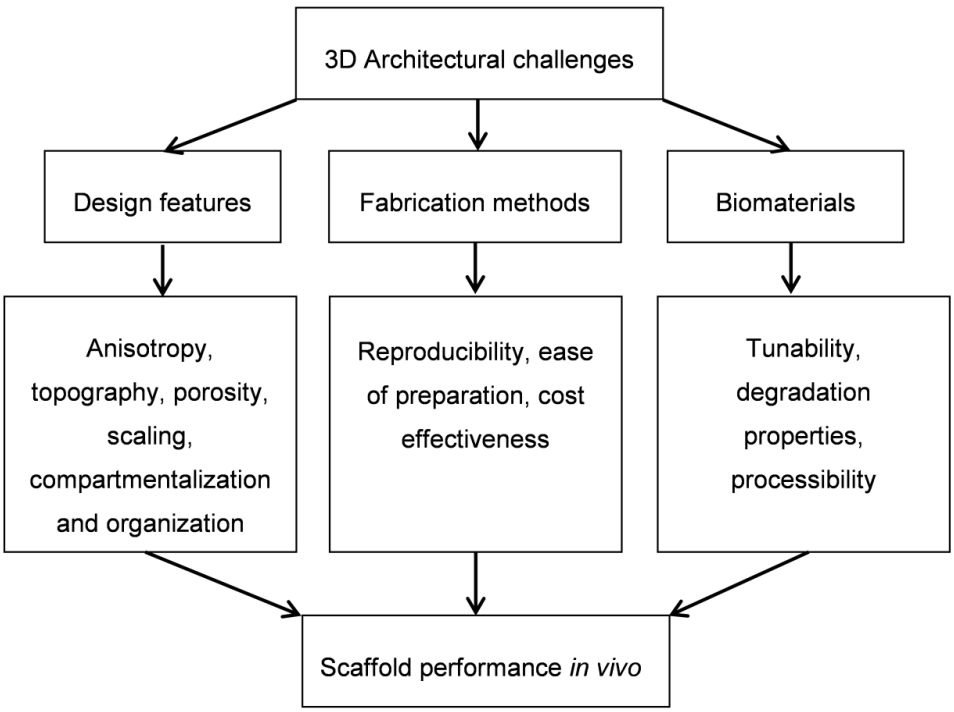

Figure 2.2. Schematic outline of the review paper for the evaluation of 3D scaffolds for neural regeneration and repair.

Table 2.1. Recent 3D scaffolds and their outcomes following *in vivo* assessment investigated for the repair of brain tissue (2011-onwards)

Reference and publication date of work	Scaffold system/type	Scaffold fabrication methods and resultant architectural features	Cell-seeding/encapsulation	*In vivo* animal model and number of animals tested and duration of implant analysis	Effect of scaffold at lesion site	Functional behavioural assessment and improvement
Jurga and co-workers, 2011 **(Jurga et al., 2011)**	Gelatin crosslinked with laminin based cryogel	Cryogelation methods yielded a macroporous sponge-like cryogel with pore size distribution of 20-160 µm and pore wall thickness of 3-35 µm	Acellular scaffold	Adult male Wistar rats weighing 250 g, the number of animals used was not stated; Surgical brain trauma was induced in rats < 24 hours of implant duration	No result for cell survival (degradation rate too rapid). Toxic by-products reported. Microglial cells and microphages detected at the edges of scaffolds.	No functional recovery testing.
Elias and Spector, 2012 **(Elias and Spector, 2012)**	Type 1 collagen based porous scaffold	Freeze-drying and dehydrothermal crosslinking yielded pore size distribution of 100-150 µm	Bromodeoxyuridine-labelled adult hippocampal neural progenitors	Male Sprague-Dawley rats, 12 animals tested using the penetrating brain injury model 4 week implant duration	Improved cell survival Progenitors differentiated into astrocytes, endothelial cells, and oligodendrocytes. Angiogenesis noted	No functional recovery testing
Huang and co-workers, 2012**(Huang et al., 2012)**	Collagen-glycosaminoglycan copolymer based porous matrix	Freeze-drying yielded 95% pore volume fraction and average pore diameter of 140±20 µm.	Acellular scaffold	Adult male Sprague-Dawley rats weighing between 300-350 g; 30 animals (10 per group); surgical brain trauma was induced 4 week implant duration	Proliferation, differentiation and migration of endogenous neural precursor cells. Increase in differentiated cells over time (DCX+). Decrease in number of inflammatory cells (ED1+) at the lesion boundary zone over time	Lowered neurological deficit (Neurological Severity Scores, mNSS, test) Improved sensorimotor recovery (tactile adhesive-removal test)
Cheng and co-workers, 2013	Laminin derived IKVAV linked to self-assembling peptide	Self-assembly yielded functionalized self-	Encapsulated rat neural stem cells (HCN-A94-2)	Sprague-Dawley rats, 24 rats used, underwent rat brain surgery model	Increased survival of embedded neural stem cells (NSC)	No functional recovery testing

Reference and publication date of work	Scaffold system/type	Scaffold fabrication methods and resultant architectural features	Cell-seeding/encapsulation	*In vivo* animal model and number of animals tested and duration of implant analysis	Effect of scaffold at lesion site	Functional behavioural assessment and improvement
(Cheng et al., 2013)	RADA16 based hydrogel	assembling peptide hydrogel		6 week implant duration	Differentiation of embedded NSCs in functionalized scaffold (increased b-tubulin positive cells) Lesion sites expressed neuronal markers such as MAP2 and NF-H Neurite outgrowth and extension GFAP positive astrocytes were significantly reduced at the boundary of damaged cavity	
Guan and co-workers, 2013 **(Guan et al., 2013)**	Collagen (type 1) based porous gelatinous scaffold	Porous gelatinous scaffold, pore sizes ranged 100-300 µm	Human bone marrow-derived mesenchymal stem cell (hMSC)	Adult male Sprague-Dawley rats, 42 animals tested, weighing 230-250 g, were subjected to a controlled cortical impact injury 4 week implant duration	Improved cell survival Improved neurite outgrowth	Improved neurological recovery (lower neurological severity score (mNSS) Improved spatial learning (Morris water maze)
Álvarez and co-workers, 2014 **(Álvarez et al., 2014)**	Poly-L/DL lactic acid (PLA70/30) nanofibers	Electrospinning yielded radially aligned electrospun nanofibers	Acellular scaffold	Mice, four days old mice 15 month implant duration	Neural tissue regeneration with: - Functional laminar organization - Postsynaptic density protein 95 (PSD95) and synaptosomal-associated protein 25 (SNAP25) indicative of functional synaptic machinery in the regenerated tissue Sustained neurogenesis	No functional recovery testing

Reference and publication date of work	Scaffold system/type	Scaffold fabrication methods and resultant architectural features	Cell-seeding/encapsulation	*In vivo* animal model and number of animals tested and duration of implant analysis	Effect of scaffold at lesion site	Functional behavioural assessment and improvement
					Sustained cell survival differentiation and integration Functional vascularization (angiogenesis noted) Integration of neurons with brain circuitry establishing synaptic contacts	
Hsieh and co-workers, 2015 **(Hsieh et al., 2015)**	Polyurethane based hydrogel	3D bioprinting (fused deposition manufacturing) yielding a thermoresponsive hydrogel	Murine neural stem cells	Adult AB (wild type) zebrafish 8 day implant duration	Increased proliferation of NSC	Improved motor response (spontaneous coiling) Improved CNS recovery (hatching rate)
Martínez-Ramos and co-workers, 2015 **(Martínez-Ramos et al., 2015)**	Ethyl acrylate (OEA) and hydroxyl ethyl acrylate (HEA) copolymer based channeled scaffold	Porogen-template leaching yielded polyacrylate copolymer channeled scaffold	Acellular scaffold	Wister female rats, weighing between 220-250g, underwent cryogenic traumatic brain injury (cryolesion) 8 week implant analysis	Infiltration and extension of neurons inside scaffold (Tuj-1) Low neuronal survival in surrounding zone Neo-angiogenesis (new blood vessels) noted - Proliferation of endothelial cells - Endothelial cells formed lumen and organized into tubules Reduced inflammatory response and glial scarring	No functional recovery testing

Reference and publication date of work	Scaffold system/type	Scaffold fabrication methods and resultant architectural features	Cell-seeding/encapsulation	*In vivo* animal model and number of animals tested and duration of implant analysis	Effect of scaffold at lesion site	Functional behavioural assessment and improvement
Rivet and co-workers, 2015 **(Rivet et al., 2015)**	Fibronection/poly-L-lactide and agarose/methylcellulose based electrospun fiber and hydrogel hybrid	A combination of electrospinning (fiber component) thermogelation (hydrogel component) yielded electrospun fiber dispersed in hydrogel	Acellular scaffold	Male Wister rat, 36 animals, underwent surgical brain trauma > 60 day implant duration	Formation of a loosely defined glial boundary Extensive infiltration of astrocytes (GFAP positive) and macrophages/microglia (ED1) at tissue-scaffold interface	No functional recovery testing
Zhang and co-workers, 2016 **(Zhang et al., 2016)**	Modified RADA16mix (RADA16-RGD and RADA16-IKVAV) based hydrogel	Self-assembly peptide nanofibrous scaffold	Acellular scaffold	Adult C57BL/6 mice 2-3 months old, weighing between 22-28 g , subjected to rat intracerebral haemorrhage 6 week implant duration	Increased neuronal survival (increased NeuN-positive cells around injured area) Decreased cell death GFAP-positive and Iba1-positive cell found inside scaffold No NeuN positive cells infiltrated inside scaffold Nerve fibers present inside scaffold Decreased inflammatory response (lowered IBA-1 and CD11b) around scaffold	Improved motor coordination skill recovery (rotarod test) Faster recovery of tension force of forelimb (grip strength test) improvement noted with catwalk analysis
Wang and co-workers, 2017 **(Wang et al., 2017)**	Polydimethylsiloxane, multiwalled carbon nanotube sheet	Printing transfer method yielded transparent multiwalled carbon nanotubes (MWNTs) coated	Acellular scaffold	Sprague-Dawley rats, 20 weeks old Duration of implant not stated	Highly transparent sheet *in vivo*	No functional recovery testing

Reference and publication date of work	Scaffold system/type	Scaffold fabrication methods and resultant architectural features	Cell-seeding/encapsulation	*In vivo* animal model and number of animals tested and duration of implant analysis	Effect of scaffold at lesion site	Functional behavioural assessment and improvement
		polydimethylsiloxane sheet				
Zhang and co-workers, 2018 **(Zhang et al., 2018)**	Sodium alginate and hyaluronic acid based hydrogel	Gelation method yielded injectable, porous hydrogel	Human umbilical cord mesenchymal stem cells (hUC-MSC)	Sprague-Dawley rats weighing 230-250 g), subjected to Feeney's weight-drop method 28 day implant duration	Improved cell viability ratio and proliferation	Functional recovery of nerve function evaluated using the modified neurologic severity score (mNSS) (motor, sensory, balance, and reflexes in rats) • Improved recovery of exercise, learning and memory abilities Learning ability and memory recall was investigated using a Morris water maze system
Motalleb and co-workers, 2018**(Motalleb et al., 2018)**	Peptide amphiphile and tenacin-C derived peptide sequence based hydrogel	Self-assembly yielded and injectable in situ gelling hydrogel	Acellular scaffold	Male Sprague-Dawley rats, 6-7 weeks old 7 days	Redirected endogenous neuroblasts towards injury site Did not elicit a neuroinflammatory response	No functional recovery testing

Abbreviations and symbols: RADA16 = AcN-RADARADARADARADA-$CONH_2$ (Cheng et al., 2013); IKVAV = isoleucine-lysine-valine-alanine-valine (Cheng et al., 2013); MAP-2=Microtubule associated protein 2; NF-H= Anti-neurofilament H antibody, GFAP= Glial fibrillary acidic protein; NeuN= Hexaribonucleotide Binding Protein-3, NSC = Neural stem cell; Tuj-1 = anti-neural class IIIB-tubulin; DCX= Neuronal migration protein doublecortin, ED1=mouse monoclonal antibody; CD11b= an alpha subunit of Mac-1, IBA-1= ionized calcium-binding adapter molecule 1

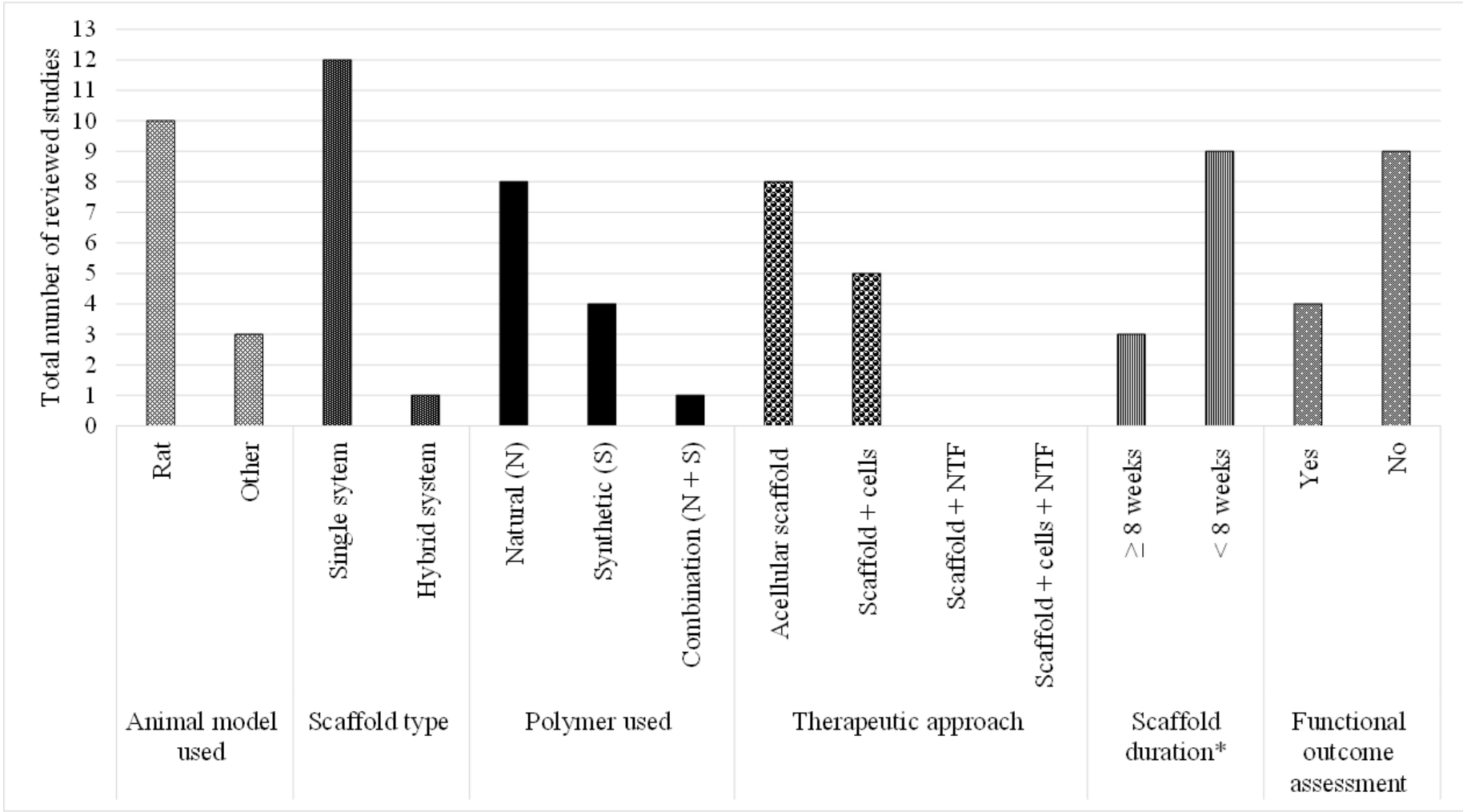

Figure 2.3. Analysis of the reviewed 3D scaffold experimental studies reported in Table 2.1

Note: The total number of reviewed studies is 13. One of the reviewed studies (Zhang et al., 2018) did not report on the duration of the implant in the animal model tested, therefore the “scaffold duration*” total is 12 instead of 13. NTF stands for neurotrophic factor.

2.3. Neural tissue-based critical architectural design challenges for neuromimicry in 3D scaffolds

Biomimicry requires modelling the 3D scaffold on the biological target tissue processes, properties and features. The current challenge of biomimicry is amplified by the incomplete understanding of the following properties of brain tissue as a biological system:

- *Heterogeneity:* Neural tissue is comprised of varied anatomical regions due to the varied density and alignment of the tissues components (e.g. different cell types, biomolecules, blood vessels, fibrous proteins) in various regions. This innate tissue heterogeneity points to the functional importance of niche areas/pockets which poses a translational challenge in biomimetic 3D architectural design when there is an incomplete understanding of the tissue as a system.
- *Complex 3D tissue:* Ultimately, 3D culturing is a process crucial to reconstructing the *in vivo* structure-function relationship of the neural tissue (McMurtrey, 2014). This would ensure that the newly formed tissue is 3D to enhance integration with the surrounding 3D tissue at the lesion zone. However, replicating the structural and functional framework has thus far been a challenge due to the high complexity of the 3D neural tissue network.
- *Unique neuronal micro-environment: In vivo*, the immediate microenvironment of neural cells is composed of the interstitial system, which accounts for approximately 20% of the total brain volume (McMurtrey, 2014; Nicholson and Syková, 1998; Shi et al., 2015). The interstitial system (ISS) or neural microenvironment comprises of the extracellular matrix and the interstitial fluid (ISF). Briefly, the interstitial fluid serves as a medium that bathes the cells in a rich environment (of for example, contains hormones, neurotransmitters) and facilitates waste removal, nutrient supply, organic molecules such as proteins; while the extracellular matrix directly attaches to and anchors the cells as depicted in Figures 2.4a and 2.4b (Lei et al., 2017; Shi et al., 2015). Figure 2.4b specifically highlights that the ECM enables intercellular adhesion and functions as a scaffold (Lei et al., 2017). The native ECM presents a macro to nanoscale topography, therefore, 3D scaffolds need to be processed to exhibit similar topographical cues (e.g. fibres and pores). Neural tissue has a dense vasculature in order to facilitate mass transport (e.g. of cells, nutrients, waste) (Bilston, 2011). Interconnected pores and channels designed in the architecture can accommodate for the absence of vasculature at the lesion site by facilitating mass transport within the 3D scaffolds.

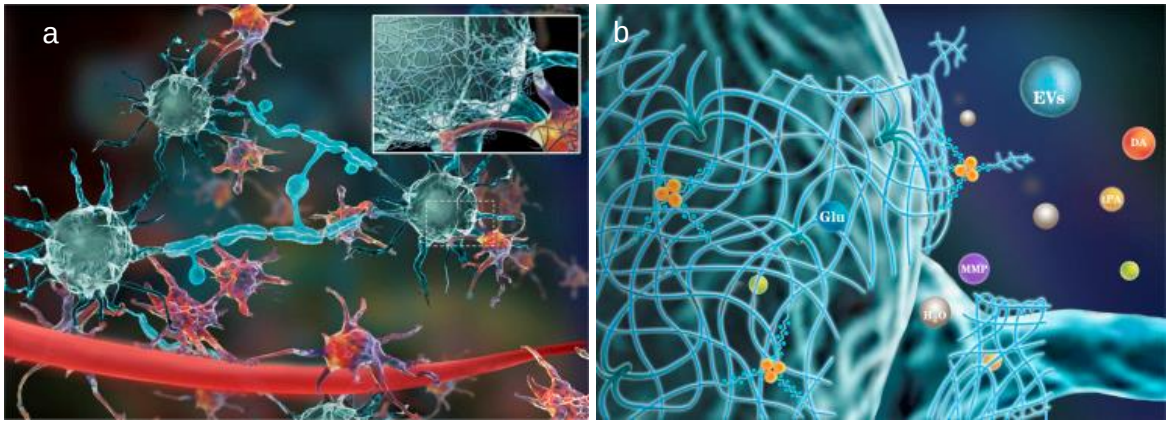

Figure 2.4. Schematic depiction of the neural environment. (a) Spatial arrangement of the brain tissue compartments (cyan cells = neurons, purple cells = astrocytes, zoom-in subplot: ECM = a net-like cover attached to the surface of neural cells. (b) Enlarged view of the zoom-in subplot of the brain ECM in (a). The net-like cover = hyaluronic acid (HA) secreted by cells acting as a trestle for the ECM net-like structure. The penniform objects crossing the gaps between the HA chains = glycoproteins. Orange triple-circle = tenascin linking glycoproteins up. Multi-coloured single circles = components of interstitial fluid (ISF), e.g., water molecules (H_2O), extracellular vesicles (EVs), matrix metallopeptidase (MMP), glucose (Glu), dopamine (DA), and tissue plasminogen activators (tPAs). This figure is reused and reprinted from Progress in Neurobiology, Lei and co-workers (Lei et al., 2017). The brain interstitial system: Anatomy, modelling, *in vivo* measurement, and applications, 2016, under the terms of the Creative Commons Attribution License (CC BY).

2.4. Macro-architectural profile of 3D scaffolds: Biomimicry of tissue properties, and translational potential

Biomimicry is an important conceptualization point for the architectural design of a scaffold for brain tissue repair. The macroscopic architecture of the brain consists of a solid phase (i.e. brain tissue) and a fluid phase (Bilston, 2011; Wagner and Ehlers, 2008). Terms such as ‘porous fluid-saturated solid’ and ‘fluid-bathed multiphase material’ have been employed to describe the properties of brain tissue (Lin et al., 2015; Martínez-Ramos et al., 2012). Table 2.1 and Figure 2.3 represented the properties of the various 3D scaffold designs developed during the period from 2011 onward for brain implantation. The type of scaffold systems noted are herein categorized into two major groups based on water content; solid systems (e.g. sponges, nanofibers) and liquid systems (hydrogels). Solid systems possess a very low water content (‘dry’) in comparison to the ‘fluid-bathed’ nature of brain tissue. Moreover the ‘dry’ scaffold at a lesion cavity serves as an inferior media for cell support in terms of the lack of an environment that enables diffusion of nutrients, oxygen and bioactive factors for cell survival and growth. Hybrids of these scaffold systems are also noted (e.g. electrospun fibres dispersed within hydrogel). The “porous fluid-saturated solid” property used to describe brain tissue may serve as the rationale behind the combination and prevalence of these two types of systems in literature. These scaffold systems are largely integrative and supportive (Jurga

et al., 2011; Sarnowska et al., 2013) due to the unique integration of common architectural features such as interconnected pores (with an average pore size ranging from 20-160 µm) (Cholas et al., 2012; Jurga et al., 2011; Martínez-Ramos et al., 2015), channels (Bosworth et al., 2013; Huang et al., 2012) and electrospun fibres (Rivet et al., 2015) (Table 2.1).

Literature (Table 2.1) reveals fabricated 3D architectures with an assortment of uniform and non-uniform architectures, hydrogels and nanofibers, various sizes of channels and pores, and various architectural compositions (polymeric biomaterial, neurotropic factors, cell adhesive proteins and peptides and cell seeding). This heterogeneity presents an assortment of data for analysis, thus rendering comparison of said data highly difficult due to innate differences in 3D architectures and study designs. Therefore, this review is limited by the lack of comparability of most investigations in this field. In light of this, the choice to review literature at an *in vivo* level enables the institution of performance (e.g. glial scar formation, cell infiltration) as an additional measurement tool to compare these 3D scaffold architectures. What is evident from these scaffold designs is the multimodal design approach, indicative of the efforts of this period (2011 to date). Three dimensional architectures enable and accommodate multimodality/complexity of design.

Incorporating multiple modes of interaction enables the scaffold to accommodate the dynamic needs of the regeneration process from biological (e.g. cell replacement, delivery of growth factors) to architectural stimulation (e.g. protective 3D environment, nanofibers to direct axonal extension).

In terms of biomimicry, both solid and liquid systems can exhibit viscoelastic behaviour similar to brain tissue. This is important in tissue engineering as it allows the 3D scaffold to retain its shape during transplantation and when experiencing the stress/strain that neural tissue is normally exposed to. Furthermore, brain tissue is stable and exhibits non-linear viscoelastic behaviour, highlighting that it can retain its shape after exposure to stress (Budday et al., 2017).

A crucial consult point in the architectural design is the translational potential of the scaffold system. That is, the scaffold architecture needs to be robust and accommodating of the clinical conditions (e.g. lesion shape) and procedures (e.g. transplantation stress) involved with the implantation process. Hydrogel scaffold systems possess numerous desirable features, i.e. they may be functionalized with bioactive compounds, have a low stiffness, high water content and conform to the geometry of any lesion (Carballo-Molina and Velasco, 2015; Grinsell and Keating, 2014; Hsieh et al., 2015; Moreira Teixeira et al., 2012; Tian et al., 2015). From a

translational potential perspective, it is the ability of hydrogels to be formed *in situ*, which is advantageous, as the liquid can be delivered via syringe and needles allowing access to deeply located lesions in the brain while minimizing further disruption of the highly complex surrounding tissue network at the implantation site (i.e. implantation associated trauma). Alternatively, solid systems (e.g. nanofibers and nerve conduits) suffer from a translational perspective. They lack the fluidity of hydrogels which enables hydrogels to fill irregular lesion geometries. Therefore, application of these scaffolds may result in further injury where tissue resection may be required to accommodate the 3D scaffold architecture. Alternatively, the 3D scaffold may need to be cut, shaped or resized to the shape of the lesion (Bosworth et al., 2013; Cholas et al., 2012; Jurga et al., 2011; Martínez-Ramos et al., 2015). Surprisingly, only a few scaffolds were inserted by the minimally invasive injection route (Chen et al., 2011; Fon et al., 2014; Hsieh et al., 2015; Motalleb et al., 2018; Wang et al., 2016; Zhang et al., 2018), while the majority were surgically implanted via manual transfer (Table 2.1). This not only adds an additional transplantation procedure, it also threatens the architectural integrity of the scaffold. This is a crucial point to consider as most 3D solid scaffolds (e.g. nanofibers) exhibit anisotropy. Elias and Spector (Paul Z. Elias and Spector, 2012) noted their pre-cut collagen scaffold failed to fill the lesion cavity; this was because the PBI lesion cavity had expanded to some extent by the time of implantation. Alterations in lesion size must thus be expected after a period of injury and considered in scaffold design, and could pose a limitation for solid scaffolds.

Cryogels are gaining interest as 3D scaffold systems for neural tissue engineering. Cryogels confer the best translational features of both liquid (e.g. hydrogels) and solid (e.g. nanofibers) scaffold systems for CNS application. They are both robust and accommodating by virtue of their shape memory properties (Béduer et al., 2014; Lim and Spector, 2017; Newland et al., 2015). Firstly, cryogels are compressible and may therefore be delivered via the minimally invasive injection route. Secondly, cryogels can withstand deformation in the needle while maintaining their predefined architecture. Furthermore, cryogels can expand to their original shape post compression and injection. Ultimately, cryogels are potentially architecturally advantageous as they are both injectable (as hydrogels are) and architecturally predefined and robust like other solid systems (e.g. nanofibers).

Cells respond to the mechanical properties of their growth substrate (Martino et al., 2011). The 3D scaffold system needs to be soft and allow for deformation, properties mimetic of neural tissue (Hopkins et al., 2015). Soft matrices simulating the mechanical properties of neural tissue (elastic modulus <1 kPa) result in improved neural stem cell differentiation, cell viability and neurite extension, which is crucial in attaining reconnection of severed neurons

Table 2.2. Macro/micro architectural profiles of acellular biomaterial scaffolds in comparison to brain tissue

(Lim and Spector, 2017; Martínez-Ramos et al., 2015). Unfortunately, this renders the scaffold vulnerable to transplantation stress. The architectural challenge associated with soft scaffold constructs is the risk of collapsing and damaging the CNS architecture and cellular network during implantation as observed by Jurga and co-workers (Jurga et al., 2011). Scaffold systems need to possess adequate mechanical properties to withstand the tension exposed to during regeneration across the lesion cavity (Stratton et al., 2016). In light of this, hybrid composite scaffold systems have been introduced. For example, Wu and co-workers (Wu et al., 2016) used an electrospun poly-L-(lactic acid) nanofibrous conduit to augment the outcome of a soft hydrogel for PNS regeneration. The hydrogel was injected inside the poly-L-(lactic acid) conduit, as the conduit possessed the required mechanical properties, which enabled it to maintain its bulk architectural morphology without collapsing before tissue could regenerate. Composite systems allow for better biomimicry of the target tissue by combining the advantages of both systems (solid and liquid) and overcoming their individual limitations (Hsieh et al., 2015; Wagner and Ehlers, 2008). Composites allow for a more realistic mimicry of the ISS that is crucial for cell survival and differentiation. The 'liquid' components such as hydrogels mimic the interstitial fluid (ISF), which is a functional gel-like media. Whereas solid components such as nanofibers offers mechanical and architectural integrity conferred by the ECM.

2.5. Micro-architectural profiles of 3D scaffolds: compartmentalization, multi-scaling, mechanical anisotropy

Neuromimetic compartmentalization and multiscale organizational architectural features

Brain tissue comprises structures of various sizes. For example, the neuronal cell body is approximately 10-50 µm in diameter, dendrites extend up to 500 µm, arteries and veins are 1-3 mm, and capillaries are approximately 4-8 µm (Hemphill et al., 2015). This indicates that the ISS is multi-compartmental with various pore sizes to accommodate these various structures. As depicted in Table 2.2, the internal structure of the brain has previously been described as resembling foam (Nicholson and Syková, 1998). The ISS (neural microenvironment) forms interconnected channels and cavities (spaces filled with cells) that are irregular in both size and shape. It is very interesting to note that the majority of the 3D scaffolds summarized in Table 2.1 are able to mimic this internal structure. The walls of the scaffolds presented in Table 2.2 can serve as the channels while the pores function as spaces to be occupied by cells. This structure is prominent in all the 3D systems (Table 2.1), regardless of whether conventional methods of fabrication (e.g. cryogelation, freeze-drying) or more advanced methods such as 3D printing were employed.

Tissue/scaffold type	Macroachitecture[a]	Microarchitecture[b]	Image reference
Brain tissue	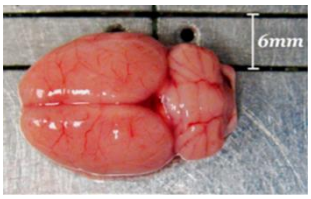 Rat brain after extraction.	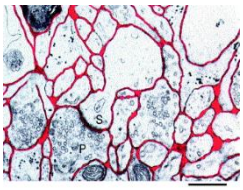 Electron micrograph showing the extracellular space (red) outline from a region of a rat cortex. The scale bar measures 1 µm. “s” points to a prominent dendritic spine while “p” shows a presynaptic terminal	(a)(Haslach Jr et al., 2017) (b)(Nicholson and Syková, 1998)
Hydrogel	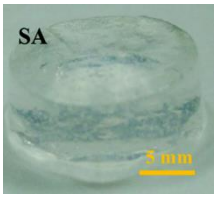 Photograph of sodium alginate (SA) hydrogel.	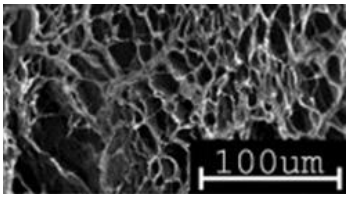 Scanning electron micrograph of a hydrogel.	(a(Zhang et al., 2018),b(Forte et al., 2016))
Nanofiber	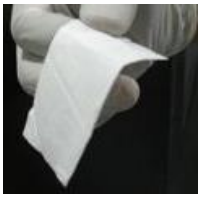 Photograph of nanofibrous mat.	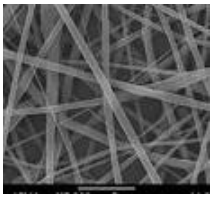 Scanning electron micrograph of nanofibrous mat. The scale measure 5 µm.	(a,b) (Ramachandran et al., 2017)
3D printed scaffold	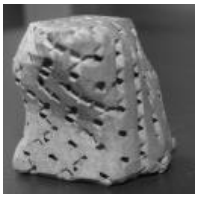	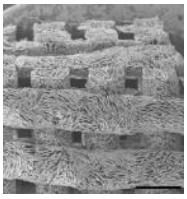	(a,b) (Fu et al., 2017)

Tissue/scaffold type	Macroachitecture[(a)]	Microarchitecture[(b)]	Image reference
	3D printed scaffold with an external shape matching a brain lesion cavity.	Scanning electron microscopy image of a cross-sectional view of the 3D printed scaffold. The scale bar measures 1 mm.	

Compartmentalization within the scaffold enables the development of various tissue structures (e.g. vascularization and neuronal networks) of various sizes and shape (Grinsell and Keating, 2014). This can be achieved through the incorporation of features such as pores, grooves and channels. Interconnected pores are prevalent in 3D scaffold designs (Tables 1 and 2). Interconnected pores impart the properties of an open integrative system, that is, pores allow integration with the surrounding native tissue by facilitating cellular infiltration and tissue ingrowth which merges with the newly formed tissue within the scaffold, a property useful for neural tissue as reconnecting severed networks/circuits is key.

Compartmentalization allows the formation of concentration gradients and specialized niche-environments within the scaffold to aid in regeneration. These concentration gradients can be in the form of hormones, nutrients, undifferentiated stem cells (McMurtrey, 2016). Sart and co-workers (Sart et al., 2014) noted a higher survival of stem cells when they were prepared under conditions of hypoxic stress. This is called hypoxic conditioning. The injury site following traumatic brain injury is associated with oxidative stress, nutrient deprivation and lack of other pro-regenerative features (e.g. extracellular matrix) required for cell survival and tissue regeneration (Liu et al., 2016). Antioxidants, survival signals and various genes related to cell migration, cell adhesion, and anti-inflammatory responses are regulated by the expression of HIF-1 (Wei et al., 2017). Hypoxia preconditioning (at sub-lethal hypoxic levels) is a strategy designed to mimic an aspect of this lesion environment to promote endogenous protective mechanisms in the cells to enhance survival in this environment (Baillieul et al., 2017; Liu et al., 2016). Hypoxic preconditioning directly induces HIF-1 upregulation which in turn increases brain-derived neurotrophic factor (BDNF), stromal-derived factor 1 (SDF-1), vascular endothelial growth factor (VEGF), erythropoietin (EPO), and many other genes that can stimulate neurogenesis, angiogenesis, vasodilatation, and increase cell survival (Wei et al., 2017). This hypoxic preconditioning effect of cells may be achieved using 3D scaffolds by simply tailoring the diffusion properties of the scaffold through architecture (e.g. compartmentalization, pore size) (McMurtrey, 2016). Therefore, 3D scaffolds can be used to replicate stages of concentration gradients (e.g. of oxygen and nutrients) that drive stem cell

differentiation, and impart biological heterogeneity through controlled spatial organizational design (Kumari and Kumar, 2017; Martínez-Ramos et al., 2015). In the same note, cells in 3D constructs run the risk of suffering core degradation from lack of adequate diffusion (e.g. waste removal, oxygen diffusion) and vascularization. Interconnected pores enable the free flow of waste products and nutrients within the scaffolds, improving overall cell viability (Chan et al., 2016). Vasculature formation is crucial to cell viability and porous structures facilitate the formation of vasculature (Chan et al., 2016).

2.6. Influencing neural cell fate through multi-scaling features

The native cell environment is inherently hierarchical/multiscaled (i.e. composed of nano- to micro- to macrostructures) (Lee et al., 2017; Tu et al., 2016). Various scales may be used to mimic the ECM within the 3D scaffold design; nano-scale at 0.001-1 µm, micro-scale at 1-1000 µm and macro-scale 1000-100000 µm (Lee et al., 2008). Cell fate is influenced differently at these various scales (Lee et al., 2017; McMurtrey, 2016; Tu et al., 2016) as depicted in Figure 2.5.

Benefits and limitations exist for the various scales. Larger scaled scaffold features easily accommodate mass transport within the matrix and mimic 3D tissue structure (Lee et al., 2008). Limitations associated with these scales is the resultant 2D flat cell shapes and an imbalance in receptor attachment which is not ideal for 3D tissue formation (Figure 2.5) (Stevens and George, 2005) and cell interaction with their surrounding via nano-scale proteins, therefore a popular design route is down-scaling the physical dimensions to nano-scale (Grinsell and Keating, 2014; Kuihua et al., 2014; Lee et al., 2008; Srinivasan et al., 2012). Nano-scale topography presents a higher surface area-volume ratio which enhances cell attachment (due to increased exposure of cells to binding sites), cell-scaffold interaction, differentiation and growth (Lee et al., 2017; Martino et al., 2011; Sart et al., 2014). Limitations of nanoscale features is that the size itself may limit cell infiltration, migration and overall mass transport within the scaffold, leading to 2D growth (a monolayer) on the surface of the scaffold instead of the desired 3D tissue (Srinivasan et al., 2012).

Table 2.1 shows scaffolds with hierarchical organization. The above-mentioned limits and benefits of individual features provide some rationale for many of macro/micro/nano-architectural features observed with many scaffolds. A hierarchical architecture shows consideration for the average size of adult neural stem cells (approximately 20 µm) and overall tissue target features. Considering the average size of an adult neural stem cell, pore sizes ranging 20-160 µm reported in Table 2.1 proved to be optimal, small enough to support 3D cell-cell contacts for neural network structures to form and large enough to allow mass

transport, and infiltration of neuro-endothelial cells for the formation of micro vessels post implantation (Cholas et al., 2012; Jurga et al., 2011; Martínez-Ramos et al., 2015). Jurga and co-workers (Jurga et al., 2011) noted that cell differentiation and spatial compartmentalization could be modulated by pore size. That is, regions of undifferentiated and differentiated (nestin positive neural cells or GFAP positive glial cells) cells were co-existing within the same scaffold. It was hypothesized that it was because small pores (<20 µm) experienced limited penetration of morphogenic factors in comparison to medium pores (80-120 µm) (Jurga et al., 2011). Furthermore, possessing niche areas of undifferentiated cells within the scaffold mimics the native regions of neurogenesis in the brain such as the sub-ventricular zone (SVZ) and the dentate gyrus (DG). These regions of neurogenesis play a crucial role in regeneration and repair in conditions such as traumatic brain injury (Chan et al., 2016; Lee et al., 2008).

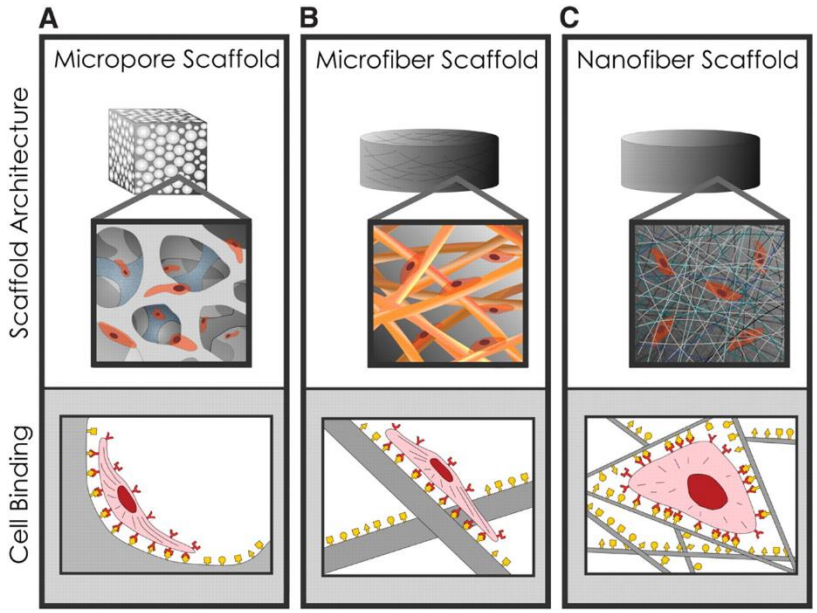

Figure 2.5. Scaffold architecture affects cell binding and spreading. (a and b) Cells binding to scaffolds with microscale architectures flatten and spread. (c) Scaffolds with nanoscale architectures possess larger surface areas for protein absorption, presenting many more binding sites to cell membrane receptors. Figures 2.5a-c are reused from Science, 310(5751), Stevens and George (Stevens and George, 2005). Exploring and engineering the cell surface interface, pp. 1135-1138, 2005, with permission from the American Association for the Advancement of Science.

Mimicking neuromechanical anisotropy through architecture

Brain tissue is non-linear, has pronounced compression-tension asymmetry, and viscoelastic behaviour (Budday et al., 2017; Srinivasan et al., 2012). These properties are an example of mechanical anisotropy, where the mechanical material behaviour is regionally dependent (mechanical properties vary when measured along different directions along the material) (Budday et al., 2017; Hemphill et al., 2015; Nava et al., 2012; Srinivasan et al., 2012; Stevens

and George, 2005). Anisotropy is a property of neural tissue imparted by the hierarchically ordered organization of its composites (e.g. cells, ECM and axonal extension) (Hemphill et al., 2015; Quinones-Hinojosa et al., 2006; Stevens and George, 2005). Mechanical anisotropy is largely linked to fibre alignment, in fact, one of the most distinctive features of nervous tissue (e.g. brain tissue), is the directionally aligned axonal tracts arising from development of axons in specific paths (Hemphill et al., 2015; Sun, 2014). Structure-activity relationships are important as cell behaviour is dependent on their environment; cells detect and respond to their substrate using mechano-transduction via nanoscale topography (Bilston, 2016; Franceschini et al., 2006; McMurtrey, 2016; Oxman et al., 2012). Cells adhere to a substrate using focal adhesion mechanically linked to their cytoskeleton which transmits signals to the cell nucleus influencing a range of cell responses (e.g. cell shape) (Figure 2.6) (Huang et al., 2012; Nathan et al., 2011; Nava et al., 2012; Steward et al., 2012). The environment experienced by the cells is anisotropic and mixed (e.g. interstitial fluid pressure and ECM strain).

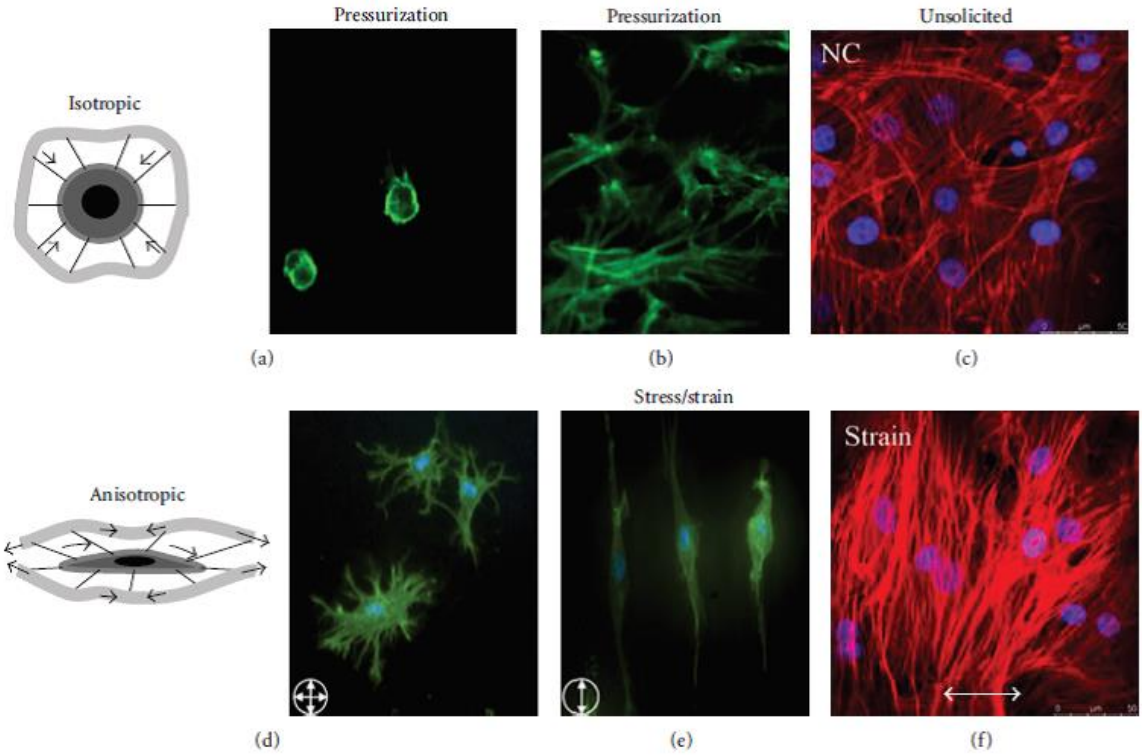

Figure 2.6. Representation of substrate-directed cell fate (images not to scale). (a) Soft isotropic force resulting in a spherical cell shape and (b) spreading on stiffer substrate. (c) Random distribution of cells in isotropic conditions. (d) Cell protrusions in multiple directions is induced with biaxial strain whereas (e) uniaxial strain induces an elongated cell shape. (f) cell elongation is observed under anisotropic strain This figure is reused and reprinted from Journal of Biomedicine and Biotechnology, Nava and co-workers (Nava et al., 2012). Controlling self-renewal and differentiation of stem cells via mechanical cues, pp. 1-12, 2012, under the terms of the Creative Commons Attribution License.

As disorganized as the idea of anisotropy and heterogeneous material properties may seem, brain tissue is highly organized into functional neural circuits as demonstrated by diffusion tensor images (DTI) in the literature. Water moves more freely along axonal bundles versus perpendicular to those bundles due to fewer obstacles to obstruct movement along the fibres, therefore DTI uses anisotropy to detect fibre organization (Mori and Zhang, 2006). Anisotropy is therefore central in establishing the architectural arrangement correlative to desired scaffold function. Adding anisotropic properties renders the 3D scaffold more similar to native tissue as it too is composed of heterogeneous elements (e.g. cells, fibres, biomolecules, blood vessels) aligned in unique, specific ways. The efforts to replicate neural tissue anisotropy include stiffness, pores, fibre alignment, channels and other topographical features (Courtney et al., 2006; Krishna et al., 2016; Mohtaram et al., 2015; Zhang et al., 2011) within the 3D scaffold structures as observed Table 2.1. Furthermore, the use of co-polymer biomaterials adds an element of anisotropy (e.g. different chemical bonding at different directions).

As popular as they may be, hydrogels generally have a poorly oriented architecture as they tend to lack the physical cellular-scale topographical features to facilitate cellular adhesion and migration, or promote directed axonal growth (Binan et al., 2014; Büyüköz et al., 2018; Du et al., 2015, 2014). This innate poor cell alignment and lack of guidance cues, renders it difficult to align cells to achieve regeneration similar to the native tissue (Stratton et al., 2016). Unlike most unmodified hydrogels, scaffold systems that demonstrate superior axonal guidance properties contain nano-scaled features (e.g. aligned fibres), laminar structures or channels (Georgiou et al., 2015; Mitchell and Tojeira, 2013).

Nanofibers present a nanoscale architecture which closely resembles the native ECM structure, with a large surface area to volume ratio, which allows the presentation of cellular-scale topographical cues across to foster guided neuronal migration and axonal extension across the lesion site (Hsieh et al., 2015; Newland et al., 2015; Tian et al., 2015). Post-implantation, Rivet and co-workers (Rivet et al., 2015) noted the ability of astrocytes to not only locate the fibres within their 3D electrospun fibre and hydrogel hybrid scaffold, but also utilize their cues for migration into the hybrid matrix. This feature of guided growth and cell communication is a crucial advantage of a 3D scaffold considering its multidimensionality to ensure neurons extend towards reconnection instead of ‘circling’ within the planes of the 3D architecture. Electrospun poly(epsilon-caprolactone) nanofiber scaffolds were shown to influence the direction of neurite extension via perpendicular contact guidance (Nisbet et al., 2009).

In tissue engineering, anisotropic topography has proven effective in promoting directional neurite/axonal extension (Li et al., 2015), which mimics the *in vivo* environment where axons extend along the bands of Büngner created by glial cells. Bands of Büngner are longitudinal bands of Schwann cells that provide pathways to guide axon regeneration following lesion-induced Wallerian degeneration in lesioned nerves (Ribeiro-Resende et al., 2009; Rotshenker, 2011). Neurons and glial cells exhibited directed growth and bipolar shapes on aligned electrospun poly-L/D,L lactic acid (PLA70/30) nanofibers scaffolds, whereas randomly oriented, multipolar shapes were observed on random nanofibers (Figure 2.7) (Álvarez et al., 2014). Another approach is the use of aligned fibres which can guide cellular orientation and direction over distances (Tian et al., 2015). A 3D aligned poly(lactic-co-glycolic acid) (PLGA) fibre scaffold used to bridge a 3 mm spinal cord defect showed cells oriented along the direction of the scaffold and axons regenerating along the length of the scaffold (Zamani et al., 2014). A 3D scaffold of parallel fibres embedded in a matrix showed guided Schwann cell migration and axonal growth in the spinal cord (Kriebel et al., 2014). Figure 2.7 depicts examples of topographical design features incorporated into 3D scaffolds.

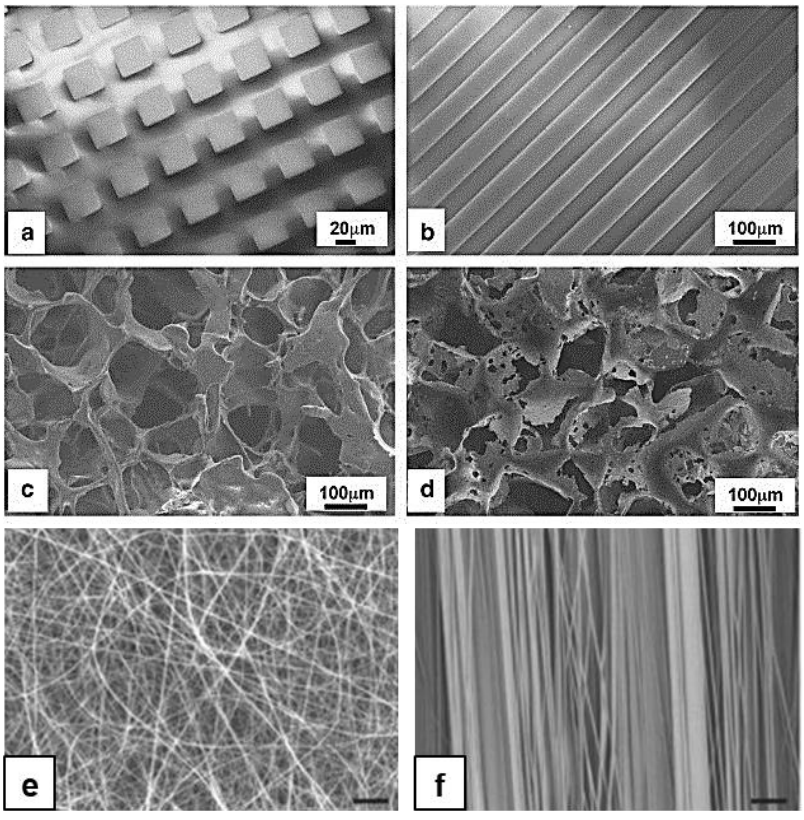

Figure 2.7. Examples of topographical design features incorporated into 3D scaffolds represented by (a) squares, (b) grooves, (c-d) pores in polymeric scaffolds and (e) random and (f) aligned electrospun fibrous mats. The scale bars for figures 2.7e and 7f measure 10 µm. Figure 2.7a-d is reused and reprinted from Biotechnology Advances, 30(1), Martino and co-workers (Martino et al., 2011). Stem cell-biomaterial interactions for regenerative medicine, pp.338–351, 2011, with permission from Elsevier. Figure 2.7e-f is reused and reprinted from

from Scientific Reports, 6(1), Beliveau and co-workers (Beliveau et al., 2016). Aligned nanotopography promotes a migratory state in glioblastoma multiforme tumor cells, p.26143, 2014, under the terms of the Creative Commons Attribution 4.0 International License.

2.7. Engineering neuromimetic architectures

Various methods have been employed to create porous 3D scaffolds in the recent years (2011 to date). Examples of these methods include cryogelation, freeze-drying, porogen template leaching, self-assembly peptides, electrospinning and 3D bioprinting (Table 2.1). Hydrogels are hydrated polymer networks whose dissolution in water is hindered by crosslinks (Aurand et al., 2012a; Pettikiriarachchi et al., 2010). They are the most commonly fabricated scaffolds for neural tissue engineering. However, hydrogels have suffered the issue of insufficient vascularisation which could be improved with the addition of interconnected macropores (Henderson et al., 2013). This could explain the frequency of pore producing methods (e.g. cryogelation, porogen-template leaching) observed in Table 2.1. The most common way of producing macroporous 3D hydrogels is by physically interrupting the hydrogel forming solution with pore forming units which are leached out post gelling leaving behind pores. The interconnections are formed in areas were the pore forming units have come into close proximity. Porogen leaching (also known as solution casting/particulate leaching), involves mixing a porogen (e.g. sodium chloride, sugar crystals) into a biodegradable polymer solution which is cast into a mould. Thereafter, the solvent is removed by lyophilisation while the porogen particles are leached out to obtain a porous structure. The limitation with this method is the poor interconnectivity, irregular pore geometry and difficulties associated with removing the porogens particles (Bencherif et al., 2013). Compared to porogen leaching, freeze-drying uses ice particulates as the porogen material, resulting in easier porogen removal. In this method, a polymer solvent solution and water emulsion is cooled, which in turn locks the liquid state structure. Thereafter the solvent and water are removed by freeze drying. Cryogelation is arguably one of the easiest methods of producing interconnected porous 3D scaffolds in comparison to other techniques (e.g. freeze-drying, porogen leaching) (Bencherif et al., 2013; Henderson et al., 2013)(Bencherif et al., 2013). A polymeric solution is cooled below freezing point, resulting in crystallization of the solvent while the gel solution is maintained in a non-frozen liquid phase. The inherent interconnectivity of the pores within the 3D scaffold is a result of the solvent crystals growing towards each other and making contact with each other during crystallization (Lozinsky et al., 2001). The porogen is removed by simple exposing the cryogel to temperatures above the solvent freezing point, which causes the solvent to melt, hydrating the polymeric gel network. The ability of these methods to produce interconnected pores is highly desired to augment free flow of nutrients, waste products, cell migration and overall cell

viability within the 3D scaffold. Self-assembly nanofiber scaffolds are alternative forms of hydrogels in which the fibrillary networks are formed either spontaneously in response to environmental changes such as pH, ionic strength and temperature (Pettikiriarachchi et al., 2010). These networks then absorb water and form hydrogels. A large number of these fabrication methods are still highly conventional, and may in part play a role in limiting the success of the architectural design of scaffolds. It is important to note that these conventional methods were previously developed with the objective of drug delivery and not tissue engineering applications, however, they are being explored extensively for scaffolding in the field of tissue engineering (Dutta et al., 2017). de Mulder and co-workers (de Mulder et al., 2009) noted that one of the limitations of conventional fabrication methods is their production of isotropic scaffolds, an architecture that is different from the complex anisotropic architecture of native neural tissue. In addition, these conventional methods offer limited control over pore size, pore geometry, interconnectivity, and spatial distribution of the internal structure of a 3D scaffold (de Mulder et al., 2009; Loh and Choong, 2013). Cryogel (Jurga et al., 2011) and freeze-dried scaffolds fabricated (Cholas et al., 2012; Jurga et al., 2011) resulted in a randomly distributed isotropic porous scaffolds, with a broad size range (20-160 μm) (Jurga et al., 2011). The problem with such results is once again the randomly distributed porous architecture, which is alternate to the hierarchically ordered anisotropic property of neural tissue to facilitate directed neuronal growth.

Nanofiber scaffolds are characterised by their high surface area to volume ratio, high porosity and small (nano range) fibre diameter(Pettikiriarachchi et al., 2010). Electrospinning is the most widely used method for fabrication of ECM-like 3D nano-fibrous scaffolds (Oxman et al., 2012; Tian et al., 2015). Electrospinning uses electrostatic forces to form fine fibres with diameters in the nanometre range. However, electrospinning suffers from limited control, reproducibility and customization of architectural parameters. For example, it is difficult to produce equal fibre sizes with variable porosity as both properties are simultaneously modulated when altering the electrospinning parameters (Carlson et al., 2016). Electrospinning is largely dependent on polymer solution properties, surface tension, conductivity and dielectric constant (Krishna et al., 2016). Some biomaterials are not suitable for scaffold fabrication via electrospinning due to high voltage or the high curing temperature and low solution viscosity (Badrossamay et al., 2014). This then limits the number of eligible materials for fabrication using this method. Additionally, a number of external factors further influence the resultant scaffold outcome via this approach, such as temperature, pressure and humidity (Krishna et al., 2016).

Moreover, the majority of these conventional methods incorporate the use of solvents which often require an additional removal step as these solvents can be toxic to cells (Du et al., 2015; Zamani et al., 2014). Modifications to address the limitations of these conventional methods are under investigation. For example, an alternative would be the use of melt-electrospinning technique which does not require the use of toxic organic solvents needed for solution-electrospinning. Wu and co-workers (Wu et al., 2016) utilized a rotating metallic rod attached to a mandrel to achieve a poly-L-(lactic acid) conduit; this modified the electrospinning process by producing orientated/aligned fibres, which are more desirable than random fibre in terms of guiding the direction of neurite growth and cellular alignment (Hemphill et al., 2015; Nisbet et al., 2009; Tian et al., 2015).

More effort needs to be directed towards the fabrication of reproducible materials. Conventional methods have thus far made it difficult to not only adequately compare 3D scaffold designs, but to also elucidate successful architectural combinations as the details of the 3D internal structures (e.g. pore size, pore shape, fibre alignment) are not often adequately described (Table 2.1). Overall, conventional methods are limited in their ability to control the internal structure and precisely mimic the microtopography required for the formation of complex 3D architectures (Büyüköz et al., 2018; Kriebel et al., 2014; Li et al., 2015; Zamani et al., 2014).

A progressive advance to accommodate the complexities of anisotropic 3D architectural scaffold fabrication is 3D printing, also known as the solid free form (SFF) technique or rapid prototyping technique (Carlson et al., 2016; de Mulder et al., 2009; Dutta et al., 2017). Three-dimensional printing techniques are computerized layer-by-layer fabrication methods capable of producing complex 3D architectures (de Mulder et al., 2009; Du et al., 2014; Dutta et al., 2017; Zamani et al., 2014). The resultant 3D printed construct is informed by a computer aided design (CAD) which is often guided by anatomically correct imaging (employing, for example, magnetic resonance imaging (MRI) or computed tomography (CT) scans). Figure 2.8 depicts an example of a typical 3D bioprinting process. The advantage of this approach is that the design can be rendered highly biomimetic, which increases the anatomical correctness of the construct. Additionally, due to application of a layer-by-layer manufacturing process, the resultant 3D printed scaffolds will display the sought after tissue property of anisotropy (Zou et al., 2016).

A reproducible fabrication process is crucial for the commercial translation and potential clinical application of the scaffold. Three-dimensional printing techniques enable precise control of the internal architecture (e.g. spatial design, pore geometry) of the 3D scaffold with

minimal material waste (Badrossamay et al., 2014; de Mulder et al., 2009; Du et al., 2014; Zamani et al., 2014). The printing techniques are numerous; they may be liquid-based (e.g. stereolithography), solid-based (fused deposition modelling) or powder based. Fused deposition modelling is the most widely used of these techniques due to cost and reliability (Zou et al., 2016). Three-dimensional bioplotting is one of the latest major advancements in 3D printing technique in the field of tissue engineering (Carlson et al., 2016; Hemphill et al., 2015). Processes such as bioplotting/bioprinting enhance the cell seeding process via co-fabrication, enabling the distribution of cells in desired locations. This removes the additional seeding stage required with conventional methods, and enables controlled spatial distribution of cells and nutrition.

Despite the potential for more controlled internal and external 3D scaffold architecture for customized patient specific scaffolds, much of the work on 3D printing in neural tissue engineering is still at the research and development (R&D) stage, evidenced by the low number of reports of *in vivo* work in the literature (Table 2.1). This can be attributed to the current challenges facing 3D fabrication techniques with regards to neural tissue engineering (Cheng et al., 2013; Zamani et al., 2014).

A current challenge with 3D printing is the inability of the fabrication processes to accommodate the low modulus of neural tissue materials to produce complex stable architectures with good resolution (Tu et al., 2016). A case in point is the 3D bioprinted neural stem cell-laden thermoresponsive biodegradable polyurethane hydrogel scaffold designed by Hsieh and co-workers (Hsieh et al., 2015). A degree of structural collapse was observed with this scaffold during fabrication. The bioink possessed the low gel modulus desired to mimic soft neural tissue, however, the layer-by-layer deposition process failed to accommodate the softness of the material employed and resulted in structural collapse of the 3D scaffold, which compromised the integrity of the architecture.

Neural tissue possesses properties of soft tissue such as high elasticity, viscosity and flexibility coupled with large pores, which creates a problem when the fabrication process requires stacking the soft material (e.g. hydrogel) layer-by-layer through 3D printing (Kim et al., 2016). Hydrogels are most commonly used for brain tissue engineering, but their weak mechanical properties render it difficult for them to retain shape (Büyüköz et al., 2018). Therefore, the conflict that arises is between the 3D printing process requirements and *in vivo* scaffold requirements. That is, for 3D printing the material needs to possess a low viscosity and gel rapidly to maintain the pre-designed geometry (Loh and Choong, 2013; Sudwilai et al., 2014), whereas *in vivo* the material is required to be a soft matrix when in close proximity to neural

tissue (< 1 kPa elastic modulus) to augment neural stem cell differentiation and limit tissue stress/injury post implantation.

Material processibility is a large hurdle which challenges 3D architectural scaffold fabrication resulting in a decline in the number of eligible materials when transitioning from conventional fabrication methods to more controlled SFF methods. With regard to 3D printing, the rheological properties and degree of crosslinking largely influence the modulus of the material and thus printability (Hsieh et al., 2015). For example, there is a limited range of biomaterials that can be processed by SFF techniques; they are limited to collagen, gelatin, fibrin, ceramics, thermoplastics or light curable composites (Badrossamay et al., 2014; Cheng et al., 2013; Mata et al., 2009; Zamani et al., 2014). Furthermore, only a few of these are eligible for soft tissue application. Only a handful of commercial bioinks are available for 3D printing for soft tissue applications (Guvendiren et al., 2016). BioInk™ (RegenHu) is an example of a bioink containing fibrin/collagen for soft tissue application, however, this BioInk™ is for skeletal muscle tissues and not neural tissues (Gu et al., 2016). To our knowledge, no bioinks currently exist for neural tissue. Moreover, none of the bioinks offer the option of functionalization (Guvendiren et al., 2016), limiting options for enhancing the pro-regenerative properties of the scaffold.

Three-dimensional printing promises reproducible, personalized, clinically translatable, biomimetic 3D constructs and potentially in situ/*in vivo* bioprinting of scaffolds (Murphy and Atala, 2014; Ventola, 2014). Three-dimensional printing is far from maturity, especially with regards to neural tissue engineering, evidenced by the lack of bioinks and limited *in vivo* reports. However, 3D printing is undergoing rapid advances (Kim et al., 2016) at a rate which needs to be met with concurrent improvements in resolution, printing speed, nozzle design, and most importantly, improvements in fabrication process compatibility with biocompatible materials and biomaterial advances (e.g. biomaterials for rapid crosslinking) (Kim et al., 2016; Murphy and Atala, 2014).

Ultimately, none of the current fabrication methods meet the standards required to create an optimal tissue-mimetic 3D architecture scaffold. Each are faced with their limitations, but strengths are also evident for each approach. For example, 3D printing is the most promising technique for controlling micro/macroscopic morphology to create the desired 3D physical structure (Park et al., 2015). With regards to neural tissue engineering, electrospinning remains the most promising technique for simulating the nanoarchitected fibrils found in the native ECM. While developments in precision printers and design of smaller needles to aid in increasing printing resolution are underway, perhaps a synergistic fabrication approach can

be used in the meantime for neural tissue scaffolding. For example, Park and co-workers (Park et al., 2015) demonstrated that combining 3D printing and electrospinning can yield a structure with improved nano-micro-macro architectural features. Even though 3D printing is the future, conventional methods are still leading in neural tissue engineering as evident in Table 2.1. Conventional fabrication methods should therefore, not be disregarded considering their large library of biomaterial options in comparison to the limited biomaterial options available for 3D printing.

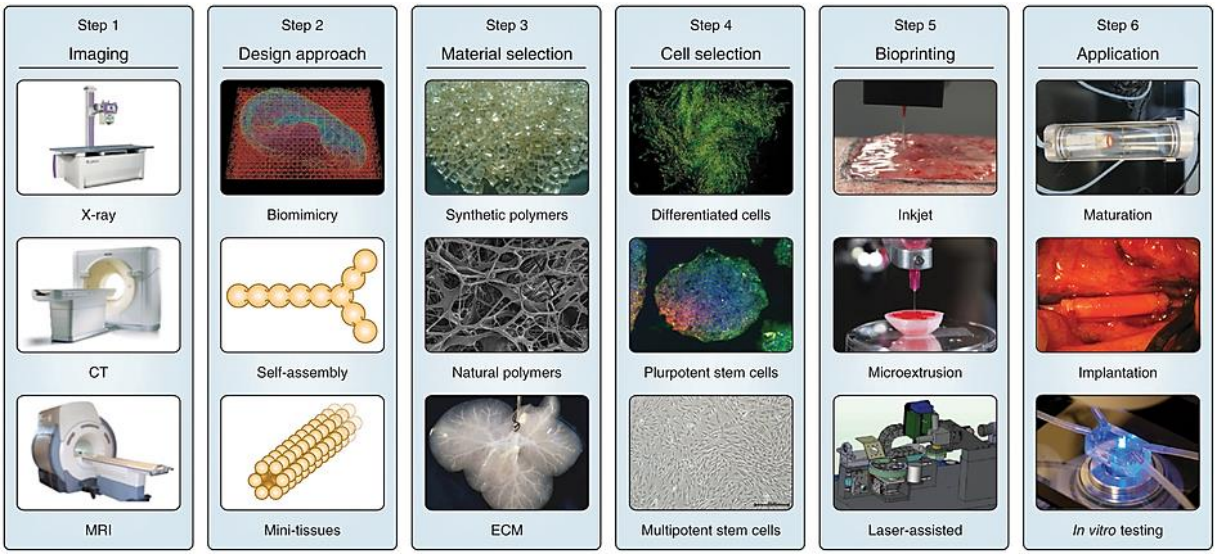

Figure 2.8. An example of a typical 3D tissue bioprinting process. The process is simple; design of the printed tissue is guided by an image of the tissue (step 1) followed by choice of design approach (step 2). This is followed by input with suitable material and biological matter (steps 3 and 4). Feeding the instrument with the CAD and suitable materials yields a 3D printed tissue-mimetic construct (steps 5 and 6). This figure is reused and reprinted from Nature Biotechnology, 32(8), Murphy and Atala (Murphy and Atala, 2014). 3D bioprinting of tissues and organs, pp. 773-785, 2014, with permission from Nature Publishing Group.

2.8. Biomaterials for 3D neuro-scaffolding

As noted in the previous section, tissue engineering efforts are progressing towards more advanced fabrication methods such as 3D printing and sophisticated CAD. This could potentially drive more focus towards scrutinizing critical architectural design parameters in future work. Presently, a current major challenge may be the availability of suitable polymeric materials that not only produce biomimetic 3D scaffold architectures but that are also compatible with the processing requirements of current fabrication methods (e.g. electrospinning, 3D printing).

Therefore, this review found it worthwhile to attempt to define material properties for the fabrication of 3D scaffolds suitable for neural tissue application. Biomaterials are essential to

the discussion and analysis of scaffold architecture. Not only do biomaterials enable the construction of these 3D architectures, they present an array of physicomechanical properties to influence, or even enhance the scaffold capabilities to mimic anatomical structures. A wide variety of materials have been employed (Table 2.1), however the suitability of these materials is challenged by 3D scaffold architectural requirements. These biomaterial-specific architectural requirements include tunability (e.g. degradation rate, ability to conform to the desired shape, processibility), maintenance of structural integrity, sterility, and biocompatibility (Snigdha et al., 2017). The tunability of the material *in vivo* is very important for tissue regeneration in so far as providing a dynamic environment to accommodate the changes that occur with the tissue specific regeneration process (e.g. cell migration, tissue formation).

Biocompatibility

Biocompatibility of materials is pertinent to facilitate scaffold tissue integration (Kumari and Kumar, 2017; von Burkersroda et al., 2002). Biocompatibility requires that the material elicit no immune response and the surface chemistry allows for cell interaction (e.g. attachment sites). It is not surprising then that the majority (~61%) of the 3D scaffolds represented in the literature are composed of natural polymers (Figure 2.3). Natural polymers such as collagen for example, display desirable properties such as sites for cell adhesion; collagen forms one of the primary structural components of the native ECM and is present in abundance *in vivo* (Mondschein et al., 2017; Newland et al., 2015; Willerth and Sakiyama-Elbert, 2007). Moreover, collagen scaffolds were noted to trigger brain-derived neurotropic factor (BDNF, which regulates adult synapse plasticity in the CNS) and glial-cell derived neurotropic factor (GDNF, which induces neuronal outgrowth release *in vivo* (Huang et al., 2012). In contrast, synthetic polymers tend to lack the sites required for cell interaction. Synthetic polymers can be tuned to enhance their biocompatibility, through the addition of bioactive molecules (e.g. fibronectin, laminin, isoleucine-lysine-valine-alanine-valine (IKVAV)) and chemical alteration (Sensharma et al., 2017). By co-spinning fibronectin (natural polymer) and poly-L-lactide, Rivet and co-workers (Rivet et al., 2015) tuned the cell adhesion properties of the poly-L-lactide nanofibers, resulting in improved cell infiltration into the matrix. Altering polymer chemical properties can also enhance the cell attraction of the construct. For example, hydrophilicity largely influences to cell attraction/affinity to the construct. Water soluble groups that contribute to hydrophilicity include amidic (-CONH-), ether, hydroxylic (-OH), sulphonic (-SO_3H), and carboxylic (-COOH) groups (Guo and Ma, 2014; Tran et al., 2011). The material and degradation products should be non-toxic ensuring no damage to newly formed/surrounding tissue (Guvendiren et al., 2016; Makadia and Siegel, 2012). The self-assembly peptide (SAP) RADA-16-I has low pH (3.5) which is toxic to cells and tissues (Zhang et al., 2016). Zhang and co-workers (Zhang et al., 2016) facilitated the formation of a hydrogel

at a safer neutral pH by appending functional motifs, RGD and IKVAV to the SAP (Table 2.1). This markedly improved biocompatibility by lowering cytotoxicity of the scaffold while increasing cell adhesion (RGD) and neurite outgrowth (IKVAV). L-lactate, the degradation product of electrospun PLA70/30 fibres, fuels angiogenesis and supports neuronal and neural cell metabolism (Álvarez et al., 2014).

Biodegradability

Biodegradability is an indicator of tunability; it is important that the material is biodegradable *in vivo.* From an architectural perspective, biodegradation of the scaffold material will enable the formation of predesigned structurally guided spaces upon which cells can deposit tissue-forming material. This also avoids unnecessary secondary injury from removal of the implant, which is ideal as scaffolds should serve as temporary surrogate support structure for neural tissue regeneration, and avoid unnecessary secondary injury on removal of the implant. In general, for a non-porous scaffold there are two forms of degradation: bulk and surface erosion. With bulk erosion, the rate of degradation is faster than the degradation of polymer bonds so degradation occurs throughout the structure, while surface erosion the degradation is limited to the polymer surface (Gu et al., 2016; Zou et al., 2016). Ideally the scaffold should exhibit surface erosion, as degradation from the outside in will maintain the shape and mechanical strength (avoiding collapse from mass loss) of the 3D construct architecture. However, with a porous material the presence of pores causes even a surface-degrading material to exhibit some degree of bulk erosion properties.

Consideration of the tissue target is crucial to the material properties of the scaffold construct. The implant site affects the degradation processes through the presence of water, immune cells or enzymes. Most biodegradable polymers undergo hydrolytic degradation. The target tissue (brain tissue) has a very high water content (approximately 80% water) (Aurand et al., 2012b). This high water content results in a high fluid flow that is able to replenish enzymes which may lead to increased degradation rates (Aurand et al., 2012b). The type of degradation and degradation rate affects the structural integrity of the scaffold *in vivo* and hence its performance. This requires careful consideration of the chemical properties of the polymer (e.g. hydrophilic:hydrophobic balance, crystallinity). For example, through consideration of functional groups, PLGA degradation rate can be tuned by altering the ratio of poly lactic acid (PLA) and poly glycolic acid (PGA) which alters its hydrophilic:hydrophobic balance. This is because the methyl side group of PLA renders it more hydrophobic than PGA (Gross et al., 2014; Gu et al., 2016; Guvendiren et al., 2016; Murphy and Atala, 2014). Therefore the more PGA present, the more hydrophilic, more water absorbing and subsequently faster degrading the PLGA.

Implant longevity *in vivo* ranged from < 24 hours to 15 months (Table 2.1). An architectural challenge observed in some studies is the mismatch between the rate of tissue regrowth and scaffold degradation profiles, evidenced by the large range in duration of lifetime of implants *in vivo* in the various studies (Table 2.1). If the degradation rate is mismatched (e.g. too low or too high), there will be a resultant restriction in cell migration, proliferation and deficiencies within the scaffold, hindering neural tissue regeneration (Cholas et al., 2012; Kumari and Kumar, 2017; Zamani et al., 2014). An example of this is observed in a study by Rivet and co-workers (Rivet et al., 2015), where the 3D scaffold retained its shape for over 60 days. This was attributed to the material used being cellulose-based (methylcellulose) hydrogels which have a limited capacity for degradation because they are enzyme resistant and indigestible by the body (Hsieh et al., 2015; Park et al., 2015; Snigdha et al., 2017). Therefore, the resilience (low degradation rate) of the methylcellulose used inhibited tissue regeneration efforts evidenced by the lack of reduction in lesion volume (Table 2.1). Another instance is when the degradation rate is too high. An example of this is observed in a study by Jurga and co-workers (Jurga et al., 2011) where the 3D scaffold could only retain its shape for less than 24 hours. This was attributed to the material employed, being gelatin, which has a high degradation rate. The degree of crosslinking for this scaffold was also limited further by the amount of crosslinker used as the crosslinker, glutaraldehyde, can be toxic to cells. The combination of weak crosslinking and innately high degradation rate resulted in an accumulation of scaffold degradation components (gelatin and laminin) which produced a toxic, hypertonic, stressful environment for cells/tissue surrounding the implant site. Therefore, the fragility of the material and fabrication limitations, including the institution of a crosslinker, resulted in loss of mechanical and structural integrity of the implant premature to tissue formation. In both cases, the importance of biomaterial degradation rate (tunability) on 3D architecture performance is highlighted.

Biomaterial swelling to enhance architectural performance

Biomaterial swelling is the increase in volume that results from the migration of solvent molecules inside the polymer network (Aamodt and Grainger, 2016; Guo and Ma, 2014; Lakhundi et al., 2015; Nasatto et al., 2015; Tam et al., 2014). This increase in volume in turn scales-up the 3D geometry of the scaffold architectural features (Dervaux and Amar, 2011). Biomaterial swelling is a considerable factor in scaffold design as it directly affects the porosity of the scaffold as well as its integration in the neural tissue. For example, if the pore walls are highly concentrated and thick, then additional water absorption within the polymeric pore walls could result in a marked reduction in pore size within the scaffold structure (Zhao et al., 2010).

Biomaterial swelling may induce softening of a scaffold (e.g. hydrogel or cryogel) which in turn influences the mechanical properties and overall architectural integrity of the scaffold.

The reason that hydrogels are highly preferred materials for neural tissue engineering is due to their ability to swell. The swelling property is advantageous in terms of permeability, flexibility and reduced tensile strength (Dumitriu, 1991; Tran et al., 2011). High water content results in an increased permeability/diffusion coefficient for enhanced mobility of solutes and metabolites (Ganji et al., 2010). The prerequisite for swelling is that the biomaterial has a deformable/flexible network. Free volume, thermal profiles (glass transition temperature) and crosslinking can aid in defining the suitability and flexibility of polymer networks. Free volume is the empty space/volume within a polymer material that is not occupied by the molecules (Budd et al., 2005), not to be confused with pores. Free volume enables mobility of the polymer chains, a characteristic of amorphous materials, whereas more crystalline materials have a lower free volume and hence lower material flexibility. Free space within the polymer chain translates to increased flexibility of the polymer, and enhanced penetration of solvent molecules resulting in swelling (Dervaux and Amar, 2011; Yang et al., 2001). Therefore, semi-crystalline materials undergo less swelling than amorphous materials.

Swelling improves mimicry of the mechanical properties of neural tissue. Viscoelasticity is the property of neural tissue that enables it to exhibit both elastic and viscous characteristics when withstanding deformation. Penetration of solvent into the polymer network forces the polymer chains into an less entropically desired figuration; the chain in turn exerts a resistive/retractive force (Aamodt and Grainger, 2016; Dumitriu, 1991; Tran et al., 2011). This retractive force is what allows the biomaterials to withstand and recover from deformation, preventing architectural collapse.

Brain tissue is ~80% water (Aurand et al., 2012b); the ability to swell allows the scaffold to maintain its architecture *in vivo* rather than dissolving. Crosslinking prevents polymers from undergoing hydrolysis in the fluid rich brain environment, and facilitates swelling (Deanin, 1991). The degree of crosslinking alters the swelling properties. Increasing the degree of crosslinking, decreases the extent of swelling by decreasing the free volume and increasing the glass transition temperature as the polymer backbones are drawn closer together and molecular mobility is reduced (Aamodt and Grainger, 2016; Nasatto et al., 2015). This relationship between crosslinking and swelling is crucial from an architectural perspective as soft tissue materials are known for their poor mechanical properties. Therefore, careful balancing of the degree of crosslinking and swelling properties is paramount in processing and fabrication.

2.9. Processibility

Materials need to be processed in order to produce the desired 3D scaffold architectural demands (Dutta et al., 2017). Therefore, processibility is a critical parameter with regard to 3D scaffolds. The general rule is that lower molecular weight materials are easier to process, however higher molecular weight materials possess better end use attributes (Davis et al., 1991; Kamaly et al., 2016; Su, 2013). The disadvantage of semi-crystalline materials is that they are stiff, hence hard to process (e.g. melt or deform) into desired architectures. At the same time, their stiffness renders them more mechanically stable. In contrast, amorphous materials are more flexible, hence easier to process into desired architectures. At the same time, their flexibility confers mechanical instability, threatening structural collapse. Both these material features challenge both the fabrication methods and design phases of scaffolding. While synthetic polymers generally withstand harsh processing conditions such as heating (required with fused deposition and laser sintering technique), biopolymers tend to be limited to certain temperature and pH processing ranges (Dutta et al., 2017).

The composition of neural tissue is a crucial reference for consult when identifying desirable material properties. Various materials deform or respond differently to stimuli. Therefore the material properties of brain tissue are a result of the sum of the properties of these various materials. This may be one of the rationales behind the progression and success behind polycomposite biomaterials and modified polymers. One material may not necessarily be able to exert the range of properties to withstand processing required to produce a biomimetic 3D scaffold, however multiple components could be more successful. As presented in Table 2.1, the majority of the scaffolds in the recent years (from 2011 onward) utilize various copolymer combinations (Bosworth et al., 2013; Cholas et al., 2012; Elias and Spector, 2012; Hsieh et al., 2015; Huang et al., 2012; Martínez-Ramos et al., 2015) whereas only a few utilized a single polymer for fabrication (Chen et al., 2011; Jurga et al., 2011). This trend of utilizing multiple polymers for fabrication highlights one of main avenues for addressing the major challenges of 3D scaffold design, which is the identification of a biocompatible, tunable, swelling biomaterial with sufficient biochemical and physicomechanical properties to withstand both the fabrication process and the demands of a porous 3D architecture for neural regeneration.

2.10. *In vivo* tissue integration and performance of 3D scaffolds

The overall goal for 3D scaffolds is such that the architecture facilitates tissue integration with no anatomical or functional differences between the newly formed and native tissue. Physicochemical and design features such as porosity, tunability, and biomaterial swelling, as discussed, aid in tissue integration. For example, interconnected pores promote integration by

facilitating penetration of native tissue into the scaffold, and newly formed tissue throughout the scaffold to encourage reconnection of circuits. The majority of scaffolds reported cellular infiltration, proliferation and enhanced cell survival qualified by qualitative markers such as microtubule-associated protein 2 (MAP-2) and NeuN inside and around the scaffold (Table 2.1). This can be attributed to the integrative nature of the 3D scaffold architectures through interconnected pores facilitating cellular infiltration, and the 3D architecture enclosing and protecting the cells from the inhibitory environment at the lesion site. Biomaterial swelling enhances bonding properties and tissue integration *in vivo* as the brain is composed of approximately 80% water. Chemical modification of the biomaterial by introducing negative charges can enhance tissue integration *in vivo*, as the highly negatively charged glycosaminoglycans (GAGs) are noted to act as ECM crosslinkers and reservoirs for water and growth factors *in vivo* (Aamodt and Grainger, 2016).

Aside from the previously noted physicochemical and design properties, tissue integration can further be enhanced through the incorporation of bioactive materials (peptides, neurotrophic factors and other ECM components) and cells (Deanin, 1991; Dumitriu, 1991; Paul Z. Elias and Spector, 2012; Hsieh et al., 2015; Mondschein et al., 2017). Functionalization with bioactive groups aids in tissue integration by 'connecting' the scaffold to the native tissue. For example, proteins and peptides aid in cell adhesion and differentiation while neurotrophic factors can assist in tissue development (Moroni and Elisseeff, 2008). Surprisingly, none of the reviewed studies utilized growth factors, failing to take advantage of this feature to potentially enhance tissue integration (Figure 2.3). Nonetheless, with the correct architectural composition, bioactive effects can still be achieved. For example, implantation of a collagen scaffold by Huang and co-workers (K. F. Huang et al., 2012) resulted in a sustained increase in tissue concentration of brain-derived neurotropic factors (BDNF and GDNF); this scaffold thus rendered the administration of exogenous growth factors unnecessary. Moreover, the scaffold resulted in a lowered neurological deficit and improved sensorimotor recovery. The incorporation of a BDNF-mimetic non-peptide ligand to a PCL nanofiber scaffold showed improved tissue integration by increasing neuronal sprouting at the scaffold-tissue interface (Fon et al., 2014). The incorporation of a self-assembling peptide amphiphile carrying tenacin-c signal showed a 24-fold increase in the number of endogenous neuroblasts directed to the injury site (Motalleb et al., 2018) The majority (~61%, Figure 2.3) of the scaffolds evaluated were acellular (Bosworth et al., 2013; Cholas et al., 2012; Hsieh et al., 2015; Huang et al., 2012; Martínez-Ramos et al., 2015) while a few scaffolds were seeded with stem cells. Examples of cells investigated included bone marrow stromal cells, human amnion-derived multipotent progenitor cells, human umbilical cord mesenchymal stem cells, rat neural stem cells (HC-A94-2), and rat hippocampal cells (Cheng et al., 2013; Guan et al., 2013; K. F.

Huang et al., 2012; Zhang et al., 2018). The purity of the cell lines vary, for example, bone marrow stromal cells have been modified to release BDNF (Günther et al., 2015). Functional recovery was reported at 14 days by Chen and co-workers (Chen et al., 2011) the presence of human amnion-derived multipotent progenitor cells in the scaffold could have enhanced the regeneration potential of the scaffold through the release neurotrophic factors.

Very few studies reported on the infiltration of endothelial cells (Elias and Spector, 2012) or neoangiogenesis (Bosworth et al., 2013; Huang et al., 2012) post-implantation. Most implants described lowered inflammation at the scaffold-tissue interface and variable degrees of glial scarring and regeneration were observed. Neuronal migration, proliferation, and differentiation of neural stem cells into 3D scaffolds was observed in the majority of the studies (Table 2.1). Neuronal/axonal extension was observed by Martinez-Ramos and co-workers (Martínez-Ramos et al., 2015).

Tissue integration failure and immunorejection is associated with the degree of reactivity of astrocytes and microglia, and scar formation (Davoust et al., 2017; Zhao et al., 2010). Following injury, immune mediators are released within minutes and microglial presence can be observed for extended periods after injury (even up to 12 months) (Budd et al., 2005; Guiseppi-Elie, 2010). Reduced inflammatory response and glial scarring were observed, qualified by lowered inflammatory cells markers such as ED1+, GFAP, IBA-1, and CD11b (Table 2.1). These are indicators of the potential for successful tissue integration. Tissue integration is usually evaluated employing optical and histological analysis (Davis et al., 1991; Dumitriu, 1991). Optical analysis provides an overall view of the injured area after implantation, which is useful for visualizing changes in lesion volume and ‘sameness’ of the regenerated and native tissue. Histological analysis enables a more detailed description of optical observations. Clinical translational challenges are observed with both optical and histological methods of analysis. Firstly, they provide qualitative results which can be misleading, rendering comparison of 3D scaffold performances in literature impractical (Morganti-Kossmann et al., 2002; Su, 2013). The misleading nature arises from the fact that 2D images may not provide an adequate representation of the 3D tissue formed (Guldberg et al., 2009). Secondly, they require tissue resection to analyse tissue integration which would defeat the efforts of tissue regeneration. There is an opportunity to enhance clinical translational assessment through developing non-invasive imaging techniques such as chemical exchange saturation transfer magnetic resonance imaging (CEST MRI), which can monitor cell viability and compositional changes of the scaffold *in vivo* (Liang et al., 2015). There needs to be a development and application of more quantitative methods of evaluation such as MRI T2 spin-spin relaxation index (Moroni and Elisseeff, 2008) to obtain improved correlation of the

homogeneity of the tissue-scaffold interface/tissue integration. MRI T2 spin-spin relaxation is a sensitive and quantifiable indicator of the proportion of bound to free water in biological tissues (Ali et al., 2015). T2 relaxation time is particularly sensitive to the degree of water compartmentalization due to the loss of magnetization of water to surrounding molecules (Ali et al., 2015). The higher the degree of compartmentalised water the lower the T2 relaxation time (Ali et al., 2015; Liachenko and Ramu, 2017). Tissue damage induces changes that result in variations in free water fraction. Therefore, T2 relaxation time deviations can be used to quantitate these changes in tissue water content correlating it to tissue damage (e.g. toxicity of scaffold) *in vivo*. Luciano and co-workers (Luciano et al., 2016) presented a protocol for brain sectioning in efforts to apply 3D printing technology in linking post-mortem MRI and histological observations more accurately, which may potentially aid in elucidating key pathological markers. Potentially this technology can further be developed to be applied on living tissue to assist in more closely monitoring and deciphering effects the 3D implanted scaffolds have at the injury site.

2.11. Translational potential of 3D scaffolds with in vivo experimental models of TBI

Functional recovery is an additional approach to assess the efficacy and success of scaffold treatment. To date recovery of nervous tissue scaffolds has been incomplete and unsatisfactory (Huang et al., 2012). Outcomes were reported as successful for ~30% of reviewed studies (Table 2.1). Examples of tests conducted were the neurological severity scores (mNSS) test (Huang et al., 2012), rotarod test (Zhang et al., 2016), and grip strength test (Zhang et al., 2016). Functional outcomes were observed at periods ranging from 2 weeks to over 8 weeks (Chen et al., 2011; Paul Z. Elias and Spector, 2012; Hsieh et al., 2015; Rivet et al., 2015). In future, efforts should be directed to establish the efficacy of the scaffolds at a functional level in animal models.

Study controls, animal models assigned, and methods of analysis require strict consult when evaluating the translational clinical potential of the scaffold and interpretation of regeneration results. In some instances the choice of controls was poor. For example Jurga and co-workers (Jurga et al., 2011) utilized hippocampal slices for comparison with implanted brain lesion results. Scaffold performance and potential is almost exclusively limited to rat models (Table 2.1). Larger animal models were popular until the 1980s, however ethical concerns led to a shifts towards the use of rodents (Vink, 2018). Although rodents have yielded mounting experimental results, there is yet to be any reported successful clinical translation (Vink, 2018). The translational success of 3D scaffolds may be related to the innate differences in the biomechanical and physiological responses of rodent and human tissue, specifically neural tissue, to injury (Luciano et al., 2016; Vink, 2018). Unlike humans, rats have a strong

regenerative potential and heal at a faster rate (Kaplan et al., 2015). Rodents may not be able to capture the complexity and the response of human tissue to injury due to anatomical differences (rodent brains are lissencephalic whereas human brains are gyrencephalic) (Vink, 2018). In addition, rodents are small animals, the 'critical nerve gap' (the nerve gap at which regeneration cannot occur without the aid of bridging/nerve graft) is 1.5 cm for rats, while for humans it is 4 cm (Kaplan et al., 2015). The lesion gaps might be too small to translate to human application. Going forward, larger animal models need to be considered to closer replicate humans where the lesion sizes can be larger. Adding variety to the choice of animal models could avoid skewed species specific results that currently exist in literature. However, the ethical implications of this and interspecies-related differences that hinder the effective translation of results from animal models to humans could also witness a shift to alternatives, such as 3D-printed models (artificial tissue organs fabricated using 3D printing technologies (Han and Hsu, 2017)).

Translational success may be augmented by establishing a clear definition of the injury (Wojnarowicz et al., 2017). Unfortunately, current traumatic brain injury models exhibit overlapping pathological outcomes (Johnson et al., 2015). This is further complicated by the innate heterogeneity of the traumatic brain injury pathophysiology (Luciano et al., 2016; Saatman et al., 2008; Vink, 2018; Wojnarowicz et al., 2017). Neural tissue engineering efforts may benefit from standardizing tests and regeneration outcome measures (e.g. determining noteworthy result criteria). The National Institute of Neurological Disorders and Stroke (NINDS) is exerting effort towards establishing common data elements that can ultimately be employed to render the accurate comparison of results possible (Johnson et al., 2015). Multi-parametic advances in imaging may assist in profiling the complex injury process and 3D scaffold-cell and 3D scaffold-tissue interaction.

2.12. Chapter two summary

The French architect, Robert le Ricolais (1894-1977) stated: 'The art of structure is where to put the holes'. For this review, a suitable phrase would then be 'the art of scaffolding is positioning of the pores and channels'. A critical and extensive review of 3D architectural challenges identified pores as one of the biggest challenges in 3D scaffolds for neural tissue engineering. This is evidenced by the pronounced influence of pores on numerous aspects of the architecture and resultant scaffold behaviour and performance. This is observed from the molecular level, where free volume affects biomaterial swelling and mechanical behaviour, to the micro/macro-level where size affects presentation of cell binding sites, cellular infiltration and tissue integration. With an increased focus on customized treatments, advances in design approaches (computer aided design) and fabrication methods (3D printing), it is crucial now

more than ever for efforts to be increasingly directed towards defining such critical parameters for improved 3D scaffolds for neural tissue engineering.

From an architectural perspective, the overall scaling and design approach, material properties, and fabrication methods should be such that the resultant architecture meets the requirements summarized in Table 2.3. Scaling and design parameters ensure that the scaffold is large enough to enable proper handling for implantation, small enough to be implanted into precise lesion locations, and should enable the ingrowth of various nervous tissue composites (e.g. extracellular matrix, neurons and neuroglia, and blood vessels) and tissue formation of appropriate size to integrate with native tissue. Biomaterial parameters affect the constructs' biomimetic profile. Fabrication parameters largely influence not only the reproducibility but affect the successful translation of the scaffold design and materials employed into functional 3D architectures.

Table 2.3. Summary of critical architectural design parameters for 3D neural scaffolds observed in this review

Parameter		**Requirement**
Design	Macro-architecture	3D construct
		Pliant and soft while sufficiently robust (for clinical implantation stressors)
	Micro-architecture	Anisotropy and compartmentalization
	Porosity	Ideally ~90% (Lee et al., 2016; Martínez-Ramos et al., 2015)
	Pore Size	Multi-scale
	Pore Structure	Interconnected
Biomaterial	Mechanical	Viscoelastic (elasticity of brain tissue: 0.1-1 kPa (Nava et al., 2012))
		Swelling properties (to provide flexibility, permeability, withstand deformation to structure)
	Stability and suitability	Tunable (degradable material)
		Non-toxic degradation products
		Sterilizable
Fabrication method		Reproducible architecture

3D neural scaffolds reviewed have shown experimental success in animal models, confirming the progressiveness of the field of tissue engineering. What is clear is that multimodality, customization and reproducibility of the 3D scaffold architecture are of major importance as there is progression towards commercial feasibility enticed by the success in *in vivo* animal models. However, more effort need to be directed towards scaffold architecture as this is the element that largely influences the success or failure of the relationship between fabrication techniques and biomaterials *in vivo*.

Another one of the major challenges identified in this review is the lack of clear and comparable data in the literature due to the versatility of the materials, fabrication methods, design approaches and injury models in this field of study. Having comparative data and controls can aid in elucidating successes and failures of these scaffolds. For example, testing of the polymeric material independently and in combination with hybrid scaffolds to determine their specific roles should be undertaken, as material composition may be important in determining which cell types are likely to migrate into the scaffold (Elias and Spector, 2012). Outcome measures of scaffold performance need to be standardized to aid in comparison.

The challenges highlighted in this review have multiple causes including the complexity of biological systems, incomplete understanding of cell-ECM interactions, inability to best apply technical advances to synthetic methods, and lack of appropriate biomaterials. This is the manifested by the current shortfall in optimizing the combination of design requirements, fabrication methods and biomaterials for 3D neural scaffolds. Architectural challenges can be addressed through the concurrent advancement of computational aided design, biomaterial advancement and fabrication techniques. This will lead to the development of a systemic understanding of architectural challenges by recognizing all elemental components from design, to processing, to product development for more effective customized features. This may simplify the complexity of architectural challenges by exposing structure-function relationships. Tissue-informed computational models could proposedly be integrated into the initial design approach of scaffolds going forward.

2.11. Conflicts of interest

The authors report no conflicts of interest.

2.12. Acknowledgements

The work reported herein was made possible through funding by the Claude Leon Foundation, the National Research Foundation (NRF) of South Africa and the South African Medical Research Council through its Division of Research Capacity Development under the National

Health Scholarship Programme from funding received from the Public Health Enhancement Fund/National Department of Health. The content hereof is the sole responsibility of the authors and do not necessarily represent the official views of the SAMRC or the funders.

2.13. References

Aamodt, J.M., Grainger, D.W., 2016. Extracellular matrix-based biomaterial scaffolds and the host response. Biomaterials. https://doi.org/10.1016/j.biomaterials.2016.02.003

Ali, T.S., Bjarnason, T.A., Senger, D.L., Dunn, J.F., Joseph, J.T., Mitchell, J.R., 2015. QuantitativeT2: interactive quantitative T2 MRI witnessed in mouse glioblastoma. Journal of medical imaging (Bellingham, Wash.) 2, 036002. https://doi.org/10.1117/1.JMI.2.3.036002

Álvarez, Z., Castaño, O., Castells, A.A., Mateos-Timoneda, M.A., Planell, J.A., Engel, E., Alcántara, S., 2014. Neurogenesis and vascularization of the damaged brain using a lactate-releasing biomimetic scaffold. Biomaterials 35, 4769–4781. https://doi.org/10.1016/j.biomaterials.2014.02.051

Aurand, E.R., Lampe, K.J., Bjugstad, K.B., 2012a. Defining and designing polymers and hydrogels for neural tissue engineering. Neuroscience Research 72, 199–213. https://doi.org/10.1016/J.NEURES.2011.12.005

Aurand, E.R., Wagner, J., Lanning, C., Bjugstad, K.B., 2012b. Building biocompatible hydrogels for tissue engineering of the brain and spinal cord. Journal of Functional Biomaterials 3, 839. https://doi.org/10.3390/JFB3040839

Badrossamay, M.R., Balachandran, K., Capulli, A.K., Golecki, H.M., Agarwal, A., Goss, J.A., Kim, H., Shin, K., Kit, K., 2014. Engineering hybrid polymer-protein super-aligned nanofibers via rotary jet spinning. Biomaterials 35, 3188–3197. https://doi.org/10.1016/j.biomaterials.2013.12.072

Baillieul, S., Chacaroun, S., Doutreleau, S., Detante, O., Pépin, J., Verges, S., 2017. Hypoxic conditioning and the central nervous system: A new therapeutic opportunity for brain and spinal cord injuries? Experimental Biology and Medicine 242, 1198–1206. https://doi.org/10.1177/1535370217712691

Béduer, A., Braschler, T., Peric, O., Fantner, G., Mosser, S., Fraering, P., Bencherif, S., Mooney, D.J., Renaud, P., 2014. Iinjectable cryogels for neural tissue engineering applications, in: 18th International Conference on Miniaturized Systems for Chemistry and Life Sciences. San Antonio, Texas, United States of America, pp. 26–30.

Beliveau, A., Thomas, G., Gong, J., Wen, Q., Jain, A., 2016. Aligned nanotopography promotes a migratory state in glioblastoma multiforme tumor cells. Scientific Reports 6, 26143. https://doi.org/10.1038/srep26143

Bencherif, S.A., Braschler, T.M., Renaud, P., 2013. Advances in the design of macroporous polymer scaffolds for potential applications in dentistry. Journal of periodontal & implant science 43, 251–61. https://doi.org/10.5051/jpis.2013.43.6.251

Bilston, L.E., 2016. The influence of microstructure on neural tissue mechanics, in: Kassab, G.S., Sacks, M.S. (Eds.), Structure-Based Mechanics of Tissues and Organs. Springer, Boston, pp. 1–14.

Bilston, L.E., 2011. Neural Tissue Biomechanics Volume 3 of Studies in Mechanobiology, Tissue Engineering and Biomaterials, Illustrate. ed. Springer Science & Business Media.

Binan, L., Tendey, C., De Crescenzo, G., El Ayoubi, R., Ajji, A., Jolicoeur, M., 2014. Differentiation of neuronal stem cells into motor neurons using electrospun poly-l-lactic acid/gelatin scaffold. Biomaterials 35, 664–674. https://doi.org/10.1016/j.biomaterials.2013.09.097

Bosworth, L.A., Turner, L., Cartmell, S.H., 2013. State of the art composites comprising electrospun fibres coupled with hydrogels : a review. Nanomedicine: Nanotechnology, Biology, and Medicine 9, 322–335. https://doi.org/10.1016/j.nano.2012.10.008

Budd, P.M., Mckeown, B., Fritsch, D., Budd, P.M., Budd, P.M., 2005. Free volume and intrinsic microporosity in polymers. Journal of Materials Chemistry 15, 1977–1986. https://doi.org/10.1039/b417402j

Budday, S., Sommer, G., Birkl, C., Langkammer, C., Haybaeck, J., Kohnert, J., Bauer, M., Paulsen, F., Steinmann, P., Kuhl, E., Holzapfel, G.A., 2017. Mechanical characterization of human brain tissue. Acta Biomaterialia 48, 319–340. https://doi.org/10.1016/J.ACTBIO.2016.10.036

Büyüköz, M., Erdal, E., Alsoy Altinkaya, S., 2018. Nanofibrous gelatine scaffolds integrated with nerve growth factor-loaded alginate microspheres for brain tissue engineering. Journal of Tissue Engineering and Regenerative Medicine 12, e707–e719. https://doi.org/10.1002/term.2353

Carballo-Molina, O.A., Velasco, I., 2015. Hydrogels as scaffolds and delivery systems to enhance axonal regeneration after injuries. Frontiers in cellular neuroscience 9, 13. https://doi.org/10.3389/fncel.2015.00013

Carlson, A.L., Bennett, N.K., Francis, N.L., Halikere, A., Clarke, S., Moore, J.C., Hart, R.P., Paradiso, K., Wernig, M., Kohn, J., Pang, Z.P., Moghe, P. V, 2016. Generation and transplantation of reprogrammed human neurons in the brain using 3D microtopographic scaffolds. Nature Communications 7, 1–10. https://doi.org/10.1038/ncomms10862

Casarosa, S., Bozzi, Y., Conti, L., 2014. Neural stem cells: ready for therapeutic applications? Molecular and Cellular Therapies 2, 31. https://doi.org/10.1186/2052-8426-2-31

Chan, E.C., Kuo, S.-M., Kong, A.M., Morrison, W.A., Dusting, G.J., Mitchell, G.M., Lim, S.Y., Liu, G.-S., 2016. Three dimensional collagen scaffold promotes intrinsic vascularisation for tissue engineering applications. PLOS ONE 11, e0149799. https://doi.org/10.1371/journal.pone.0149799

Chen, Z., Lu, X.C.M., Shear, D.A., Dave, J.R., Davis, A.R., Evangelista, C.A., Duffy, D., Tortella, F.C., 2011. Synergism of human amnion-derived multipotent progenitor (AMP) cells and a collagen scaffold in promoting brain wound recovery: Pre-clinical studies in an experimental model of penetrating ballistic-like brain injury. Brain Research 1368, 71–81. https://doi.org/10.1016/j.brainres.2010.10.028

Cheng, T.Y., Chen, M.H., Chang, W.H., Huang, M.Y., Wang, T.W., 2013. Neural stem cells encapsulated in a functionalized self-assembling peptide hydrogel for brain tissue engineering. Biomaterials 34, 2005–2016. https://doi.org/10.1016/j.biomaterials.2012.11.043

Cholas, R.H., Hsu, H.P., Spector, M., 2012. The reparative response to cross-linked collagen-based scaffolds in a rat spinal cord gap model. Biomaterials 33, 2050–2059. https://doi.org/10.1016/j.biomaterials.2011.11.028

Courtney, T., Sacks, M.S., Stankus, J., Guan, J., Wagner, W.R., 2006. Design and analysis of tissue engineering scaffolds that mimic soft tissue mechanical anisotropy. Biomaterials 27, 3631–3638. https://doi.org/10.1016/j.biomaterials.2006.02.024

Daly, W.T., Knight, A.M., Wang, H., Boer, R. De, Giusti, G., Dadsetan, M., Spinner, R.J., Yaszemski, M.J., Windebank, A.J., 2013. Comparison and characterization of multiple biomaterial conduits for peripheral nerve repair. Biomaterials 34, 8630–8639. https://doi.org/10.1016/j.biomaterials.2013.07.086

Das, S., Carnicer-Lombarte, A., Fawcett, J.W., Bora, U., 2016. Bio-inspired nano tools for neuroscience. Progress in Neurobiology 142, 1–22. https://doi.org/10.1016/j.pneurobio.2016.04.008

Davis, P., Huang, S.J., Nicholais, L., Ambrosio, L., 1991. Modified PHEMA hydrogels, in: Szycher, M. (Ed.), High Performance Biomaterials: A Complete Guide to Medical and Pharmceutical Applications. CRC Press, pp. 343–367.

Davoust, C., Plas, B., Béduer, A., Demain, B., Salabert, A.-S., Sol, J.C., Vieu, C., Vaysse, L., Loubinoux, I., 2017. Regenerative potential of primary adult human neural stem cells on micropatterned bio-implants boosts motor recovery. Stem Cell Research & Therapy 8, 253. https://doi.org/10.1186/s13287-017-0702-3

de Mulder, E.L.W., Buma, P., Hannink, G., 2009. Anisotropic porous biodegradable scaffolds for musculoskeletal tissue engineering. Materials 2, 1674–1696. https://doi.org/10.3390/ma2041674

Deanin, R., 1991. Structure property relations in polyurethanes, in: Szycher, M. (Ed.), High Performance Biomaterials: A Complete Guide to Medical and Pharmceutical Applications. CRC Press, pp. 51–69.

Delcroix, G.J.R., Schiller, P.C., Benoit, J.P., Montero-Menei, C.N., 2010. Adult cell therapy for brain neuronal damages and the role of tissue engineering. Biomaterials 31, 2105–2120. https://doi.org/10.1016/j.biomaterials.2009.11.084

Dervaux, J., Amar, M. Ben, 2011. Journal of the mechanics and physics of solids buckling condensation in constrained growth. Journal of the Mechanics and Physics of Solids 59, 538–560. https://doi.org/10.1016/j.jmps.2010.12.015

Du, B.L., Zeng, C.G., Zhang, W., Quan, D.P., Ling, E.A., Zeng, Y.S., 2014. A comparative study of gelatin sponge scaffolds and PLGA scaffolds transplanted to completely transected spinal cord of rat. Journal of Biomedical Materials Research - Part A 102, 1715–1725. https://doi.org/10.1002/jbm.a.34835

Du, B.L., Zeng, X., Ma, Y.H., Lai, B.Q., Wang, J.M., Ling, E.A., Wu, J.L., Zeng, Y.S., 2015. Graft of the gelatin sponge scaffold containing genetically-modified neural stem cells promotes cell differentiation, axon regeneration, and functional recovery in rat with spinal cord transection. Journal of Biomedical Materials Research - Part A 103, 1533–1545. https://doi.org/10.1002/jbm.a.35290

Dumitriu, S., 1991. Polymeric biomaterials, revised and expanded, in: Szycher, M. (Ed.), High Performance Biomaterials: A Complete Guide to Medical and Pharmceutical Applications. CRC Press, p. 824.

Dutta, R.C., Dey, M., Dutta, A.K., Basu, B., 2017. Competent processing techniques for scaffolds in tissue engineering. Biotechnology Advances 35, 240–250. https://doi.org/10.1016/J.BIOTECHADV.2017.01.001

Elias, Paul Z., Spector, M., 2012. Implantation of a collagen scaffold seeded with adult rat hippocampal progenitors in a rat model of penetrating brain injury. Journal of Neuroscience Methods 209, 199–211. https://doi.org/10.1016/j.jneumeth.2012.06.003

Elias, Paul Z, Spector, M., 2012. Characterization of a bilateral penetrating brain injury in rats and evaluation of a collagen biomaterial for potential treatment. Journal of neurotrauma 29, 2086–102. https://doi.org/10.1089/neu.2011.2181

Fon, D., Zhou, K., Ercole, F., Fehr, F., Marchesan, S., Minter, M.R., Crack, P.J., Finkelstein, D.I., Forsythe, J.S., 2014. Nanofibrous scaffolds releasing a small molecule BDNF-mimetic for the re-direction of endogenous neuroblast migration in the brain. Biomaterials 35, 2692–2712. https://doi.org/10.1016/j.biomaterials.2013.12.016

Forte, A.E., Galvan, S., Manieri, F., Rodriguez y Baena, F., Dini, D., 2016. A composite hydrogel for brain tissue phantoms. Materials and Design 112, 227–238. https://doi.org/10.1016/j.matdes.2016.09.063

Franceschini, G., Bigoni, D., Regitnig, P., Holzapfel, G.A., 2006. Brain tissue deforms similarly to filled elastomers and follows consolidation theory. Journal of the Mechanics and Physics of Solids 54, 2592–2620. https://doi.org/10.1016/j.jmps.2006.05.004

Fu, F., Qin, Z., Xu, C., Chen, X.-Y., Li, R.-X., Wang, L.-N., Peng, D.-W., Sun, H.-T., Tu, Y., Chen, C., Zhang, S., Zhao, M.-L., Li, X.-H., 2017. Magnetic resonance imaging-three-dimensional printing technology fabricates customized scaffolds for brain tissue engineering. Neural regeneration research 12, 614–622. https://doi.org/10.4103/1673-5374.205101

Ganji, F., Vasheghani-Farahani, S., Vasheghani-Farahani, E., 2010. Theoratical description of hydrogel swelling: A review. Iranian Poly Journal 19, 375–398.

Georgiou, M., Golding, J.P., Loughlin, A.J., Kingham, P.J., Phillips, J.B., 2015. Engineered neural tissue with aligned, differentiated adipose-derived stem cells promotes peripheral nerve regeneration across a critical sized defect in rat sciatic nerve. Biomaterials 37, 242–251. https://doi.org/10.1016/j.biomaterials.2014.10.009

Ghuman, H., Modo, M., 2016. Biomaterial applications in neural therapy and repair. Chinese Neurosurgical Journal 2, 34. https://doi.org/10.1186/s41016-016-0057-0
Grinsell, D., Keating, C.P., 2014. Peripheral nerve reconstruction after injury : A review of clinical and experimental therapies. BioMed Research International 2014, 13.
Gross, B.C., Erkal, J.L., Lockwood, S.Y., Chen, C., Spence, D.M., 2014. Evaluation of 3D printing and its potential impact on biotechnology and the chemical sciences. Analytical Chemistry 86, 3240–3253. https://doi.org/10.1021/ac403397r
Gu, B.K., Choi, D.J., Park, S.J., Kim, M.S., Kang, C.M., Kim, C.-H., 2016. 3-dimensional bioprinting for tissue engineering applications. Biomaterials Research 20, 12. https://doi.org/10.1186/s40824-016-0058-2
Guan, J., Zhu, Z., Zhao, R.C., Xiao, Z., Wu, C., Han, Qin, Chen, L., Tong, W., Zhang, J., Han, Qianqian, Gao, J., Feng, M., Bao, X., Dai, J., Wang, R., 2013. Transplantation of human mesenchymal stem cells loaded on collagen scaffolds for the treatment of traumatic brain injury in rats. Biomaterials 34, 5937–5946. https://doi.org/10.1016/j.biomaterials.2013.04.047
Guiseppi-Elie, A., 2010. Electroconductive hydrogels: Synthesis, characterization and biomedical applications. Biomaterials 31, 2701–2716. https://doi.org/10.1016/j.biomaterials.2009.12.052
Guldberg, R.E., Duvall, C.L., Peister, A., Oest, M.E., Lin, A.S.P., Palmer, A.W., Levenston, M.E., 2009. 3D Imaging of tissue integration with porous biomaterials. Biomaterials 29, 3757–3761. https://doi.org/10.1016/j.biomaterials.2008.06.018.3D
Günther, M.I., Weidner, N., Müller, R., Blesch, A., 2015. Cell-seeded alginate hydrogel scaffolds promote directed linear axonal regeneration in the injured rat spinal cord. Acta Biomaterialia 27, 140–150. https://doi.org/10.1016/j.actbio.2015.09.001
Guo, B., Ma, P., 2014. Synthetic biodegradable funtional polymers for tissue engineering: a brief review. Science China Chemistry 57, 490–500. https://doi.org/10.1007/s11426-014-5086-y
Guvendiren, M., Molde, J., Soares, R.M.D., Kohn, J., 2016. Designing biomaterials for 3D printing. ACS Biomaterials Science & Engineering 2, 1679–1693. https://doi.org/10.1021/acsbiomaterials.6b00121
Han, H.-W., Hsu, S.-H., 2017. Using 3D bioprinting to produce mini-brain. Neural regeneration research 12, 1595–1596. https://doi.org/10.4103/1673-5374.217325
Hao, P., Duan, H., Hao, F., Chen, L., Sun, M., Fan, K.S., Sun, Y.Eve., Williams, D., Yang, Z., Li, X., 2017. Neural repair by NT3-chitosan via enhancement of endogenous neurogenesis after adult focal aspiration brain injury. Biomaterials 140, 88–102. https://doi.org/10.1016/j.biomaterials.2017.04.014
Haslach Jr, H.W., Gipple, J.M., Leahy, L.N., 2017. Influence of high deformation rate , brain region , transverse compression , and specimen size on rat brain shear stress morphology and magnitude. Journal of the Mechanical Behavior of Biomedical Materials 68, 88–102. https://doi.org/10.1016/j.jmbbm.2017.01.036
He, J., Wang, X., Spector, M., Cui, F., 2012. Scaffolds for central nervous system tissue engineering. Frontiers of Materials Science 6, 1–25. https://doi.org/10.1007/s11706-012-0157-5
Heile, A., Brinker, T., 2011. Clinical translation of stem cell therapy in traumatic brain injury: the potential of encapsulated mesenchymal cell biodelivery of glucagon-like peptide-1. Dialogues in Clinical Neuroscience 13, 279–286.
Hemphill, M.A., Dauth, S., Yu, C.J., Dabiri, B.E., Parker, K.K., 2015. Traumatic brain injury and the neuronal microenvironment: A potential ole for neuropathological mechanotransduction. Neuron 85, 1177–1192. https://doi.org/10.1016/J.NEURON.2015.02.041
Henderson, T.M.A., Ladewig, K., Haylock, D.N., McLean, K.M., O'Connor, A.J., 2013. Cryogels for biomedical applications. Journal of Materials Chemistry B. https://doi.org/10.1039/c3tb20280a

Hopkins, A.M., DeSimone, E., Chwaleka, K., Kaplan, D., 2015. 3D in vitro modeling of the central nervous system. Progress in Neurobiology 0, 1–25. https://doi.org/10.1016/j.pneurobio.2014.11.003.3D

Hsieh, F.Y., Lin, H.H., Hsu, S. hui, 2015. 3D bioprinting of neural stem cell-laden thermoresponsive biodegradable polyurethane hydrogel and potential in central nervous system repair. Biomaterials 71, 48–57. https://doi.org/10.1016/j.biomaterials.2015.08.028

Huang, K.F., Hsu, W.C., Chiu, W.T., Wang, J.Y., 2012. Functional improvement and neurogenesis after collagen-GAG matrix implantation into surgical brain trauma. Biomaterials 33, 2067–2075. https://doi.org/10.1016/j.biomaterials.2011.11.040

Huang, Y., Zheng, L., Gong, X., Jia, X., Song, W., Liu, M., Fan, Y., 2012. Effect of cyclic strain on cardiomyogenic differentiation of rat bone marrow derived mesenchymal stem cells. PLoS ONE 7, e34960. https://doi.org/10.1371/journal.pone.0034960

Hwang, D.W., Jin, Y., Lee, D.H., Kim, H.Y., Cho, H.N., Chung, H.J., Park, Y., Youn, H., Lee, S.J., Lee, H.J., Kim, S.U., Wang, K.-C., Lee, D.S., 2014. In vivo bioluminescence imaging for prolonged survival of transplanted human neural stem cells using 3D biocompatible scaffold in corticectomized rat model. PLoS ONE 9, e105129. https://doi.org/10.1371/journal.pone.0105129

Johnson, V.E., Meaney, D.F., Cullen, D.K., Smith, D.H., 2015. Animal models of traumatic brain injury. Handbook of Clinical Neurology 127, 115–128. https://doi.org/10.1016/B978-0-444-52892-6.00008-8

Jurga, M., Dainiak, M.B., Sarnowska, A., Jablonska, A., Tripathi, A., Plieva, F.M., Savina, I.N., Strojek, L., Jungvid, H., Kumar, A., Lukomska, B., Domanska-Janik, K., Forraz, N., McGuckin, C.P., 2011. The performance of laminin-containing cryogel scaffolds in neural tissue regeneration. Biomaterials 32, 3423–3434. https://doi.org/10.1016/j.biomaterials.2011.01.049

Kamaly, N., Yameen, B., Wu, J., Farokhzad, O.C., 2016. Degradable controlled-release polymers and polymeric nanoparticles: mechanisms of controlling drug release. Chemical Reviews 116, 2602–2663. https://doi.org/10.1021/acs.chemrev.5b00346

Kaplan, H.M., Mishra, P., Kohn, J., 2015. The overwhelming use of rat models in nerve regeneration research may compromise designs of nerve guidance conduits for humans. Journal of Materials Science: Materials in Medicine 26, 1–5. https://doi.org/10.1007/s10856-015-5558-4

Kehoe, S., Zhang, X.F., Boyd, D., 2012. FDA approved guidance conduits and wraps for peripheral nerve injury : A review of materials and efficacy. Injury 43, 553–572. https://doi.org/10.1016/j.injury.2010.12.030

Kim, J.I., Hwang, T.I., Aguilar, L.E., Park, C.H., Kim, C.S., 2016. A Controlled Design of Aligned and Random Nanofibers for 3D Bi-functionalized Nerve Conduits Fabricated via a Novel Electrospinning Set-up. Scientific Reports 6, 23761. https://doi.org/10.1038/srep23761

Kriebel, A., Rumman, M., Scheld, M., Hodde, D., Brook, G., 2014. Three-dimensional configuration of orientated fibers as guidance structures for cell migration and axonal growth. Journal of Biomedical Materials Research Part B 11, 356–365. https://doi.org/10.1002/jbm.b.33014

Krishna, L., Dhamodaran, K., Jayadev, C., Chatterjee, K., Shetty, R., Khora, S.S., 2016. Nanostructured scaffold as a determinant of stem cell fate. Stem Cell Research & Therapy 7, 1–12. https://doi.org/10.1186/s13287-016-0440-y

Kuffler, D.P., 2015. Promoting axon regeneration and neurological recovery following traumatic peripheral nerve injuries. International Journal of Neurorehabilitation 2, 1–17. https://doi.org/10.4172/2376-0281.1000148

Kuihua, Z., Chunyang, W., Cunyi, F., Xiumei, M., 2014. Aligned SF/P(LLA-CL)-blended nanofibers encapsulating nerve growth factor for peripheral nerve regeneration. Journal of Biomedical Materials Research Part A: 102A, 2680–2691. https://doi.org/10.1002/jbm.a.34922

Kumar, P., Choonara, Y., Girish, M., Dinesh, N., Pillay, V., 2015. Multifunctional Therapeutic Delivery Strategies for Effective Neuro-Regeneration Following Traumatic Spinal Cord Injury., in: Current Pharmaceutical Design. Bentham Science Publishers., pp. 1517–1528.

Kumari, J., Kumar, A., 2017. Development of polymer based cryogel matrix for transportation and storage of mammalian cells. Scientific 7, 1–13. https://doi.org/10.1038/srep41551

Lakhundi, S., Siddiqui, R., Khan, N.A., 2015. Cellulose degradation : a therapeutic strategy in the improved treatment of Acanthamoeba infections. Parasites and Vectors 8, 1–16. https://doi.org/10.1186/s13071-015-0642-7

Lee, J., Cuddihy, M.J., Kotov, N.A., 2008. Three-dimensional cell culture matrices: State of the art. Tissue Engineering Part B: Reviews 14, 61–86. https://doi.org/10.1089/teb.2007.0150

Lee, S., Zhu, W., Heyburn, L., Nowicki, M., Harris, B., Zhang, L.G., 2017. Development of novel 3-D printed scaffolds with core-shell nanoparticles for nerve regeneration. IEEE Transactions on Biomedical Engineering 64, 408–418.

Lee, S.-J., Nowicki, M., Harris, B., Zhang, L.G., 2016. Fabrication of a highly aligned neural scaffold via a table top stereolithography 3D printing and electrospinning. Tissue Engineering Part A 00, ten.TEA.2016.0353. https://doi.org/10.1089/ten.TEA.2016.0353

Lei, Y., Han, H., Yuan, F., Javeed, A., Zhao, Y., 2017. The brain interstitial system: Anatomy, modeling, in vivo measurement, and applications. Progress in Neurobiology. https://doi.org/10.1016/j.pneurobio.2015.12.007

Li, W., Tang, Q.Y., Jadhav, A.D., Narang, A., Qian, W.X., Shi, P., Pang, S., 2015. Large-scale topographical screen for investigation of physical neural-guidance cues. Scientific Reports 2, 1–8. https://doi.org/10.1038/srep08644

Liachenko, S., Ramu, J., 2017. Quantification and reproducibility assessment of the regional brain T2 relaxation in naïve rats at 7T. Journal of Magnetic Resonance Imaging 45, 700–709. https://doi.org/10.1002/jmri.25378

Liang, Y., Bar-Shir, A., Song, X., Gilad, A.A., Walczak, P., Bulte, J.W.M., 2015. Label-free imaging of gelatin-containing hydrogel scaffolds. Biomaterials 42, 144–150. https://doi.org/10.1016/j.biomaterials.2014.11.050

Liang, Y., Walczak, P., Bulte, J.W.M., 2013. The survival of engrafted neural stem cells within hyaluronic acid hydrogels. Biomaterials 34, 5521–5529. https://doi.org/10.1016/j.biomaterials.2013.03.095

Lim, T.C., Spector, M., 2017. Biomaterials for enhancing CNS repair. Translational Stroke Research 8, 57–64. https://doi.org/10.1007/s12975-016-0470-x

Lin, X., Huang, J., Shi, Y., Liu, W., 2015. Tissue Engineering and Regenerative Medicine in Applied Research: A Year in Review of 2014. Tissue Engineering Part B: Reviews 21, 177–186. https://doi.org/10.1089/ten.teb.2015.0004

Liu, S., Zhou, J., Zhang, X., Liu, Y., Chen, J., Hu, B., Song, J., Zhang, Y., 2016. Strategies to Optimize Adult Stem Cell Therapy for Tissue Regeneration. International Journal of Molecular Sciences 17, 982. https://doi.org/10.3390/ijms17060982

Loh, Q.L., Choong, C., 2013. Three-dimensional scaffolds for tissue engineering applications: role of porosity and pore size. Tissue engineering. Part B, Reviews 19, 485–502. https://doi.org/10.1089/ten.TEB.2012.0437

Lozinsky, V.I., Plieva, F.M., Galaev, I.Y., Mattiasson, B., 2001. The potential of polymeric cryogels in bioseparation. Bioseparation 10, 163–88.

Luciano, N.J., Sati, P., Nair, G., Guy, J.R., Ha, S.-K., Absinta, M., Chiang, W.-Y., Leibovitch, E.C., Jacobson, S., Silva, A.C., Reich, D.S., 2016. Utilizing 3D printing technology to merge MRI with histology: A protocol for brain sectioning video link. Journal of Visualized Experiments : JoVE 118. https://doi.org/10.3791/54780

Makadia, H., Siegel, S., 2012. Poly Lactic-co-Glycolic Acid (PLGA) as biodegradable controlled drug delivery carrier. Polymers (Basel) 3, 1–19. https://doi.org/10.3390/polym3031377.Poly

Martínez-Ramos, C., Gómez-Pinedo, U., Esparza, M.A.G., Soria, J.M., Barcia, J.A., Monleón Pradas, M., 2015. Neural tissue regeneration in experimental brain injury model with channeled scaffolds of acrylate copolymers. Neuroscience Letters 598, 96–101. https://doi.org/10.1016/j.neulet.2015.05.021

Martínez-Ramos, C., Vallés-Lluch, A., Verdugo, J.M.G., Ribelles, J.L.G., Barcia, J.A., Orts, A.B., López, J.M.S., Pradas, M.M., 2012. Channeled scaffolds implanted in adult rat brain. Journal of Biomedical Materials Research - Part A 100 A, 3276–3286. https://doi.org/10.1002/jbm.a.34273

Martino, S., Angelo, F.D., Kenny, J.M., Martino, S., Angelo, F.D., Armentano, I., Maria, J., Orlacchio, A., 2011. Stem cell-biomaterial interactions for regenerative medicine. Biotechnology Advances 30, 338–351. https://doi.org/10.1016/j.biotechadv.2011.06.015

Mata, A., Jung, E., Boehm, C.A., Fleischman, A.J., Muschler, G.F., Roy, S., 2009. A three-dimensional scaffold with precise micro-architecture and surface. Biomaterials 30, 4610–4617. https://doi.org/10.1016/j.biomaterials.2009.05.023

McMurtrey, R.J., 2016. Multi-compartmental biomaterial scaffolds for patterning neural tissue organoids in models of neurodevelopment and tissue regeneration. Journal of Tissue Engineering 7, 1–8. https://doi.org/10.1177/2041731416671926

McMurtrey, R.J., 2014. Patterned and functionalized nano fiber scaffolds in three-dimensional hydrogel constructs enhance neurite outgrowth and directional control. Journal of Neural Engineering 11, 15. https://doi.org/10.1088/1741-2560/11/6/066009

Mitchell, G.R., Tojeira, A., 2013. Role of anisotropy in tissue engineering. Procedia Engineering 59, 117–125. https://doi.org/10.1016/j.proeng.2013.05.100

Mohtaram, N.K., Ko, J., King, C., Sun, L., Muller, N., Jun, M.B., Willerth, S.M., 2015. Electrospun biomaterial scaffolds with varied topographies for neuronal differentiation of human-induced pluripotent stem cells. Journal of Biomaterials Research Part A 103A, 2591–2601. https://doi.org/10.1002/jbm.a.35392

Mondschein, R.J., Kanitkar, A., Williams, C.B., Verbridge, S.S., Long, T.E., 2017. Polymer structure-property requirements for stereolithographic 3D printing of soft tissue engineering scaffolds. Biomaterials. https://doi.org/10.1016/j.biomaterials.2017.06.005

Moreira Teixeira, L.S., Feijen, J., van Blitterswijk, C.A., Dijkstra, P.J., Karperien, M., 2012. Enzyme-catalyzed crosslinkable hydrogels: Emerging strategies for tissue engineering. Biomaterials 33, 1281–1290. https://doi.org/10.1016/j.biomaterials.2011.10.067

Morganti-Kossmann, M., Rancan, M., Stahel, P., Kossmann, T., 2002. Inflammatory response in acute traumatic brain injury: a double-edged sword. Current Opinion in Critical Care 8, 101–105. https://doi.org/10.1097/00075198-200204000-00002

Mori, S., Zhang, J., 2006. Principles of diffusion tensor imaging and its applications to basic neuroscience research. Neuron 51, 527–539. https://doi.org/10.1016/j.neuron.2006.08.012

Moroni, L., Elisseeff, J.H., 2008. Biomaterials engineered for integration. Materials Today 11, 44–51. https://doi.org/10.1016/S1369-7021(08)70089-0

Motalleb, R., Berns, E.J., Patel, P., Gold, J., Stupp, S.I., Kuhn, H.G., 2018. In vivo migration of endogenous brain progenitor cells guided by an injectable peptide amphiphile biomaterial. Journal of Tissue Engineering and Regenerative Medicine 12, e2123–e2133. https://doi.org/10.1002/term.2644

Murphy, S. V, Atala, A., 2014. 3D bioprinting of tissues and organs. Nature Biotechnology. https://doi.org/10.1038/nbt.2958

Nasatto, P.L., Pignon, F., Silveira, J.L.M., Duarte, M.E.R., Noseda, M.D., Rinaudo, M., 2015. Methylcellulose, a cellulose derivative with original physical properties and extended applications. Polymers 7, 777–803. https://doi.org/10.3390/polym7050777

Nathan, A.S., Baker, B.M., Nerurkar, N.L., Mauck, R.L., 2011. Mechano-topographic modulation of stem cell nuclear shape on nanofibrous scaffolds. Acta Biomaterialia 7, 57–66. https://doi.org/10.1016/j.actbio.2010.08.007

Nava, M.M., Raimondi, M.T., Pietrabissa, R., 2012. Controlling self-renewal and differentiation of stem cells via mechanical cues. Journal of Biomedicine and Biotechnology. https://doi.org/10.1155/2012/797410

Newland, B., Welzel, P.B., Newland, H., Renneberg, C., Kolar, P., Tsurkan, M., Rosser, A., Freudenberg, U., Werner, C., 2015. Tackling cell transplantation anoikis: An injectable, shape memory cryogel microcarrier platform material for stem cell and neuronal cell growth. Small 11, 5047–5053. https://doi.org/10.1002/smll.201500898

Nicholson, C., Syková, E., 1998. Extracellular space structure revealed by diffusion analysis. Trends in Neurosciences 21, 207–21. https://doi.org/10.1016/S0166-2236(98)01261-2

Nisbet, D.R., Rodda, A.E., Horne, M.K., Forsythe, J.S., Finkelstein, D.I., 2009. Neurite infiltration and cellular response to electrospun polycaprolactone scaffolds implanted into the brain. Biomaterials 30, 4573–4580. https://doi.org/10.1016/j.biomaterials.2009.05.011

Oxman, N., Tsai, E., Firstenberg, M., 2012. Digital anisotropy: A variable elasticity rapid prototyping platform: This paper proposes and demonstrates a digital anisotropic fabrication approach by employing a multi-material printing platform to fabricate materials with controlled gradient propertie. Virtual and Physical Prototyping 7, 261–274. https://doi.org/10.1080/17452759.2012.731369

Panagopoulos, G.N., Megaloikonomos, P.D., Mavrogenis, A.F., 2016. The present and future for peripheral nerve regeneration. Orthopedics 40, e141–e156. https://doi.org/10.3928/01477447-20161019-01

Park, S.-H., Koh, U.H., Yang, D.-Y., Lee, N.-K., Hyun, J., 2015. Development of 3D Printed Biomimetic Scaffold for Tissue Engineering. 2015 15th International Conference on Control, Automation and Systems (ICCAS 1958–1960. https://doi.org/10.1109/ICCAS.2015.7364687

Pettikiriarachchi, J.T.S., Parish, C.L., Shoichet, M.S., Forsythe, J.S., Nisbet, D.R., 2010. Biomaterials for brain tissue engineering. Aust. J. Chem 63, 1143–1154. https://doi.org/10.1071/CH10159

Pfister, B.J., Gordon, T., Loverde, J.R., Kochar, A.S., Mackinnon, S.E., Cullen, D.K., Luther, M., Boulevard, K., 2011. Biomedical engineering strategies for peripheral nerve repair: Surgical applications, state of the art, and future challenges. Critical Reviews™ in Biomedical Engineering 39, 81–124.

Quinones-Hinojosa, A., Sanai, N., Soriano-Navarro, M., Gonzalez-Perez, O., Mirzadeh, Z., Gil-Perotin, S., Romero-Rodriguez, R., Berger, M.S., Garcia-Verdugo, J.M., Alvarez-Buylla, A., 2006. Cellular composition and cytoarchitecture of the adult human subventricular zone : A niche of neural stem cells. The Journal of Comparative Neurology 494, 415–434. https://doi.org/10.1002/cne.20798

Ramachandran, R., Junnuthula, V.R., Gowd, G.S., Ashokan, A., Thomas, J., Peethambaran, R., Thomas, A., Unni, A.K.K., Panikar, D., Nair, S. V., Koyakutty, M., 2017. Theranostic 3-Dimensional nano brain-implant for prolonged and localized treatment of recurrent glioma. Scientific Reports 7, 43271. https://doi.org/10.1038/srep43271

Ribeiro-Resende, V.T., Koenig, B., Nichterwitz, S., Oberhoffner, S., Schlosshauer, B., 2009. Strategies for inducing the formation of bands of Büngner in peripheral nerve regeneration. Biomaterials 30, 5251–5259. https://doi.org/10.1016/J.BIOMATERIALS.2009.07.007

Rivet, C.J., Zhou, K., Gilbert, R.J., Finkelstein, D.I., Forsythe, J.S., 2015. Cell infiltration into a 3D electrospun fiber and hydrogel hybrid scaffold implanted in the brain. Biomatter 5, e1005527. https://doi.org/10.1080/21592535.2015.1005527

Rotshenker, S., 2011. Wallerian degeneration: the innate-immune response to traumatic nerve injury. Journal of neuroinflammation 8, 109. https://doi.org/10.1186/1742-2094-8-109

Saatman, K.E., Duhaime, A.-C., Bullock, R., Maas, A.I.R., Valadka, A., Manley, G.T., 2008. Classification of traumatic brain injury for targeted therapies. Journal of Neurotrauma 25, 719–738. https://doi.org/10.1089/neu.2008.0586

Samer, B., Grant, B., Lin, J., Epameinondas, K., Robert, W., Petros, K., 2018. The surgical management of nerve gaps. Annals of Plastic Surgery 80, 252–261. https://doi.org/10.1097/SAP.0000000000001252

Sarnowska, A., Jablonska, A., Jurga, M., Dainiak, M., Strojek, L., Drela, K., Wright, K., Tripathi, A., Kumar, A., Jungvid, H., Lukomska, B., Forraz, N., McGuckin, C., Domanska-Janik, K., 2013. Encapsulation of mesenchymal stem cells by bioscaffolds protects cell survival and attenuates neuroinflammatory reaction in injured brain tissue after transplantation. Cell Transplantation 22. https://doi.org/10.3727/096368913X672172

Sart, S., Ma, T., Li, Y., 2014. Preconditioning stem cells for in vivo delivery. BioResearch Open Access 3, 137–49. https://doi.org/10.1089/biores.2014.0012

Sedaghati, T., Seifalian, A.M., 2015. Nanotechnology and bio-functionalisation for peripheral nerve regeneration. Neural Regeneration Research 10, 1191–1194. https://doi.org/10.4103/1673-5374.162678

Sensharma, P., Madhumathi, G., Jayant, R.D., Jaiswal, A.K., 2017. Biomaterials and cells for neural tissue engineering: Current choices. Materials Science and Engineering: C 77, 1302–1315. https://doi.org/10.1016/J.MSEC.2017.03.264

Shi, C., Lei, Y., Han, H., Zuo, L., Yan, J., He, Q., 2015. Transportation in the interstitial space of the brain can be regulated by neuronal excitation. Scientific Reports 5, 1–11. https://doi.org/10.1038/srep17673

Snigdha, S., Sabu, T., Radhakrishnan, E., 2017. Polymer based tissue engineering strategies for neural regeneration. Advances in Tissue Engineering and Regenerative Medicine 2, 1–6. https://doi.org/10.15406/atroa.2017.02.00016

Srinivasan, S., Jayakumar, R., Chennazhi, K.P., Levorson, E.J., Mikos, A.G., Nair, S. V, 2012. Multiscale fibrous scaffolds in regenerative medicine. Advances in Polymer Science 246, 1–20. https://doi.org/10.1007/12

Stevens, M.M., George, J.H., 2005. Exploring and engineering the cell surface interface. Science 310, 1135–1138. https://doi.org/10.1126/science.1106587

Steward, A.J., Thorpe, S.D., Vinardell, T., Buckley, C.T., Wagner, D.R., Kelly, D.J., 2012. Cell–matrix interactions regulate mesenchymal stem cell response to hydrostatic pressure. Acta Biomaterialia 8, 2153–2159. https://doi.org/10.1016/J.ACTBIO.2012.03.016

Stratton, S., Shelke, Namdev, B., Hoshino, K., Rudraiah, S., Kumbar, Sangamesh, G., 2016. Bioactive polymeric scaffolds for tissue engineering. Bioactive Materials 1, 93–108. https://doi.org/10.1016/J.BIOACTMAT.2016.11.001

Su, W.-F., 2013. Principles of Polymer Design and Synthesis Volume 82 of Lecture Notes in Chemistry, Illustrated. ed. Springer Science & Business Media.

Su, Z., Niu, W., Liu, M.-L., Zou, Y., Zhang, C.-L., 2014. In vivo conversion of astrocytes to neurons in the injured adult spinal cord. Nature Communications 5, 3338. https://doi.org/10.1038/ncomms4338

Sudwilai, T., Ng, J.J., Boonkrai, C., Israsena, N., Chuangchote, S., Supaphol, P., 2014. Polypyrrole-coated electrospun poly(lactic acid) fibrous scaffold: effects of coating on electrical conductivity and neural cell growth. Journal of Biomaterials Science Polymer Edition 2512, 1240–1252. https://doi.org/10.1080/09205063.2014.926578

Sun, D., 2014. The potential of endogenous neurogenesis for brain repair and regeneration following traumatic brain injury. Neural Regeneration Research 9, 688–692.

Tam, R.Y., Fuehrmann, T., Mitrousis, N., Shoichet, M.S., 2014. Regenerative therapies for central nervous system diseases: a biomaterials approach. Neuropsychopharmacology 39, 169–88. https://doi.org/10.1038/npp.2013.237

Tamariz, E., Varela-EchavarrÃ-a, A., 2015. The discovery of the growth cone and its influence on the study of axon guidance. Frontiers in Neuroanatomy 9, 51. https://doi.org/10.3389/fnana.2015.00051

Tian, L., Prabhakaran, M.P., Ramakrishna, S., 2015. Strategies for regeneration of components of nervous system: scaffolds, cells and biomolecules. Regenerative Biomaterials 2, 31–45. https://doi.org/10.1093/rb/rbu017

Tran, R., Dey, J., Gyawali, D., 2011. Biodegradable elastomeric polymers and MEMS in tissue engineering, in: Chiao, M., Chiao, J.-C. (Eds.), Biomaterials for MEMS. Pan Stanford Publishing Pte. Ltd.

Tu, X., Wang, L., Wei, J., Wang, B., Tang, Y., Shi, J., Zhang, Z., Chen, Y., 2016. 3D printed PEGDA microstructures for gelatin scaffold integration and neuron differentiation. Microelectronic Engineering 158, 30–34. https://doi.org/10.1016/j.mee.2016.03.007

Tung, T.H., 2015. Clinical strategies to enhance nerve regeneration. Neural Regeneration Research 10, 22–24.

Ventola, C.L., 2014. Medical applications for 3D printing: current and projected uses. P & T : a peer-reviewed journal for formulary management 39, 704–711. https://doi.org/10.1016/j.infsof.2008.09.005

Vink, R., 2018. Large animal models of traumatic brain injury. Journal of Neuroscience Research. https://doi.org/10.1002/jnr.24079

von Burkersroda, F., Schedl, L., Göpferich, A., 2002. Why degradable polymers undergo surface erosion or bulk erosion. Biomaterials 23, 4221–4231.

Wagner, A., Ehlers, W., 2008. A porous media model to describe the behaviour of brain tissue. Proceedings in Applied Mathematics and Mechanics 8, 10201–10202. https://doi.org/10.1002/pamm.200810201

Wang, C., Oh, S., Lee, H.A., Kang, J., Jeong, K.-J., Kang, S.W., Hwang, D.Y., Lee, J., 2017. In vivo feasibility test using transparent carbon nanotube-coated polydimethylsiloxane sheet at brain tissue and sciatic nerve. Journal of Biomedical Materials Research Part A 105, 1736–1745. https://doi.org/10.1002/jbm.a.36001

Wang, T.-Y., Bruggeman, K.F., Kauhausen, J.A., Rodriguez, A.L., Nisbet, D.R., Parish, C.L., 2016. Functionalized composite scaffolds improve the engraftment of transplanted dopaminergic progenitors in a mouse model of Parkinson's disease. Biomaterials 74, 89–98. https://doi.org/10.1016/j.biomaterials.2015.09.039

Wei, Z.Z., Zhu, Y.-B., Zhang, J.Y., McCrary, M.R., Wang, S., Zhang, Y.-B., Yu, S.-P., Wei, L., 2017. Priming of the cells: Hypoxic preconditioning for stem cell therapy. Chinese medical journal 130, 2361–2374. https://doi.org/10.4103/0366-6999.215324

Willerth, S.M., Sakiyama-Elbert, S.E., 2007. Approaches to neural tissue engineering using scaffolds for drug delivery. Advanced drug delivery reviews 59, 325–38. https://doi.org/10.1016/j.addr.2007.03.014

Wojnarowicz, M.W., Fisher, A.M., Minaeva, O., Goldstein, L.E., 2017. Considerations for experimental animal models of concussion, traumatic brain injury, and chronic traumatic encephalopathy-these matters matter. Frontiers in Neurology. https://doi.org/10.3389/fneur.2017.00240

Wu, X., He, L., Li, W., Li, H., Wong, W.-M., Ramakrishna, S., Wu, W., 2016. Functional self-assembling peptide nanofiber hydrogel for peripheral nerve regeneration. Regenerative Biomaterials 21–30. https://doi.org/10.1093/rb/rbw034

Yang, S., Leong, K.-F., Du, Z., Chua, C., 2001. The design of scaffolds for use in tissue engineering. Part I. Traditional factors. Tissue Engineering 7, 679–689.

Zamani, F., Amani-Tehran, M., Latifi, M., Shokrgozar, M.A., Zaminy, A., 2014. Promotion of spinal cord axon regeneration by 3D nanofibrous core-sheath scaffolds. Journal of Biomedical Materials Research - Part A 102, 506–513. https://doi.org/10.1002/jbm.a.34703

Zhang, K., Shi, Z., Zhou, J., Xing, Q., Ma, S., Li, Qinghua, Zhang, Y., Yao, M., Wang, X., Li, Qian, Li, J., Guan, F., 2018. Potential application of an injectable hydrogel scaffold loaded with mesenchymal stem cells for treating traumatic brain injury. Journal of Materials Chemistry B 6, 2982–2992. https://doi.org/10.1039/C7TB03213G

Zhang, N., He, L., Wu, W., 2016. Self-assembling peptide nanofibrous hydrogel as a promising strategy in nerve repair after traumatic injury in the nervous system. Neural Regeneration Research. https://doi.org/10.4103/1673-5374.182687

Zhang, Y., Xu, B., Chow, M.J., 2011. Experimental and modeling study of collagen scaffolds with the effects of crosslinking and fiber alignment. International Journal of Biomaterials 2011, 10.1155/2011/172389. https://doi.org/10.1155/2011/172389

Zhao, Q., Sun, J., Lin, Y., Zhou, Q., 2010. Study of the properties of hydrolyzed polyacrylamide hydrogels with various pore structures and rapid pH-sensitivities. Reactive and Functional Polymers 70, 602–609. https://doi.org/10.1016/j.reactfunctpolym.2010.04.010

Zhu, W., George, J.K., Sorger, V.J., Zhang, L.G., 2017. 3D printing scaffold coupled with low level light therapy for neural tissue regeneration. Biofabrication 9, 1–10.

Zhu, W., Masood, F., O'Brien, J., Zhang, L.G., 2015. Highly aligned nanocomposite scaffolds by electrospinning and electrospraying for neural tissue regeneration . electrospraying for neural tissue regeneration. Nanomedicine: Nanotechnology, Biology, and Medicine 11, 693–704. https://doi.org/10.1016/j.nano.2014.12.001

Zou, R., Xia, Y., Liu, S., Hu, P., Hou, W., Hu, Q., Shan, C., 2016. Isotropic and anisotropic elasticity and yielding of 3D printed material. Composites Part B: Engineering 99, 506–513. https://doi.org/10.1016/j.compositesb.2016.06.009

CHAPTER THREE

REPOSITIONING N-ACETYLCYSTEINE (NAC): NAC-LOADED ELECTROSPUN DRUG DELIVERY SCAFFOLDING FOR POTENTIAL NEURAL TISSUE ENGINEERING APPLICATION

Published in Pharmaceutics

Mahumane GD, Kumar P, Pillay V, Choonara YE., 2020. Repositioning *N*-acetylcysteine (NAC): NAC-Loaded electrospun drug delivery scaffolding for potential neural tissue engineering application. *Pharmaceutics*, *12*, 934. doi.org/10.3390/pharmaceutics12100934.

3.1. Abstract:

Traumatic brain injury (TBI) presents a serious challenge for modern medicine due to the poor regenerative capabilities of the brain, complex pathophysiology, and lack of effective treatment for TBI to date. Tissue-engineered scaffolds have shown some experimental success in vivo; unfortunately, none have yielded consummate results of clinical efficacy. N-acetylcysteine has shown neuroprotective potential. To this end, we developed a N-acetylcysteine (NAC)-loaded poly(lactic-co-glycolic acid) (PLGA) electrospun system for potential neural tissue application for TBI. Scanning electron microscopy showed nanofiber diameters ranging 72–542 nm and 124–592 nm for NAC-free and NAC-loaded PLGA nanofibers, respectively. NAC loading was obtained at 28%, and drug entrapment efficacy was obtained at 84%. A biphasic NAC release pattern that featured an initial burst release (13.9%) stage and a later sustained release stage was noted, thus enabling the prolonged replenishing of NAC and drastically improving cell viability and proliferation. This was evidenced by a significantly higher cell viability and proliferation on NAC-loaded nanofibers for rat pheochromocytoma (PC12) and human glioblastoma multiform (A172) cell lines in comparison to PLGA-only nanofibers. The increased cell viability and cell proliferation on NAC-loaded nanofiber substantiates for the repositioning of NAC as a pharmacological agent in neural tissue regeneration applications.

3.2. Introduction

Traumatic brain injury (TBI) is the greatest contributor to global death and disability among all trauma-related injuries. The global incidence of traumatic brain injury (TBI) is generally reported as ~200 in 100,000 with a mortality of 20 per 100,000 people (Reilly, 2007). Although common, the impact of neurotrauma is difficult to describe and may be underestimated due to the variable way statistics are recorded; trauma registries are poor (even in developed countries), and most figures are based on admission and do not include pre-hospital deaths, which account for ≈50% of road trauma deaths (Reilly, 2007; Rubiano et al., 2015). Therefore, traumatic brain injury is a silent global epidemic for which surveillance and interventions are sorely lacking (therapies, funding, dedicated research centers, and human resource).

This is in part due to the complex evolutionary pathophysiology of TBI. Complete neurological damage does not all occur immediately at the moment of primary injury. Secondary injury (follows within hours of primary TBI) has been identified as the leading cause of in-hospital deaths post TBI (Marshall et al., 1991). An estimated 80 to 90% of the patients who die reportedly show evidence of ischemic brain damage in histopathological examinations (Bullock et al., 1999). This secondary injury is a result of brain swelling, leading to a decreased brain perfusion and thus ischemia, which ultimately contributes to the observed brain damage and ultimate morbidity in some patients. The innate inflammatory response induced by injury is crucial to maintain homeostasis; however, if left unbridled into a chronic state, this leads to oxidative stress and glial scarring (Hara et al., 2017; Kim et al., 2018). The glial scar tissue not only secretes inhibitory molecules (e.g., chondroitin sulphate proteoglycans (CSPGs) and myelin-associated glycoproteins), it further creates a mechanical barrier that hinders axonal regrowth (He et al., 2020),(Zhang et al., 2018).

Current treatment approaches for TBI are largely focused on preventing further damage (pharmacological agents and rehabilitation) instead of facilitating regeneration (Pettikiriarachchi et al., 2010). Several pharmacological agents such as free-radical scavengers and calcium channel blockers have been investigated to prevent the secondary injury cascade associated with TBI, to no avail (Ghajar, 2000).

Tissue engineering aims to engender scaffolds based on biological systems, particularly, the nano–micro–macro extracellular matrix environment of the cell to aid in tissue repair and regeneration. Biological systems constitute a myriad of nanoscale structures, and the benefits of the nanotherapies have been widely reported in the literature (Bobo et al., 2016). In particular, the neuron has been likened to a nanofiber with the fundamental function to receive, conduct, and transmit neurochemical-induced signals (Kimizuka, 2008). Therefore, several approaches have been used for the design of nanoscale scaffolds for neurotherapies, and many prototypes are

based on well-established knowledge of the brain extracellular matrix (ECM). The ECM has been described as an interwoven network of nanofibers embedded in a hydrated gel-like matrix (Kim et al., 2018; Lee et al., 2008) with the ECM cells (astrocytes, neurons, oligodendrocytes, and microglia) constituting the framework of the milieu at the nanometer scale (viz. proteinaceous collagen fibrils ranging between 50 and 200 nm and fibronectin fibrils of 2–3 nm thick and 60–70 nm long) (Kim et al., 2018; Lau et al., 2013) that facilitate interaction with the ECM (Lee et al., 2008). Therefore, it follows logic to design biomimetic scaffolds with precise nanoscale features to provide pseudo-in vivo architectural cues to optimally restore cell-cell interactions for neural (brain) tissue engineering applications.

Tissue-engineered biomaterial scaffolds have shown various degrees of experimental success (Mahumane et al., 2018). For instance, Zhou et al., showed that cells could adhere better on a mesenchymal stem cell (MSC)–PLGA scaffold complex than the PLGA with improved to cell adhesion and migration in vivo 14 days after TBI (Zhou et al., 2018). Yang et al. observed that the rate of neural stem cell differentiation was higher for poly(l-lactic acid (PLLA) nanofibers than that of micro fibers, independent of nanofiber alignment (Yang et al., 2005). Unfortunately, there is yet to be a 3D scaffold that exhibits consummate results of an effective clinical standard to date (Mahumane et al., 2018).

This study focused on the design of electrospun PLGA nanofibers based on a clinical pharmacological drug, creating a localized therapeutic signal within the nanofibers for brain tissue engineering with optimal porosity, superior surface area to volume ratio, and cell viability and proliferation biocompatibility, which were fabricated from biocompatible materials in order to improve localized drug delivery at the brain lesion site.

The therapeutic focus of the current study will be *N*-acetylcysteine (NAC). *N*-acetylcysteine is commonly used to loosen thick mucus in patients with chronic obstructive pulmonary disease (COPD) or cystic fibrosis and an antidote to acetaminophen and carbon monoxide poisoning (Heard, 2008; Shen et al., 2014). Several preclinical models of CNS injury have reported on the neuroprotective properties of NAC to control inflammation and ischemia (Chen et al., 2008; Clark et al., 2017; Farr et al., 2003; Gilgun-Sherki et al., 2002; Hoffer et al., 2017; Katz et al., 2015; Khan et al., 2004). For instance, Khan et al. reported that the administration of NAC after ischemia onset protected the brain tissue from free radical injury, inflammation, and apoptosis in a rat model of experimental stroke (Khan et al., 2004). Xiong et al. reported that NAC could restore brain glutathione levels and mitochondrial glutathione levels after TBI (Xiong et al., 2009). Although NAC crossed the blood–brain barrier (BBB) (Farr et al., 2003; Katz et al., 2015), its potential neurotherapeutic effects have been largely limited by multiple

factors. NAC has a low oral bioavailability estimated at 6–10% as a result of extensive first-pass metabolism (Ahmaditabar et al., 2017; Chen et al., 2012; Dodd et al., 2008; Lancheros et al., 2018). In addition, when administered intravenously, systemically, NAC binds to plasma proteins, and about 30% undergoes renal elimination resulting in a short half-life (Ahmaditabar et al., 2017). In addition, increasing systemic doses of NAC for superior (passive) transport of NAC across the BBB may result in increasing the blood pressure (Lancheros et al., 2018). Incorporating the NAC in a biocompatible substrate will enable localized delivery of the NAC at the target site, bypassing its limitations from alternate administrations routes (oral, intravenous) and thereby enhancing its therapeutic effect.

We used poly(D-L-lactide-*co*-glycolide) (PLGA) as the substrate to embed and deliver the therapeutic agent (NAC). Poly(D-L-lactide-*co*-glycolide) (PLGA) nanofibers have been explored as desirable biodegradable synthetic polymeric materials for nanoscale electrospinning in neural tissue engineering (Kim et al., 2016; Lee et al., 2009; Subramanian et al., 2012). The available flexibility in its polylactic acid (PLA) and poly glycolic acid (PGA) ratios enable the precise control of scaffold properties (e.g., mechanical strength, biotensile properties, biodegradation, bioactive release kinetics, porosity, neuro-durability, anti-fouling) for neural tissue engineering (Ramazani et al., 2016).

Therefore, we hypothesize that embedding NAC within the electrospun PLGA nanofibers as a neuro-insert will overcome the extensive plasma protein binding observed after oral delivery and will also provide preferential spatial delivery of NAC to the injured brain tissue to ensure neuroavailability (Pillay et al., 2013) and optimal neuroprotective effects within a neuromimetic scaffold. In order to control the release of the low molecular weight and hydrophilic NAC from the nanofibers inserted at the TBI site, PLGA with a 85:15 PLA/PGA polymer ratio was selected as the ideal polymer platform for nanofiber synthesis. The NAC-embedded PLGA nanofibers were electrospun into a neuromimetic scaffold and fully characterized to determine its potential for neural tissue engineering in TBI. Several pharmaceutical stability and chemical integrity experiments were undertaken to support the function of the nanosystem via Fourier Transform Infrared (FTIR), TGA, DSC, SEM, BET, physicomechanical analysis, contact angle, XRD, and NAC release kinetics as reported herein. In addition, ex vivo cytotoxicity studies were undertaken on PC12 and A172 cell lines to assess the neurocompatibility of the nanosystem.

3.3. Materials and Methods

3.3.1. Materials

Poly(D,L-lactide-coglycolide Resomer RG 858 S(PLGA) 85:15 (PLGA) was supplied Ex gratia from Evonik Nutrition & Care GmbH, Essen, Germany. This particular PLGA Resomer 858 used herein is a bioresorbable poly(D,L-lactide-*co*-glycolide) (85:15) grade suitable for pharmaceutical applications such as controlled release and acting as a long acting medication delivery material. *N*-acetylcysteine (NAC), 2,2,2-trifluoroethanol (≥ 99% GC), formic acid, Dulbecco's Modified Eagles Medium—high glucose, Roche Cell Proliferation Kit I (MTT), dimethyl sulfoxide (DMSO), and trypsin–EDTA solution were obtained from Sigma Aldrich (Johannesburg, South Africa). Donor Equine Serum (DES) was purchased from Hyclone. Ethanol (99% absolute) was purchased from LabChem, Edenvale, Johannesburg, South Africa. Gibco Fetal Bovine Serum and Ham's F-12 Nutrient Mix (F12) were purchased from Thermofischer Scientific (Germiston, Gauteng, South Africa). Rat (Rattus Norvegicus) adrenal gland pheochromocytoma PC12 and human glioblastoma multiforme A172 cells were purchased from Cellonex (Separations, South Africa). Pencillin/Streptomycin/Amphotericin B (P/S/AB) solution was purchased from Lonza, Oregon, USA.

3.3.2. Fabrication of the NAC-loaded electrospun system

The electrospun systems were prepared via the electrospinning technique using the NanoSpinner24 (Inovenso Ltd., Co., Istanbul, Turkey). A 1:1 ratio comprising 2,2,2-trifluoroethanol/formic acid (TFE/FA) electrospinning solvent mixture was prepared. The PLGA and NAC (one part NAC to two parts PLGA) were added to the TFE/FA solvent mixture at room temperature and stirred under magnetic stirring for 2 h. This NAC/PLGA ratio enabled the maximal NAC amount while maintaining electrospinnability of the solution (no erratic fiber deposition, beading, or precipitation of drug particles out of the solution). Then, the solutions were transferred into 10 mL syringes, and a pump was used to dispense the solution through a spinneret (0.8 mm) at a controlled rate of 300 µL/hr. The applied voltage was controlled between 24 and 26 kV. The distance between the spinneret tip and the aluminum-clad rotating cylindrical collector was set at 200 mm with the collector rotating at 400 rpm and a stroke velocity of 200. The pure PLGA electrospun scaffold was subsequently used as the control. Electrospinning experiments were performed at room temperature under the relative humidity of ≤ 40%. The resultant nanofibers were subsequently collected and vacuum dried for 24 h at room temperature for the removal of any residual solvent.

3.3.3. Characterization of the NAC-loaded electrospun system

These processes could lead to significant changes on the polymer and crystal structure of the incorporated NAC. Therefore, FTIR, TGA, DSC, and XRD studies were performed in order to confirm the presence of the NAC in the electrospun fibers and to evaluate the structural changes in the polymer matrix and NAC crystallinity after the electrospinning process. The

chemical transitions of the electrospun nanofibers before and after NAC loading were determined using a Fourier Transform Infrared (FTIR) spectrometer (PerkinElmer Spectrum 100, FT-IR Spectrometer, Beconfield, UK) fitted with a universal ATR Polarization Accessory (PerkinElmer Ltd., Beconfield, UK). The samples were analyzed at high resolution over a 4000–650 cm^{-1} wavelength range on a Nicolet Impact 400D FTIR Spectrophotometer coupled with Omnic FTIR research grade software (Nicolet Instrument Corp., Madiso, WI, USA). The presence/absence of specific functional groups was noted and analyzed. Systems need to be stable at the physiological tissue target temperatures in vivo.

Effects of NAC-loading on thermal stability were characterized using thermogravimetic analysis (Perkin Elmer, TGA 400, Waltham, MA, USA). Samples (10–15 mg) were placed in an unsealed ceramic pan under nitrogen atmosphere at a flow rate of 20 $mL.min^{-1}$. Thermograms were recorded in the temperature range of 30–600 °C with a heating rate of 10 °C/min, revealing the mass changes with increasing temperature, thermal stability, and degradation temperature of the sample material.

The effects of NAC-loading on thermal transitions was characterized using differential scanning calorimetry (DSC) (Mettler Toledo, STARe System, Schwerzernback, Zurich, Switzerland). Dried samples (5–10 mg) were weighed into aluminum crucible pans (40 mL) and sealed shut. Thereafter, samples were heated at a temperature range of 10–300 °C at a rate of 10 $°C \cdot min^{-1}$. Heating took place under nitrogen atmosphere (Afrox, Germiston, Gauteng, South Africa) at a flow rate of 200 $mL \cdot min^{-1}$, acting as the purge gas to reduce oxidation. The thermal profiles were analyzed.

Amorphization of NAC will contribute to improved solubility and increased NAC at the target site. X-ray diffraction (XRD) studies were performed using an X-ray diffractometer (Rigaku Miniflex 600, Rigaku Corporation, Matsubara-cho, Akishima-shi, Tokyo, Japan) to obtain information about the crystalline or amorphous state of NAC after electrospinning. The X-ray diffractograms were attained with the scanning scope of 2θ from 3° to 90° at room temperature. XRD was operated at a voltage of 40 kV, a current of 15 mA at a scan step of 0.02°, and a speed of 10°/min. Integrated X-ray Powder Diffraction software (PDXL 2.1, Rigaku, Tokyo, Japan) was employed for sample analysis.

The size and morphological characteristics of all electrospun scaffolds were characterized utilizing scanning electron microscopy (SEM) FEI Nova NanoLab SEM (FEI Company, Hillsboro, OR, USA). Gold isotope and carbon were used to sputter coat the sample using the Micromeritics Porositometer (Micromeritics ASAP 2020, Norcross, GA, USA); surface areas,

pore sizes, shapes, and distributions can be measured according to the parameters presented in Table 3.1 and analyzed with reference to the parameters in Table 3.2. Adequate mechanical stiffness is necessary to not only provide a suitable micromechanical environment and promote neuronal anchoring but also to avoid injuring the surround soft neural tissue at the lesion site. The mechanical properties of electrospun fiber mats were determined with a texture analyzer (TA.XTplus texture analyser, Stable Microsystems, Surrey, UK) fitted with two clamps. The width, height, and length of the samples were measured with a digital Vernier calliper (Krafft, DV150GW, Schoellerstr Düren, German) having a precision of 1 µm. A rectangular 40 × 10 mm strip of 1 mm thickness was fixed at 20 mm between the two clamps. Tests were conducted at 0.167 mm/s while applying a 0.5 N trigger force.

Table 3.1. Parameters and settings employed during degassing and analysis of the nanofibers

Sample Tube	**Value**
Warm free space:	1.0000 cm^3
Cold free space:	1.0000 cm^3
Non-ideality factor:	0.0000620
Use isothermal jacket:	Yes
Use filler rod:	Yes
Vacuum seal type:	Seal Frit
Analysis Conditions	
Preparation	
Fast evacuation:	No
Unrestricted evacuation from:	5.0 mmHg
Vacuum set point:	10 µmHg
Evacuation time:	0.10 h
Leak test:	No
Use Trans Seal:	No
Free Space	
Free-space type:	Measured
Lower dewar for evacuation:	Yes
Evacuation time:	0.10 h
Outgas test:	No
Po and Temperature	

Po and T type:	Measure Po at intervals during analysis. Calculate the Analysis Bath Temperature from these values.
Measurement interval:	120 min
Dosing	
Use first pressure fixed dose:	No
Use maximum volume increment:	No
Target tolerance:	5.0% or 5.000 mmHg
Low pressure dosing:	No
Equilibration	
Equilibration time (P/Po = 1.000000000):	20 s
Minimum equilibration delay at P/Po > = 0.995:	600 s
Sample Backfill	
Backfill at start of analysis:	Yes
Backfill at end of analysis:	Yes
Backfill gas:	N2
Adsorptive Properties	
Adsorptive:	Nitrogen @ 77.35 K
Maximum manifold pressure:	925.00 mmHg
Non-ideality factor:	0.0000620
Density conversion factor:	0.0015468
Therm. tran. hard-sphere diameter:	3.860 Å
Molecular cross-sectional area:	0.162 nm²
Inside diameter of sample tube:	9.53 mm

Table 3.2. Surface area and porosity criteria.

Surface Area	Pore Size
Very low surface area < 0.01 $m^2.g^{-1}$	Micropores < 2 nm (Sing et al., 2008, 1985)

Low surface area < 10 $m^2.g^{-1}$	Mesopores 2–50 nm (Sing et al., 2008, 1985)
High surface area > 250 $m^2.g^{-1}$	Macropores > 50 nm (Sing et al., 2008, 1985)

3.3.4. NAC-loading, entrapment efficiency, and NAC release kinetics

Scaffold hydrophilicity can impact the NAC release rate; therefore, the hydrophilicity of the nanofiber systems was evaluated using the DataPhysics Instruments contact angle goniometer by measuring the water contact angle using the sessile drop method. The nanofiber mats were placed on the testing plate and kept smooth. Subsequently, 2 µL of distilled water was dispensed onto the surface at a dosing rate of 2 µL/s using a Hamilton syringe. The images of the water droplet were recorded by camera software after the droplet was stable. Thereafter, the water contact angle was measured using the SCA202 version 4.1.12 build 1019 software. Five different samples were measured, and the average values were calculated. Drug entrapment efficiency, drug loading, and cumulative NAC release from the scaffolds was quantified by WinASPECT® Spectro analytical Software (Analytik Jena AG, Jena) through ultraviolet spectroscopy at a wavelength of 224 nm.

3.3.5. Effect of NAC loading in electrospun nanofiber system on PC12 and A172 cell viability and proliferation *in vitro*

The MTT assay was used (MTT-based Roche Cell Proliferation Kit I was utilised) to quantitatively measure cell death during cell culture which is crucial in determining the cytotoxic effects of the scaffolds. The culturing and cytotoxicity assay are described in greater detail in Chapter 5. The PC12 cells were cultured in F12 media containing 15% DES, 2.5% FBS, and 1% P/S/AB solution. The A172 cells were cultured in Dulbecco's Modified Eagles Medium (DMEM) supplemented with 20% FBS and 1% P/S/AB solution. Both cell lines were maintained under 5% CO_2 atmosphere at 37 °C. Before the test was performed, the nanofibers were cut into 0.5 × 0.5 cm mats and sterilized under UV light for 30 min (UV-C 254 nm, UV Equip, Johannesburg, South Africa). The sterilization of scaffolds is a crucial step relating to the applications for tissue engineering *in vitro* and ultimately, clinical use of the biomaterial scaffold. Braghirolli and co-workers evaluated the effects of sterilization methods on electrospun PLGA nanofibers and the subsequent adhesion efficacy of mesenchymal stem cells. Their observation noted that other methods of sterilization such as ethanol (70%) or using an antimicrobial solution resulted in morphological and structural alterations to the scaffold, respectively (Braghirolli et al., 2014). UV sterilization was noted to generate sterile scaffolds without visible changes in the morphological appearance of the electrospun scaffold. Therefore, UV sterilization was used herein to sterilize the scaffold prior to *in vitro* evaluation. The PC12 and A172 cells were seeded onto the scaffolds in 96-well plates at a density of 1 ×

10^4 cells per well. Absorbance was measured at 570 nm with a background subtraction at 690 nm using a multi-plate reader (Biotek, Winooski, VT, USA). The absorbance reading of the blank (690 nm) was subtracted from all the samples.

3.4. Results and Discussion

3.4.1. NAC-polymer interaction analysis by fourier transform infrared spectroscopy (FTIR)

The FTIR spectra of native PLGA and the PLGA nanofibers characterized by bands in the regions 2995 and 2947 cm^{-1} are present due to the alkyl groups (Fouad et al., 2013; Zhou et al., 2008) and carbonyl stretching around 1749 cm^{-1} and C-O bands in the 1067–1454 cm^{-1} region of both spectra, indicating the presence of the ester group (Figure 3.1). These groups contribute to the NAC delivery properties of the PLGA nanofiber system. PLGA biodegrades by hydrolysis of its ester linkages in water (Makadia and Siegel, 2011), resulting in PLGA degradation-induced NAC release. Since the hydrophobic portion forms that majority (PLGA 85:15), rapid degradation will be avoided, contributing to a sustained NAC release profile. Comparison of the IR spectra of the native PLGA and PLGA nanofibers revealed that there were no significant changes in the two FTIR spectra. This indicated the molecular stability of PLGA in the electrospinning process during nanofiber formation. In keeping with the literature (Picquart et al., 1998), the FTIR spectrum of NAC showed a narrow N-H stretching band at 3371 cm^{-1} indicative of a free NH and the strong S-H stretching band at 2546 cm^{-1}. At lower frequencies, a strong C=O stretching band of the carboxylic group, amide I, II, and III was observed at 1714, 1560, 1530, and 1274–1371 cm^{-1}, respectively. Loading NAC in PLGA caused some shielding of some of the NAC functional groups (NAC was in lower quantity to PLGA), which can be used as evidence of success in NAC loading. Moreover, the presence of both NAC and PLGA were discerned in the FTIR spectra of NAC-loaded nanofibers. In comparison to the PLGA nanofiber spectrum, the composite NAC-loaded PLGA spectrum showed additional peaks at 1533 cm^{-1} (amide II), 1606 cm^{-1} (amide I), 1710 cm^{-1} (carboxylic group), 2548 cm^{-1} (S-H), and a low-intensity peak at 3375 cm^{-1} (NH), respectively, indicating the presence of NAC in the nanofibers.

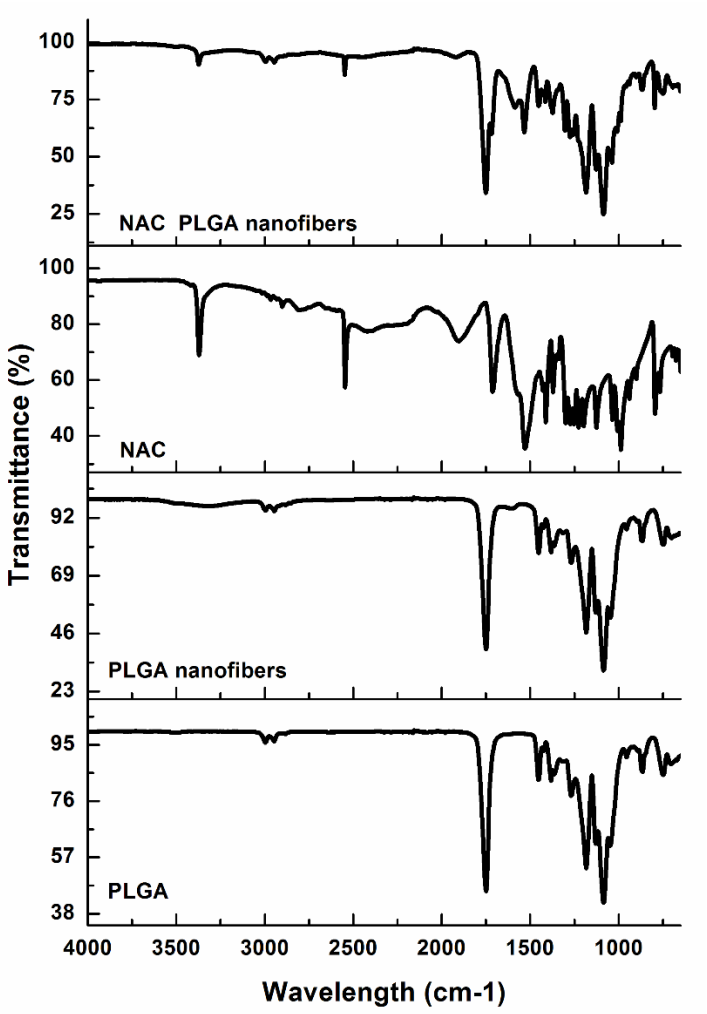

Figure 3.1. Fourier transform infrared (FTIR) spectra of the native materials (NAC, PLGA), electrospun PLGA and NAC-loaded nanofiber. NAC: N-acetylcysteine, PLGA: poly(lactic-co-glycolic acid).

3.4.2. Analysis of NAC loading on thermal stability of electrospun system

Thermogravimetric analysis was conducted to evaluate the thermal stability and extension of degradation effects during processing by comparing the native PLGA and NAC and the resultant scaffold (Figure 3.2). Thermogravimetric analysis also detected the moisture content (water or solvent). The thermograms revealed a weight loss in the curves under 110 °C, which was attributed to the evaporation of volatile materials/moisture content; for all curves, these depressions were < 5%. (Figure 3.2), contributing to greater stability over time. Both native PLGA and PLGA nanofibers presented thermal stability in a lower temperature range (< 250 °C) where significant weight loss occurred in the range of 268–340 °C (native PLGA) and 253–330 °C (PLGA nanofibers). The closeness between the respective values of T_{onset} and $T_{deg.max}$ for bulk PLGA and PLGA nanofibers obtained from electrospinning indicates the good preservation of polymer thermal properties during nanofiber fabrication. However, the PLGA

nanofibers were more reactive than the native PLGA, in part due to their larger surface area, and consequently, they suffered thermal decomposition more quickly. However, the thermal decomposition T_{onset} was well above the physiological temperatures in vivo. NAC weight loss was observed in the range 170–600 °C, which was attributed to thermal decomposition. Two significant mass loss stages (168–245 °C and 282–362 °C) were observed for the NAC-loaded PLGA nanofibers attributed to the presence of both NAC and PLGA in the nanofibers. This observation was also confirmed by DSC and XRD, reinforcing the idea that NAC exists in both the amorphous and crystalline phases. The second decomposition temperature range of NAC-loaded PLGA nanofibers is similar to that of bulk PLGA, which is indicative of the preservation of polymer (PLGA) thermal properties during nanofiber fabrication. The initial degradation temperature of NAC when loaded in the nanofibers is higher, suggesting an improvement in thermal stability in comparison to the NAC alone in vivo. The thermal degradation temperature for the NAC/PLGA nanofibers is well above the physiological and processing temperature. Therefore, the fabrication process did not induce significant NAC/PLGA losses, and the NAC-loaded nanofibers have potential thermal stability properties at ambient and physiological temperatures.

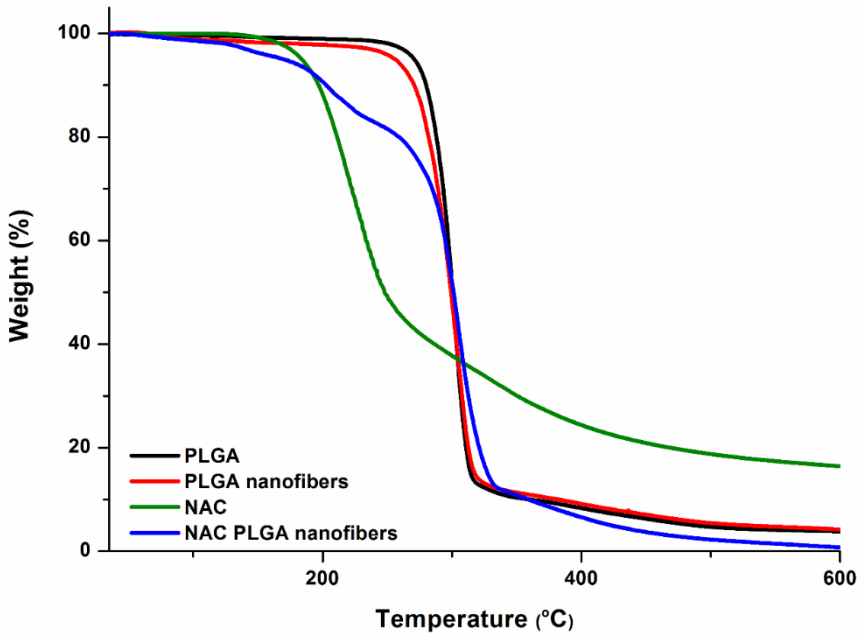

Figure 3.2. Thermogravimetric curves of PLGA (bulk), PLGA nanofibers, NAC and NAC/PLGA nanofibers.

3.4.3. **Evaluation of NAC distribution and crystallinity in NAC-loaded PLGA nanofibers**

Drug distribution in the PLGA nanofibers as a function of NAC loading was studied by XRD and DSC analysis. Blend electrospinning was used to fabricate NAC-loaded PLGA nanofibers. With blend electrospinning, the NAC and polymer are present in one solution; this allows the hydrophilic small molecular drug, NAC, to be incorporated not only on the surface of the

nanofibers, but it also enables physical entrapment of the NAC inside the polymer matrix of the nanofibers (Feng et al., 2019). The X-ray powder diffraction (XRD) patterns showed that the major crystalline diffraction peaks of NAC crystals were observed at the 2θ values of 14.08°, 15.5°, 19.8°, 21.02°, 22.82°, 24.14°, 26.8°, 28.5°, 30.08°, and 32.26° (Figure 3.3a).

The NAC-loaded nanofibers displayed a much weaker intensity than that of the PLGA-only nanofibers, indicating a different and lesser degree of crystallinity/ordered structure. Moreover, the diffraction peaks of the NAC crystals were absent in the XRD pattern of NAC-loaded nanofibers, and only the XRD pattern characteristic of the PLGA was observed. These results strongly suggest that electrospinning the NAC/PLGA blend may have resulted in the NAC molecule simultaneously (1) dissolved in the polymer matrix and (2) dispersed in and throughout the nanofiber matrices (Desai et al., 2008). This reduced intensity indicates the reduced crystallinity of the NAC, which signified some amorphization. The amorphous phase of PLGA fibers may increase solubility, as the increased surface area enables the NAC to be wet by solvent easier (Hara et al., 2017; Khadka et al., 2014). This can help improve the solubility of NAC in the implant site. Although NAC crosses the blood–brain barrier, very little reaches the brain via oral or intravenous routes. This is because NAC has a very low bioavailability due to its binding to plasma proteins in the blood and loss (± 0%) through urine (Desai et al., 2008). The presence of the NAC crystalline peaks confirms the incorporation of NAC into the nanofibers. The nanofibers can serve as a delivery vehicle to improve NAC delivery to the implant site. The glass transition temperature (T_g) of bulk PLGA and NAC-loaded PLGA nanofibers were observed at approximately 59 and 51 °C, respectively (Figure 3.3b). The T_g of the NAC-loaded PLGA nanofibers was slightly lower than that of the bulk PLGA due to the larger surface area to volume ratio of the electrospun nanofibers as well as the improved orientation of molecular chains (Fouad et al., 2013). An endothermic peak was noted at 203 °C, which was attributed to the decomposition temperature of PLGA nanofibers (Fouad et al., 2013). The DSC thermogram of pure NAC showed a sharp endothermic peak that corresponds to melting at 114 °C, indicating its crystalline nature. This crystallinity was further confirmed by the XRD. In addition, an endothermic peak was observed in the NAC/PLGA nanofibers (105 °C) corresponding to NAC. This corroborates the crystalline NAC XRD peaks observed, which suggests that NAC is dissolved in the nanofiber polymer matrix. Thermal decomposition of the NAC peaks was noted in the range 160–240 °C similar to the observed TGA curves. The T_g (glass transition temperature) of the PLGA and NAC/PLGA nanofibers were all above the physiological temperature of 37 °C. Therefore, the nanofibers potentially possess a fairly stable chain structure and enough mechanical strength at ambient and physiological temperatures to be fabricated into thermostable implants/delivery devices.

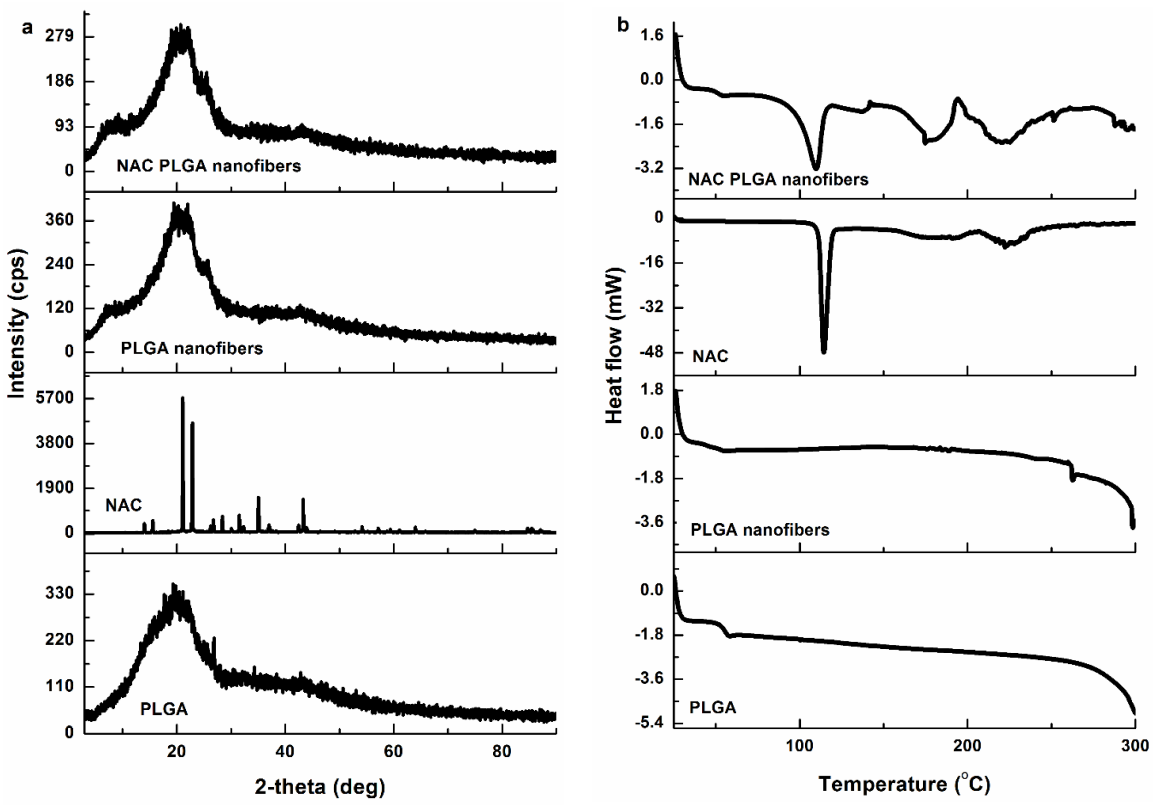

Figure 3.3. (**a**) X-ray diffraction patterns of PLGA nanofibers, NAC, and NAC/PLGA nanofibers. (**b**) DSC curves of bulk PLGA, PLGA nanofibers, NAC and NAC/PLGA nanofibers.

3.4.4. Morphological analysis of electrospun nanofibers

The morphological characteristics, orientation, and diameter distribution of the electrospun nanofibers are shown in the SEM images (Figure 3.4). The electrospinning process confirmed that for nanofiber formation, a critical entanglement concentration (CEC) was required and determined empirically by screening several candidate polymer concentrations. Below the CEC value (Figure 3.4a,b), thinner fibers were obtained; however, Rayleigh instability was also observed (Amariei et al., 2017). Above the CEC value, stable jets were achieved, resulting in the formation of continuous fibers (Figure 3.4c), which were augmented by the increased polymer chain entanglements. Further increase in the concentration resulted in larger average fiber diameters 1700 ± 416 nm accompanied by a broad diameter distribution (diameter size ranging 254–1733 nm) (Figure 3.4c). An increase in fiber diameter as a result of increased concentration is a well-noted phenomenon in electrospinning (Amariei et al., 2017; Brown and Stevens, 2007; Pillay et al., 2013). Moreover, high concentration presented a challenge to the electrospinning process due to the high viscosity of the polymer solution. This resulted in blocking of the needle tip. At 18% PLGA concentration, stable jets were achieved, resulting in the formation of continuous beadles—randomly aligned nanofibers (Figure 3.4d,e).

Nanofiber diameters ranged 72–542 nm and 124–592 nm for NAC-free and NAC-loaded PLGA nanofibers, respectively (Figure 3.4). The average diameter for PLGA nanofibers was 320 ± 128 nm (Figure 3.4d), whereas the average diameter of NAC-loaded nanofibers was 415 ± 124 nm (Figure 3.4e). In the native extracellular matrix, randomly oriented collagen fibers range from 50 to 500 nm (You et al., 2006). The nanofibers produced herein are randomly oriented with interconnected pores. The randomly oriented fibers confer a 'branching' effect with intersections creating a net-like structure resulting in porous features (Figure 3.4a). This is important for achieving cell–cell contact by providing contact guidance and allowing cells to signal processes across multiple fibers. The dimensions of the PLGA nanofibers produced are biomimetic with the native ECM. He and co-workers previously reported 500 nm as the most suitable fiber diameter for a nerve scaffold (He et al., 2010). The incorporation of NAC led to an increased average fiber diameter. The addition of NAC may have increased the viscosity of the solution, which in turn induced a higher chain entanglement of the polymer, resulting in the observed increase in diameter compared to the NAC-free nanofibers. Regardless, the average NAC-loaded nanofiber diameter (415 nm) produced is within the desired fiber diameter range found in the native ECM 50–500 nm (You et al., 2006).

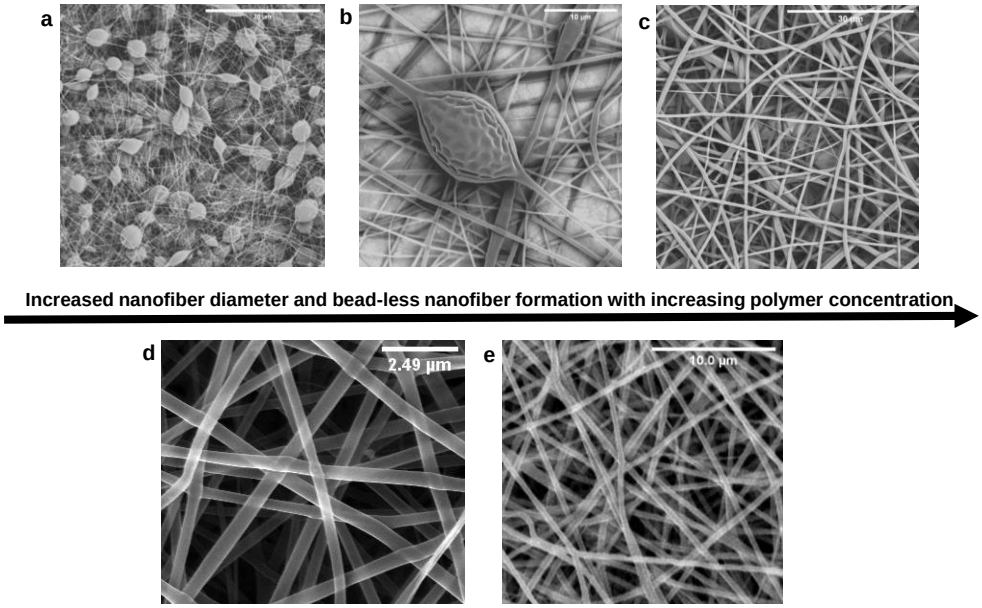

Figure 3.4. Scanning electron micrograph of electrospun nanofibers. (**a**,**b**) Beaded fibers are formed at low concentrations: (**a**) 10% and (**b**) 15%. (**c**) Bead-less nanofibers were formed at higher concentrations 20%. (**d**): The critical entanglement concentration was noted at 18% PLGA. (**e**) The incorporation of NAC in the nanofibers did not alter nanofiber formation at 18%.

The interconnected porous structure is ideal, as it will aid in functioning as a temporary reservoir for the accumulation of the NAC and facilitating the permeability of the nanofibers for uninterrupted passage of cells, nutrients, and waste in the implant site. The high surface area

and porous nature of the scaffold was further confirmed by BET analysis. Figure 3.5 displays the nitrogen adsorption–desorption isotherms of the nanofibers. It was noted that the samples exhibit Type III sorption, confirming the porous nature of the nanofibers. Surface area and porosity were classified according to the criteria stipulated in Table 3.2. Based on the BET surface area analysis, the specific surface area of the PLGA nanofibers was noted at 401.7019 $m^2 \cdot g^{-1}$. The high surface area noted for PLGA is attributable to the nanoarchetype that will potentially enhance the surface area for cell–substrate contact and provide a large surface area for cells to adhere in vivo. The lowered NAC/PLGA nanofiber surface area (82.9030 $m^2 \cdot g^{-1}$) in comparison could be attributed to the larger diameter of the fibers. The isotherm is not closed, which may be due to the swelling phenomenon due to the formation of very narrow slip pores or bottle-shaped pores present over the microporous structure. Nitrogen adsorption below the relative pressure of P/Po < 1 was indicative of the formation of micropores (Gnanasekar et al., 2019). The nanofibers have a pore size distribution covering both the micro and mesoporous ranges. Figure 3.5 shows the results for the Barrett, Joyner, and Halenda (BJH) pore size distribution obtained. The plot of pore volume versus pore diameter shows a broad pore size distribution ranging 1.7–86.1 nm for PLGA and 1.7–208.6 nm for NAC/PLGA, respectively. Both nanofiber mats presented with similar peak values in the regions 1.7, 2.9, 5.1, 10, and a broad peak in the region 13–25 nm. This is pore size distribution may be a result of the layered and intersecting arrangement of nanofibers consistent with the SEM imaging (Figure 3.4).

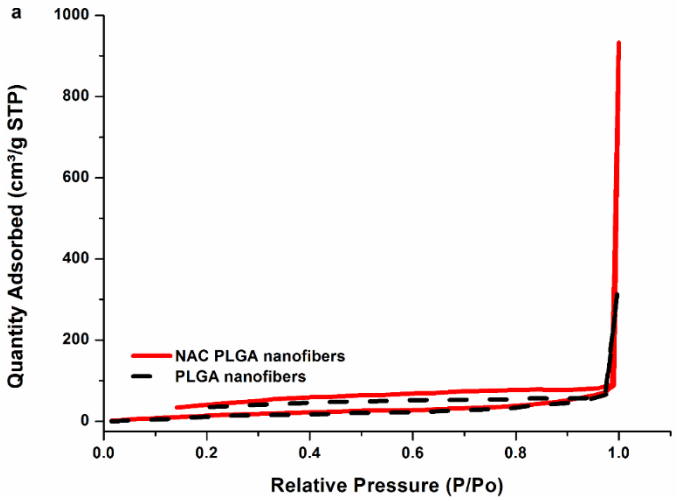

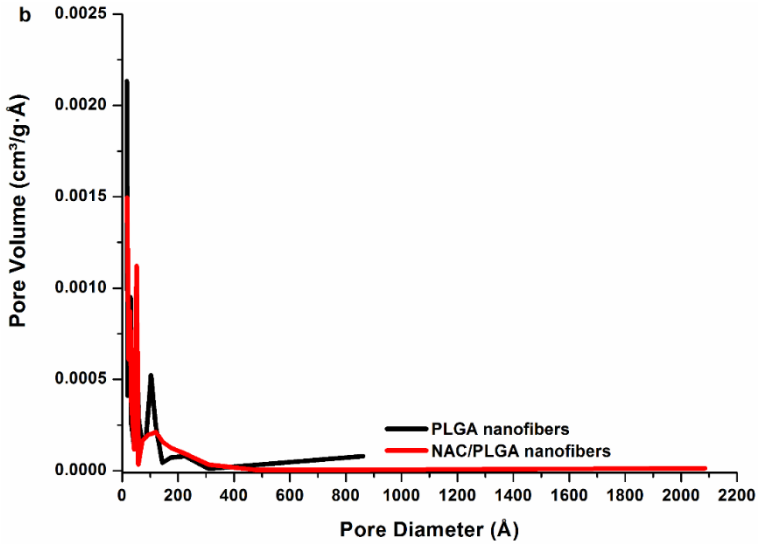

Figure 3.5. Equilibrium (**a**) adsorption/desorption isotherms and (**b**) pore size distribution of PLGA and NAC/PLGA nanofibers.

3.4.5. Mechanical Characterization of NAC-Loaded Nanofibers

Yield stress is vital to the translational success when choosing a material for structural purposes such as a scaffold. As a support structure, the scaffold needs to be robust enough to structurally accommodate tissue repair needs (hold cellular weight, fluid turbulence, adhering proteins, withstand remodeling) and the implantation process. Simultaneously, it must possess an elastic modulus similar to that of neural tissue and have the ability to encourage neuronal viability and extension (Stukel and Willits, 2016). The tensile yield stress of the NAC-loaded PLGA nanofibers was noted at 1294 kPa, which was significantly higher than that of PLGA nanofibers (765 kPa). The addition of NAC to the polymer matrix significantly modulates the stress–strain relationships for the nanofiber matrix (Figure 3.6). The NAC/PLGA curve exhibited a short toe region extending out to about 3% strain, followed by a linear rise in stress with strain and a sharp drop of the curve at 8.4% strain after nanofibers reached their tensile maximum stress. This implies that the majority of the NAC/PLGA nanofibers break simultaneously at the maximum load. Therefore, the tensile strength of the nanofiber mats may be approximately estimated as the sum of the tensile strength of all individual nanofibers that are subjected to strain during the test. In comparison, an extended plastic-like deformation region characterized by irreversible failure with progressive tearing and reduction in stress was noted for PLGA nanofibers only. The lack of adhesion between the polymer matrix due to dispersed NAC may be responsible for the early sharp drop of the curve observed for NAC/PLGA nanofibers as opposed to the extended deformation observed with unloaded PLGA nanofibers. PC12 neuronal cells have been previously noted to grow and spread on substrates as with a Youngs modulus of 184 kP (Wu et al., 2019). The Youngs

moduli were noted at 199 and 378 kPa respectively for NAC-free and NAC-loaded PLGA nanofibers.

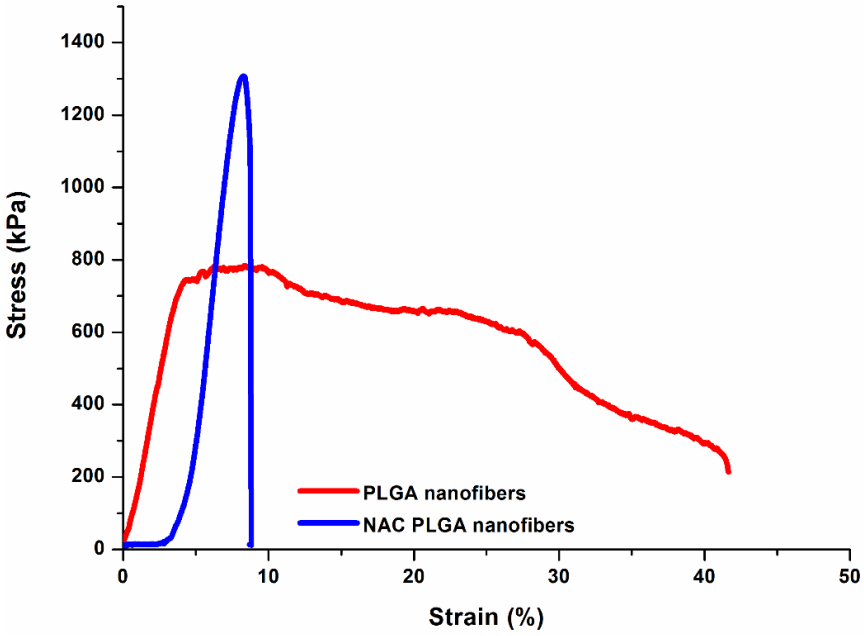

Figure 3.6. Stress–strain curves of the PLGA and NAC/PLGA nanofiber matrices obtained under a test speed of 0.167 mm/s.

3.4.6. Analysis of NAC-loading, encapsulation, and cumulative NAC release

A NAC encapsulation efficiency (DEE) value of 84% was calculated for the NAC-loaded PLGA nanofibers at 28% NAC loading. This high DEE can be attributed to the method of nanofiber formation, where electrospinning of the NAC polymer solution ensures that the NAC is entrapped within the nanofibers during fiber formation, and therefore, the NAC is embedded within the solid nanofibers. The hydrophilicity of the nanofibers determined by water contact angle measurement can actively influence the extent to which water diffuses through the scaffold (Figure 3.7). In turn, this will influence the hydrolysis of the nanofibers and release kinetics of the NAC released from the scaffold. In order to achieve a controllable delivery of NAC for efficient targeted localized delivery, we produced a delivery system based on electrospun fibrous poly(lactide-coglycolide) (PLGA), with a 85:15 lactide-to-glycolide ratio. The lactide portion is hydrophobic in comparison to the glycolide portion, and it makes up the larger ratio. Contact angles at < 90° indicate high wettability, whereas angles >90° indicate lower wettability (Zhu et al., 2019). As shown in Figure 3.7a–c, the water contact angles of both PLGA and NAC/PLGA are > 90°, indicating the low wettability of the nanofibers. N-acetylcysteine is a hydrophilic drug (e.g., carboxyl groups), and its improvement on hydrophilicity is observed (Figure 3.7). However, this is largely limited because PLGA was the major/main component of the scaffold and therefore, the hydrophobic properties of PLGA dominated (contact angle remained above >90). This means that the rate of water diffusion

into the delivery system will be slow. This is desirable, as it is expected to aid in prolonging the release of the entrapped drug in the localized implanted area of the nanofiber scaffold. N-Acetylcysteine release from nanofibers is typically a biphasic process (Leung and Ko, 2011). This process comprises of (1) burst release and (2) slower release rate (Fu and Kao, 2010; Leung and Ko, 2011; Sedaghati and Seifalian, 2015). The drug release profiles and characteristics of NAC/PLGA nanofibers are presented in Figure 3.7d. The plot of the cumulative NAC release as a function of time at 37 °C in PBS (pH: 7.4) shows biphasic drug release kinetics. The first stage, burst release, is characterized with an initial burst release during the first 8 h (13.9% cumulative release), where the rate of NAC release is very high in the initial 15 min and decreased considerably until 8 h. This is the initial release of surface associated drug molecules concurrently with fast diffusion into the aqueous phase. The initial burst release of NAC-loaded nanofibers resulted from the presence of phase separation of NAC particles on the fiber surface during the electrospinning process. The second stage was observed after 8 h with release of the remaining drug in a slow and stable manner. This is a solid-state diffusion of the drug from within the solid nanofibers (controlled slower release rate), which corroborates with the amorphization of the drug within the polymer phase observed in the XRD pattern. A percentage cumulative release of 21.0% was noted at 240 h (10 days) (Figure 3.7).

Following brain injury, reactive oxygen species (ROS) and reactive nitrogen species (RNS) are produced, which leads to cell and tissue death (via damage of proteins, nucleic acid, and lipids, and the depletion of endogenous antioxidants) (Bharadwaj et al., 2018). However, the secondary injury of TBI evolves over hours and days, which provides a window of opportunity for intervention (Lamade et al., 2019). Clinical trials have noted the short half-life of antioxidants due to their oxidation as an inhibitory limitation. Therefore, entrapping the drug within the polymer matrix not only protects the drug, it also improves shelf life and provides localized delivery, circumventing systemic side effects. From a pharmaceutical perspective, drug release observed herein in the form of an initial burst may replenish endogenous antioxidant activity via glutathione up-regulation, while the subsequent controlled release offers sustained release of this antioxidant over a period of time during a critical intervention period (the first few hours to days prior to secondary injury evolution). Glutathion (GSH) is used by cellular enzymes to detoxify reactive oxygen and nitrogen species and to repair oxidatively damaged proteins; however, GSH cannot be taken up by neurons, but NAC can restore GSH levels by serving as a cell-permeable source of cysteine, which is a substrate for GSH synthesis (Katz et al., 2015). Clark and co-workers conducted a randomized, double-blind Phase I study following TBI using NAC and probenecid, and they noted NAC concentrations ranging from 269.3 ± 113.0 to 467.9 ± 262.7 ng/mL in cerebrospinal fluid (CSF) at 24 to 72 h post-

bolus, respectively (Clark et al., 2017). Detection of these NAC drug amounts revealed no adverse effects following the surveillance of serum brain injury biomarkers attributable to drug treatment (Clark et al., 2017). In this study, embedding the NAC-eluting PLGA nanofibers within the scaffold is proposed to potentially result in NAC accumulation within the scaffold matrix at the injury site from the biphasic release profile observed, which may potentially further result in neuroprotection at the injury site. The nanofibers are effective in acting as a drug delivery system.

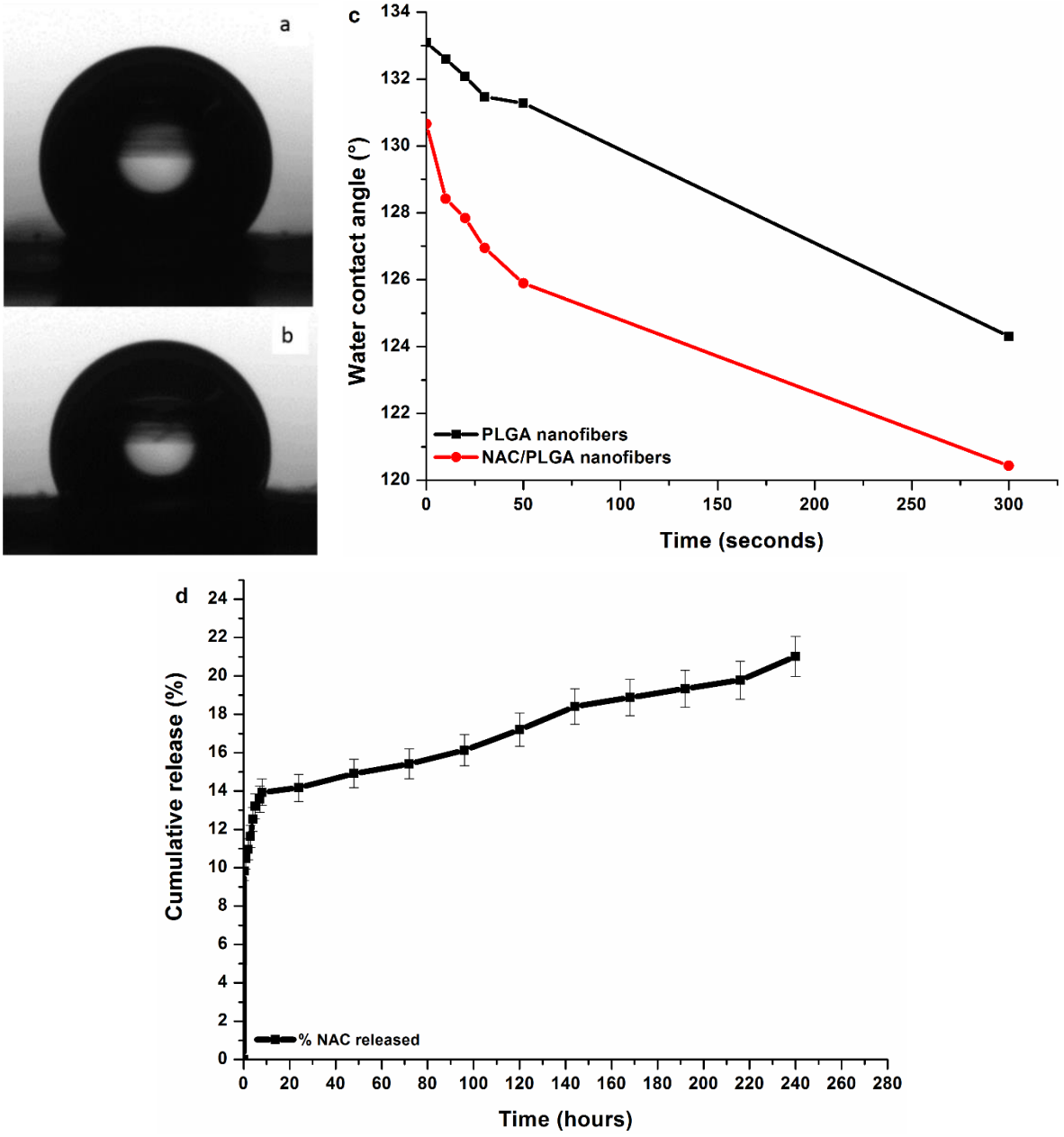

Figure 3.7. Water contact angle images of (**a**) NAC-free nanofibers and (**b**) NAC-loaded nanofibers (**c**) and changes within a 5-min period. (**d**) *In vitro* drug release (percent cumulative drug released) profile of NAC from PLGA nanofibers in PBS at 37 °C observed over 10 days (240 h).

3.4.7. Effect of NAC-loading on cell viability and proliferation

Figure 3.8 shows the indirect cytotoxicity evaluation of the electrospun fiber mats based on the viability of PC12 and A172 cell lines that were cultured for 72 h. The percentage viability of the cells was reported as the percentage with respect to that of the control (media). In accordance with ISO 10993-5, cytotoxicity is determined as follows: cell viability above 80% is considered non-cytotoxic, cell viability within 80–60% is considered weak, 60–40% indicates moderate cytotoxicity, and below 40% indicates strong cytotoxicity, respectively (International Organization for Standardization, 2009).

According to ISO 10993-5, the PLGA and NAC-loaded PLGA nanofibers were non-toxic to both PC12 and A172 cell lines, as their percentage viability values were well above 80% (Figure 3.8). This is indicative of the cytocompatility of these systems, as they did not release any toxic substances in the cell culture medium toward PC12 and A172 cell lines. This was expected, as the carefully selected polymers materials NAC and PLGA herein are FDA-approved and noted for their biocompatibility, biodegradability, and non-toxic properties (Blasi, 2019; Ershad and Vearrier, 2020; Mahumane et al., 2018; Wang Yan et al., 2016).

A percentage cell viability higher than that of the control was observed with the nanofibers (Figure 3.8). This suggests that the nanofibrous scaffold further enhanced the growth of cells. The observed favorability toward the nanofibers compared to the control as a substrate by the cells could be attributed to their architecture. Nanofibers most closely mimic the ECM and provide a high surface area to volume ratio for cell attachment and proliferation.

The percentage viability on NAC-loaded nanofibers was higher than that of the NAC-free nanofibers. Ramburrun also noted an increase in neuronal cell (PC12) proliferation compared to NAC-free poly(3-hyroxybutyric acid-co-3-hydroxyvaleric acid) (PHBV) blended with magnesium-oleate (MgOl) fibrous films ascribed to NAC incorporation into the nanofiber system (Ramburrun et al., 2019). This may be attributed in part to the hydrophilicity imparted by the NAC (SH and NH groups). By comparison, moderate to strong cytotoxicity was noted for both A172 and PC12 cell lines when treated with NAC only (Figure 3.8). The NAC test was conducted at a concentration of 1000 ug/ml concentration. In comparison, the concentration of the released nanofibers was noted at approximately 15% (Figure 3.7) of the drug loaded in the nanofibers which is approximately 84ug/ml. Media comprising of NAC crystal as a solute may have impeded cell growth by the formation of a hypertonic media, thereby altering cell tonicity. When NAC is embedded in the nanofibers, the slow release rate of the NAC from the nanofiber system may favor cell proliferation as opposed to burst exposure to the bare concentrated drug crystals. Overall, the incorporation of NAC into the nanofiber system

confers a synergistic interaction from the observed improvement in neuronal survival and proliferation in comparison to the NAC-free nanofibers and the control.

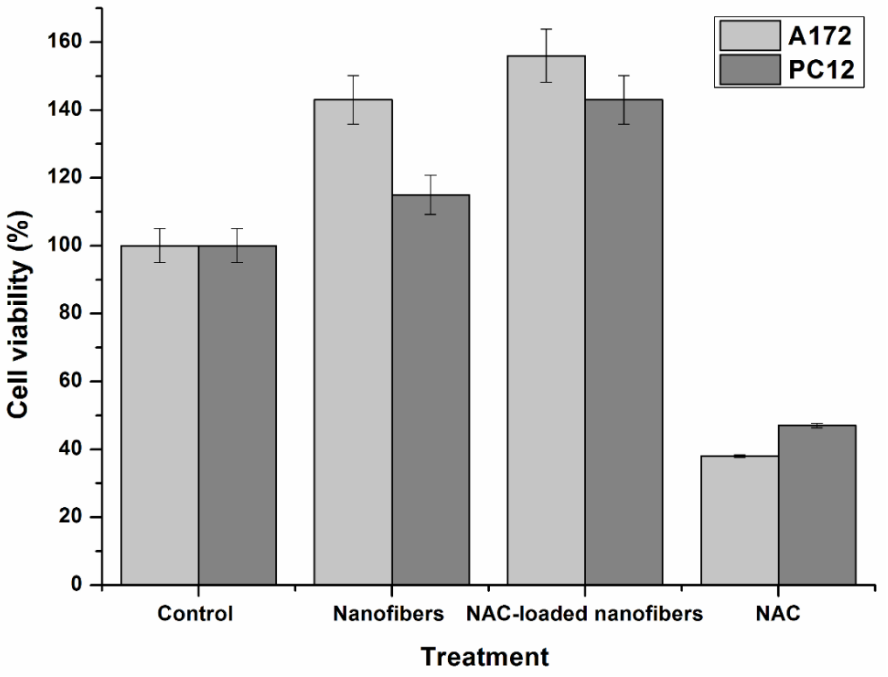

Figure 3.8. Cell viability and proliferation on control, and scaffold treatment of (**a**) PC12 and (**b**) A172 cell lines after 72 h incubation. Indirect cytotoxicity evaluation of various treatments based on the viability of PC12 and A172 cell lines that were cultured for 72 h.

3.5. Conclusions

Biomimetic NAC-loaded PLGA nanofibers were produced via electrospinning. The presence, interactions between the native PLGA and the scaffold, and chemical integrity and performance of the nanosystem were confirmed by detailed physicochemical and physicomechanical studies. Scanning electron microscopy revealed the formation of a 3D nanofibrous structure with interconnected pores to support nutrient, oxygen, and cell migration as well as enable integrate surrounding cells into the scaffold within the ECM of brain tissue. Appendix I provides further details fo the drug release study of this published Chapter. *In vitro* release experiments of NAC demonstrated a biphasic release profile comprising an initial phase of 13.9% release within 8 h followed by more sustained release for a further 240 h. This is ideal for the nanosystem to function as a reservoir and elute the neuroprotective NAC at a TBI lesion. *Ex vivo* studies confirmed that the NAC-loaded nanosystem was non-toxic toward PC-12 and A172 cells with a positive effect on cell proliferation. Overall, the results showed that the nanosystem has promising potential for simultaneous application in both neural tissue repair and as a neuroprotectant in a spatial and temporal manner from a biomimetic neuroscaffold.

Author Contributions: G.D.M., P.K., V.P., Y.E.C., conceived and designed the experiments; G.D.M. performed the experiments. P.K., V.P., Y.E.C. supervised the research work. G.D.M., P.K., V.P., Y.E.C. analyzed the data; wrote the paper. All authors have read and agreed to the published version of the manuscript.

Funding: The work was funded by the National Research Foundation (NRF) of South Africa; the South African Medical Research Council (SAMRC) through its Division of Research Capacity Development under the Bongani Mayosi National Health Scholars Program from funding received from the Public Health Enhancement Fund/South African National Department of Health and the SIR Grant; and the University of the Witwatersrand, Johannesburg.

Acknowledgments: The authors are grateful to Evonik Nutrition & Care GmbH, Germany for the ex gratia supply of PLGA.

Conflicts of Interest: The authors declare no conflict of interest. The funders had no role in the design of the study; in the collection, analyses, or interpretation of data; in the writing of the manuscript, or in the decision to publish the results.

3.6. References

Ahmaditabar, P., Momtazi-Borojeni, A.A., Rezayan, A.H., Mahmoodi, M., Sahebkar, A., Mellat, M., 2017. Enhanced Entrapment and Improved in Vitro Controlled Release of N-Acetyl Cysteine in Hybrid PLGA/Lecithin Nanoparticles Prepared Using a Nanoprecipitation/ Self-Assembly Method. J. Cell. Biochem 118, 4203–4209. https://doi.org/10.1002/jcb.26070

Amariei, N., Manea, L.R., Bertea, A.P., Bertea, A., Popa, A., 2017. The influence of polymer solution on the properties of electrospun 3D nanostructures. IOP Conference Series: Materials Science and Engineering 209, 012092–012092. https://doi.org/10.1088/1757-899X/209/1/012092

Bharadwaj, V.N., Nguyen, D.T., Kodibagkar, V.D., Stabenfeldt, S.E., 2018. Nanoparticle-Based Therapeutics for Brain Injury. Advanced healthcare materials 7. https://doi.org/10.1002/adhm.201700668

Blasi, P., 2019. Poly (lactic acid)/poly(lactic-co-glycolic acid)-based microparticles: an overview. J. Pharm. Investig. 49, 337–346. https://doi.org/10.1007/s40005-019-00453-z

Bobo, D., Robinson, K.J., Islam, J., Thurecht, K.J., Corrie, S.R., 2016. Nanoparticle-Based Medicines: A Review of FDA-Approved Materials and Clinical Trials to Date. Pharm. Res. 33, 2373–2387. https://doi.org/10.1007/s11095-016-1958-5

Braghirolli, D.I., Steffens, D., Quintiliano, K., Acasigua, G.A.X., Gamba, D., Fleck, R.A., Petzhold, C.L., Pranke, P., 2014. The effect of sterilization methods on electronspun poly(lactide-co-glycolide) and subsequent adhesion efficiency of mesenchymal stem cells. Journal of Biomedical Materials Research Part B: Applied Biomaterials 102, 700–708. https://doi.org/10.1002/jbm.b.33049

Brown, P., Stevens, K., 2007. Nanofibers and Nanotechnology in Textiles. Elsevier.

Bullock, M.R., Lyeth, B.G., Muizelaar, J.P., 1999. Current Status of Neuroprotection Trials for Traumatic Brain Injury: Lessons from Animal Models and Clinical Studies. Neurosurgery 45, 207–220. https://doi.org/10.1097/00006123-199908000-00001

Chen, G., Shi, J., Hu, Z., Hang, C., 2008. Inhibitory Effect on Cerebral Inflammatory Response following Traumatic Brain Injury in Rats: A Potential Neuroprotective Mechanism of N-Acetylcysteine. Mediators Inflamm 2008. https://doi.org/10.1155/2008/716458

Chen, W., Ercal, N., Huynh, T., Volkov, A., Chusuei, C.C., 2012. Characterizing N-acetylcysteine (NAC) and N-acetylcysteine amide (NACA) binding for lead poisoning treatment. Journal of colloid and interface science 371, 144–9. https://doi.org/10.1016/j.jcis.2011.12.052

Clark, R.S.B., Empey, P.E., Bayir, H., Rosario, B.L., Poloyac, S.M., Kochanek, P.M., Nolin, T.D., Au, A.K., Horvat, C.M., Wisniewski, S.R., Bell, M.J., 2017. Phase I randomized clinical trial of N-acetylcysteine in combination with an adjuvant probenecid for treatment of severe traumatic brain injury in children. PLoS ONE 12, e0180280–e0180280. https://doi.org/10.1371/journal.pone.0180280

Desai, K.G.H., Mallery, S.R., Schwendeman, S.P., 2008. Formulation and characterization of injectable poly(DL-lactide-co-glycolide) implants loaded with N-acetylcysteine, a MMP inhibitor. Pharmaceutical research 25, 586–97. https://doi.org/10.1007/s11095-007-9430-1

Dodd, S., Dean, O., Copolov, D.L., Malhi, G.S., Berk, M., 2008. N-acetylcysteine for antioxidant therapy: pharmacology and clinical utility. Expert Opin. Biol. Ther. 8, 1955–1962.

Ershad, M., Vearrier, D., 2020. N Acetylcysteine, in: StatPearls. StatPearls Publishing, Treasure Island (FL).

Farr, S.A., Poon, H.F., Dogrukol-Ak, D., Drake, J., Banks, W.A., Eyerman, E., Butterfield, D.A., Morley, J.E., 2003. The antioxidants α-lipoic acid and N-acetylcysteine reverse memory impairment and brain oxidative stress in aged SAMP8 mice. Journal of Neurochemistry 84, 1173–1183. https://doi.org/10.1046/j.1471-4159.2003.01580.x

Feng, X., Li, J., Zhang, X., Liu, T., Ding, J., Chen, X., 2019. Electrospun polymer micro/nanofibers as pharmaceutical repositories for healthcare. Journal of Controlled Release 302, 19–41. https://doi.org/10.1016/j.jconrel.2019.03.020

Fouad, H., Elsarnagawy, T., Almajhdi, F.N., Khalil, K.A., 2013. Preparation and in vitro thermo-mechanical characterization of electrospun PLGA nanofibers for soft and hard tissue replacement. International Journal of Electrochemical Science 8, 2293–2304.

Fu, Y., Kao, W.J., 2010. Drug release kinetics and transport mechanisms of non-degradable and degradable polymeric delivery systems. Expert opinion on drug delivery 7, 429–44. https://doi.org/10.1517/17425241003602259

Ghajar, J., 2000. Traumatic brain injury. the Lancet 356, 923–29.

Gilgun-Sherki, Y., Rosenbaum, Z., Melamed, E., Offen, D., 2002. Antioxidant therapy in acute central nervous system injury: current state. Pharmacological reviews 54, 271–84.

Gnanasekar, S., Kollu, P., Jeong, S.K., Grace, A.N., 2019. Pt-free, low-cost and efficient counter electrode with carbon wrapped VO 2 (M) nanofiber for dye-sensitized solar cells. Scientific Reports 9, 5177–5177. https://doi.org/10.1038/s41598-019-41693-1

Hara, Y., McKeehan, N., Dacks, P.A., Fillit, H.M., 2017. Evaluation of the neuroprotective potential of N-acetylcysteine for prevention and treatment of cognitive aging and dementia. The Journal of Prevention of Alzheimers Disease 4, 201–2016. https://doi.org/10.14283/jpad.2017.22

He, L., Liao, S., Quan, D., Ma, K., Chan, C., Ramakrishna, S., Lu, J., 2010. Synergistic effects of electrospun PLLA fiber dimension and pattern on neonatal mouse cerebellum C17.2 stem cells. Acta Biomaterialia 6, 2960–2969. https://doi.org/10.1016/J.ACTBIO.2010.02.039

He, Y., Liu, X., Chen, Z., 2020. Glial Scar—a Promising Target for Improving Outcomes After CNS Injury. J Mol Neurosci 70, 340–352. https://doi.org/10.1007/s12031-019-01417-6

Heard, K.J., 2008. Acetylcysteine for Acetaminophen Poisoning. N Engl J Med 359, 285–292. https://doi.org/10.1056/NEJMct0708278

Hoffer, B.J., Pick, C.G., Hoffer, M.E., Becker, R.E., Chiang, Y.H., Greig, N.H., 2017. Repositioning drugs for traumatic brain injury - N-acetyl cysteine and Phenserine. Journal of Biomedical Science 24, 71–71. https://doi.org/10.1186/s12929-017-0377-1

International Organization for Standardization, 2009. ISO - ISO 10993-5:2009 - Biological evaluation of medical devices — Part 5: Tests for in vitro cytotoxicity, 3rd ed, ISO/TC 194 Biological and clinical evaluation of medical devices.

Katz, M., Won, S.J., Park, Y., Orr, A., Jones, D.P., Swanson, R.A., Glass, G.A., 2015. Cerebrospinal fluid concentrations of N-acetylcysteine after oral administration in Parkinson's disease. Parkinsonism & Related Disorders 21, 500–503. https://doi.org/10.1016/j.parkreldis.2015.02.020

Khadka, P., Ro, J., Kim, Hyeongmin, Kim, I., Kim, J.T., Kim, Hyunil, Cho, J.M., Yun, G., Lee, J., 2014. Pharmaceutical particle technologies: An approach to improve drug solubility, dissolution and bioavailability. Asian Journal of Pharmaceutical Sciences 9, 304–316. https://doi.org/10.1016/j.ajps.2014.05.005

Khan, M., Sekhon, B., Jatana, M., Giri, S., Gilg, A.G., Sekhon, C., Singh, I., Singh, A.K., 2004. Administration of N-acetylcysteine after focal cerebral ischemia protects brain and reduces inflammation in a rat model of experimental stroke. Journal of Neuroscience Research 76, 519–527. https://doi.org/10.1002/jnr.20087

Kim, J.I., Hwang, T.I., Aguilar, L.E., Park, C.H., Kim, C.S., 2016. A Controlled Design of Aligned and Random Nanofibers for 3D Bi-functionalized Nerve Conduits Fabricated via a Novel Electrospinning Set-up. Scientific reports 6, 23761–23761. https://doi.org/10.1038/srep23761

Kim, Y., Meade, S.M., Chen, K., Feng, H., Rayyan, J., Hess-Dunning, A., Ereifej, E.S., 2018. Nano-Architectural Approaches for Improved Intracortical Interface Technologies. Front. Neurosci. 12. https://doi.org/10.3389/fnins.2018.00456

Kimizuka, N., 2008. Self-Assembly of Supramolecular Nanofibers, in: Shimizu, T. (Ed.), Self-Assembled Nanomaterials I: Nanofibers, Advances in Polymer Science. Springer, Berlin, Heidelberg, pp. 1–26. https://doi.org/10.1007/12_2008_170

Lamade, A.M., Kenny, E.M., Anthonymuthu, T.S., Soysal, E., Clark, R.S.B., Kagan, V.E., Bayır, H., 2019. Aiming for the target: Mitochondrial drug delivery in traumatic brain injury. Neuropharmacology 145, 209–219. https://doi.org/10.1016/J.NEUROPHARM.2018.07.014

Lancheros, R., Guerrero, C.A., Godoy-Silva, R.D., 2018. Improvement of N-acetylcysteine loaded in PLGA nanoparticles by nanoprecipitation method. Journal of Nanotechnology 2018, 1–11. https://doi.org/10.1155/2018/3620373

Lau, L.W., Cua, R., Keough, M.B., Haylock-Jacobs, S., Yong, V.W., 2013. Pathophysiology of the brain extracellular matrix: a new target for remyelination. Nat. Rev. Neurosci. 14, 722–729. https://doi.org/10.1038/nrn3550

Lee, J., Cuddihy, M.J., Kotov, N.A., 2008. Three-Dimensional Cell Culture Matrices: State of the Art. Tissue Engineering Part B: Reviews 14, 61–86. https://doi.org/10.1089/teb.2007.0150

Lee, J.Y., Bashur, C.A., Goldstein, A.S., Schmidt, C.E., 2009. Polypyrrole-coated electrospun PLGA nanofibers for neural tissue applications. Biomaterials 30, 4325–4335. https://doi.org/10.1016/j.biomaterials.2009.04.042

Leung, V., Ko, F., 2011. Biomedical applications of nanofibers. Polymers for Advanced Technologies 22, 350–365. https://doi.org/10.1002/pat.1813

Mahumane, G.D., Kumar, P., Du Toit, L.C., Choonara, Y.E., Pillay, V., 2018. 3D scaffolds for brain tissue regeneration: Architectural challenges. Biomaterials Science 6, 2812–2837. https://doi.org/10.1039/c8bm00422f

Makadia, H.K., Siegel, S.J., 2011. Poly Lactic-co-Glycolic Acid (PLGA) as Biodegradable Controlled Drug Delivery Carrier. Polymers (Basel) 3, 1377–1397. https://doi.org/10.3390/polym3031377

Marshall, L.F., Gautille, T., Klauber, M.R., Eisenberg, H.M., Jane, J.A., Luerssen, T.G., Marmarou, A., Foulkes, M.A., 1991. The outcome of severe closed head injury. Journal of Neurosurgery 75, S28–S36. https://doi.org/10.3171/sup.1991.75.1s.0s28

Pettikiriarachchi, J.T.S., Parish, C.L., Shoichet, M.S., Forsythe, J.S., Nisbet, D.R., 2010. Biomaterials for brain tissue engineering. Aust. J. Chem 63, 1143–1154. https://doi.org/10.1071/CH10159

Picquart, M., Abedinzadeh, Z., Grajcar, L., Baron, M.H., 1998. Spectroscopic study of N-acetylcysteine and N-acetylcystine/hydrogen peroxide complexation. Chemical Physics 228, 279–291. https://doi.org/10.1016/S0301-0104(97)00337-6

Pillay, V., Dott, C., Choonara, Y.E., Tyagi, C., Tomar, L., Kumar, P., du Toit, L.C., Ndesendo, V.M.K., 2013. A Review of the Effect of Processing Variables on the Fabrication of Electrospun Nanofibers for Drug Delivery Applications [WWW Document]. Journal of Nanomaterials. https://doi.org/10.1155/2013/789289

Ramazani, F., Chen, W., Van Nostrum, C.F., Storm, G., Kiessling, F., Lammers, T., Hennink, W.E., Kok, R.J., 2016. Strategies for encapsulation of small hydrophilic and amphiphilic drugs in PLGA microspheres: State-of-the-art and challenges. International Journal of Pharmaceutics 499, 358–367. https://doi.org/10.1016/j.ijpharm.2016.01.020

Ramburrun, P., Kumar, P., Choonara, Y.E., du Toit, L.C., Pillay, V., 2019. Design and characterisation of PHBV-magnesium oleate directional nanofibers for neurosupport. Biomed. Mater. 14, 065015. https://doi.org/10.1088/1748-605X/ab453c

Reilly, P., 2007. The impact of neurotrauma on society: an international perspective, in: Weber, J.T., Maas, A.I.R. (Eds.), Progress in Brain Research, Neurotrauma: New Insights into Pathology and Treatment. Elsevier, pp. 3–9. https://doi.org/10.1016/S0079-6123(06)61001-7

Rubiano, A.M., Carney, N., Chesnut, R., Puyana, J.C., 2015. Global neurotrauma research challenges and opportunities. Nature 527, S193–S197. https://doi.org/10.1038/nature16035

Sedaghati, T., Seifalian, A.M., 2015. Nanotechnology and bio-functionalisation for peripheral nerve regeneration. Neural Regeneration Research 10, 1191–1194. https://doi.org/10.4103/1673-5374.162678

Shen, Y., Cai, W., Lei, S., Zhongheng, Z., 2014. Effect of High/Low Dose N-Acetylcysteine on Chronic Obstructive Pulmonary Disease: A Systematic Review and Meta-analysis: COPD: Journal of Chronic Obstructive Pulmonary Disease 11. https://doi.org/10.3109/15412555.2013.858315

Sing, K.S.W., Everet, D.H., Haul, R.A.W., Moscou, L., R.A.Pierot, Rouquerol, J., Siemieniewska, T., 1985. Reporting physisorption data for gas/solid systems with special reference to the determination of surface area and porosity (Recomendations 1984). Pure and Applied Chemistry 57, 603–619. https://doi.org/10.1351/pac198557040603

Sing, K.S.W., Everett, D.H., Haul, R. a. W., Moscou, L., Pierotti, R.A., Rouquerol, J., Siemieniewska, T., 2008. Reporting Physisorption Data for Gas/Solid Systems, in: Handbook of Heterogeneous Catalysis. American Cancer Society, pp. 1217–1230. https://doi.org/10.1002/9783527610044.hetcat0065

Stukel, J.M., Willits, R.K., 2016. Mechanotransduction of neural cells through cell-substrate interactions. Tissue Engineering: Part B 22, 173–182. https://doi.org/10.1089/ten.teb.2015.0380

Subramanian, A., Krishnan, U.M., Sethuraman, S., 2012. Fabrication, characterization and in vitro evaluation of aligned PLGA-PCL nanofibers for neural regeneration. Annals of Biomedical Engineering 40, 2098–2110. https://doi.org/10.1007/s10439-012-0592-6

Wang Yan, Choi Stephanie, Qu Wen, 2016. FDA's Regulatory Science Program for Generic PLA/ PLGA-Based Drug Products [WWW Document]. URL http://www.americanpharmaceuticalreview.com/Featured-Articles/188841-FDA-s-Regulatory-Science-Program-for-Generic-PLA-PLGA-Based-Drug-Products/

Wu, Y., Xiang, Y., Fang, J., Li, X., Lin, Z., Dai, G., Yin, J., Wei, P., Zhang, D., 2019. The influence of the stiffness of GelMA substrate on the outgrowth of PC12 cells. Bioscience Reports 39, BSR20181748–BSR20181748. https://doi.org/10.1042/bsr20181748

Xiong, Y., Peterson, P., Peterson, P.L., 2009. Effect of N-Acetylcysteine on Mitochondrial Function Following Traumatic Brain Injury in Rats | Journal of Neurotrauma [WWW Document]. URL https://www.liebertpub.com/doi/10.1089/neu.1999.16.1067 (accessed 8.12.20).

Yang, F., Murugan, R., Wang, S., Ramakrishna, S., 2005. Electrospinning of nano/micro scale poly(l-lactic acid) aligned fibers and their potential in neural tissue engineering. Biomaterials 26, 2603–2610. https://doi.org/10.1016/J.BIOMATERIALS.2004.06.051

You, Y., Lee, S., Min, B.-M., Park, W., 2006. Effect of solution properties on nanofibrous structure of electrospun poly(lactic-co-glycolic acid). Journal of Applied Polymer Science 99, 1214 –1221–1214 –1221.

Zhang, L., Lei, Z., Guo, Z., Pei, Z., Chen, Y., Zhang, F., Cai, A., Mok, Y.K., Lee, G., Swaminnathan, V., Wang, F., Bai, Y., Chen, G., 2018. Reversing Glial Scar Back To Neural Tissue Through NeuroD1-Mediated Astrocyte-To-Neuron Conversion (preprint). Neuroscience. https://doi.org/10.1101/261438

Zhou, L., Tu, J., Fang, G., Deng, L., Gao, X., Guo, K., Kong, J., Lv, J., Guan, W., Yang, C., 2018. Combining PLGA Scaffold and MSCs for Brain Tissue Engineering: A Potential Tool for Treatment of Brain Injury. Stem Cells Int 2018. https://doi.org/10.1155/2018/5024175

Zhou, Z.H., Liu, X.P., Liu, L.H., 2008. Preparation and biocompatibility of poly(L-lactide-co-glycolide) scaffold materials for nerve conduits. Designed Monomers and Polymers 11, 447–456. https://doi.org/10.1163/156855508X328149

Zhu, Y., Song, F., Ju, Y., Huang, L., Zhang, L., Tang, C., Yang, H., Huang, C., 2019. NAC-loaded electrospun scaffolding system with dual compartments for the osteogenesis of rBMSCs in vitro. International journal of nanomedicine 14, 787–798. https://doi.org/10.2147/IJN.S183233



© 2020 by the authors. Submitted for possible open access publication under the terms and conditions of the Creative Commons Attribution (CC BY) license (http://creativecommons.org/licenses/by/4.0/).

CHAPTER FOUR

FABRICATION AND CHARACTERIZATION OF A CROSSLINKED GELATIN-ELASTIN HYDROGEL

4.1. Introduction

The aim of the project was to design a novel brain tissue-mimicking scaffold for application in neural tissue regeneration. This was fabricated by the design of a 3-in-1 system wherein nanofibers were “in-process” embedded into a cryogel scaffold followed by filling of the macro-microporous architecture with an ECM-mimicking hydrogel.

It is important to consider the unique composition of the brain ECM when designing ECM-mimetic scaffolds. The brain ECM has a unique composition of relatively high amounts of linear polysaccharides, such as glycosaminoglycan’s and small amounts of fibrous proteins, such as collagen, laminin and fibronectin (Baiguera et al., 2014; Lee et al., 2008; Mouw et al., 2014). Though present in relatively smaller amount, the role of proteins is critical in the ECM. Proteins play structural and functional roles. Cells interact with the ECM via nanoscale proteins enabling them to modulate cellular activities in response to the environment (Lee et al., 2008). This study proposes a gelatin-BDDE-elastin based hydrogel as one of three (1/3) of the 3-in-1 system proposed in this study to further improve the structural integrity (strength, elasticity) and confer cell adhesion motifs. Gelatin/collagen based hydrogels are not entirely physiological as these proteins are poorly represented in the brain parenchyma (Kornev et al., 2018). Therefore, HA remains the backbone of the 3-in-1 scaffold system and the protein based (gelatin/elastin) hydrogel will serve to fill the pores of the nanoreinforced cryogel scaffold.

Elastin is an extracellular protein commonly known for providing elasticity and resilience to tissues (Klimek and Ginalska, 2020; Popescu et al., 2010; Vindin et al., 2019). The elasticity is coded by the valine, proline, and glycine repeating amino acid sequence (Klimek and Ginalska, 2020). Elastin was added to improve on the elasticity of the hydrogel. In addition to elasticity, the presence of the RGD sequence in its molecule enables elastin to support cell adhesion and growth (Vindin et al., 2019). Moreover, elastin-like peptides have been shown to promote neurite outgrowth (Lampe et al., 2013).

Gelatin is a denatured protein obtained from the hydrolysis of collagen. As a denatured product, gelatin has the advantages of being less antigenic and less immunogenic compared to collagen in physiological conditions while still retaining the properties necessary for cell-biomaterial interactions such as exposure to ligands (e.g. peptide motifs, such as arginine-glycine-aspartic acid, RGD sequence) that acts as a cell adhesive motif by integrin mediated ligands and possesses target sites for cellular metalloproteinases (MPP) required for ECM remodeling and *in vivo* biodegradation (Boni et al., 2018; Campiglio et al., 2019). Gelatin based systems (nanofibers, nanoparticles, hydrogels) have shown potential for neural tissue engineering application (Baiguera et al., 2014; Binan et al., 2014; Boni et al., 2018). Gelatin is not without its limitations as a potential biomaterial polymer. Gelatin is a water soluble protein, presents with high water solubility, low elasticity and thermal instability at physiological temperature (Dias et al., 2017; Shankar et al., 2017).

Methods for countering these limitations are highly desirable for application as a biomaterial scaffolding material. In order to reduce solubility in aqueous environments, improve the physical properties and augment its use *in vivo*, gelatin is stabilized by crosslinking. 1,4-Butanediol diglycidyl ether is used as a chemical crosslinker. 1,4-Butanediol diglycidyl ether is a commercially available epoxy crosslinker (Martucci et al., 2015a). Epoxy crosslinkers are preferred for stabilizing collagen based materials for biomedical applications due to their lower toxicity (compared to commonly used dialdehydes) (Dias et al., 2017). Residual BDDE might undergo hydrolysis yielding diol-ether (3,3′(butane-1,4-diylbis(oxy)) bis propane-1,2-diol), which have been proven non-toxic (De Boulle et al., 2013; Martucci et al., 2015a). The cross-linking method chosen to stabilize gelatin structures for biomedical applications is critical. Scaffold properties such as degradation kinetics, mechanical and rheological properties, biocompatibility can be modified during the cross linking step. Chemical crosslinking was used herein using 1,4-butanediol diglycidyl ether. The lower toxicity (compared to commonly used dialdehydes) makes epoxy compounds the preferred stabilizing agents for collagen-based materials such as gelatin for biomedical applications (Martucci et al., 2015b).

The gelatin-BDDE-elastin hydrogel was fabricated in an attempt to incorporate soluble signaling molecules within a resultant 3-in-1 hybrid scaffold matrix. Several pharmaceutical characterization analyses were undertaken to evaluate potential soft tissue application as function of the crosslinking, thermal stability, chemical transitions, and mechanical properties and swelling the hydrogel via Fourier Transform Infrared (FTIR), XRD, TGA, DSC, SEM, swelling, and rheological assessment prior to incorporation into and fabrication of the final 3-in-1 hybrid scaffold in Chapter five.

4.2. Materials and Methods

4.2.1. Preparation of hydrogel component

Elastin (from bovine neck ligament, Sigma-Aldrich) and Type-B gelatin obtained from bovine skin, with a bloom of 225 (Sigma-Aldrich, South Africa) was used. Gelatin was dissolved in deionized water to a concentration of 5% (w/v) at 50°C. Gelatin was allowed to cool to 25°C and elastin was added at various ratios (4:1 and 10:1). The pH was adjusted to 8.5 using NaOH. Gelatin denatures (loss of the tertiary structure) at pH values > 9 (Vargas et al., 2008). Because gelatin is soluble in water, it is necessary to crosslink the material to preserve the hydrogel structure. 1,4-Butanediol diglycidyl (BDDE) ether (Sigma Aldrich, South Africa) was added as a crosslinking agent followed by rapid stirring to ensure homogenous crosslinking. It is expected that under alkaline pH, BDDE may predominantly react with hydroxyl groups of elastins tyrosine, threonine and serine groups to yield stable ether bonds (Leach et al., 2005). The resulting solution was poured into a petri dish and allowed to crosslink and gel over 48 hours.

4.2.2. Characterization of hydrogel

FTIR, DSC, XRD and TGA were performed as stated in Chapter three.

4.2.3. Swelling ratio

Dynamic swelling measurements were made using gravimetric measurements. Swelling experiments were carried out to determine the equilibrium swelling ratio (ESR). Three replicas of lyophilized samples were kept immersed in aCSF at 37°C. Both non-crosslinked (gelatin only and Ge-Ela gels) and cross-linked (gelatin-BDDE and Ge-BDDE-Ela hydrogels) samples were tested. Samples were resized to 8mm by 5mm dimensions using a digital Vernier calliper (Krafft, DV150GW, Schoellerstr Düren, German). Samples were periodically withdrawn from the solution at at 1, 2, 3, 4, 8, 24, 48 and 72 hour intervals. These were gently blotted with absorbent paper and weighed on an analytical balance (Analytical Balance 220 g × 0.1 mg, Radwag AS 220/C/2) at regular intervals of time until the swelling equilibrium was reached. Then, swelling ratio was calculated as: Swelling ratio (Sr) = $(W_t - W_i)/W_i$, where W_t is the gel weight at each time point and W_i is the original dried weight of the hydrogel. Following each essay, the swelling medium was replenished.

4.2.4. Rheological evaluation of the viscoelastic properties of the protein based hydrogel

Rheological analysis of the hydrogels was carried out using a HAAKE Modular Advanced Rheometer System (II) (Thermo Fisher Scientific, Johannesburg, South Africa), using a cone plate geometry (Rotor C35/1, D = mm, 1 Titan) with a gap measurement of 0.050 mm. The hydrogels were allowed to reach equilibrium swelling overnight before determining their

rheological properties. The rheological experiments were conducted at 37 °C: Yield stress (0-200 Pa), stress sweep (0.01 Pa to 200 Pa at a fixed frequency of 1 Hz) and oscillation frequency sweep.

4.3. Results

4.3.1. Stabilizing Interactions of crosslinking: FTIR, XRD, thermal stability, thermal transitions, swelling ratio of hydrogel.

4.3.1.1. Fourier-transform infrared spectroscopy analysis of hydrogel

The potential interactions resulting from chemical crosslinking with BDDE were assessed by FTIR analysis (Figure 4.1). The spectra of gelatin and elastin both presented peaks that arise from their protein structure such as amide I (~1630cm^{-1}) associated with C=O stretching, and amide II (1530cm^{-1}) assigned to N-H bending and C-N stretching, and amide III (1239cm^{-1}) associated with N-H in-plane bending and C-N stretching coupled with C-H and N-H deformation (Martucci et al., 2015a; Popescu et al., 2010). The amide A region (3288cm^{-1}) for native gelatin was less intense that elastin. The FTIR spectrum of the uncrosslinked Ge/Ela gels was similar to the native elastin and gelatin, exhibiting C=O stretching at 1631cm^{-1}, N-H stretching at 1537cm^{-1}, and N-H bend at 1236cm^{-1}. The alkaline conditions did not significantly alter the proteins. In the FTIR spectrum of BDDE (Figure 4.1), the characteristics peaks at 2926, 2862, 1253, 1099, and 907 cm^{-1} are responsible for C-H stretching of the epoxy ring, C-H stretching -CH2 bond, C-C bond, C-O-C stretching, and C-O stretching vibrations of epoxy ring, respectively (Bang et al., 2017). Changes were notable following the addition of BDDE, an increase in the intensity of the absorption band at 1100cm^{-1} related to C-O stretching. This is likely caused by the epoxy-amine reaction resulting in the appearance of secondary alcohol groups (Martucci et al., 2015a). This is indicative of the effective chemical crosslinking with BDDE. Peaks at 2874cm^{-1} and 2941cm^{-1} were observed in the crosslinked hydrogel associated with the contribution of the aliphatic moieties from the BDDE crosslinker. This further confirms the incorporation of the BDDE in the gelatin-elastin hydrogel matrix. Changes in the intensity of the amide I and amide II peaks was negligible suggesting hydrogen bonds to be negligible. The observations herein are in agreement of the reaction mechanism taking place at alkaline pH which involves opening of the oxirane rings in BDDE by the nucleophilic attack of the amino side chain groups in the proteins (Nicoletti et al., 2013; Zeeman et al., 2000). FTIR confirmed the effective chemical crosslinking with BDDE.

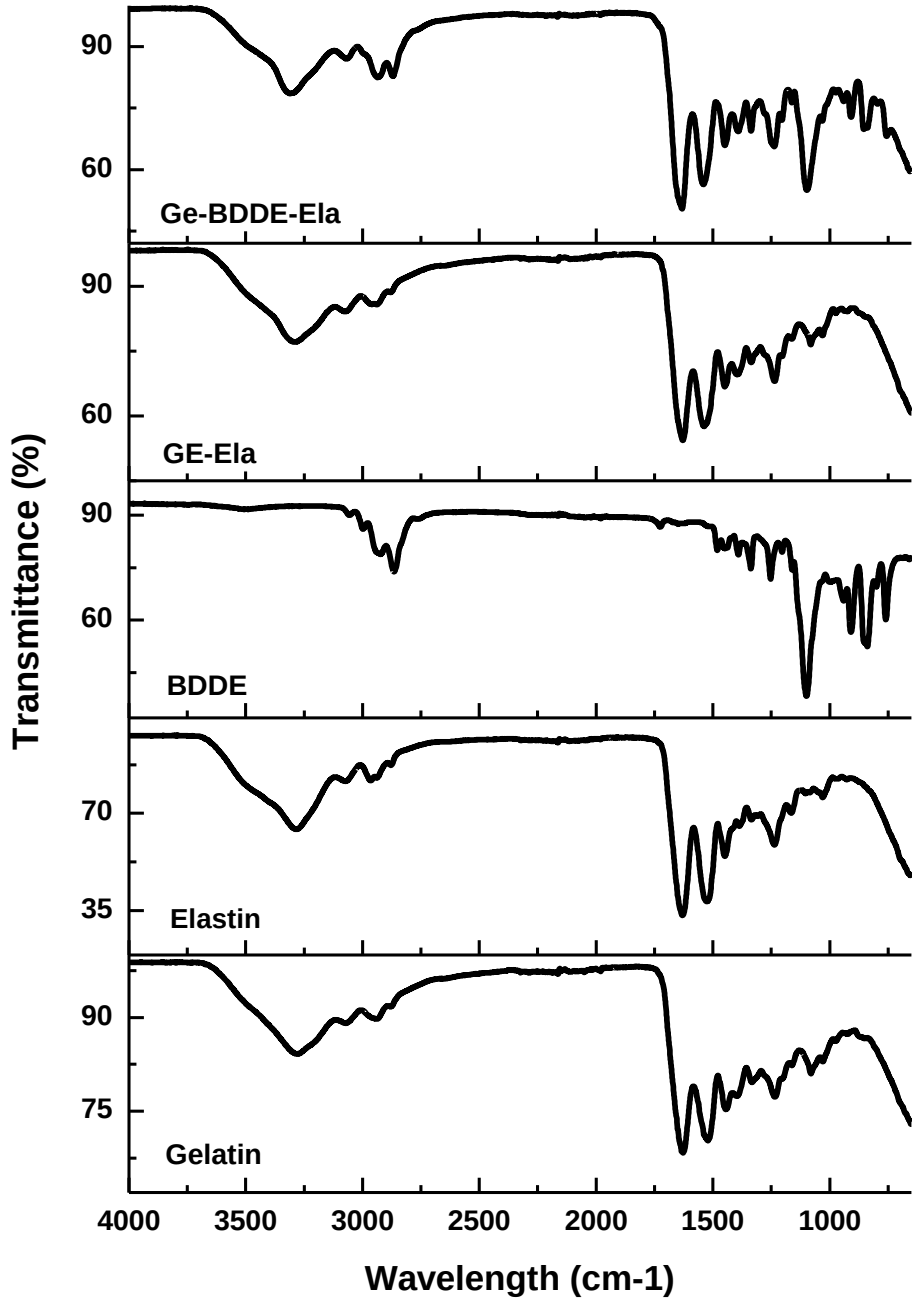

Figure 4.1. FTIR spectra of Gelatin, Elastin, BDDE, non-crosslinked Ge-Ela gels and BDDE crosslinked hydrogels (Ge-BDDE-Ela).

4.3.1.2. X-ray powder diffraction analysis of Ge-BDDE-Ela hydrogel

The XRD profile of the cross-linked hydrogel is given in Figure 4.2. X-ray powder diffraction was used to characterize the existence of both gelatin and elastin in the hydrogel network. The cross-linked hydrogel showed peaks representing both gelatin and elastin were observed.

An amorphous large broadening diffraction peak where 2 theta equals 20.9° that can be attributed to the formation of small crystalline structures owing to the secondary structure of gelatin (Alavijeh et al., 2017; Morsy, 2016). The cross-linked hydrogel displayed a much weaker diffraction at 31.7° shifting 3° (from 28.3°) to the right and 45.5° shifting 2.3° (from 43.2°) degree to the right of the elastin peaks, indicating a different type of crystal form with different D spacing within the crystal lattice post crosslinking and hydrogel formation. The cross-linked hydrogel had an overall weaker intensity than that of the pure gelatin and elastin, indicating a different crystal form and a lesser degree of crystallinity/ordered structure in the cross-linked hydrogel material. The diffraction peaks that appeared in the hydrogel agree with the native gelatin and elastin, which indicated that the gelatin/elastin hydrogel has been successfully synthesized.

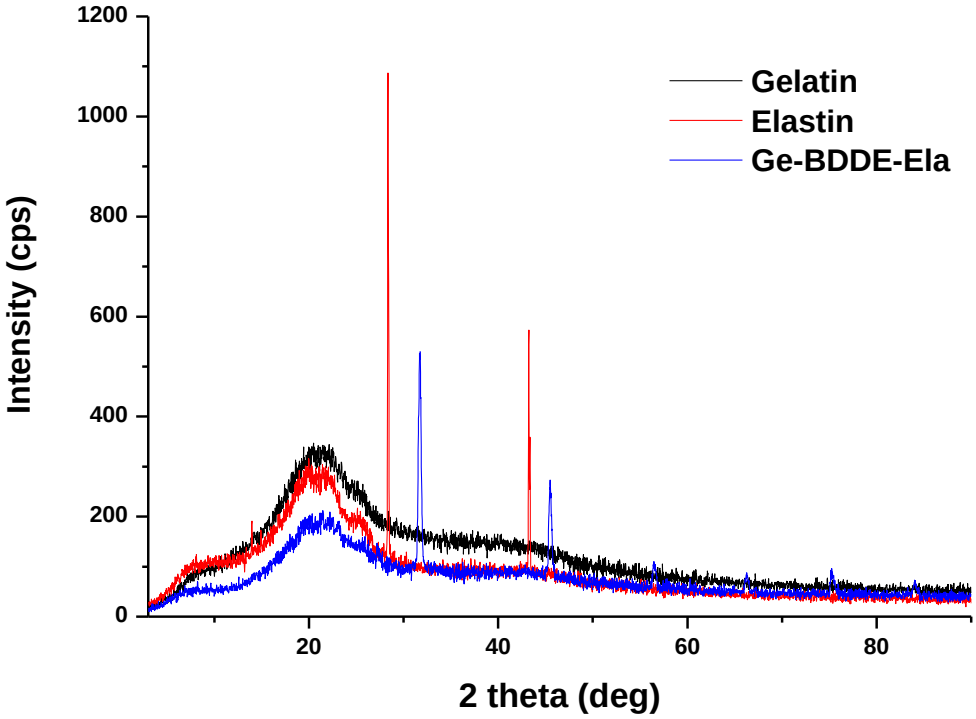

Figure 4.2. X-ray diffraction (XRD) pattern of gelatin, elastin and Ge-BDDE-Ela hydrogel (4:1 Ge-Ela ratio).

4.3.1.3. Thermogravimetric analysis

Thermogravimetric analysis also detected the moisture content. The initial mass loss is generally attributed to the volatilization of sample moisture, as hydrogen-bound water, related to desorption of bound water and dehydration reactions. This first stage, attributed to the loss of moisture, occurs from 40°C to about 170°C. Weight losses were noted at 11%, 17%, 11%

and 3% for Gelatin, Elastin, non-crosslinked hydrogel and crosslinked hydrogel (Ge-BDDE-Ela) respectively (Figure 4.3). Omwoyo and coworkers previously noted that a moisture content of less than 5% is acceptable in the pharmaceutical industry (Omwoyo et al., 2014). A low moisture content is desirable as excessive moisture content can adversely impact the stability of the pharmaceutical product by altering critical parameters such as the crystal structure, chemical stability, and degradation rate. The second stage of the mass loss corresponding to the main thermal degradation region where the peptide bonds break was observed at a similar region: 286°C, 282°C, 280°C and 284°C for elastin, gelatin, non-crosslinked Ge-Ela gel and crosslinked Ge-BDDE-Ela hydrogel. This observed similarity indicates preservation of native polymer properties throughout processing and hydrogel formation. Mean brain temperature readings assessed in resting clinical patients were noted at 36.9 ±0.4°C in normothermic groups (Soukup et al., 2002). The addition of BDDE contributed to improved thermal stability of the hydrogel at the physiological temperature range of brain tissue.

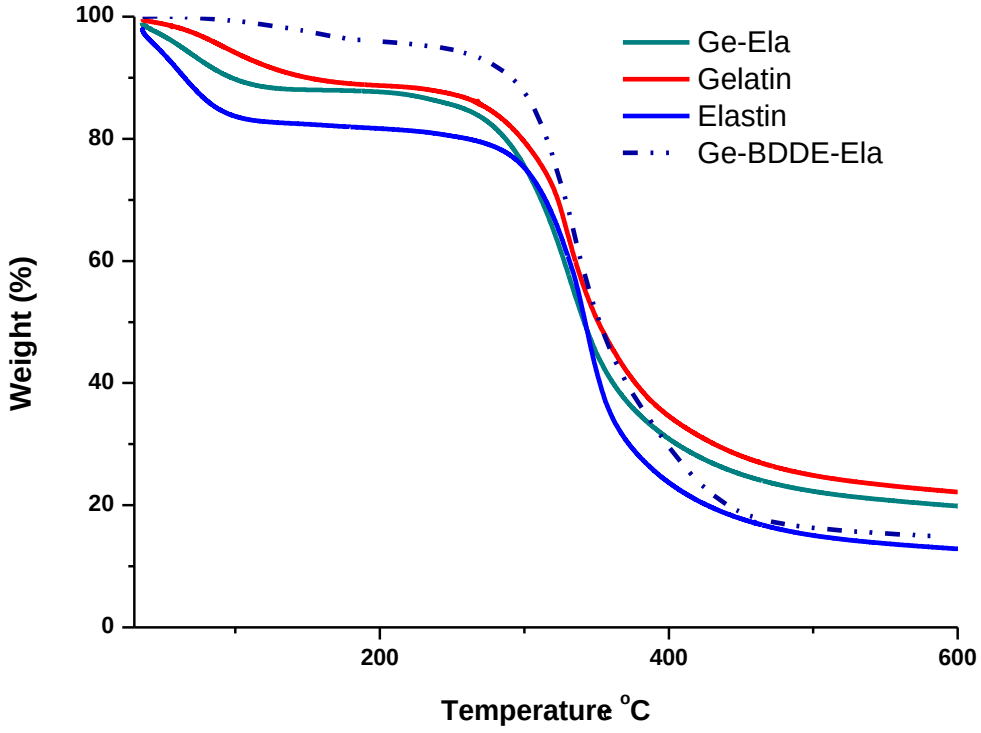

Figure 4.3. Thermogravimetric analysis (TGA) thermograms of Gelatin, Elastin, Ge-Ela gel and crosslinked Ge-BDDE-Ela hydrogel.

4.3.1.4. Differential scanning calorimetry

Thermal properties of the hydrogel were analyzed by DSC (Figure 4.4). For gelatin, an endothermic peak at 118°C was noted ascribed to protein degeneration caused by overlapping processes such as gelatin dehydration, melting of the triple-helix crystalline structure associated with the hydrogen bond breakage, random recombination of triple helix, melting and recrystallization of crystallites and glass transition of α-amino acid blocks in the polypeptide chain (Shehap et al., 2015; Zhan et al., 2016). Another two successive endothermic peaks are located at 223°C and 278°C respectively. The endothermic peak at 223°C is the decomposition temperature of gelatin (imino acids, proline, hydroxyproline with glycine) (Shehap et al., 2015). The DSC curve of gelatin also showed an exothermic peak at about 283°C, which may be attributed to the disintegration of intermolecular side chain (Shehap et al., 2015). Elastin exhibited peaks at 109°C and 210°C onward. Water loss is observed in all sample but to a lesser degree in the crosslinked hydrogel as previously noted with TGA observations.The non-crosslinked hydrogel exhibited a thermogram exhibiting both features of elastin and gelatin with an endothermic peak at 107°C and a high denaturation temperature of 215°C. The crosslinked hydrogel exhibits an exothermic peak at 167°C indicating the change in phase after crosslinking. This is also noted with the shift in XRD peaks indicating a different type of crystal form with different D-spacing within the crystal lattice post crosslinking and hydrogel formation.

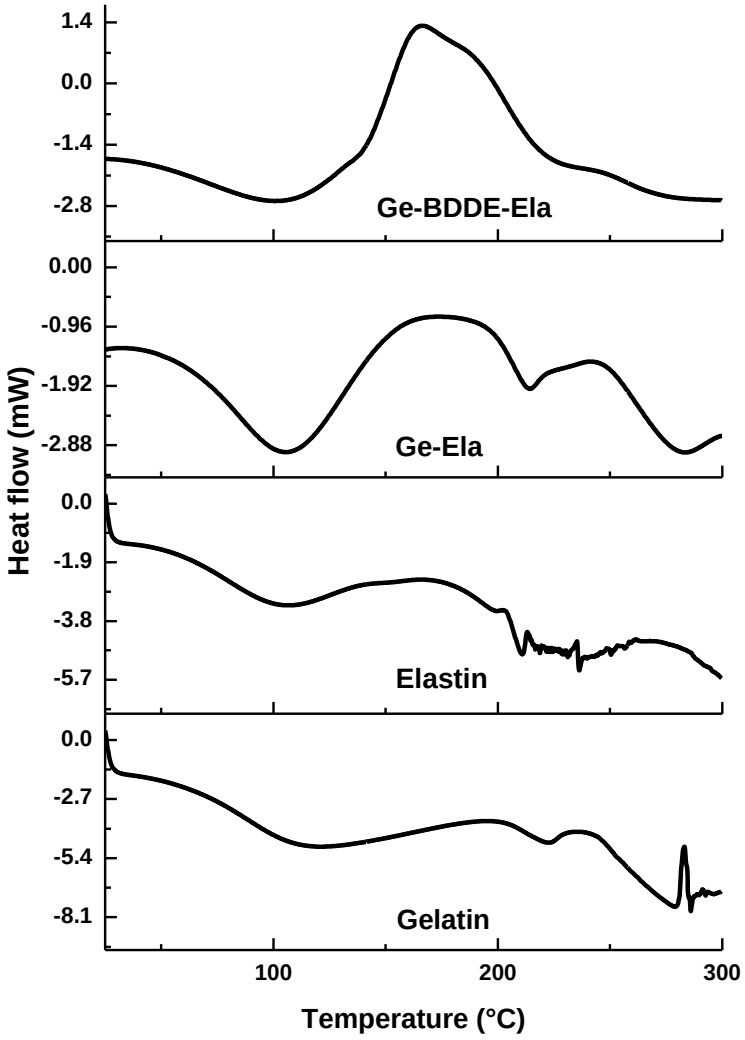

Figure 4.4. Differential Scanning Calorimetry (DSC) curves of gelatin, elastin, uncrosslinked gel (Ge-El) and crosslinked hydrogel (Ge-BDDE-Ela).

4.3.1.5. Swelling characteristics of the hydrogels

Swelling ratio is a simple method to characterize the water absorption and potential aqueous stability of a biomaterial. This is important as the brain is a highly hydrated soft tissue. Gelatin based hydrogels are noted to have poor stability in water and physiological temperatures 37°C. All non-crosslinked gels (gelatin only and Ge-Ela gels) solubilized completely. Cross-linked polymers were insoluble in the aCSF solvents because the polymer chains are tied together by strong covalent bonds. This further indicates the successful crosslinking noted with FTIR (Figure 4.1). Using BDDE as a crosslinker was effective in making the gelatin based hydrogel stable at *in vitro* simulated physiological conditions (aCSF, 37°C). As shown in Figure 4.5, the swelling degree was observed in the following order: hydrogel 10:1 > Ge-BDDE only

> hydrogel 4:1 ratio. The incorporation of elastin yielded interesting results. The ratio of 10:1 contains a lesser amount of the crosslinkable polymer gelatin compared to the Ge-BDDE hydrogel, and thus presented a more permeable polymer network evidenced by the faster and higher swelling ratio. In contrast, the hydrogel with the 4:1 ratio of gelatin:elastin displayed the lowest mass swelling ratio. Surprisingly, this hydrogel was formed by a lesser concentration of cross-linkable polymer gelatin however still presented with the lowest swelling ratio. This can be explained by the higher amounts of elastin, the non-polar amino acids, of the elastin may have further contributed to the blocking of pores and exclusion of water uptake. This curious outcome was also noted by Byju and co-workers (Byju et al., 2013). This is a noteworthy difference in the swelling properties of the hydrogels, indicative of the degree of tunability of the swelling properties of the scaffold through crosslinking (prevent immediate solubilisation) and composition. Therefore the ability to fine-tune swellability in the fabrication process enables adaptations to the formulation of this hydrogel for application as a scaffold implant in a hydrated tissue (brain tissue). Depending on the target tissue, swelling ratios of scaffolds can be tuned as per the design requirements for the target tissue application. High water content of hydrogel systems make them suitable for tissue engineering applications by providing a highly permeable environment for the diffusion of nutrients, metabolic waste and oxygen. Alternatively, limited swelling may be favorable too for application in brain tissue environments which are highly hydrated (80% water (Mahumane et al., 2018)). The limited swelling of the 4:1 Ge-BDDE-Ela hydrogel herein will avoid excessive swelling, thus avoiding increasing the interstitial pressure at the brain injury site post implantation.

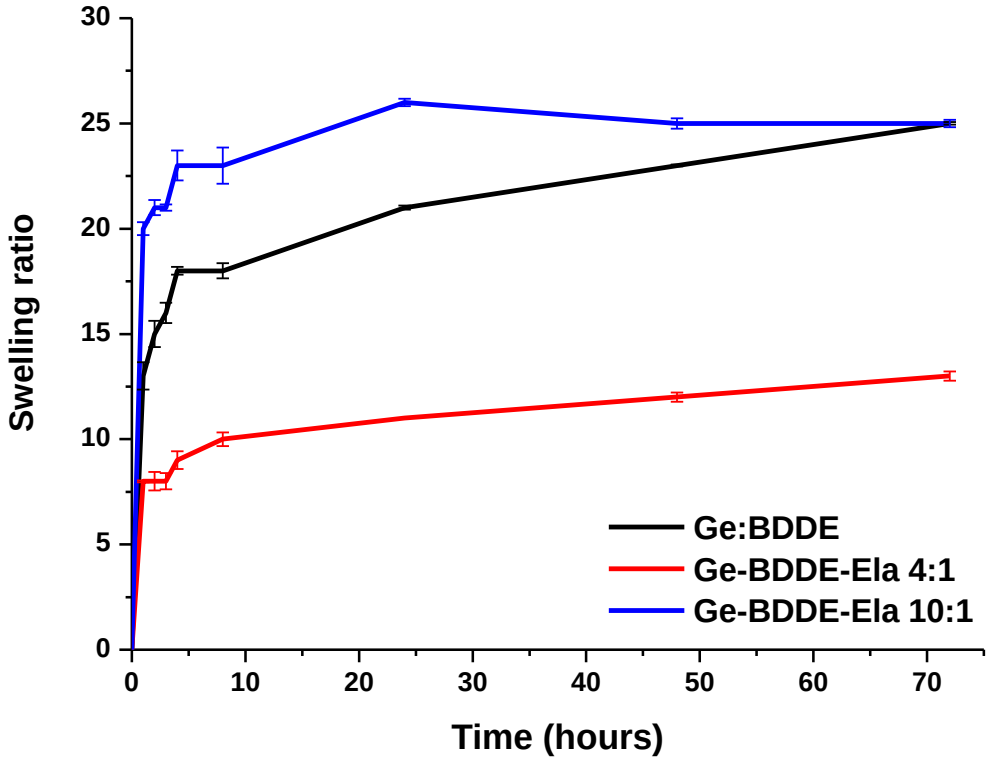

Figure 4.5. Swelling ratios of the hydrogels in aCSF.

4.3.1.6. Mechanical analysis of Ge-BDDE-Ela hydrogel

Rheological measurements were aimed at characterizing the mechanical behavior of the hydrogel in for comparison with CNS tissue behavior previously noted in literature. The hydrogels were soft with a storage moduli not exceeding 362Pa and 180Pa for the 4:1 and 10:1 Ge-Elastin ratios respectively (Figure 4.6a,c). It was initially hypothesized that the addition of elastin would result in a more elastic behaviour, indeed the increased content of elastin resulted in a more pronounced elastic behaviour in the 4:1 Ge-BDDE-Ela gel versus the 10:1 Ge-BDDE-Ela hydrogel. Frequency sweep test (within the linear viscoelastic region) was used to determine the material frequency dependence (Figure 4.6a). A high frequency region corresponds to rapid motion while a low frequency zone mimics long term behavior. The hydrogels typically exhibited solid-like behavior, elastic behavior was constantly dominant, i.e., G′ > G” (Figure 4.6a,c). This indicates that the elastic region is always dominant when force load is applied. The decreasing G", with an increasing G' at high frequencies indicated a decreasing loss tangent, and thus a highly elastic response for at high frequencies. This behavior was previously noted on brain tissue (Bilston et al., 2001; Lu et al., 2006). The hydrogels exhibited a similar pattern to previously determined behavior for brain tissue (Bilston

et al., 2001; Galford and McElhaney, 1970): a constant near stable/constant G* and a η* that increases with decreasing frequency (Figure 4.6b,d)..

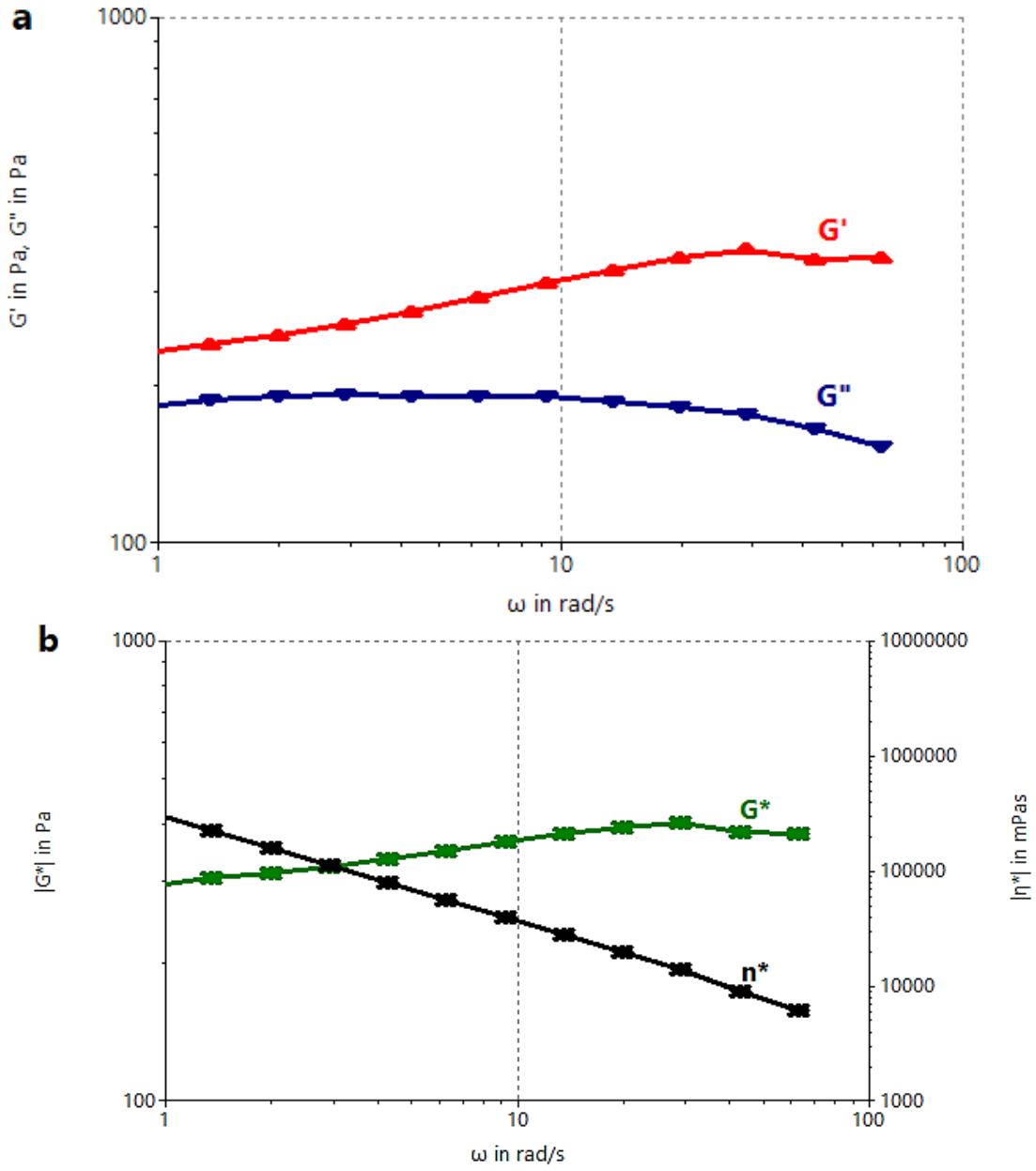

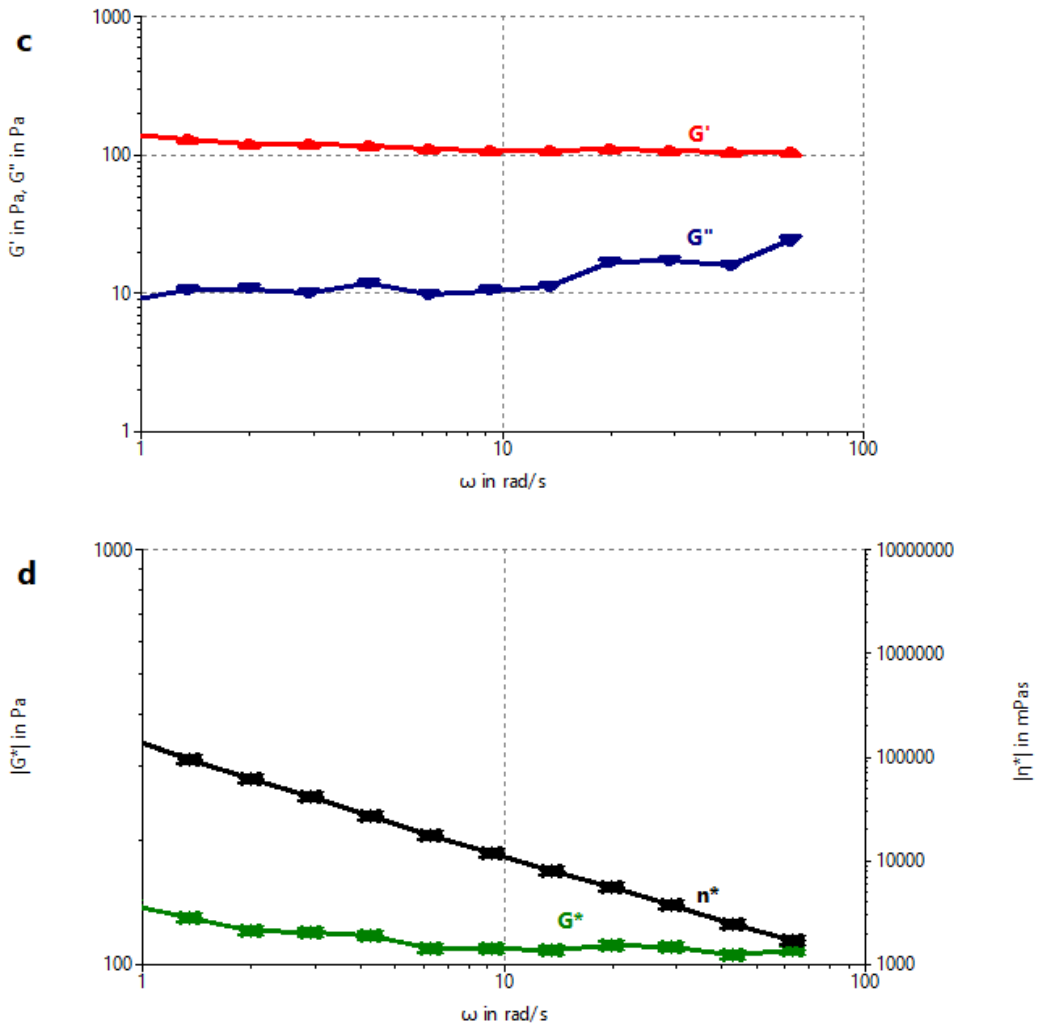

Figure 4.6. The Rheological mechanical properties of the hydrogels (a, c) dynamic moduli, G′ and G″, as function of frequency for the Ge-BDDE-Ela hydrogel at 37 °C. (b, d) Linear material functions, G* and η*, of the Ge-BDDE-Ela: a constant G* and a η* that increased with decreasing frequency. a,b =4:1 Ge-Ela ratio and c,d= 10:1 Ge-Ela ratio.

4.4. Chapter four summary

In this chapter, we described the BDDE crosslinked gelatin-elastin hydrogel at a 4:1 Gelatin elastin ratio. Crosslinking with 1,4-butanediol diglycidyl ether imparted aqueous stability to the water soluble polymers for potential application in the highly hydrated brain tissue. The infrared spectroscopy confirmed the gelatin/elastin protein structures were not significantly altered during the cross-linking treatment, and the effective chemical crosslinking with BDDE. The TGA thermogram indicated that the addition of BDDE led to decrease in the moisture content contributing to potential greater pharmaceutical stability over time and an improved thermal stability of the hydrogel at the physiological temperature range (36.9 ±0.4°C) of brain tissue as observed by TGA. Swelling ratios were tunable based on the gelatin-elastin ratio. The hydrogel design may serve as a prototype for future composites that will combine the benefits of gelatin and elastin for tissue engineering applications targeting various soft tissues (e.g.

pulmonary tissues, bold vessels, cardiac tissue). However, for the purpose of this study, the limited swelling of the 4:1 hydrogel herein is desirable for application in the hydrated brain tissue to avoid further increasing potentially damaging pressure to the surrounding structures at the injury site post implantation. The effect of the hydrogel on neural cell line (PC12 and A172) viability and proliferation is discussed in the next Chapter (Chapter five).

4.5. References

Alavijeh, R.Z., Shokrollahi, P., Barzin, J., 2017. A thermally and water activated shape memory gelatin physical hydrogel, with a gel point above the physiological temperature, for biomedical applications. 2302 | J. Mater. Chem. B 5, 2302–2302. https://doi.org/10.1039/c7tb00014f

Baiguera, S., Del Gaudio, C., Lucatelli, E., Kuevda, E., Boieri, M., Mazzanti, B., Bianco, A., Macchiarini, P., 2014. Electrospun gelatin scaffolds incorporating rat decellularized brain extracellular matrix for neural tissue engineering. Biomaterials 35, 1205–1214. https://doi.org/10.1016/j.biomaterials.2013.10.060

Bang, S., Das, D., Yu, J., Noh, I., 2017. Evaluation of MC3T3 cells proliferation and drug release study from sodium hyaluronate-1,4-butanediol diglycidyl ether patterned gel. Nanomaterials 7, 328. https://doi.org/10.3390/nano7100328

Bilston, L.E., Liu, Z., Phan-Thien, N., 2001. Large strain behaviour of brain tissue in shear: Some experimental data and differential constitutive model. Biorheology 38, 335–345.

Binan, L., Tendey, C., De Crescenzo, G., El Ayoubi, R., Ajji, A., Jolicoeur, M., 2014. Differentiation of neuronal stem cells into motor neurons using electrospun poly-l-lactic acid/gelatin scaffold. Biomaterials 35, 664–674. https://doi.org/10.1016/j.biomaterials.2013.09.097

Boni, R., Ali, A., Shavandi, A., Clarkson, A., 2018. Current and novel polymeric biomaterials for neural tissue engineering | Journal of Biomedical Science | Full Text. Journal of Biomedial Science 25. https://doi.org/10.1186/s12929-018-0491-8

Byju, A.G., Kulkarni, A., Gundiah, N., 2013. Mechanics of Gelatin and Elastin based hydrogels as Tissue Engineered Constructs. Presented at the ICF13.

Campiglio, C.E., Contessi Negrini, N., Farè, S., Draghi, L., 2019. Cross-Linking Strategies for Electrospun Gelatin Scaffolds. Materials 12, 2476. https://doi.org/10.3390/ma12152476

De Boulle, K., Glogau, R., Kono, T., Nathan, M., Tezel, A., Roca-Martinez, J.X., Paliwal, S., Stroumpoulis, D., 2013. A review of the metabolism of 1,4-butanediol diglycidyl ether-crosslinked hyaluronic acid dermal fillers. Dermatologic Surgery. https://doi.org/10.1111/dsu.12301

Dias, J.R., Baptista-Silva, S., Oliveira, C.M.T. de, Sousa, A., Oliveira, A.L., Bártolo, P.J., Granja, P.L., 2017. In situ crosslinked electrospun gelatin nanofibers for skin regeneration. European Polymer Journal 95, 161–173. https://doi.org/10.1016/j.eurpolymj.2017.08.015

Galford, J.E., McElhaney, J.H., 1970. A viscoelastic study of scalp, brain, and dura. J Biomech 3, 211–221. https://doi.org/10.1016/0021-9290(70)90007-2

Klimek, K., Ginalska, G., 2020. Proteins and Peptides as Important Modifiers of the Polymer Scaffolds for Tissue Engineering Applications—A Review. Polymer 12. https://doi.org/10.3390/polym12040844

Kornev, V.A., Grebenik, E.A., Solovieva, A.B., Dmitriev, R.I., Timashev, P.S., 2018. Hydrogel-assisted neuroregeneration approaches towards brain injury therapy: A state-of-the-art review. Computational and structural biotechnology journal 16, 488–502. https://doi.org/10.1016/j.csbj.2018.10.011

Lampe, K.J., Antaris, A.L., Heilshorn, S.C., 2013. Design of three-dimensional engineered protein hydrogels for tailored control of neurite growth. Acta Biomaterialia 9, 5590–5599. https://doi.org/10.1016/j.actbio.2012.10.033

Leach, J.B., Wolinsky, J.B., Stone, P.J., Wong, J.Y., 2005. Crosslinked α-elastin biomaterials: Towards a processable elastin mimetic scaffold. Acta Biomaterialia 1, 155–164. https://doi.org/10.1016/j.actbio.2004.12.001

Lee, J., Cuddihy, M.J., Kotov, N.A., 2008. Three-Dimensional Cell Culture Matrices: State of the Art. Tissue Engineering Part B: Reviews 14, 61–86. https://doi.org/10.1089/teb.2007.0150

Lu, Y.-B., Franze, K., Seifert, G., Steinhäuser, C., Kirchhoff, F., Wolburg, H., Guck, J., Janmey, P., Wei, E.-Q., Käs, J., Reichenbach, A., 2006. Viscoelastic properties of individual glial cells and neurons in the CNS. PNAS 103, 17759–17764. https://doi.org/10.1073/pnas.0606150103

Mahumane, G.D., Kumar, P., Du Toit, L.C., Choonara, Y.E., Pillay, V., 2018. 3D scaffolds for brain tissue regeneration: Architectural challenges. Biomaterials Science 6, 2812–2837. https://doi.org/10.1039/c8bm00422f

Martucci, J.F., Espinosa, J.P., Ruseckaite, R.A., 2015a. Physicochemical properties of films based on bovine gelatin cross-linked with 1,4-butanediol diglycidyl ether. Food and Bioprocess Technology 8, 1645–1656. https://doi.org/10.1007/s11947-015-1524-x

Martucci, J.F., Espinosa, J.P., Ruseckaite, R.A., 2015b. Physicochemical properties of films based on bovine gelatin cross-linked with 1,4-butanediol diglycidyl ether. Food and Bioprocess Technology 8, 1645–1656. https://doi.org/10.1007/s11947-015-1524-x

Morsy, R., 2016. Thermal Treatment of gealtin solution improves the quality of electrospun gelain fibrous mats for medical applicationsS. Romanian Journal of Biophysics 26, 83–92.

Mouw, J.K., Ou, G., Weaver, V.M., 2014. Extracellular matrix assembly: a multiscale deconstruction. Nat Rev Mol Cell Biol 15, 771–785. https://doi.org/10.1038/nrm3902

Nicoletti, A., Fiorini, M., Paolillo, J., Dolcini, L., Sandri, M., Pressato, D., 2013. Effects of different crosslinking conditions on the chemical–physical properties of a novel bio-inspired composite scaffold stabilised with 1,4-butanediol diglycidyl ether (BDDGE). Journal of Materials Science: Materials in Medicine 24, 17–35. https://doi.org/10.1007/s10856-012-4782-4

Omwoyo, W.N., Ogutu, B., Oloo, F., Swai, H., Kalombo, L., Melariri, P., Mahanga, G.M., Gathirwa, J.W., 2014. Preparation, characterization, and optimization of primaquine-loaded solid lipid nanoparticles. International journal of nanomedicine 9, 3865–74. https://doi.org/10.2147/IJN.S62630

Popescu, M.C., Vasile, C., Craciunescu, O., 2010. Structural analysis of some soluble elastins by means of FT-IR and 2D IR correlation spectroscopy. Biopolymers 93, 1072–1084. https://doi.org/10.1002/bip.21524

Shankar, K.G., Gostynska, N., Montesi, M., Panseri, S., Sprio, S., Kon, E., Marcacci, M., Tampieri, A., Sandri, M., 2017. Investigation of different cross-linking approaches on 3D gelatin scaffolds for tissue engineering application: A comparative analysis. International Journal of Biological Macromolecules 95, 1199–1209. https://doi.org/10.1016/j.ijbiomac.2016.11.010

Shehap, A.M., Mahmoud, Kh.H., Abd El-Kader, M.F.H., El-Basheer, T.M., 2015. Preparation and Thermal Properties of Gelatin/TGS Composite Films. Middle East Journal of Applied Sciences 5, 157–170.

Soukup, J., Zauner, A., Doppenberg, E.M.R., Menzel, M., Gilman, C., Young, H.F., Bullock, R., 2002. The importance of brain temperature in patients after severe head injury: relationship to intracranial pressure, cerebral perfusion pressure, cerebral blood flow, and outcome. J. Neurotrauma 19, 559–571. https://doi.org/10.1089/089771502753754046

Vargas, G., Acevedo, J.L., López, J., Romero, J., 2008. Study of cross-linking of gelatin by ethylene glycol diglycidyl ether. Materials Letters 62, 3656–3658. https://doi.org/10.1016/j.matlet.2008.04.020

Vindin, H., Mithieux, S.M., Weiss, A.S., 2019. Elastin architecture. Matrix Biol 84, 4–16. https://doi.org/10.1016/j.matbio.2019.07.005

Zeeman, R., Dijkstra, P.J., van Wachem, P.B., van Luyn, M.J., Hendriks, M., Cahalan, P.T., Feijen, J., 2000. The kinetics of 1,4-butanediol diglycidyl ether crosslinking of dermal sheep collagen. Journal of biomedical materials research 51, 541–8.

Zhan, J., Morsi, Y., Ei-Hamshary, H., Al-Deyab, S.S., Mo, X., 2016. In vitro evaluation of electrospun gelatin–glutaraldehyde nanofibers. Frontiers of Materials Science 10, 90–100. https://doi.org/10.1007/s11706-016-0329-9

CHAPTER FIVE

FABRICATION AND CHARACTERIZATION OF A NOVEL HYBRID 3-IN-1 NANO-REINFORCED HYDROFILLED CRYOGEL SCAFFOLD

5.1. Introduction

Patients urgently require new technologies and treatment options to counter the irreversible damage and loss of function resulting from neural tissue damage (Miller et al., 2018). To date there are no known effective therapies for the treatment of brain tissue injury. Tissue engineered three-dimensional (3D) scaffolds have shown various degrees of experimental success in augmenting cell survival. Scaffolds are designed to serve as temporary supportive constructs that augment the repair/regeneration process (Lee et al., 2008). In the body, cells reside in an extracellular matrix (ECM) comprising of a complex 3D fibrous network providing multiple biochemical and physical cues. As such, tissue engineered scaffolds are often designed to structurally mimic the *in vivo* stem cell nano/micro/macro-environment to augment cell survival and ultimately functional tissue repair (Hosseinkhani et al., 2014).

Scaffold systems (e.g. nanofibers, cryogels, hydrogels) though promising, present with various limitations that contribute to a lack of successful clinical translation. Hydrogels have remained the most popular of scaffold systems due in part to their three-dimensional (3D) architecture and mechanical properties that are similar to soft tissues (Li et al., 2019; Mahumane et al., 2018). However, hydrogels have poor architectural resilience. Cryogels have large interconnected pores to facilitate potential cell migration and surrounding tissue structure integration. However, the large cryogel pores may hinder 3D cell-cell interaction (Jurga et al., 2011a). Moreover, cryogels and hydrogels often require crosslinkers in their fabrication process which may result in toxicity. Fibrous structures such as nanofibers are explored in part because of their high surface area to volume ratio (large area for protein cell binding site presentation) and topographical and structural similarity to native ECM structures such as collagen, fibronectin and elastin fibres (Lee et al., 2017). However, generally, nanofibers lack the defined volume and encapsulating protective structure required to protect the cells from the harsh lesion environment (Li et al., 2019). This is in part because pores between nanofibers are often not accommodating to the size of cell and penetrating tissue structures to serve as an integrative protective scaffold.

Hybrid composite scaffolds may hold promise for addressing some of the deficiencies of previous biomaterials scaffolds for tissue engineering application. For example, combining the integrative (cells to be housed/localized inside the scaffold providing better physical protection from toxic environments and mechanical injury during implantation) properties of the hydrogel/cryogels with the high surface area, ECM mimetic nanoscale cell guiding and reinforcing properties of nanofibers.

To enhance biocompatibility and mimic the extracellular microenvironment, careful selection of scaffolding materials is required. These polymers used herein are FDA-approved and noted for their biocompatibility, biodegradability, and non-toxic properties (Lee et al., 2008; Hosseinkhani et al., 2014; Li et al., 2019). For example, hyaluronic acid is the main structural backbone of the brain ECM (Balashova et al., 2019; Bignami et al., 1993, p. 19). Hyaluronic acid has a desired high water retention and swelling capacity, to augment cell migration and attachment to the scaffold (Chang et al., 2013). Mounting literature has shown the potential neural tissue engineering application of poly (lactic-co-glycolic acid) (PLGA) (Lee et al., 2009; Mahumane et al., 2020; Zhou et al., 2018). Zhou and co-workers reported the proliferation, neural differentiation of mesenchymal stem cells, neuronal growth and migration on PLGA scaffolds (Zhou et al., 2018). N-acetylcysteine incorporated into the nanofibers may offer therapeutic aid against oxidative stress. Mahumane and co-workers previously noted an increase in PC12 and A172 cell viability and proliferation in NAC loaded PLGA nanofibers in comparison to NAC-free PLGA nanofibers (Mahumane et al., 2020). The proteins, polylysine, gelatin, and elastin were selected to facilitate cell attachment and augment the physicomechanical properties of the scaffold. Positively charged polymers like polylysine are routinely used in neural cell culture to aid cell attachment (Pedron and Harley, 2019; Tian et al., 2005). Moreover, PLL has been noted to possess a wide range of antimicrobial spectrum (both gram positive and gram negative bacteria, yeast, fungi, and phage) (Alkekhia and Shukla, 2019; Liu et al., 2015; Chen Shi et al., 2015; Tan et al., 2019). Its antimicrobial activity is linked to the electrostatic adsorption to the cell surface which strips the outer membrane causing abnormal distribution of the cytoplasm and ultimate physiological cell death (Chen Shi et al., 2015). Gelatin, contains amino acid sequences, such as the arginine-glycine-aspartic acid (RGD) on its surface which provides an adherent surface for cells, thereby potentially enhancing cell attachment (Chang et al., 2013; Kumari and Kumar, 2017). The biocompatibility and biodegradability of these materials (MMP sensitive moiety on gelatin (Pedron and Harley, 2019)) make them very attractive materials for the fabrication of drug delivery systems. This biodegradability is ideal as it facilitates the efforts of cells during neo-tissue formation. This enables the cells to remodel the scaffold by breaking down or adding new ECM elements. However, the degradation rate needs to be controlled to accommodate the duration of this

process. This is because brain tissue comprises approximately 80% water (Aurand et al., 2012b) and these polymers (e.g. PLGA, hyaluronic acid, gelatin) are subject to hydrolytic degradation. Therefore, for scaffolding purposes, the solubilisation rates of the scaffold in physiological media need tight control. Crosslinking is effective in retarding hydrolytic degradation, which rapidly takes place in biological environments (Lan et al., 2015). Moreover, crosslinking enables some control over the structural (porosity) and mechanical properties of the scaffold. 1,4-Butanediol diglycidyl ether (BDDE, a homobifunctional crosslinker) reacts with nucleophiles in the protein and polysaccharide components of the polymers under basic conditions. 1,4-Butanediol diglycidyl ether crosslinked hyaluronic acid has been approved by the US Food and Drug Administration (FDA) as a soft tissue filler. The stability, biodegradability and a long safety record has spanned for over 15 years (Yang et al., 2016). Lan and co-workers investigated the perineural toxicity profile BDDE-crosslinked HA, using *in vitro* and *in vivo* experiments in a rat model (Lan et al., 2015). Experiments showed that BDDE-crosslinked HA was not toxic to the smooth muscle cells, vascular endothelial cells, Schwann cells, fibroblasts, and neuronal cells (Lan et al., 2015). However, the safety of BDDE crosslinker has not been carefully evaluated in the context of central nervous system application. In this study we also investigated the potential application of BDDE as a scaffolding crosslinker from *in vitro* assays on neuronal A172 and PC12 adherent cells and a follow-up *in vivo* study (Chapter six) will be conducted on Sprague-Dawley rats.

The native ECM is an interwoven matrix of fibres embedded in a hydrated gel like material (Lee et al., 2008). The unique heterogeneous composition of the ECM supplies an interplay of therapeutic, structural and chemical cues/functions that influence cellular organization (Lee et al., 2008; Mahumane et al., 2018). The aim of this chapter is to fabricate a scaffold that mimics the hierarchical, multiscale, hybrid, heterogenous, 3D ECM features using a combination of scaffold systems and composite biomaterials. The study proposes a novel 3-in-1 scaffold design wherein nanofibers are embedded into a cryogel matrix followed by filling with a hydrogel component (Figure 5.1), for potential application as a novel acellular implant to aid in neural tissue regeneration. This system is unique as it uses a combination of scaffold systems and composite biomaterials to capture the multi-scale, multi-porous (micro/meso/macro-porous), intricate hierarchical properties of native ECM (a key component of neural regeneration) in its design.

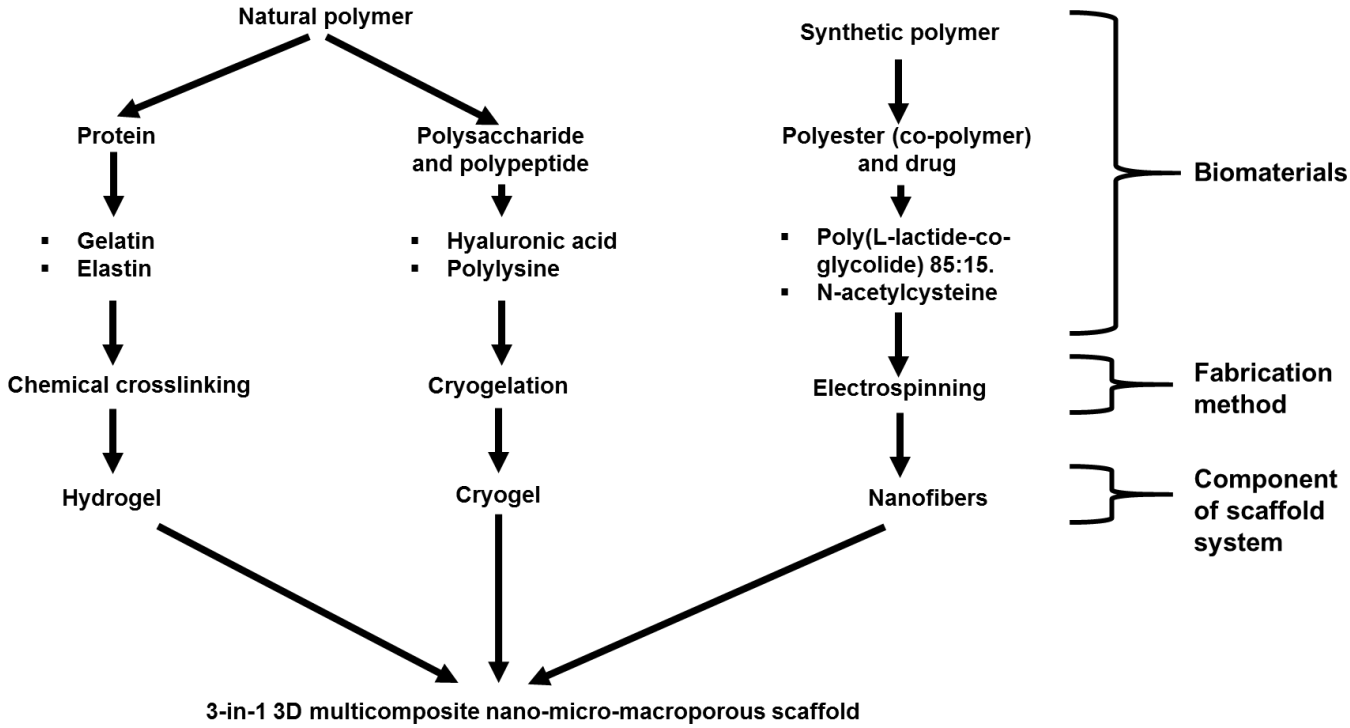

Figure 5.1. Schematic of the biomaterial composition and fabrication process and to achieve the proposed novel 3-in-1 scaffold.

5.2. Materials and methods

5.2.1. Fabrication of a novel 3-in-1 nano-reinforced, hydro-filled scaffold

Preparation of a nano-reinforced cryogel component

Polylysine hydrobromide (PLL, mol wt 30,000-70,000 Da; Sigma Aldrich, South Africa) was dissolved in deionized water (D/I). Hyaluronic acid (High molecular weight hyaluronic acid (HA) from *Streptococcus equi* (molecular weight 1.5-1.8 x10^6 Da; Sigma Aldrich) was added to the PLL solution and stirred until the HA was completely dissolved. The addition of HA to PLL resulted in the formation of an opalescent/milky solution, indicating polyelectrolyte complexation. Ratios of HA:PLL were varied at 10:1 and 4:1 relative to 4%(w/v) and 2%(w/v) HA concentrations. Thereafter the HA/PLL solution was adjusted to pH 13 using NaOH. Then BDDE (hydrophilic crosslinker with short length) was added to the alkaline HA/PLL solution and mixed for a further 15minutes to form a HA/PLL/BDDE gel solution. The nanofibers (Previously described in chapter three) were cut into 5mm X 5mm lengths and suspended in the HA/BDDE/PLL gel. The mixtures were then transferred to well plates and subjected to cryogelation for polymerization to take place over 96 hours at a temperature of -20°C. To prepare hydro-filled scaffolds, lyophilized nano-reinforced cryogels were submerged into the Ge-BDDE-Ela hydrogel solution (at the 4:1 gelatin;elastin ratio previously described in Chapter four) solution for a period of 48hours for the hydrogel solution to fill the porous nano-reinforced cryogel scaffold while crosslinking and gelation simultaneously occurred. After the reaction

was complete, the scaffold was neutralized by adding an equivalent amount of 0.1M HCl to a pH of approximately 7.0. Thereafter, dialyzed (Membra-Cel MD 34-14 x 100CLR, nominal dry flat width: 34 mm, dry diameter: 22 mm. (Viskase Corporation, Chicago, USA)) against PBS then distilled water to remove un-reacted components fragments and BDDE crosslinker residue. Thereafter, the scaffolds were frozen overnight at -80°C in preparation for lyophilisation (Freezone 12, Labcono, Kansas City, USA). Lyophilization is the process of preservation by removing water from the system (residual moisture may trigger hydrolysis) to low levels to increase stability and shelf life. Finally, the scaffolds were stored at 8°C until the characterization studies were carried out.

5.2.2. Characterization of 3-in-1 scaffold

FTIR, DSC, XRD, Rheology and TGA analysis were performed as described in Chapter three.

5.2.3. Mechanical and swelling ratio and mass loss

Compressive mechanical properties were carried out using a Texture analyser (TA.XTplus texture analyser, Stable Microsystems, Surrey, UK). Unconfined compression was carried out at a rate of 1mm/min (Tan et al., 2018a; Wang et al., 2018) at room temperature. Cyclic compression tests were conducted at a constant crosshead speed of 1mm/min. The compression modulus, was determined as the initial linear slope of the stress−strain curve, where the stress= F(compressive force applied)/$A_{0\ (}$initial surface area$_{)}$ and the strain= ΔL (change in height)/L_0 (initial sample height) are defined with respect to the initial dimensions of the sample. The swelling properties of the scaffolds was determined by immersion in 4mL PBS (pH=7.4) in an orbital shaking incubator (LM-530-2, MRC Laboratory Instruments Ltd., Hahistadrut, Holon, Israel) maintained at 37°C set at 50rpm for sample agitation. Scaffolds were allowed to reach equilibrium swollen state in 24 hours and excess liquid was removed with absorption paper. The weight of the scaffolds was measured at predetermined intervals and the change in mass was measured for the determination of swelling ratio after carefully blotting the hydrated samples with tissue paper for the removal of excess water. The swelling ratio was determined as follows: Swelling ratio = (W_h-W_0), where W_0 represents the initial mass of the lyophilised scaffold, W_h represents the mass of the swollen scaffold (Al-Sibani et al., 2016). Percentage mass loss was determined for the scaffold to access potential stability in aqueous media over a period of time. The scaffold obtained after lyophilisation were weighed to determine the initial dry weight (W0), placed in aCSF, and gently shaken at 37 °C for 24 h. Then, the samples were vacuum air dried at room temperature for 72hours to determine the final dry weight (Wf). The percentage mass loss was calculated as described by Ginjupalli and coworkers (Ginjupalli et al., 2014) as follows: mass loss percentage (%) = (W0-Wf)/W0×100 %. The measurements of each gel sample were performed in triplicate.

5.2.4. Cytotoxicity: PC12 and A172 cell culture and MTT assay

Rat adrenal gland pheochromocytoma PC12 mixed adherent cell line from Cellonex (Separations, South Africa) was cultured in tissue culture treated (TPP) T-75 flasks using DMEM supplemented with 10%v/v DES, 5%v/v FBS and 1%v/v P/S/AB solution in a humid 5% CO_2 atmosphere at 37˚C. The culture medium was replaced every 48 hours. The A-172 cell line purchased from Cellonex (Separations, South Africa) was cultured in tissue culture treated (TPP) T-75 flasks using DMEM supplemented with 20%v/v FBS and 1%v/v P/S/AB solution in a humid 5% CO_2 atmosphere at 37˚C. The culture medium was replaced every 48 hours.

The MTT assay was used (MTT-based Roche Cell Proliferation Kit I was utilised) to quantitatively measure cell death during cell culture which is crucial in determining the cytotoxic effects of the biomaterial scaffold prior to implantation. The commonly used viability assay is the MTT assay. The MTT assay is based on calorimetric principles, using the reduction of a yellow tetrazolium salt (3-(4,5-dimethylthiazol-2-yl)-2,5-diphenyltetrazolium bromide, or MTT) to measure cellular metabolic activity as an indicator for cell viability. Viable cells contain NADP(P)H-dependent oxidoreductase enzymes which reduce the MTT reagents to formazin. Formazin is an insoluble crystalline product with a deep purple colour. Formazin crystals are then dissolved using a solubilizing solution and absorbance is measured at 590 nm using a plate-reader. The darker the solution the greater the number of metabolically active viable cells. Culture medium (100 µl) containing 10 000 cells/well were added to each well of a 96-well plate and incubated for 24 hours at 37˚C at 5% CO2 to allow the cells to attach to the well before treating with scaffolds. To treat the cells, scaffolds were sterilized under UV light and added into each well. The treatment (scaffold) was removed and 20µL of MTT solution (5 mg/ml in phosphate buffered saline) was added into each well followed by a further 4 hour incubation. Thereafter, the entire contents of the wells were removed leaving behind only the cells at the bottom of the well to which 100µL DMSO was added as a solubilising agent to dissolve the formazan crystals. This was followed by incubation at 37˚C for 24 hours to allow the cells to lyse and the purple crystals to fully dissolve. The supernatant in each well was transferred into another 96-well plate to avoid inaccuracy in results resulting from fragments of the scaffold and debri in the wells. Absorbance was measured at 570nm with a background subtraction at 690nm using a multi-plate reader (Biotek USA). The absorbance reading of the blank (690nm) was subtracted from all the samples. Percentage viability/proliferation was determined by dividing the absorbance reading of the test samples by the control and multiplying by 100 (**Equation 4**). Absorbance values greater than the control indicate cell proliferation, while lower values suggest cell death or inhibition

Equation 4: $\%\ viable\ cells\ = 100 \times \frac{(Sample\ absorbance - Blank\ absorbance)}{(Control\ absorbance - Blank\ absorbance)}$

5.3. Results and discussion

5.3.1. FTIR: Analysis of vibrational molecular changes of the chemical constituents and 3-in-1 scaffold

Hyaluronic acid is unable to form stable hydrogels without modification. Mutliple strategies can be used to modify HA based systems for potential biomedical applications. Polyelectrolyte complexes and chemical crosslinking are such examples. Polyelectrolyte complexes are formed by interactions between oppositely charged polymers (Hahn and Hoffman, 2005; Lankalapalli and Kolapalli, 2009). Hyaluronic acid is a polyanion and polylysine is a polycation, their opposite charges enable electrostatic interaction between them avoiding the need for chemical crosslinking (reducing resultant toxicity) (Hahn and Hoffman, 2005; Lankalapalli and Kolapalli, 2009). The electrostatic interactions occur between the positively charged primary amine groups of PLL (pKa = ~10.5) and the negatively charged carboxyl of the HA (pKa = 2.9) (Amorim et al., 2014; Prokopović et al., 2015) Hyaluronic acid and PLL make weak electrolytes and hydrogels (e.g. their physicochemical properties may be altered by the surrounding medium) (Tračuma and Loca, 2020).Therefore BDDE was added as a chemical crosslinker to stabilise the complex further. The iso-electric point of the lysine residues is roughly in the range pKa 10 and 11 pKa. This means that a large population of lysine amino groups would no longer be positively charged (Koh, 2013), therefore crosslinking at a high alkaline pH in this study would work. Cross-linking of poly-l-lysine using a BDDE may involve the addition reaction of epoxide groups with amine groups of lysine residues under alkaline conditions yielding a secondary amine and hydroxyl group. 1,4-Butanediol diglycidyl ether is a homobifunctional crosslinker, it has two identical reactive epoxide ends. The epoxide rings open to crosslink molecules containing nucleophiles such as amines, sulfhydrals, hydroxyls, resulting in secondary amine, thioether and ether bonds respectively (Hermanson, 2013; Zeeman et al., 1999). Because it is a homobifuntional crosslinker, it is anticipated in this study that one end of the epoxide reacts with the HA to from ether linkages. The additional epoxide may be used to couple to the amine of the poly-l-lysine, thus aiding in the covalent bonding of HA (HA/BDDE/poly-l-lysine).

Fourier-transform infrared spectroscopy analysis was used as a tool to investigate the molecular composition and occurrence of interaction/complexation between the polymer matrices (Figure 5.2). The NAC-loaded PLGA nanofibers and Ge-BDDE-Ela hydrogels and their components were discussed in Chapter three and Chapter four of this thesis,

respectively. They were added herein to substantiate the composition and observed spectrum of the scaffold.

The FTIR spectrum of HA, indicated peaks in the regions 3259, 2882, 1604, 1556, 1400, and 1024cm^{-1} due to O–H/N–H bond, stretching SP^3 hydrocarbon C-H bond, C=O bond, amide-II, C-O bond of –COONa group, and C-O-C bond stretching vibrations, respectively. The peaks at 1377 and 946cm-1 were due to the vibrations of C-H bending and C-O-H deformation respectively. This was congruent with literature observations (Abu Elella et al., 2018; Bang et al., 2017; Chang et al., 2013; Thomas et al., 2017). 1,4-Butanediol diglycidyl ether is a zero-length crosslinker. It contains epoxy groups on both sides enabling it to function as a homobifunctional crosslinker that can react with nucleophiles such as amino groups, hydroxyls and sulfhydryls (Khunmanee et al., 2017; Okay, 2014). In the FTIR spectrum of BDDE (Figure 5.2), the characteristics peaks at 2931, 2869, 1254, 1102, and 911 cm^{-1} were responsible for C-H stretching of the epoxy ring, C-H stretching -CH_2 bond, C-C bond, C-O-C stretching, and C-O stretching vibrations of epoxy ring, respectively (Bang et al., 2017).

In the FTIR spectrum of the 3-in-1 scaffold, some bands were noted to have shifted, the intensities of some of the bands have decreased, other absorption peaks overlap (e.g. the existence of amide groups in gelatin and ester bonds in HA) and some have disappeared with the blend of the polymer systems in comparison to the pure polymers. This suggests coordination/interaction between the composite polymer systems. (Figure 5.2). Carbonyl stretching is observed in the region 1750cm^{-1}, indicating the presence of the ester group of the PLGA nanofibers embedded within the scaffold. The 3-in-1 scaffold exhibited C=O stretching at 1643cm^{-1}, N-H stretching at 1540cm^{-1}, C-N stretching at 1387cm^{-1} and N-H bend at 1241cm^{-1}, similar to the native proteins. This indicates that the process of scaffold formation did not significantly change the chemical structure of gelatin or elastin molecules. A significant signal increment was noted in the Amide A region ranging from 3200-3500cm^{-1} (attributed to the intermolecular bonded hydroxyl group and the stretching of N-H bond) and 1081 cm-1 related to C-O stretching could be attributed to the appearance of new OH groups and the transformation from primary to secondary amino groups (protein-BDDE crosslinking (Martucci et al., 2015)). The epoxy amine reaction results in the appearance of secondary alcohol groups (Martucci et al., 2015). This may be indicative of the effective crosslinking of the proteins with BDDE. Increased peak intensity was noted in the regions 2871-2931cm^{-1}, which confirm the presence of the BDDE alkyl chains (C-H) stretching in the crosslinked scaffold. The merging of the peaks for C-O-C stretching vibrations of BDDE and HA moieties could be attributed to the broad high intensity peak observed in the region 1081cm^{-1}. In the spectrum of the 3-in-1 scaffold, the decrease of the peak for C-O bond (911cm^{-1}) of the epoxy ring may be indicative

of the reaction between -OH groups of HA and epoxy rings of BDDE (Figure 5.2) (Bang et al., 2017).

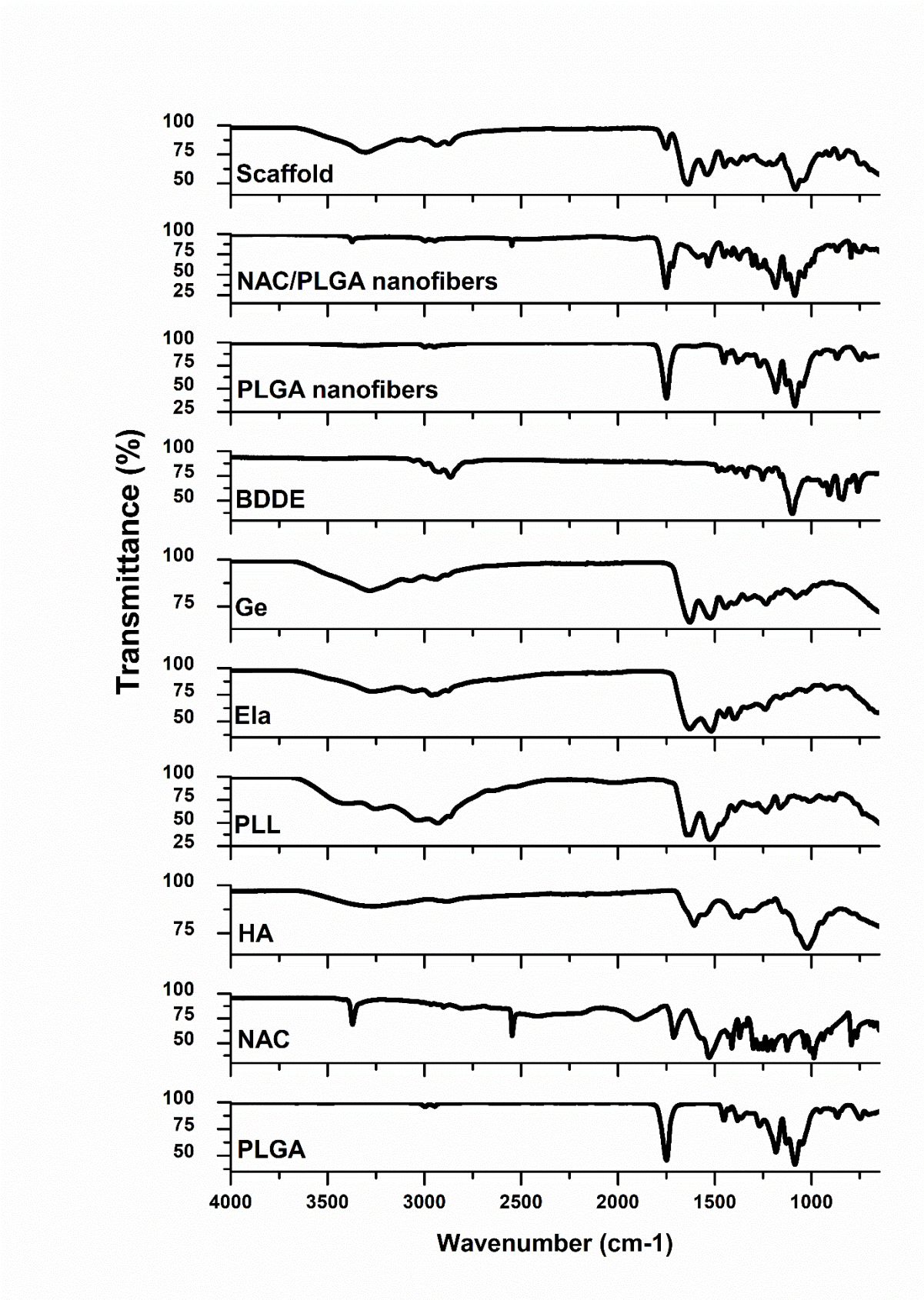

Figure 5.2. Spectra showing the FTIR spectra of the native materials and scaffold.

5.3.2. Thermogravimetric analysis

Thermogravimetric analysis was conducted to evaluate the thermal stability and extension of degradation effects during processing by comparing the component materials and the processed scaffold. Thermogravimetric analysis can also detect the moisture content (water or solvent). Initial weight percentage losses of 2%, 7%, 9% and 6% were observed for NAC-loaded PLGA nanofibers, HA, gelatin and elastin respectively up to ±145°C. This initial weight loss may be due to the loss of absorbed water/moisture evaporation (Figure 5.3). Low moisture content is desirable. This is partly because the having too much moisture in the system may directly impact the quality (stability and shelf life by triggering hydrolysis) over time. The HA curve presented ±66% weight loss. A sharp weight loss was observed between 234-270 °C, then relatively slow decomposition was noted between 271-600°C attributed to the complete breakdown of polysaccharide residue (Bang et al., 2017). The gelatin curve presented ±78% weight loss A sharp weight loss was observed between 278-373°C, then relatively slow decompositions are noticed between 374-600°C. This is congruent with literature observation (Biazar and Keshel, 2014). The elastin curve presented ±83% weight loss. A weight loss was observed between 218-377°C, then relatively slow decompositions are noticed between 378-600°C. This is congruent with literature observation (Samouillan et al., 1999). The PLGA curve presented a total weight loss. A sharp weight loss was observed between 287-372°C. The NAC curve presented ±84% weight loss. The NAC weight loss was observed between 170-600°C attributed to the elimination of organic matter. Two significant mass loss stages (168-245°C and 282-362°C) were observed for the NAC-loaded PLGA nanofibers which may be attributed to the presence of both NAC and PLGA in the nanofiber system. The second initial decomposition temperatures of NAC-loaded PLGA nanofibers is similar to that of bulk PLGA, indicative of the preservation of polymer (PLGA) thermal properties during nanofiber fabrication. The initial degradation temperature of NAC when loaded in the nanofibers is higher, suggesting an improvement in thermal stability in comparison to the drug alone. When the temperature reached 600°C, there was still some char content in the case of NAC-loaded nanofibers (±95% weight loss) but no char content left in the case of PLGA. This might be due to the difference in crystallinity/physical state of between NAC and PLGA. Increased stability may in part be due to the crystalline properties of the NAC within the fibres. This corroborates with the XRD findings exhibited in (Chapter three). The scaffold exhibited an initial weight loss pattern like its composite materials (hyaluronic acid, gelatin and elastin). This was a weight loss of ±8% from the initial temperature up to ±120°C. This moisture content is within the range observed for the native materials. The thermal degradation temperature for the composite scaffold was observed in the range 224-474°C. This range could be interpreted as a representative combination of its composites attributed to the early thermal decomposition of

composites with lower thermal stability (e.g. NAC) and composites with higher thermal stability (gelatin, PLGA). The temperature at which the scaffold was produced was below the degradation temperatures of its components, therefore it may be possible to conclude that the fabrication process did not induce significant composite material losses.

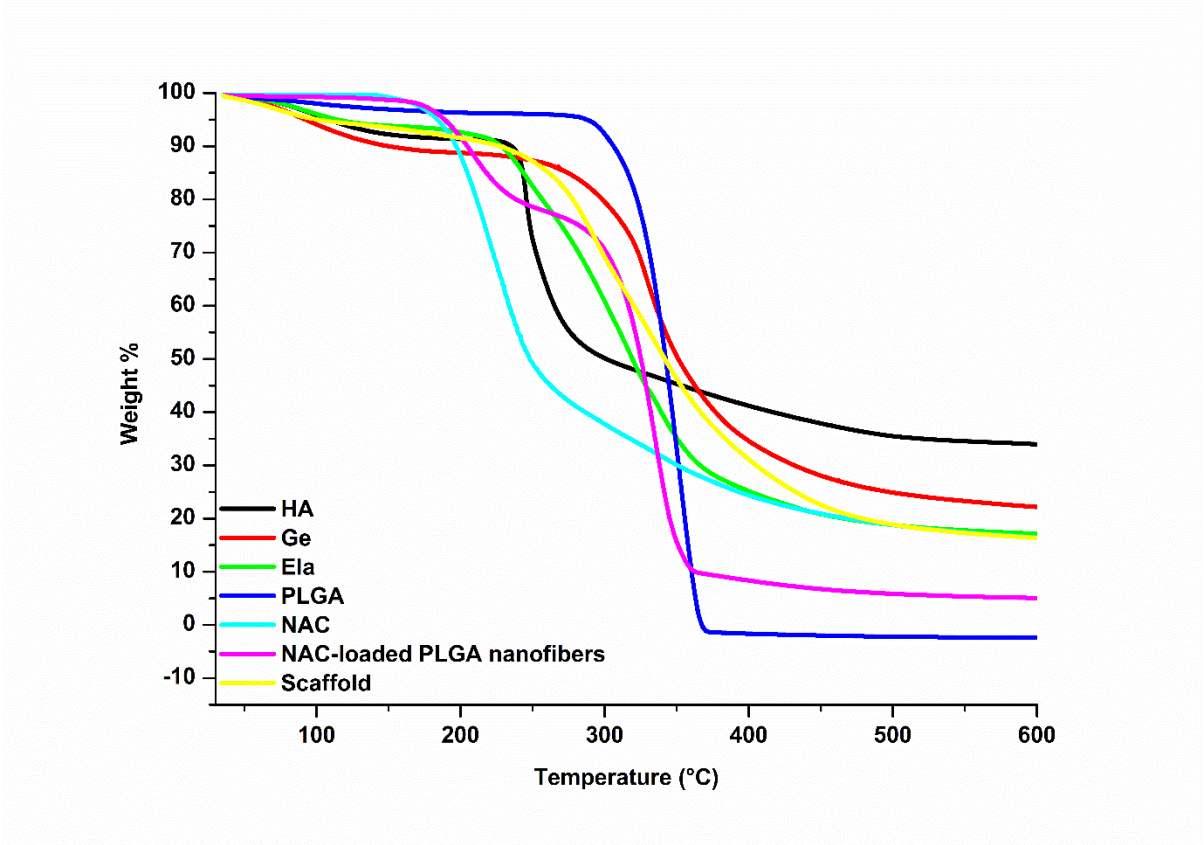

Figure 5.3. Thermogravimetric analysis curves of composite materials and scaffold.

5.3.3. XRD and Differential scanning calorimetry analysis

The XRD pattern of the scaffold is shown in Figure 5.4. Comparing the patterns, the 3-in-1 scaffold had a composition similar to the composite systems (nanofibers, hydrogel and cryogel). There was a broad peak at 2θ = ~20° among the patterns of the cryogel, hydrogel and nanofibers and the resultant 3-in 1 system (Figure 5.4a). This characteristic peak is assigned to the triple-helical crystalline structures of the proteins (e.g. gelatin, elastin), crystalline structure in hyaluronic acid. In the case of the proteins peaks from the cryogel and hydrogel components, these peaks could not be observed in the composite scaffold indicating that the systems were incorporated within the hyaluronic acid cryogel. From this we can infer that the crystallinity of the scaffold is mainly due to the major components of its composite systems (PLGA, HA, gelatin).

Figure 5.4b illustrates the DSC heating curves providing qualitative and quantitative data about the physical state of the scaffold components, the nanofibers and hydrogel components were discussed previously in chapters 3 and 4 respectively. Under nitrogen atmosphere, the HA curve showed two peaks. The first endothermic peak suggests that a dehydration process occurred at around 121 °C and the second was an exothermic peak at 238°C attributed to the decomposition of the polysaccharide resulting in a cabonized residue (Larrañeta et al., 2018; Shabani Ravari et al., 2016). This exothermic peak at 238°C is congruent with the observations from the TGA thermal profile of HA in Figure 5.3. An extrinsic transition (melting) is noted below 17°C, this is attributed to the amount of freezable water (bound water) in the protein (Samouillan et al., 2011) (elastin). The characteristic endotherm at 114°C attributed to the melting of NAC was absent in the scaffold. This could be attributed to 1) either the absence of NAC, or 2) the formation of a solid-solution or solid dispersion in the HA/PLL cryogel. What we can conclude is that, since the DSC thermograms of the NAC-loaded PLGA nanofibers embedded within the scaffold proved the incorporation of NAC, the absence of the melting endotherm of NAC cannot be attributed to the absence of NAC. Instead, the NAC may have merely dissolved in the liquified contents during heating (Mandal et al., 2002). The scaffold shows broad endothermic peaks at 101, 210, 274°C and a broad exothermic peak at 166°C. The endothermic peaks could be attributed to the combination of obscured peaks representative of overlapping processes, such as dehydration processes in the polymers and transitions in proteins (melting of the triple-helix crystalline structure associated with the hydrogen bond breakage, random recombination of triple helix, melting and recrystallization of crystallites and glass transition of α-amino acid blocks in the polypeptide chain). The broad exothermic peak at 166°C could be attributed in part to the shift in the degradation temperature of HA. These observations are congruent with the TGA thermal profile as a representative combination of its composites.

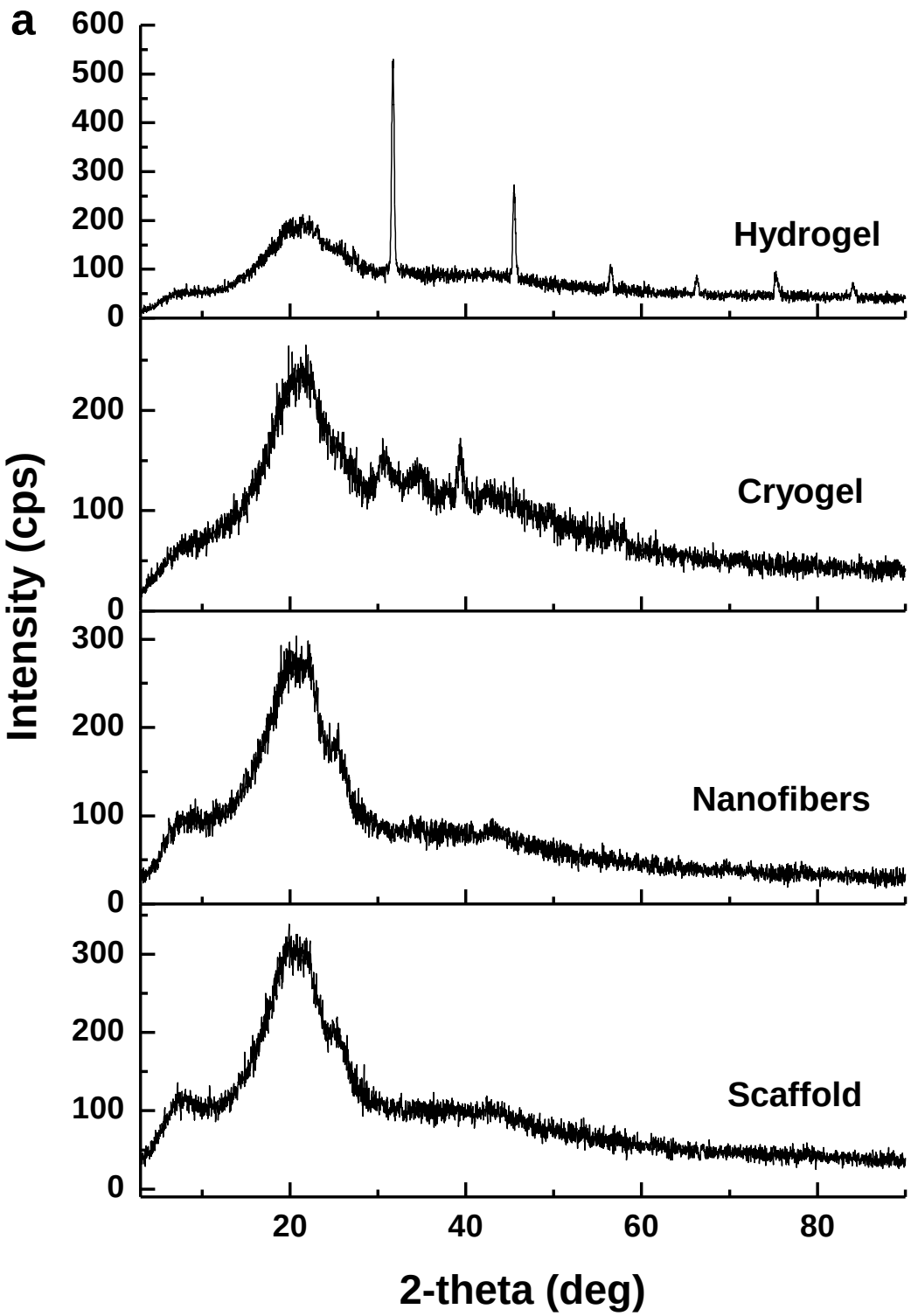

Figure 5.4. a) A comparison the X-ray diffraction patterns of the 3-in-1 scaffold (scaffold) and its composite systems (nanofibers, hydrogel and cryogel).

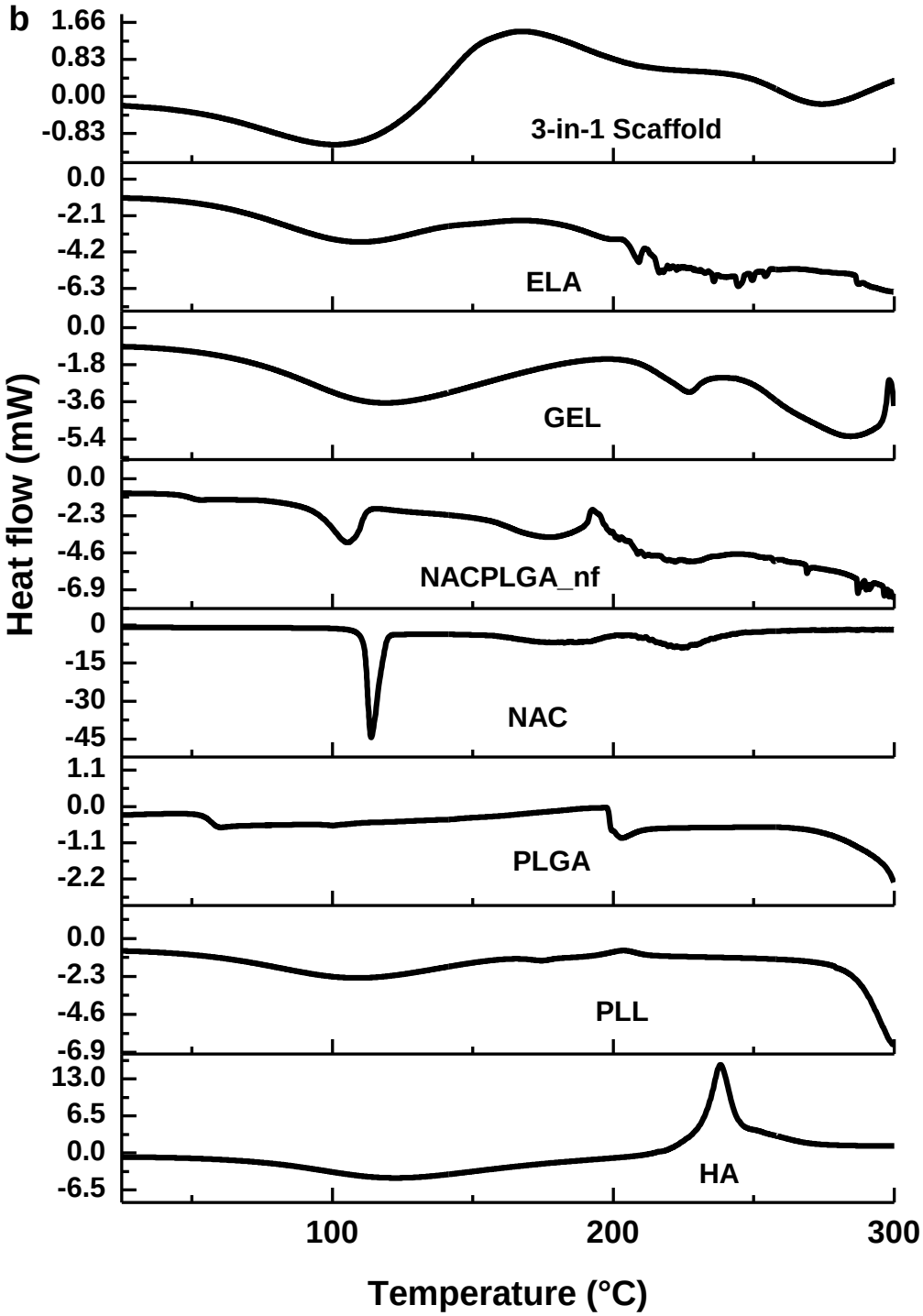

Figure 5.4. b) Differential Scanning Calorimetry (DSC) thermograms of hyaluronic acid (HA), gelatin (Ge), Elastin (Ela), polylysine (PLL), poly(lactic-co-glycolic acid) (PLGA), NAC-loaded nanofibers (NACPLGA) and the 3-in-1 scaffold recorded at 10 °C/min between 10°C and 300°C.

5.3.4. Morphology, swelling and morphological properties

The cryogel was obtained using the cryogelation method. Cryogelation occurred at subzero temperatures, this involved freezing the initial gel forming gel solution (HA, PLL and BDDE) and carrying out polymerization at temperatures below the freezing point of the solvent. In this particular study the solvent used was water (non-toxic porogen), the freezing point of water is 0°C. Therefore, polymerization was carried out at -20°C (20°C below the freezing point of water). During the cryogelation process, the solvent freezes (free from precursors/solute) while the precursor/solute concentrates the unfrozen liquid micro-phase (ULMP) (Kumar, 2016). The crystal formation of the solvent state defines the internal pore structures while ULMP is concentrated with the gel forming solution. Cryo-concentration results in the acceleration of the reaction due to the high concentration of precursors/solute in the ULMP. When the gel is thawed, the ice crystals melt, giving rise to an interconnected supermacroporous 3D architecture, while the ULMP reactions give rise to the solute concentrated cryogel walls, contributing to the thick walled interconnected macroporous structure of the cryogel (Figure 5.5d). The structure of the cryogels can be defined as a solid foam/spongle-like product with multiple void pockets distributed throughout the bulk due to the interconnected network (Figure 5.5). The polymers form the interconnected network wall that supports the internal structure of the cryogel. The end result is the interconnected foam-like structure characteristic of cryogels. The cryogelation process parameters are extremely flexible allowing for flexibility in the resulting scaffold structure.

5.3.4.1. Effect of monomer ratio on HA-PLL cryogel internal structure.

While all cryogel presented with scaffold has a highly porous structure composed of interconnecting pores, at a lower monomer concentration (2%) (Figure 5.5a,b) versus the higher concentrations (4% Figure 5.5c,d) the cryogel walls were notably thinner and sparse. The architecture of the scaffold changed with the HA:PLL ratio (Figure 5.5a,b). Decreasing the HA:PLL ratio resulted in a decrease in pore diameter and an increase in wall thickness. The pore diameters ranged 1563µm-143µm and 15µm-190µm for 10:1 (HA:PLL) and 4:1 (HA:PLL) respectively. Scaffolds prepared at a higher HA:PLL ratio were made of interconnected filament-like struts whereas scaffolds prepared at a lower HA:PLL ratio resulted in sheet-like walls (Figure 5.5b). The sheet-like structure produces a more robust architecture in comparison to the filamentous structure. Moreover, this favours an increased amount of PLL in the HA-PLL system, this is desirable as PLL may aid in improved neural cell attachment and confer antimicrobial activity. Polylysine is routinely used in neural cell culture to aid cell attachment (Pedron and Harley, 2019; Tian et al., 2005). Moreover, PLL has been

noted to possess a wide range of antimicrobial spectrum (both gram positive and gram negative bacteria, yeast, fungi, and phage) (Alkekhia and Shukla, 2019; Liu et al., 2015; Chen Shi et al., 2015; Tan et al., 2019).

5.3.4.2. Effect of freezing temperature HA-PLL cryogel structure

Cryogelation (freezing) temperature is a critical parameter for internal structure. Ström and co-workers determined that pore sizes decreased from 300µm to 150µm at -10°C and -18°C freezing temperatures respectively (Ström et al., 2015). Oelschlaeger and co-workers observed pores becoming smaller as the freezing temperature decreased, from 233µm to 136µm as the temperature decreased from -15°C to -18°C. Collins and co-workers have observed average pore diameter of HA hydrogels decreasing form 215µm-156µm from freezing temperatures of -20°C and -40°C respectively (Collins and Birkinshaw, 2011). In our method of cryogelation, we observed a similar behaviour when freezing our gel solution at -80°C versus -20°C: pores became smaller and the wall matrix thinner as the freezing temperature decreased (Figure 5.5c,d). At -80°C (Figure 5.5c) the pores range 13µm -246µm with the mean at ~100µm, whereas at -20°C the pores ranged 18.5µm -424µm. This is because the freezing rate is faster at lower freezing temperatures; the solvent (water) crystallises faster resulting in a larger number of smaller ice crystals activing as pore-forming agents.

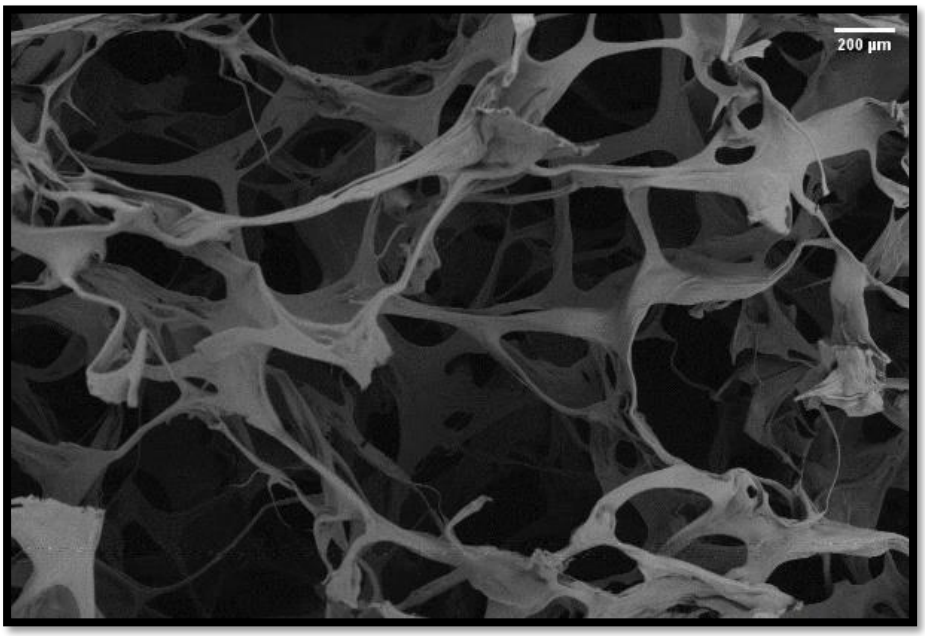

a)

4:1 ratio (HA:PLL)



b)

10:1 ratio (HA:PLL)

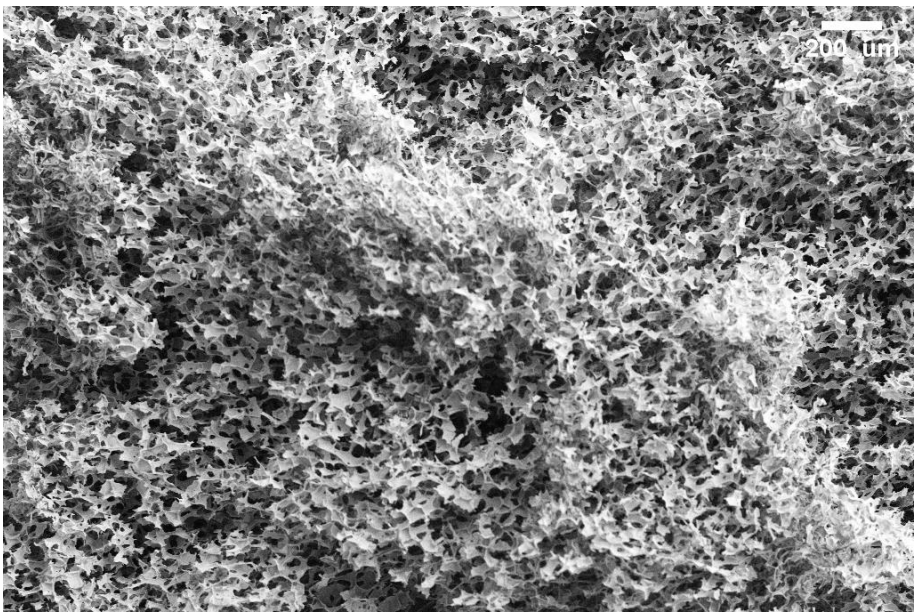

c)

-80°C. 4:1 ratio (HA:PLL)

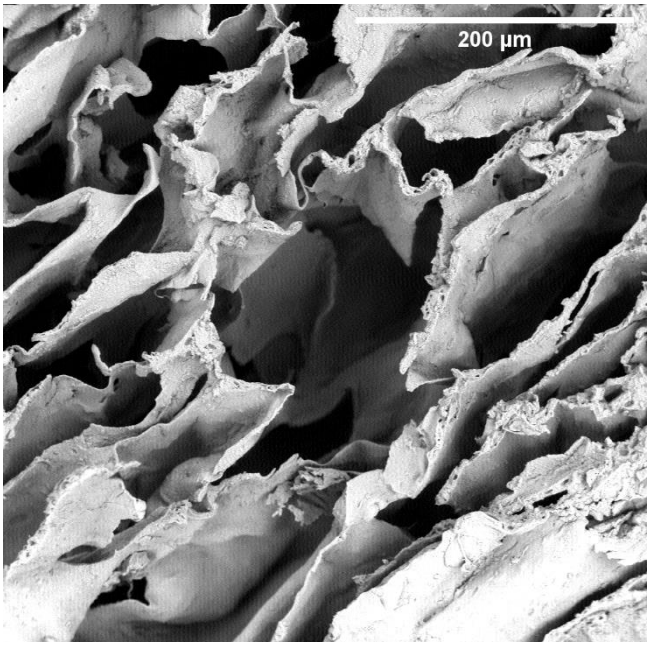

d)

-20°C. 4:1 ratio (HA:PLL)

Figure 5.5 Analysis from SEM images. a) Filament-like internal cryogel structure of BDDE-crosslinked HA-PLL cryogel at a 4:1 ratio. scale bar:200µm. b) Sheet-like internal cryogel structure of BDD- crosslinked HA-PLL cryogel at a 10:1 ratio. scale bar: 320µm.c) result of cryogelation at -80°C d) result of cryogelation at -20°C.

The preferred cryogel parameters resulted in a cryogel with pore size ranging 18.5-424µm and pore wall thickness ranged 5-83µm as demonstrated by analysis SEM images (Figure 5.5d). It has been previously noted that pore sizes ranging 20-160µm support 3D cell-cell contact, while larger pores contribute to cell viability (allow distribution of nutrients and oxygen there). Moreover, having larger pores observed in the cryogel up to 424µm may be useful in facilitating the infiltration of surrounding tissue structures, and the formation of neuroendothelial cells and micro-vessel after implantation. Compared to gels, nanofibers more closely imitate the topographical features of the natural extracellular matrix. Therefore, in addition to acting as a drug delivery system (Chapter three) and their similarity to the ECM, the nanofiber loaded hybrid scaffold provides nanoscale topographies that may potentially modulate cellular responses (Lee et al., 2009). The topographical cues aid in contact guidance whereby cells may potentially align and elongate along grooves and ridges of the scaffold. Close examination of the nanofiber reinforced cryogel revealed the presence of randomly aligned, three-dimensionally distributed nanofibers within the cryogel (Table 5.1). Embedding the nanofibers did not alter their alignment nor dissolve the nanofibers during the cryogelation process. Nanofibers maintained their morphology, indicating the successful incorporation of

nanofibers and successful formation of a nano-reinforced cryogel system (Table 5.1). This ability to withstand dissolution at the cryogelation processing conditions (e.g. strongly alkaline high pH and below zero freezing temperature and hydrolysis (water (porogen)) may be attributed to the carefully selected PLGA. This selected PLGA has a high lactide:glycolide ratio (85:15) designed by the manufacturer for application as a bioresorbable material with long degradation times (stable) ("Biodegradable polymers for controlled release - Evonik Health Care," n.d.).

Table 5.1 shows the SEM image of the hydrogel pores sizes ranging 14-142µm. The hydrogel networks consist of continuous polymer walls, in contrast to the observed discontinuous morphology of the cryogel walls (two-phase structure, consisting of polymer phase separated by irregular shaped voids (pores)). This observed structural difference is due to the porogen action in the cryogelation fabrication process which does not occur during hydrogel formation.

The resultant 3-in-1 nanoreinforced hydrofilled cryogel scaffold pore size ranged 4-320µm following the filling with the gelatin-elastin based hydrogel (Table 5.1). The 3-in-1 scaffold scaffold (Table 5.1) showed a resultant distribution of pore sizes previously noted by Jurga and co-workers (Jurga et al., 2011b) as small pores (<80 um), medium pores (80-120um) and large pores (>120um). These small, medium and large pores are optimal for stem cell niche formation, neural network growth and medium and gas exchange respectively (Jurga et al., 2011b). Pore sizes of 5-400nm are comparable those of the native ECM and aid in creating a gradient signalling profile by the slow diffusion of soluble molecules within the matrix (Zhang, 2003). These pore seize ranges are presented by the NAC-loaded nanofiber pores within the scaffold. The scaffold accommodates the average size of an adult mammalian cell (approximately 20um) (Jurga et al., 2011b). It has been previously noted that pore sizes ranging 20-160 µm support 3D cell-cell contact, while larger pores contribute to cell viability (allow distribution of nutrients and oxygen there). The ECM is what remains after removing the cells/cellular contents from the native tissues. It is the 'home' of the cell. The ECM of each tissue has a unique architecture and biochemical composition. The brain has been previously described as resembling foam, a porous fluid-saturated solid (Wagner and Ehlers, 2008)' and 'fluid-bathed multiphase material' with interconnected channels of irregular size and shape. Or the more descriptive "intricate interwoven fibre meshwork of collagen and elastic fibres embedded in a highly hydrated gel-like material of glycosaminoglycans, proteoglycans, and glycoproteins (Lee et al., 2008). The scaffold herein aimed to mimic the unique architecture hierarchical composite structure of the ECM. The scaffold is a nano-micro-macro 3-in-1 system wherein nanofibers are embedded in a cryogel matrix followed by filling with a protein-based hydrogel. Moreover, the 3D nature of the scaffold herein is structurally

supportive (tissue-mimetic platform) and integrative (interconnected pores). Cells may grow on the surface while penetrating the core of 3D scaffold due to its interconnected pores. Therefore the 3D scaffold herein may potentially offer better physical barrier against the harsh lesion environment *in vivo* (Sarnowska et al., 2013).

Table 5.1. The bulk and macro/microarchitectural properties of the scaffolds and their architectural similarity to brain ECM features. The alphabets e.g. ***a, b, c…"*** in the last two columns indicate the corresponding features of the scaffold and brain ECM structure.

Scaffold	Bulk structure	Macro/microarchitecture	Architectural similarity to brain ECM	Corresponding ECM architectural feature component (based on literature)
Nanofibers • Component one • Chapter three		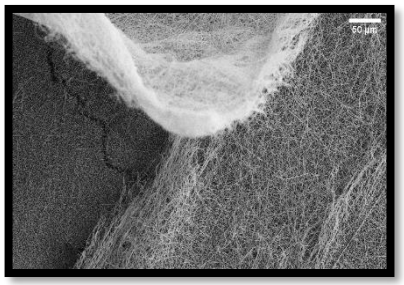	a) Nanoscale. b) Nanofibers ranged 124-592nm. c) Randomly oriented nanofibers conferring a branching netlike structure.	a) Nanoscale features (e.g. collagen fibrils ranging between 50-200nm; fibrils (2-3nm)(Lau et al., 2013). b) Collagen fibers ranging 50-500nm) (You et al., 2006). c) Randomly oriented fibers (You et al., 2006) and randomly oriented grey matter myelinated axons (Bilston, 2016).
Hydrogel • Component two • Chapter four		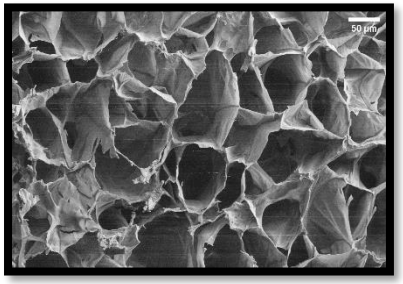	a) Protein-rich hydrogel filling the pores of the nanoreinfored cryogel to serve medium to bathe cells. b) Protein based hydrogel with gelatin (derived from collagen).	a) Interstitial fluid that serves as a rich medium that bathes cells in a rich environment environments (Lei et al., 2017; Chunyan Shi et al., 2015). b) Brain ECM structural composition contains relatively low content of fibrous matrix proteins such as collagens (Baiguera et al., 2014; Mouw et al., 2014; Ruoslahti, 1996).

Cryogel • Component three • Chapter five	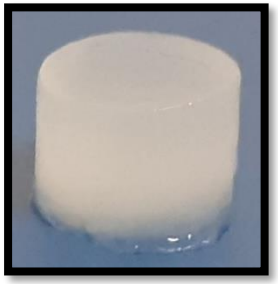	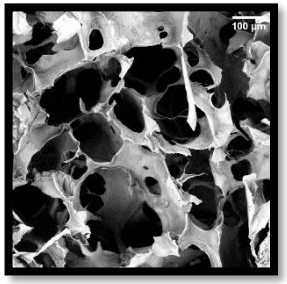	c) Hyaluronic acid backbone of cryogel and major component. d) Structure and composition (HA) contributes poroviscoelasticity: viscous properties of pores in combination with local viscoelastic properties of polymer metrics. e) Interconnected porous channels function as architected vasculature.	c) Hyaluronic acid is the main structural backbone of the Brain ECM (Baiguera et al., 2014; Balashova et al., 2019; Bignami et al., 1993; Mouw et al., 2014). d) Non-linear viscoelastic structure (Bilston, 2016). e) Internal vasculature for nutrient, cell flow (Bilston, 2011).
Novel 3-in-1 scaffold • Multicomposite (nanofibers, hydrogel, cryogel)system • Chapter five	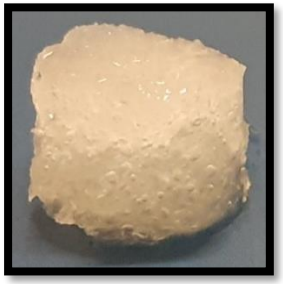	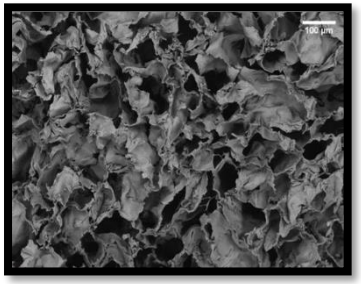	a) Sponge-like scaffold resembling foam. b) Interconnected pores size range 4-320µm separated by pore walls to create lakes filled with of gelatin-elastin hydrogel c) Non-linear viscoelastic mechanical behaviour d) Soft (525Pa) e) Preformed interconnected pores and channels to accommodate for the absence of vasculature *in vivo* for mass transport. f) Polysaccharide-protein rich environment and protein based hydrogel filling to bathe cells and aid in cell attachment. g) 3D structure.	a) The structure of brain extracellular space resembles foam (Nicholson and Syková, 1998). b) Pore sizes vary and contain 'lakes' (Nicholson and Syková, 1998). c) Non-linear viscoelastic mechanical behaviour (Bilston, 2016). d) Soft tissue with stiffness of around 500Pa (Tan et al., 2018b). e) Neural tissue vasculature to facilitate mass transport (cells, nutrients, waste)(Bilston, 2011). f) Interstitial fluid bathes cells in rich environment while ECM to anchors cells in a rich environments (Lei et

		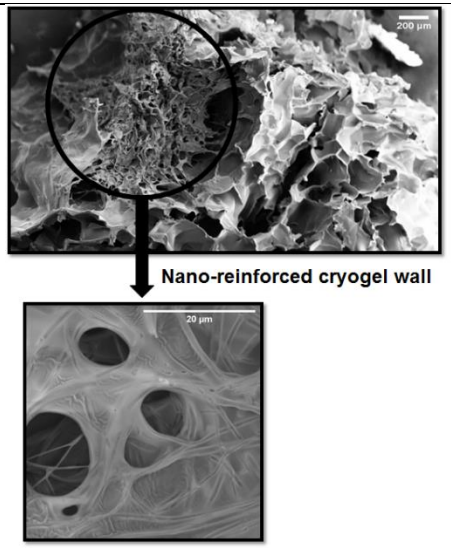	h) 3-in-1-multiscale,hierarchical, heterogenous mutlicomposite hybrid system wherein nanofibers are embedded in a cryogel matrix followed by filling of the nano-micro-macroporous structure with a protein based hydrogel. i) Multicomposite (e.g. hyaluronic acid, gelatin, PLGA, elastin, polylysine) j) Hyaluronic acid the main structural backbone with a smaller ratio of nanofibers and protein-based hydrogel.	al., 2017; Chunyan Shi et al., 2015). g) 3D brain tissue. h) Highly complex structure (e.g. “porous fluid-saturated solid”; “fluid-bathed multiphase material’ with interconnected channels of irregular size and shape”,or an “intricate interwoven fibre meshwork of collagen and elastic fibres embedded in a highly hydrated gel-like material of glycosaminoglycans, proteoglycans, and glycoproteins”(Bilston, 2016; Lee et al., 2008; Wagner and Ehlers, 2008). i) Multicomposite: biomaterials (e.g. glycosaminoglycans (GAGs), including hyaluronic acid, proteoglycans such as lecticans and glycoproteins such as tenascin) (Lee et al., 2008; Ruoslahti, 1996; Zimmermann and Dours-Zimmermann, 2008). j) Brain ECM has a high ratio of polysaccharides (hyaluronic acid is the main structural backbone of the Brain ECM) with smaller

				amounts of fibrous proteins (Baiguera et al., 2014; Balashova et al., 2019; Bignami et al., 1993; Mouw et al., 2014).

5.3.5. Biomaterial swelling and mass loss.

Swelling behaviour is an important property to observe in tissue engineering as it relates to the diffusion of molecules and nutrients (Pan et al., 2014). It shows that the scaffold has a permeable and deformable network. When hydrated the scaffold appeared to soften. Swelling further introduces an element of structural tuning. This may allow the formation of a robust scaffold in the dry state and with adequate hydration the scaffold softens, as brain tissue is described as soft tissue. The scaffolds were able to maintain their architecture and shape without additional support even when hydrated (Figure 5.6b,d). This confirmed the successful formation of a predefined architecture capable of maintaining its structure in aqueous environment. This is important as the brain is a highly hydrated tissue (80% water) (Aurand et al., 2012a). In order to serve as the structural temporary implanted neuro-ECM mimetic platform, the scaffold must be able to keep its structure in an aqueous environment. The hydrated scaffolds further confirmed the porous nature of the scaffold previously noted SEM imaging (Table 5.1). The pores within the scaffolds was visualised with the help of bulk aCSF (visible liquid pockets) within the scaffold (Figure 5.6b,d). When compresses the scaffold expelled the water from the pores indicating that the scaffold allows free flow within its structure, this is desirable for the infiltration of cells, building factors and waste removal for during ECM remodelling during healing and surrounding tissue integration.

Swelling ratio describes the fractional increase in the weight of the scaffold upon absorption of solvent (Memic et al., 2019). As shown in Figure 5d, the swelling ratios were in the following order: cryogel ($S_r = 24 \pm 7.5$) > scaffold ($S_r = 15 \pm 2.9$) > hydrogel ($S_r = 13 \pm 0.6$) > nanofibers ($S_r = 2 \pm 0.21$). Swelling consists of two processes: a) Filling the pores by the solvent, and b) Swelling of the polymer walls. Therefore, the observed results can be explained in part to structure (Table 5.1) and composition (biomaterials). From a structural perspective, as expected the cryogel has the highest swelling ratio, structurally it has largest interconnected pore size compared to the scaffold, hydrogel and nanofibers. The large interconnected pore sizes of the cryogel accommodates larger volumes of solvent in comparison to other the scaffolds (hydrogel and nanofibers). By comparison using the SEM imaging (Table 5.1), pore sizes ranged as follows cryogel > scaffold > hydrogel > nanofibers. Composition also supports the observed results. Material hydrophilicity is also a contributing factor to the observed differences in swelling ratio. Hyaluronic acid is the most hydrophilic polymer (the carboxylic groups of HA complex with other water molecules(Romagnoli and Belmontesi, 2008)) while PLGA is the most hydrophobic polymer used. Therefore, an increase in the HA fraction leads to an increase in the equilibrium swelling ratio. The swelling ratio was tunable, hydrofilling the cryogel reduced the swelling ratio. This is an important observation as swelling needs to be

controlled under physiological condition to avoid weakening the structure of the system too much and to avoid rapid degradation. This is important as the brain is a highly hydrated soft tissue. Biomaterial swelling observed herein is desired to minimise irritation to surrounding tissues post-implantation, as swelling softens the scaffold and in a fully hydrated state gels exhibit low interfacial tension with biological fluids (Memic et al., 2019). This may aid in avoiding the scaffold from escaping the implant point easily (Pan et al., 2014). Moreover, swelling increases the pore size to maximize surface area/volume ratio which will aid nutrient and cell infiltration during cell culture (Kao et al., 2019; Wang et al., 2018). The observed swelling of the scaffold is suggestive of a combination of the swelling properties of its composite systems. The hydrophilic HA component and interconnectivity of the large cryogel pores contributes to increased swelling in the scaffold versus the hydrogel and nanofibers. In contrast the hydrofilling the nanoreinforced cryogel pores with a hydrogel contributes to the observed decreased swelling of the scaffold in comparison to the cryogel as the swelling kinetics of hydrogels are more controlled by the diffusion of solvent molecules through the gel network, a slower process that than the interconnected macrospores of cryogels. Composition and structure can be used to tune the swelling properties of the scaffold.

From Figure 5.6e, the percentage mass loss is noted, readings were taken at 3 days, 7 days, 14 days and 28 days correlating to the *in vivo* time points in which the *in vivo* implanted scaffolds would be observed later in Chapter six. The percentage mass loss of control films at 28 days was 36.5% ± 6.78%. Due to their inherent hydrophilicity and water solubility, the materials (e.g. gelatin, hyaluronic acid) used to fabricate the scaffold herein, especially hyaluronic acid readily dissolve in aqueous solution within 24hours. The low mass loss of 36.5% at 28 days further supports the successful crosslinking observed with FTIR and swelling observations. Non-crosslinked gels resulted in complete dissolution within 24 hours in the aCSF. On the other hand, the covalently BDDE crosslinking scaffold showed signs of aqueous stability. The rate of degradation should match the rate of tissue formation to enable the smooth integration of the surrounding tissue while the cells remodel and form a new ECM (Mahumane et al., 2018; Moore et al., 2020). This slow degradation is desired for potential application of the scaffold *in vivo*. The stability of the material is an important parameter, especially considering the practical application of the scaffold in the highly hydrated brain tissue.



a) Lyophilised



b) Hydrated

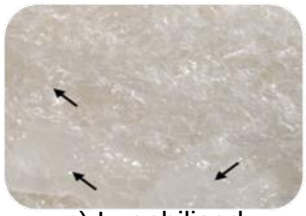

c) Lyophilised



d) Hydrated

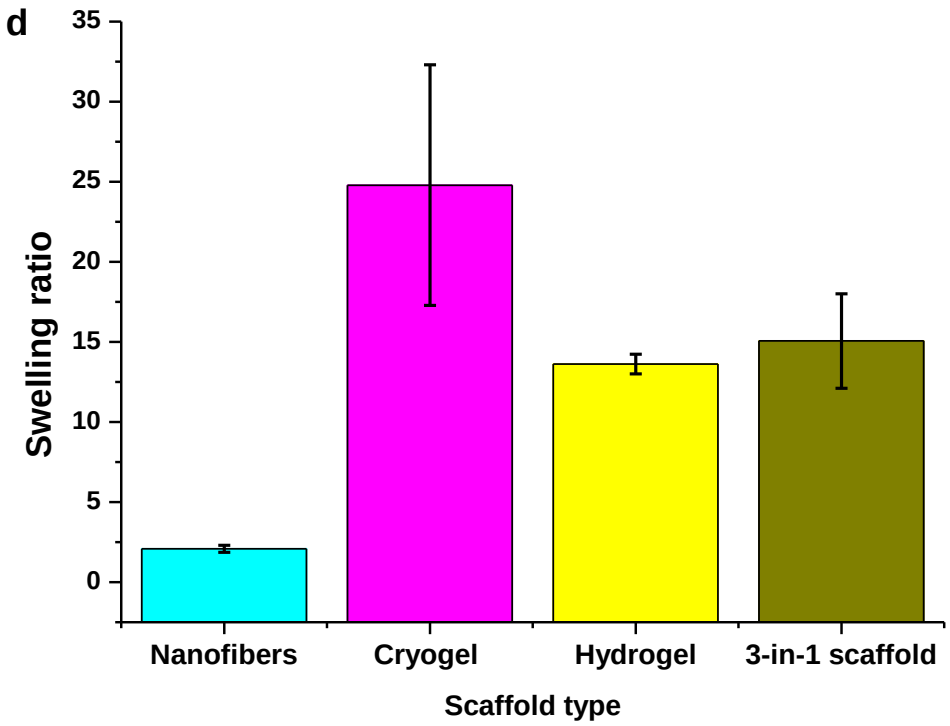

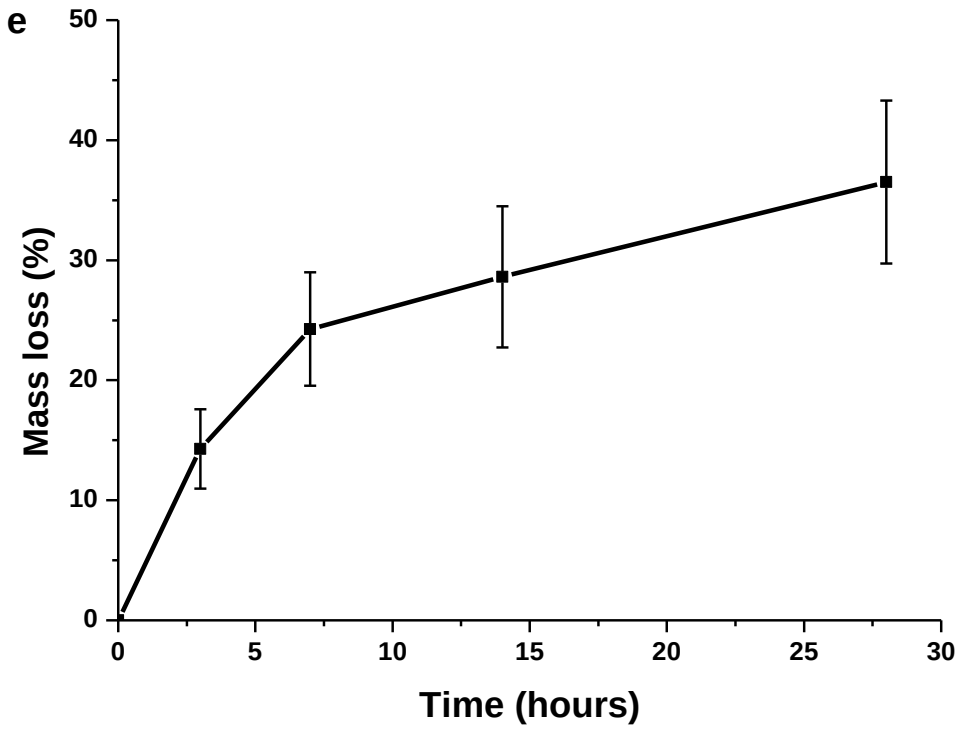

Figure 5.6. a) Lyophilised cryogel b) hydrated cryogel. c) Lyophilised scaffold d) hydrated scaffold withlack arrows indicating to the nanofiber mats embedded within the cryogel matrix. Swelling ratios of scaffolds in aCSF. Error bars represent standard deviations for 3 parallel measurements. e) Percentage mass loss of 3-in-1 scaffolds over a 28 day period in aCSF.

5.3.6. Biomechanical properties

Compression tests have been widely used to characterize the mechanical behaviour of brain tissue and its rate dependency (Forte et al., 2017; Prevost et al., 2011; Tan et al., 2018a). Therefore, compression modulus was determined, from the linear region corresponding to 0-5% strain (Pedron and Harley, 2019) The composite scaffold had a compressive modulus of 0.12kPa and 1.45 kPa for the hydrated and dry samples, respectively (Figure 5.7a, b**)**. Scaffolds with a moduli <1kPa have been noted in literature to be within the range that neural stem cells prefer, above 1kPa neuronal stem cells have been noted to differentiate toward glia (Stukel and Willits, 2018). Stukel and Willitis (Stukel and Willits, 2018) noted that neuronal differentiation preferred substrates at 0.1-0.8kPa as opposed to stiffer substrates. Tan and co-workers conducted a study to determine the stiffness of brain tissue and noted that brain tissue exhibited stiffness of approximately 0.5kPa. The scaffold stiffness in the hydrated form (0.12kPa) is within the range of <1kPa. In mechanobiology, the mechanical properties (stiffness tunability, fidelity, compatibility) are important because mechanical stiffness affects cell biology (cells generate mechanical traction forces at the cell-substrate interface due to cell

adhesion, migration and proliferation) (Tan et al., 2018a) and may avoid inducing scar formation.

In vivo, surgeons try to minimize the repeated motion and handling of the brain tissue during surgery (Navarro-Lozoya et al., 2019). Therefore, preconditioning was not performed in this study as normally brain tissue does not experience cyclic loading inside the brain during the surgical procedures. Moreover, first loading cycle (virgin/unconditioned tissue) may sometimes induce non-reversible structural damage due to the delicacy of the sample as it is designed to mimic soft tissue. Nonetheless, cyclic compression was observed to determine recoverability/shape memory properties of the hydrated scaffold. The scaffold response exhibited hysteretic features (Figure 5.7c). The hysteric feature is indicative of the viscoelastic property of the scaffold where it deforms slowly when exposed to external force (viscous) and once the force is removed it returns to its original configuration (elastic). This response is similar to brain tissue. Brain tissue is a soft material with hyper-elasticity and viscoelasticity (Zhongmeng Zhu et al., 2019). The hyper elasticity enables the brain tissue to undergo large, recoverable deformation under severe external loads, while the viscoelastic nature of the brain helps it to dissipate the deformation energy which is crucial in reducing the probability of traumatic brain injury (Zhongmeng Zhu et al., 2019). This shape-memory property was confirmed by the hysteresis curves obtained during 3 successive loading-unloading cycles 1minute and 30 seconds (recovery period). This shape memory property is important from a translational application perspective. One of the properties anticipated in the surgical scenarios with the scaffold insertion is compression.

Another notable feature was the substantial degree of ‘conditioning’ associated with the first loading cycle. There was a resultant increase in compliance between the initial cycle and subsequent cycles. This characteristic conditioning can be attributed to fluid leaking out of the scaffold (change in tissue/scaffold state), when fluid escapes it is no longer able to offer the exact same resistance to loading. The scaffold undergoes a slight microstructural reconfiguration (cell wall bending (Goga Vladimír, 2010; Sadighi and Salami, 2012).) that may be recovered given adequate recovery time, provided there is no permanent microstructural damage. This is likely because the fluid-filled state of the scaffold forces the polymer chain to exert restrictive force which contributes to the biomaterials ability to withstand and recover form deformation, preventing total architectural collapse (Mahumane et al., 2018). Similar to human brain tissue under compression (Budday et al., 2017), the offset of force at zero strain continued to increase for compression while the ‘elastic’ response (average curve between loading and unloading) remained constant. This pre-conditioning behaviour in response to

cyclic compression has been previously noted when characterizing brain tissue (Budday et al., 2019, 2017; Prevost et al., 2011).

There is a noteworthy difference in scaffold stiffness between the hydrated and non-hydrated/dry states. This is indicative of the degree of tunability of the mechanical properties of the scaffold through hydration, observed herein where the hydrated state is 12 times softer than the dry state. Biomaterial swelling may induce softening of a scaffold which in turn influences the mechanical properties and overall architectural integrity of the scaffold (Mahumane et al., 2018).

Brain tissue has been modelled as a hyper-viscoelastic spongelike porous matrix saturated with CSF (Forte et al., 2017). Herein we prepared a nanoreinforced hydrofilled spongelike porous cryogel composite scaffold. The observed compression modulus, viscoelastic and shape memory property of the scaffold, indicates its potential to withstand the translational requirements of implantation in the *in vivo* setting where the scaffold will 1) retain its shape after implantation, 2) fill the lesion cavity to enable surrounding tissue contact (facilitates tissue integration) 3) maintain its structure, 4) biomaterial swelling (not dissolve in the fluid bathed brain) and 5) have the stiffness that augments neuronal differentiation.

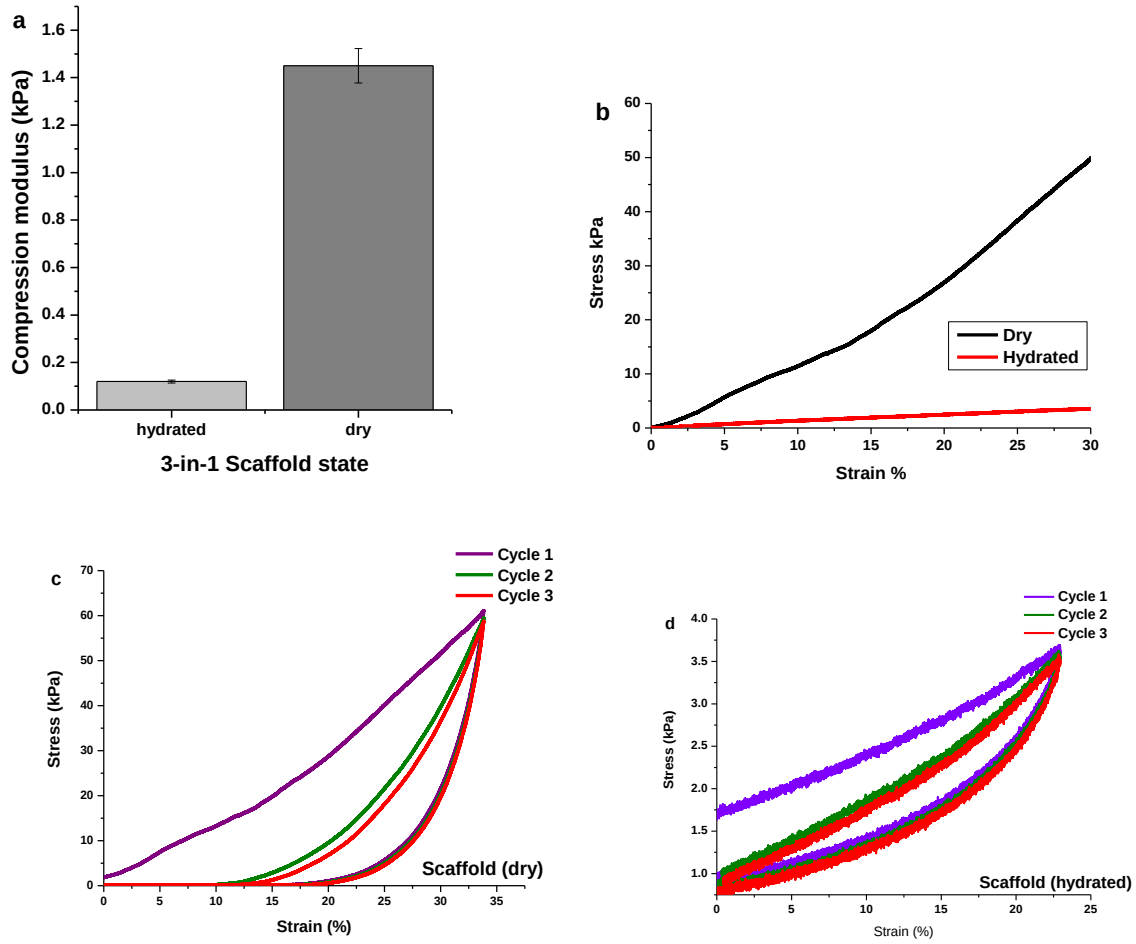

Figure 5.7. a) Compression moduli of composite hybrid scaffold in hydrated and dry state; b) Typical compressive stress–stain curves of the dry and hydrated scaffolds; c) Compression stress-strain curve of hydrated and d) dry scaffold (=3 load cycles).

Rheological measurements enabled characterization of the mechanical behaviour of the scaffold for comparison with brain tissue behaviour previously noted in literature. The scaffold was soft with a storage modulus ~525Pa (Figure 5.8). Tan and co-workers previously noted that the stiffness of porcine brain was around 500Pa (Tan et al., 2018a). Frequency sweep test (within the linear viscoelastic region) was used to determine the material frequency dependence (Figure 5.8). A high frequency region corresponds to rapid motion while a low frequency zone mimics long term behaviour. The scaffold typically exhibited solid-like behaviour, elastic behaviour was constantly dominant, i.e., G′ > G” (Figure 5.8). This indicates that the elastic region is always dominant when force load is applied. This behaviours was previously noted for brain tissue (Bilston et al., 2001; Lu et al., 2006; Pervin and Chen, 2011). The gel exhibited a similar pattern to previously determined behaviours for brain tissue (Bilston et al., 2001; Galford and McElhaney, 1970): a constant near stable/constant G* and a η* that

increases with decreasing frequency (Figure 5.8). The mechanical characterization herein then allows us to understand how the scaffold will deform during critical scenarios e.g. surgical operations. The scaffold is soft, has a deformable to undergo successful implantation without collapsing.

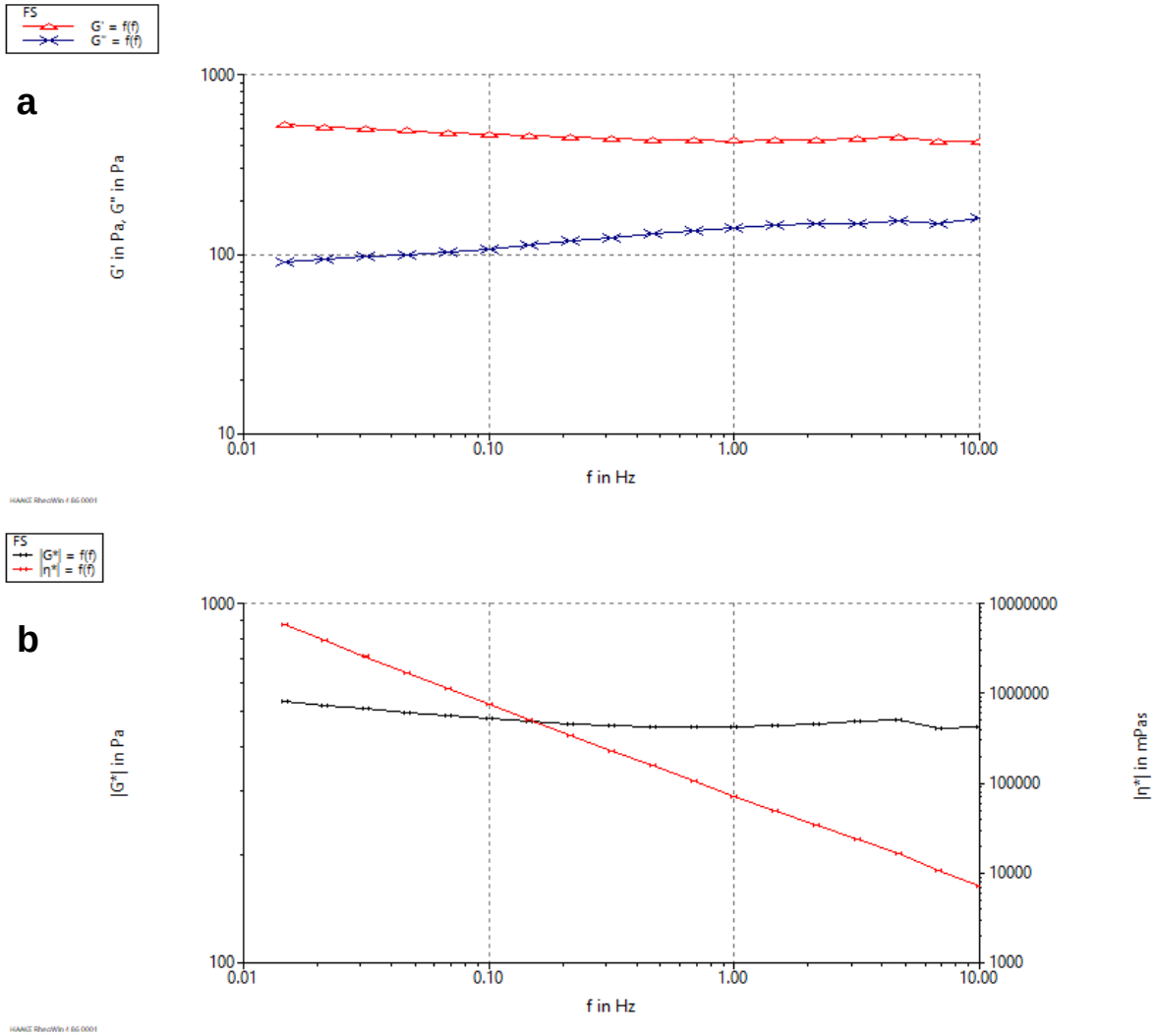

Figure 5.8. The Rheological mechanical properties of the scaffold (a) dynamic moduli, G′ and G″ as a function of frequency. (b) Linear material functions, G* and η*, of the scaffold at 37 °C: a constant G* and a η* that increases with decreasing frequency.

5.3.7. Cell cytotoxicity evaluation of scaffold

Percentage cell viability was significantly different between scaffolds. In accordance with ISO 10993-5, cytotoxicity is determined as follows: percentage of cell viability above 80% are considered non-cytotoxic; 80-60% weak; 60-40% moderate and below 40% strong cytotoxicity respectively (International Organization for Standardization, 2009). According to ISO 10993-5, the nanofibers, NAC-loaded nanofibers, 1,4-butanediol diglycidyl ether (BDDE) crosslinked 3-in-1 composite scaffold, and hydrogel were non-toxic to both PC12 and A172 cell lines as their percentage viability values we well above 80% (Figure 5.8a,b). The BDDE crosslinked

cryogel also displayed non-toxicity towards the A172 cell line according to the ISO 10993-5 standard. This is indicative of the potential biocompatibility of these systems. This was expected as the carefully selected polymers (e.g. hyaluronic acid, PLGA, gelatin) used herein include are FDA-approved, and well-known for their biocompatibility, biodegradability, and non-toxic properties (Lee et al., 2008; Hosseinkhani et al., 2014; Li et al., 2019).

A percentage cell viability higher than that of the control was noted with the nanofibers (Figure 5.9). This suggests that the nanofibrous scaffold further enhanced the growth of cells. The observed favourability towards the nanofibers as a substrate for cell growth in comparison to the other scaffolds (hydrogels, cryogels) could be attributed to their architecture. Nanofibers most closely mimic the ECM and provide a high surface area to volume ratio for cell attachment and proliferation.

The percentage viability on drug loaded nanofibers was higher than the NAC-free nanofibers. This may be attributed in part to the hydrophilicity imparted by the NAC (SH and NH groups). By comparison, moderate to strong cytotoxicity was noted for both A172 and PC12 cell lines when treated with NAC only (Figure 5.9). Media comprising of NAC crystal as a solute may have impeded cell growth by the formation of a hypertonic media thereby altering cell tonicity. When NAC is embedded in the nanofibers, the slow release rate of the NAC from the nanofiber system may favour cell proliferation as opposed to burst exposure to the bare concentrated drug crystals. Overall, the incorporation of NAC into the nanofiber system confers a synergistic interaction from the observed improvement in neuronal survival and proliferation in comparison to the individual treatments.

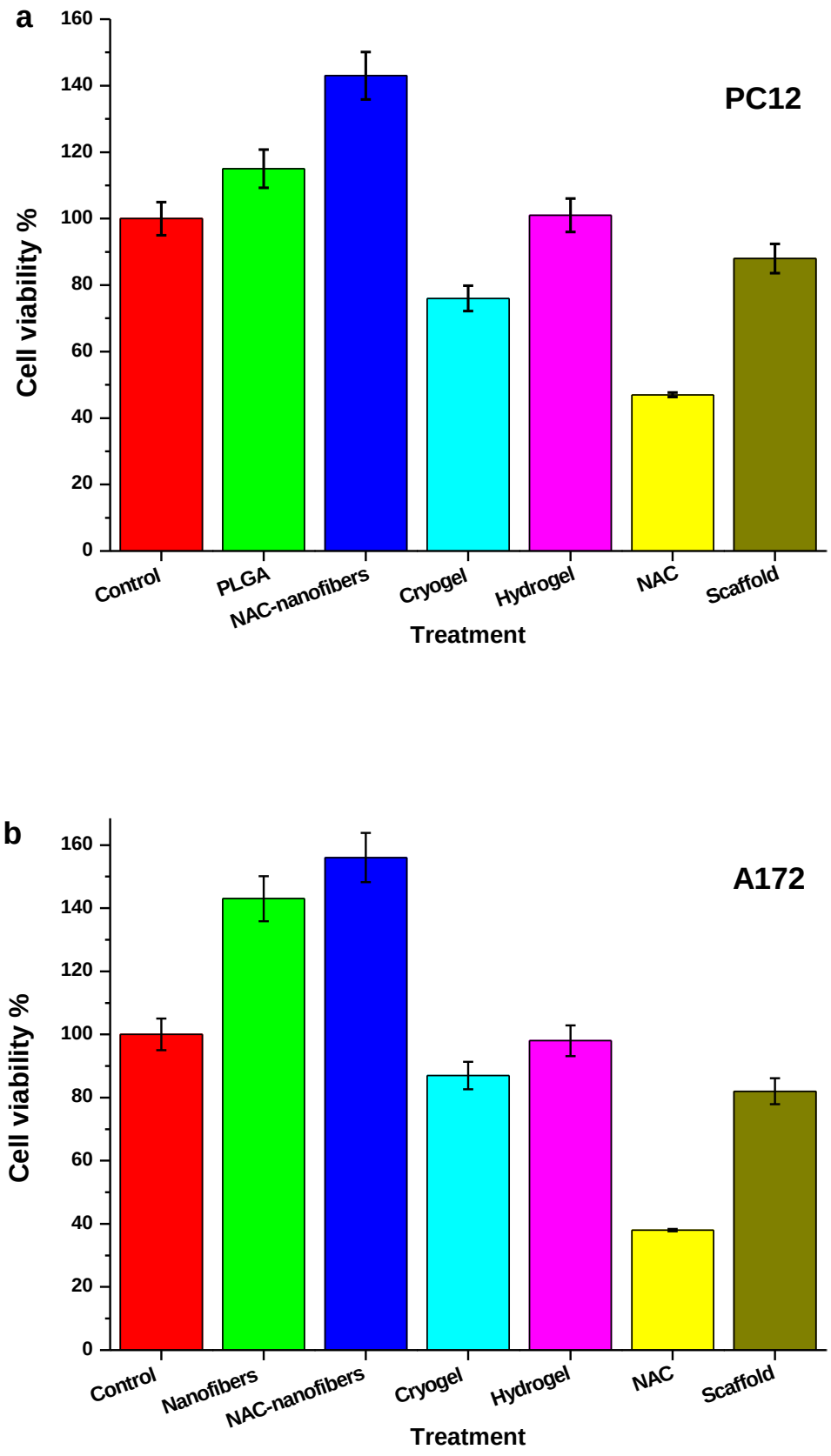

Figure 5.9. Cell cytotoxicity on control, and scaffold treatment of a) PC12 and b) A172 cell lines after 72 hours incubation.

5.8. Chapter five summary

The objective of this study was to construct a 3D porous biomimetic scaffold with a hierarchical nano, micro, macro-scale structure like that of the native ECM. The hierarchical structure was successfully fabricated comprised of a nanofiber reinforced hydro-filled cryogel. The fabrication process was inexpensive, simple. The presence of and coordination/interaction between the composite polymer materials in the scaffold was observed via FTIR analysis. The use of BDDE is reported herein for neural application and proved to be an effective crosslinker. The BDDE crosslinked 3-in-1 composite scaffold not only combined the advantages of processing conditions (electrospinning, cryogelation), biomaterials (gelatin, HA, PLGA, NAC) and components (hydrogel, nanofibers and cryogel), but exhibited new features, for example glass transition temperature, architecture, swelling ratio, cytotoxicity which arose from new interactions occurring between scaffold components. The temperature related observations from DSC and TGA analysis revealed the scaffolds thermal profile to be influenced by the combination of its composites which showed thermal stability of the scaffold at ambient and physiological temperatures (e.g. 37°C). Scanning electron microscopy revealed a 3D nanoreinforced structure with interconnected pores, this indicates that the scaffold structure is simultaneously supportive and integrative. The observed mechanical and swelling properties of the scaffold, indicates its potential to withstand the translational requirements of implantation in the *in vivo* setting where the scaffold will 1) retain its shape after implantation, 2) fill the lesion cavity to enable surrounding tissue contact (facilitates tissue integration) 3) maintain its structure, 4) biomaterial swelling (not dissolve in the fluid bathed brain) and 5) have the stiffness that augments neuronal differentiation (<1kPA). The nanofibers are effective in acting as a drug delivery system. Independently cells have proven insufficient, losses as high as 99% of transplanted cells have been reported (Mahumane et al., 2018). The MTT assay showed that the 3-in-1 scaffold was non-toxic to PC12 and A172 cells and is therefore promising option to support neural cell survival. This study demonstrated that the scaffold has the potential to be used for neural tissue engineering applications.

5.9. References

Abu Elella, M.H., Mohamed, R.R., Sabaa, M.W., 2018. Synthesis of novel grafted hyaluronic acid with antitumor activity. Carbohydrate Polymers 189, 107–114. https://doi.org/10.1016/j.carbpol.2018.02.004

Alkekhia, D., Shukla, A., 2019. Influence of poly-l-lysine molecular weight on antibacterial efficacy in polymer multilayer films. Journal of Biomedical Materials Research Part A 107, 1324–1339. https://doi.org/10.1002/jbm.a.36645

Al-Sibani, M., Al-Harrasi, A., Neubert, R.H.H., 2016. Study of the effect of mixing approach on cross-linking efficiency of hyaluronic acid-based hydrogel cross-linked with 1,4-

butanediol diglycidyl ether. European Journal of Pharmaceutical Sciences 91, 131–137. https://doi.org/10.1016/J.EJPS.2016.06.010
Amorim, S., Martins, A., Neves, N.M., Reis, R.L., Pires, R.A., 2014. Hyaluronic acid/poly-L-lysine bilayered silica nanoparticles enhance the osteogenic differentiation of human mesenchymal stem cells. Journal of Materials Chemistry B 2, 6939–6946. https://doi.org/10.1039/c4tb01071j
Aurand, E.R., Lampe, K.J., Bjugstad, K.B., 2012a. Defining and designing polymers and hydrogels for neural tissue engineering. Neuroscience Research 72, 199–213. https://doi.org/10.1016/J.NEURES.2011.12.005
Aurand, E.R., Wagner, J., Lanning, C., Bjugstad, K.B., 2012b. Building biocompatible hydrogels for tissue engineering of the brain and spinal cord. Journal of Functional Biomaterials 3, 839. https://doi.org/10.3390/JFB3040839
Baiguera, S., Del Gaudio, C., Lucatelli, E., Kuevda, E., Boieri, M., Mazzanti, B., Bianco, A., Macchiarini, P., 2014. Electrospun gelatin scaffolds incorporating rat decellularized brain extracellular matrix for neural tissue engineering. Biomaterials 35, 1205–1214. https://doi.org/10.1016/j.biomaterials.2013.10.060
Balashova, A., Pershin, V., Zaborskaya, O., Tkachenko, N., Mironov, A., Guryev, E., Kurbatov, L., Gainullin, M., Mukhina, I., 2019. Enzymatic Digestion of Hyaluronan-Based Brain Extracellular Matrix in vivo Can Induce Seizures in Neonatal Mice. Front Neurosci 13. https://doi.org/10.3389/fnins.2019.01033
Bang, S., Das, D., Yu, J., Noh, I., 2017. Evaluation of MC3T3 cells proliferation and drug release study from sodium hyaluronate-1,4-butanediol diglycidyl ether patterned gel. Nanomaterials 7, 328. https://doi.org/10.3390/nano7100328
Biazar, E., Keshel, S.H., 2014. Unrestricted somatic stem cells loaded in nanofibrous scaffolds as potential candidate for skin regeneration. International Journal of Polymeric Materials and Polymeric Biomaterials 63, 741–752. https://doi.org/10.1080/00914037.2013.879447
Bignami, A., Hoslcy, M., Dahl, D., 1993. Hyaluronic acid and hyaluronic acid-binding proteins in brain extracellular matrix. Anat Embryol (Berl) 188, 419–433. https://doi.org/doi:10.1007/BF00190136
Bilston, L.E., 2016. The influence of microstructure on neural tissue mechanics, in: Kassab, G.S., Sacks, M.S. (Eds.), Structure-Based Mechanics of Tissues and Organs. Springer, Boston, pp. 1–14.
Bilston, L.E., 2011. Neural Tissue Biomechanics: Volume 3 of Studies in Mechanobiology, Tissue Engineering and Biomaterials, Illustrate. ed. Springer Science & Business Media.
Bilston, L.E., Liu, Z., Phan-Thien, N., 2001. Large strain behaviour of brain tissue in shear: Some experimental data and differential constitutive model. Biorheology 38, 335–345.
Biodegradable polymers for controlled release - Evonik Health Care [WWW Document], n.d. URL https://healthcare.evonik.com/product/health-care/en/products/biomaterials/resomer/pages/controlled-release.aspx (accessed 8.5.20).
Budday, S., Ovaert, T.C., Holzapfel, G.A., Steinmann, P., Kuhl, E., 2019. Fifty Shades of Brain: A Review on the Mechanical Testing and Modeling of Brain Tissue. Archives of Computational Methods in Engineering 1–44. https://doi.org/10.1007/s11831-019-09352-w
Budday, S., Sommer, G., Birkl, C., Langkammer, C., Haybaeck, J., Kohnert, J., Bauer, M., Paulsen, F., Steinmann, P., Kuhl, E., Holzapfel, G.A., 2017. Mechanical characterization of human brain tissue. Acta Biomaterialia 48, 319–340. https://doi.org/10.1016/J.ACTBIO.2016.10.036
Chang, K.H., Liao, H.T., Chen, J.P., 2013. Preparation and characterization of gelatin/hyaluronic acid cryogels for adipose tissue engineering: In vitro and in vivo studies. Acta Biomaterialia 9, 9012–9026. https://doi.org/10.1016/j.actbio.2013.06.046

Collins, M.N., Birkinshaw, C., 2011. Morphology of crosslinked hyaluronic acid porous hydrogels. Journal of Applied Polymer Science 120, 1040–1049. https://doi.org/10.1002/app.33241

Forte, A.E., Gentleman, S.M., Dini, D., 2017. On the characterization of the heterogeneous mechanical response of human brain tissue. Biomechanics and Modeling in Mechanobiology 16, 907–920. https://doi.org/10.1007/s10237-016-0860-8

Galford, J.E., McElhaney, J.H., 1970. A viscoelastic study of scalp, brain, and dura. J Biomech 3, 211–221. https://doi.org/10.1016/0021-9290(70)90007-2

Ginjupalli, K., Averineni, R.K., K, M.B., N, U., 2014. Preparation and characterization of biodegradable scaffolds of poly(lactide-co-glycolide) 50:50 and hydroxyapatite for dental applications. Composite Interfaces 21, 31–44. https://doi.org/10.1080/15685543.2013.830523

Goga Vladimír, 2010. Testing and Application of New Phenomenological Material Model for Foam Materials 1–11.

Hahn, S.K., Hoffman, A.S., 2005. Preparation and characterization of biocompatible polyelectrolyte complex multilayer of hyaluronic acid and poly-l-lysine. International Journal of Biological Macromolecules 37, 227–231. https://doi.org/10.1016/j.ijbiomac.2005.11.010

Hermanson, G.T., 2013. Bioconjugate techniques, 3rd Ed. ed. Academic Press.

Hosseinkhani, M., Mehrabani, D., Karimfar, M.H., Bakhtiyari, S., Manafi, A., Shirazi, R., 2014. Tissue engineered scaffolds in regenerative medicine. World journal of plastic surgery 3–7.

International Organization for Standardization, 2009. ISO - ISO 10993-5:2009 - Biological evaluation of medical devices — Part 5: Tests for in vitro cytotoxicity, 3rd ed, ISO/TC 194 Biological and clinical evaluation of medical devices.

Jurga, M., Dainiak, M.B., Sarnowska, A., Jablonska, A., Tripathi, A., Plieva, F.M., Savina, I.N., Strojek, L., Jungvid, H., Kumar, A., Lukomska, B., Domanska-Janik, K., Forraz, N., McGuckin, C.P., 2011a. The performance of laminin-containing cryogel scaffolds in neural tissue regeneration. Biomaterials 32, 3423–3434. https://doi.org/10.1016/j.biomaterials.2011.01.049

Jurga, M., Dainiak, M.B., Sarnowska, A., Jablonska, A., Tripathi, A., Plieva, F.M., Savina, I.N., Strojek, L., Jungvid, H., Kumar, A., Lukomska, B., Domanska-Janik, K., Forraz, N., McGuckin, C.P., 2011b. The performance of laminin-containing cryogel scaffolds in neural tissue regeneration. Biomaterials 32, 3423–3434. https://doi.org/10.1016/j.biomaterials.2011.01.049

Kao, H.-H., Kuo, C.-Y., Chen, K.-S., Chen, J.-P., 2019. Preparation of Gelatin and Gelatin/Hyaluronic Acid Cryogel Scaffolds for the 3D Culture of Mesothelial Cells and Mesothelium Tissue Regeneration. International Journal of Molecular Sciences 20, 4527. https://doi.org/10.3390/ijms20184527

Khunmanee, S., Jeong, Y., Park, H., 2017. Crosslinking method of hyaluronic-based hydrogel for biomedical applications. Journal of tissue engineering 8, 2041731417726464. https://doi.org/10.1177/2041731417726464

Koh, et al, 2013. Epoxy cross-linked collagen and collagen-laminin peptide hydrogels as corneal substitutes. Journal of Functional Biomaterials 4, 162–177. https://doi.org/doi:10.3390/jfb4030162

Kumar, A., 2016. Supermacroporous Cryogels: Biomedical and Biotechnological Applications, Illustrate. ed. CRC Press.

Kumari, J., Kumar, A., 2017. Development of polymer based cryogel matrix for transportation and storage of mammalian cells. Scientific 7, 1–13. https://doi.org/10.1038/srep41551

Lan, S.-M., Jou, I.-M., Wu, P.-T., Wu, C.-Y., Chen, S.-C., 2015. Investigation into the safety of perineural application of 1,4-butanediol diglycidyl ether-crosslinked hyaluronan in a rat model. Journal of Biomedical Materials Research Part B: Applied Biomaterials 103, 718–726. https://doi.org/10.1002/jbm.b.33251

Lankalapalli, S., Kolapalli, V.R.M., 2009. Polyelectrolyte Complexes: A Review of their Applicability in Drug Delivery Technology. Indian journal of pharmaceutical sciences 71, 481–7. https://doi.org/10.4103/0250-474X.58165

Larrañeta, E., Henry, M., Irwin, N.J., Trotter, J., Perminova, A.A., Donnelly, R.F., 2018. Synthesis and characterization of hyaluronic acid hydrogels crosslinked using a solvent-free process for potential biomedical applications. Carbohydrate Polymers 181, 1194–1205. https://doi.org/10.1016/J.CARBPOL.2017.12.015

Lau, L.W., Cua, R., Keough, M.B., Haylock-Jacobs, S., Yong, V.W., 2013. Pathophysiology of the brain extracellular matrix: a new target for remyelination. Nat. Rev. Neurosci. 14, 722–729. https://doi.org/10.1038/nrn3550

Lee, J., Cuddihy, M.J., Kotov, N.A., 2008. Three-dimensional cell culture matrices: State of the art. Tissue Engineering Part B: Reviews 14, 61–86. https://doi.org/10.1089/teb.2007.0150

Lee, J.Y., Bashur, C.A., Goldstein, A.S., Schmidt, C.E., 2009. Polypyrrole-coated electrospun PLGA nanofibers for neural tissue applications. Biomaterials 30, 4325–4335. https://doi.org/10.1016/j.biomaterials.2009.04.042

Lee, S., Kim, H.S., Yoo, H.S., 2017. Electrospun nanofibrils embedded hydrogel composites for cell cultivation in a biomimetic environment. RSC Advances 7, 54246–54253. https://doi.org/10.1039/c7ra08595h

Lei, Y., Han, H., Yuan, F., Javeed, A., Zhao, Y., 2017. The brain interstitial system: Anatomy, modeling, in vivo measurement, and applications. Progress in Neurobiology 157, 230–246. https://doi.org/10.1016/j.pneurobio.2015.12.007

Li, X., Cho, B., Martin, R., Seu, M., Zhang, C., Zhou, Z., Choi, J.S., Jiang, X., Chen, L., Walia, G., Yan, J., Callanan, M., Liu, H., Colbert, K., Morrissette-McAlmon, J., Grayson, W., Reddy, S., Sacks, J.M., Mao, H.Q., 2019. Nanofiber-hydrogel composite–mediated angiogenesis for soft tissue reconstruction. Science Translational Medicine 11. https://doi.org/10.1126/scitranslmed.aau6210

Liu, H., Pei, H., Han, Z., Feng, G., Li, D., 2015. The antimicrobial effects and synergistic antibacterial mechanism of the combination of ε-Polylysine and nisin against Bacillus subtilis. Food Control 47, 444–450. https://doi.org/10.1016/j.foodcont.2014.07.050

Lu, Y.-B., Franze, K., Seifert, G., Steinhäuser, C., Kirchhoff, F., Wolburg, H., Guck, J., Janmey, P., Wei, E.-Q., Käs, J., Reichenbach, A., 2006. Viscoelastic properties of individual glial cells and neurons in the CNS. PNAS 103, 17759–17764. https://doi.org/10.1073/pnas.0606150103

Mahumane, G.D., Kumar, P., Du Toit, L.C., Choonara, Y.E., Pillay, V., 2018. 3D scaffolds for brain tissue regeneration: Architectural challenges. Biomaterials Science 6, 2812–2837. https://doi.org/10.1039/c8bm00422f

Mahumane, G.D., Kumar, P., Pillay, V., Choonara, Y.E., 2020. Repositioning N-Acetylcysteine (NAC): NAC-Loaded Electrospun Drug Delivery Scaffolding for Potential Neural Tissue Engineering Application. Pharmaceutics 12, 934. https://doi.org/10.3390/pharmaceutics12100934

Mandal, T.K., Bostanian, L.A., Graves, R.A., Chapman, S.R., 2002. Poly(d,l-Lactide-Co-Glycolide) Encapsulated Poly(Vinyl Alcohol) Hydrogel as a Drug Delivery System. Pharmaceutical Research 19, 1713–1719. https://doi.org/10.1023/A:1020765615379

Martucci, J.F., Espinosa, J.P., Ruseckaite, R.A., 2015. Physicochemical properties of films based on bovine gelatin cross-linked with 1,4-butanediol diglycidyl ether. Food and Bioprocess Technology 8, 1645–1656. https://doi.org/10.1007/s11947-015-1524-x

Memic, A., Colombani, T., Eggermont, L.J., Rezaeeyazdi, M., Steingold, J., Rogers, Z.J., Navare, K.J., Mohammed, H.S., Bencherif, S.A., 2019. Latest Advances in Cryogel Technology for Biomedical Applications. Advanced Therapeutics 2, 1800114. https://doi.org/10.1002/adtp.201800114

Miller, R.J., Chan, C.Y., Rastogi, A., Grant, A.M., White, C.M., Bette, N., Schaub, N.J., Corey, J.M., 2018. Combining electrospun nanofibers with cell-encapsulating hydrogel fibers for neural tissue engineering. Journal of Biomaterials Science, Polymer Edition 29, 1625–1642. https://doi.org/10.1080/09205063.2018.1479084

Moore, K.M., Graham-Gurysh, E.G., Bomba, H.N., Murthy, A.B., Bachelder, E.M., Hingtgen, S.D., Ainslie, K.M., 2020. Impact of composite scaffold degradation rate on neural stem cell persistence in the glioblastoma surgical resection cavity. Materials Science and Engineering: C 111, 110846. https://doi.org/10.1016/j.msec.2020.110846

Mouw, J.K., Ou, G., Weaver, V.M., 2014. Extracellular matrix assembly: a multiscale deconstruction. Nat Rev Mol Cell Biol 15, 771–785. https://doi.org/10.1038/nrm3902

Mukherjee, I., Rosolen, M., 2013. Thermal transitions of gelatin evaluated using DSC sample pans of various seal integrities. Journal of Thermal Analysis and Calorimetry 114, 1161–1166. https://doi.org/10.1007/s10973-013-3166-4

Navarro-Lozoya, M., Kennedy, M.S., Dean, D., Rodriguez-Devora, J.I., 2019. Development of phantom material that resembles compression properties of human brain tissue for training models. Materialia 8, 100438. https://doi.org/10.1016/j.mtla.2019.100438

Nicholson, C., Syková, E., 1998. Extracellular space structure revealed by diffusion analysis. Trends in Neurosciences 21, 207–21. https://doi.org/10.1016/S0166-2236(98)01261-2

Okay, O., 2014. Polymeric cryogels macroporous gels with remarkable properties, Illustrate. ed, Advances in Polymer Science. Springer. https://doi.org/10.1007/978-3-319-05846-7

Pan, J., Liu, N., Sun, H., Xu, F., 2014. Preparation and Characterization of Electrospun PLCL/Poloxamer Nanofibers and Dextran/Gelatin Hydrogels for Skin Tissue Engineering. PLoS One 9. https://doi.org/10.1371/journal.pone.0112885

Pedron, S., Harley, B.A.C., 2019. Biomaterials for Brain Therapy and Repair. Frontiers Media SA.

Pervin, F., Chen, W.W., 2011. Mechanically Similar Gel Simulants for Brain Tissues, in: Dynamic Behavior of Materials, Volume 1, Conference Proceedings of the Society for Experimental Mechanics Series. Springer, New York, NY, New York, pp. 9–13. https://doi.org/10.1007/978-1-4419-8228-5_3

Prevost, T.P., Balakrishnan, A., Suresh, S., Socrate, S., 2011. Biomechanics of brain tissue. Acta Biomaterialia 7, 83–95. https://doi.org/10.1016/j.actbio.2010.06.035

Prokopović, V.Z., Duschl, C., Volodkin, D., 2015. Hyaluronic Acid/Poly-l-Lysine Multilayers as Reservoirs for Storage and Release of Small Charged Molecules. Macromolecular Bioscience 15, 1357–1363. https://doi.org/10.1002/mabi.201500093

Romagnoli, M., Belmontesi, M., 2008. Hyaluronic acid–based fillers: theory and practice. Clinics in Dermatology 26, 123–159. https://doi.org/10.1016/J.CLINDERMATOL.2007.09.001

Ruoslahti, E., 1996. Brain extracellular matrix. Glycobiology 6, 489–492. https://doi.org/10.1093/glycob/6.5.489

Sadighi, M., Salami, S.J., 2012. An investigation on low-velocity impact response of elastomeric and crushable foams. Central European Journal of Engineering 2, 627–637. https://doi.org/10.2478/s13531-012-0026-0

Samouillan, V., Dandurand-Lods, J., Lamure, A., Maurel, E., Lacabanne, C., Gerosa, G., Venturini, A., Casarotto, D., Gherardini, L., Spina, M., 1999. Thermal analysis characterization of aortic tissues for cardiac valve bioprostheses. Journal of Biomedical Materials Research 46, 531–538. https://doi.org/10.1002/(SICI)1097-4636(19990915)46:4<531::AID-JBM11>3.0.CO;2-2

Samouillan, V., Delaunay, F., Dandurand, J., Merbahi, N., Gardou, J.-P., Yousfi, M., Gandaglia, A., Spina, M., Lacabanne, C., 2011. The Use of Thermal Techniques for the Characterization and Selection of Natural Biomaterials. Journal of Functional Biomaterials 2, 230–248. https://doi.org/10.3390/jfb2030230

Sarnowska, A., Jablonska, A., Jurga, M., Dainiak, M., Strojek, L., Drela, K., Wright, K., Tripathi, A., Kumar, A., Jungvid, H., Lukomska, B., Forraz, N., McGuckin, C., Domanska-Janik, K., 2013. Encapsulation of mesenchymal stem cells by bioscaffolds protects cell survival and attenuates neuroinflammatory reaction in injured brain tissue after transplantation. Cell Transplantation 22, 67–82. https://doi.org/10.3727/096368913X672172

Shabani Ravari, N., Goodarzi, N., Alvandifar, F., Amini, M., Souri, E., Khoshayand, M.R., Hadavand Mirzaie, Z., Atyabi, F., Dinarvand, R., 2016. Fabrication and biological evaluation of chitosan coated hyaluronic acid-docetaxel conjugate nanoparticles in CD44+ cancer cells. DARU Journal of Pharmaceutical Sciences 24, 21. https://doi.org/10.1186/s40199-016-0160-y

Shi, Chen, He, Y., Feng, X., Fu, D., 2015. ε-Polylysine and next-generation dendrigraft poly-L-lysine: chemistry, activity, and applications in biopharmaceuticals. null 26, 1343–1356. https://doi.org/10.1080/09205063.2015.1095023

Shi, Chunyan, Lei, Y., Han, H., Zuo, L., Yan, J., He, Q., 2015. Transportation in the interstitial space of the brain can be regulated by neuronal excitation. Scientific Reports 5, 1–11. https://doi.org/10.1038/srep17673

Ström, A., Larsson, A., Okay, O., 2015. Preparation and physical properties of hyaluronic acid-based cryogels. Journal of Applied Polymer Science 132, 1–11. https://doi.org/10.1002/app.42194

Stukel, J.M., Willits, R.K., 2018. The interplay of peptide affinity and scaffold stiffness on neuronal differentiation of neural stem cells. Biomedical Materials 13, 024102. https://doi.org/10.1088/1748-605X/aa9a4b

Tan, Z., Dini, D., Rodriguez y Baena, F., Forte, A.E., 2018a. Composite hydrogel: A high fidelity soft tissue mimic for surgery. Materials and Design 160, 886–894. https://doi.org/10.1016/j.matdes.2018.10.018

Tan, Z., Dini, D., Rodriguez y Baena, F., Forte, A.E., 2018b. Composite hydrogel: A high fidelity soft tissue mimic for surgery. Materials and Design 160, 886–894. https://doi.org/10.1016/j.matdes.2018.10.018

Tan, Z., Shi, Y., Xing, B., Hou, Y., Cui, J., Jia, S., 2019. The antimicrobial effects and mechanism of ε-poly-lysine against Staphylococcus aureus. Bioresour. Bioprocess. 6, 11. https://doi.org/10.1186/s40643-019-0246-8

Thomas, R.G., Muthiah, M., Moon, M.J., Park, I.K., Jeong, Y.Y., 2017. SPION loaded poly(L-lysine)/hyaluronic acid micelles as MR contrast agent and gene delivery vehicle for cancer theranostics. Macromolecular Research 25, 446–451. https://doi.org/10.1007/s13233-017-5053-5

Tian, W.M., Hou, S.P., Ma, J., Zhang, C.L., Xu, Q.Y., Lee, I.S., Li, H.D., Spector, M., Cui, F.Z., 2005. Hyaluronic acid–poly-D-lysine-based three-dimensional hydrogel for traumatic brain injury. Tissue Engineering 513–525. https://doi.org/10.1089/ten.2005.11.513

Tračuma, E., Loca, D., 2020. Hyaluronic Acid/Polylysine Composites for Local Drug Delivery: A Review. KEM 850, 213–218. https://doi.org/10.4028/www.scientific.net/KEM.850.213

Wagner, A., Ehlers, W., 2008. A porous media model to describe the behaviour of brain tissue. Proceedings in Applied Mathematics and Mechanics 8, 10201–10202. https://doi.org/10.1002/pamm.200810201

Wang, B., Huang, C., Chen, S., Xing, X., Zhang, M., Wu, Q., Wang, H., 2018. Hybrid scaffolds enhanced by nanofibers improve in vitro cell behavior for tissue regeneration. Cellulose 25, 7113–7125. https://doi.org/10.1007/s10570-018-2087-6

Yang, R., Tan, L., Cen, L., Zhang, Z., 2016. An injectable scaffold based on crosslinked hyaluronic acid gel for tissue regeneration. RSC Advances 6, 16838–16850. https://doi.org/10.1039/c5ra27870h

You, Y., Lee, S., Min, B.-M., Park, W., 2006. Effect of solution properties on nanofibrous structure of electrospun poly(lactic-co-glycolic acid). Journal of Applied Polymer Science 99, 1214 –1221–1214 –1221.

Zeeman, R., Dijkstra, P.J., van Wachem, P.B., van Luyn, M.J.A., Hendriks, M., Cahalan, P.T., Feijen, J., 1999. Successive epoxy and carbodiimide cross-linking of dermal sheep collagen. Biomaterials 20, 921–931. https://doi.org/10.1016/S0142-9612(98)00242-7

Zhang, S., 2003. Fabrication of novel biomaterials through molecular self-assembly. Nature Biotechnology 21, 1171–1178. https://doi.org/doi.org/10.1038/nbt874

Zhongmeng Zhu, Chengkai Jiang, Han Jiang, 2019. A visco-hyperelastic model of brain tissue incorporating both tension/compression asymmetry and volume compressibility. acta mech 230, 2125–2135.

Zhou, L., Tu, J., Fang, G., Deng, L., Gao, X., Guo, K., Kong, J., Lv, J., Guan, W., Yang, C., 2018. Combining PLGA Scaffold and MSCs for Brain Tissue Engineering: A Potential Tool for Treatment of Brain Injury. Stem Cells Int 2018. https://doi.org/10.1155/2018/5024175

Zimmermann, D.R., Dours-Zimmermann, M.T., 2008. Extracellular matrix of the central nervous system: from neglect to challenge. Histochem Cell Biol 130, 635–653. https://doi.org/10.1007/s00418-008-0485-9

CHAPTER SIX

IN VIVO ANALYSIS OF THE NOVEL 3-IN-1 SCAFFOLD IMPLANT IN SPRAGUE-DAWLEY RAT TBI MODEL

6.1. Introduction

In vivo analysis enables assessment of the clinical translational potential of the proposed 3-in-1 3D scaffold intervention under realistic conditions. The toxicity, cell behaviour, biodegradation profile of therapeutic agents is known to vary between *in vitro* and *in vivo* settings (Jurga et al., 2011). Therefore, it is very crucial to be able to show reliable tissue integration profile under *in vivo* environments to assess potential safety, pharmacokinetic and pharmacodynamics profile of the therapeutic intervention. There is no standard clinically approved therapy for TBI, therefore *in vivo* testing is a progressive platform for the exploration of potential treatments.

Numerous TBI animal models have been developed over the years (Johnson et al., 2015; Xiong et al., 2013). These animal models have proven effective in progressing the understanding of the pathophysiology of TBI (Xiong et al., 2013). Furthermore, animals are effective platforms to explore potential therapeutic treatments (Nyanzu et al., 2017). This is in part because animals share both physiological and genetic similarities to humans which aids in assessing the clinical translation potential of the therapeutic agents being tested. *In vivo* testing with animals is preferable because, testing can be performed under controlled laboratory environments, using quantifiable models, something which is difficult to do with humans from an ethical perspective. Due to their easy postsurgical needs, costs, availability and simplicity, rodents (e.g. mice, rats) currently dominate as animal choices for *in vivo* TBI studies (Marklund, 2016; Nyanzu et al., 2017). This means that there is a respectable amount of established protocols and data available for reference and comparative analysis to determine the efficacy of our scaffold design. Therefore, Sprague-Dawley rats were used as the animal model of choice.

The purpose of this chapter was to induce a survivable, reproducible localized penetrating brain injury with observable sensory and motor weakness. The effect of the surgical method and model was determined using behavioral tests. Contralateral limb motor performance was evaluated using the cylinder test, somatosensory performance was evaluated using the adhesive removal test, a composite of motor, sensory, balance and reflex tests were evaluated

using the modified neurological severity score (mNSS) and ladder rung test. The therapeutic potential of the novel 3D scaffolds implanted at the induced TBI lesion cavity was evaluated via histomorphological analysis.

6.2. Materials and Methods

6.2.1. Animal procurement

The Sprague-Dawley (SD) rats (female, 6-8 weeks) utilized for the traumatic brain injury model in this study were procured from the Central Animal Services of the University of the Witwatersrand. Ethics clearance for the study was obtained from the Animal Ethics Screening Committee of the University of the Witwatersrand (Ethics clearance number: 2017/08/49/D).

6.2.2. Animal care/pre-surgical preparation of animals

Healthy female Sprague–Dawley rats (6-8weeks 189-230g) were utilized in this study. SD rats were housed individually, in cages at room temperature (± 25°C), maintained under a 12 hour light:dark cycle. The animals were fed a commercial diet (pelleted rat chow, Epol, Johannesburg, South Africa), and given water *ad libitum*. Rats were allowed to acclimatize to the environment for a week prior to surgery. Food intake and body mass were measured daily, before dark cycle. Food intake was quantified by subtracting the food remaining in the container from the amount of food placed in the container. Animals were weighed daily, the weight was used as an indicator of the general health of the animals (an animal exhibiting loss of 15% or more of its expected body weight would be removed from the study). All procedures were done in accordance with the standard operating procedures (SOPs) of the CAS and conforming to the South African standard for the use and care of animals for scientific purposes.

6.2.3. Experimental design for an intervention study

In light of the intensity and delicacy of a traumatic brain injury, the proposed injury model and proposed intervention, the surgical technique was first tested on Sprague-Dawley rat cadavers (n=2) for the purpose of refining the injury technique. The purpose of the first phase is to test the feasibility, equipment, statistical variability and proposed injury induction methods to identify and improve on the study design to not only achieve objectives in the most effective way but also avoid being wasteful of animals. Thereafter intervention tests were conducted on live SD rats to ascertain a) reproducible outcomes and recovery post TBI induction and b) effects of the proposed intervention in Sprague-Dawley rat model with TBI. The rats were divided into three groups: Group 1 “control” (normal brain: n=1); Group 2 “sham” (TBI induced with no scaffold n=6) and Group 3 “intervention” (rats with TBI that received scaffold intervention: n=9).

6.3.4. Design of *in vivo* experimental study

Traumatic brain injury was induced in Sprague-Dawley rats (SD) using a corticectomized rat model for TBI (Lee et al., 2009). A randomized controlled test was implemented, whereby a group of Sprague-Dawley rats (6-8 weeks old, ±250g) were randomly assigned to two sub-groups (Group 2, Group 3). To the best of our knowledge, to date, there have been no clinically approved TBI treatments for comparison of the efficacy of our intervention. Therefore, changes in the injury progression sham group was used to elucidate the direct impact of our proposed scaffold implant intervention. The only difference/variance between the two groups (sham and intervention) was the scaffold intervention. The control group was used as a control (normal uninjured cortex) for histological analysis. All other conditions and experiences were controlled (e.g. husbandry, TBI severity and behavioral assessments).

6.3.4.1. Description of surgical procedures with recovery

Introduced in this chapter is a modified corticectomized rat model of traumatic brain injury previously developed by Lee and co-workers (Lee et al., 2009) for surgical brain injury. The surgical procedure was executed in the following sequence: a) surgical preparation, b) craniectomy, c) corticectomy and d) injury site closure and post-surgical recovery.

a) ***Surgical preparation***

The rats were anaesthetized with an intraperitoneal injection of a 2.7 ml/kg mixture containing: midazolam (1.25 mg/ml), fluanisone (2.5 mg/ml) and 0.079 mg/ml fentanyl. Thereafter the rats were secured in a stereotaxic frame (Kopf/Stoelting, IL, USA) using the ear bars and bite plate. Securing the animal ensured the brain was stable during surgery. A heating pad was placed beneath the animal to maintain body core temperature. Petroleum-based jelly was applied to the eyes of the rat to prevent drying out during surgery. The head of the rat between the ears was shaved to expose the scalp, followed by cleaning with 70% ethanol. A 0.1ml injection of 10ug adrenaline (Merck, SA) and lignocaine hydrochloride (0.02g) (Bayer, South Africa) solution was administered subcutaneously over the skull near the implantation site to minimise post-surgical bleeding. An anti-inflammatory agent (e.g. metacam) was injected intramuscularly for the management of pain. Midazolam and fentanyl-fluanisone were noted to produce substantial analgesia and good muscle relaxation (Flecknell and Mitchell, 1984). Moreover, metacam (NSAID analgesia) was administered during the surgical procedure to provide pain relief and reduce inflammation. For procedures anticipated to result in moderate to severe pain, the use of multiple drugs has been noted to maximise the benefits of analgesia

(McEarlane, 2016). Therefore, the metacam in conjunction with local anaesthetic (lignocaine hydrochloride) and the opioid (fentanyl) were used to provide analgesic effect.

b) ***Craniectomy***

A midline scalp and temporal muscle incision was made to expose the skull. A stereotaxic atlas was used to guide the co-ordinates of the induced TBI lesion. A craniectomy of about 15mm^2 in size was made on the left side of the skull at the area of the motor cortex. A portion of the exposed skull was stereotactically removed using a dental drill and rongeur at the following co-ordinates of three points using the bregma as the reference point (Lee et al., 2009): 1) 4mm rostral and 1 mm lateral, 2) 2mm caudal and 1mm lateral, and 3) 4mm rostral and 6mm lateral. After removal of the skull, the dura was carefully removed using a surgical blade.

c) ***Corticectomy***

A cortical resection method is used. For the corticectomy, the underlying cortex was resected using a punch biopsy technique. The forelimb area of the primary motor cortex with be targeted at the following co-ordinates previously described by Keyvani and co-workers (Keyvani et al., 2000): 1 mm anterior to bregma and 3 mm lateral to the midsagittal suture. A coring tool (Harris Uni-Core (Sigma-Aldrich)) was used to create corticectomy lesions of reproducible size, with minimal damage to the surrounding tissue. The tissue was resected to a depth of 4mm and a diameter of 3mm. The resultant lesion cavity was filled with the proposed scaffold implant in the intervention group, while the sham group was be left to heal naturally. Evidence of survival post a 4mm deep corticectomy in rats has been previously noted, with experimental mortality rate of zero (0) (Hwang et al., 2014; Lee et al., 2013, 2009).

d) ***Injury site closure and post-surgical recovery***

Post injury induction and scaffold implantation, the resected area was sealed with sterile (beeswax/gelfoam) followed by suturing of the wound. The wound was sterilised with an antiseptic. In consideration of the blood loss (minimal), animals were administered Ringers lactate solution for hydration post-surgery. An anaesthetic reversal agent was given to the animal, followed by placement back into their individually housed clean cages in a heated room to allow them to recover. Animals were monitored for TBI associated behavioural abnormalities. Meloxicam Jello cubes were given to the animal's twice daily post-surgery for pain relief at 1mg/kg (when missed 0.2mg/ml). The Meloxicam jello cubes were prepared by adding 30ml flavoured jello powder, 10ml gelatin powder mixing with 100ml hot water. This was allowed to cool till approximately 40°C (5-7minutes), thereafter 86ml jello was mixed with

21mg (14ml) metacam. This was then poured into little rectangular containers and allowed to set in the fridge (2-8°C) and finally cut into 1x1cm squares. One square per 200g Sprague-Dawley rat was given. F10 Germicidal Barrier Ointment was applied not only to prevent infection as a broad-spectrum disinfectant to fight bacteria, fungi and viruses in on the stitches, but to also keep the stitched area from drying and thus improve healing. If allowed to dry, it would lead to irritation of the stitched area, resulting in the rats scratching the area and disturbing the lesion. Qualitative cage side observations of the grooming (SD rat coat), eating and general behavior were made throughout the course of the study in order to monitor the recovery, pain and general well-being of the animal (Figure 6.1.) (Sotocinal et al., 2011). According to the Figure 6.1, observable the pain expression is notable as a progression from zero (no pain present) to a value of two (obvious pain) to allow for notable real-time monitoring and intervention. Food consumption was monitored daily by weight (in grams) of food provided less that recovered and monitoring the weight gain and loss of the animals.



Figure 6.1. Rat Grimace scale. This image was reused from Molecular pain, 7. Sotocinal and co-workers (Sotocinal et al., 2011). The Rat Grimace Scale: A partially automated method for quantifying pain in the laboratory rat via facial expressions, pp 55, 2011, under the terms of the Creative Commons Attribution License (http://creativecommons.org/licenses/by/2.0).

e) ***Terminal procedure***

Rats will be euthanized with an intraperitoneal administration of phenobarbitone (200mg/kg) in order to collect the brain for analysis. Samples were preserved in 10% (v/v) neutral buffered formalin (NBF) at room temperature until histological analysis. Time to fixation is critical, the

between as stress responses are initiated almost immediately after the tissue is deprived of its blood supply. The time between death and initiation of fixation was maintained at less than 20 minutes and recorded.

6.3.5. Histomorphological analysis of brain samples

After sufficient fixation of the collected specimens in 10% buffered formalin, the organs were cut according to the IdexxSA-AP-SOP-26 standard operating procedure and processed according to routine histological tissue processing in an automated tissue processor with standard operating procedures IdexxSA-AP-SOP-27. Following tissue processing, sections were cut of 5-6µm (IdexxSAAP-SOP-30) and the slides produced stained in an automated Haematoxylin and Eosin tissue stainer (IdexxSA AP-SOP-205) before histological evaluation. The complete brain tissue submitted from all 16 cases was sectioned at 3 coronal/transverse cross-sectional areas through the cranial cerebrum (at the broadest level of the lesion), caudal cerebrum and at the cerebellum, including the brain stem attached at the cerebellar peduncles. The broadest cross-sectional microscopic measurement of the defect was taken. Scanning was performed on a Philips scanner, UK Wetherby lab number 1006366093.

6.3.6. Behavioral assessment

6.3.6.1. The cylinder test (limb use asymmetry)

To evaluate forelimb deficits, the animal was placed in a transparent cylinder, 20 cm diameter and 22 cm high (sufficient to allow free rearing and turning around while simultaneously avoiding the animal climbing out) and observed. When placed in the cylinder the rats will engage in exploratory behavior in which they rear and contact the wall of the cylinder with their forepaws (Woodlee et al., 2005). When assessing behavior, the number of independent wall placements observed for the right forelimb (contralateral), left forelimb (ipsilateral) and both forelimbs were recorded for a period of three minutes. No pre-training is required for this test (Schaar et al., 2010). An asymmetry score was calculated as shown by equation 1, where >50% indicate a greater reliance on the ipsilateral limb whereas lower scores <50% indicate a greater reliance on the contralateral limb(Woodlee et al., 2005). Woodlee and co-workers (2005) note this scoring system to enhance sensitivity and reduce variability in the observed results (Woodlee et al., 2005).

6.3.6.2. Adhesive removal test

Somatosensory deficit was measured both before and after surgery. All rats were familiarized with the testing environment. In the initial test, small pieces of adhesive-backed paper squares (of equal size, 1x1cm) were used as tactile stimuli occupying the distal-radial region on the

wrist of each forelimb. The time to notice and remove each the tape was recorded (Chen Jieli et al., 2001).

6.3.6.3. Modified Neurological severity score (mNSS)

A modified Neurological severity score (mNSS) test is a composite of motor (raising the rat by the tail, placing the rat on the floor), sensory (placing test and proprioceptive test) and reflex (reflex and abnormal movements) and balance (beam balance) tests, which enables the assessment of injury severity graded on a scale of 0-18 (Table 6.1 (Yao et al., 2015) (Wen et al., 2017) (Morris et al., 2017). One point is awarded for the inability to perform the tasks or for the lack of a tested reflex. A score of 13-18 indicates severe injury; 7-12 indicates moderate injury; 1-6 indicates mild injury (Chen Jieli et al., 2001). Normal score is represented by a value of 0 and maximal neurological deficit represented by a value of 18(Wen et al., 2017), therefore the higher the score the more severe the injury. This test has been used in previous studies (Guan et al., 2014; Meng et al., 2014; Yao et al., 2015). The mNSS test was carried out on all animals, pre-injury and at various intervals post-injury. The welfare monitoring scoresheet was provided by the CAS and used in combination with the mNSS for welfare monitoring and neurological observation post surgery.

Table 6.1. Modified Neurological Severity Scores (mNSS) is reused and reprinted from PLoS ONE. Yao and co-workers (Yao et al., 2015). Transdifferentiation-Induced Neural Stem Cells Promote Recovery of Middle Cerebral Artery Stroke Rats, 2015 under the terms of the Creative commons Attribution License (CC BY).

S1 Table: Modified neurological severity score (mNSS)

Tests	Points
Motor tests	6
Raising rat by the tail (normal=0; maximum=3)	3
Flexion of forelimb	1
Flexion of hindlimb	1
Head moved >10° to vertical axis within 30 s	1
Placing rat on the floor (normal=0; maximum=3)	3
Normal walk	0
Inability to walk straight	1
Circling toward the paretic side	2
Fall down to the paretic side	3
Sensory tests	2
Placing test (visual and tactile test)	1
Proprioceptive test (deep sensation, pushing the paw against the table edge to stimulate limb muscles)	2
Beam balance tests (normal=0; maximum=6)	6
Balances with steady posture	0
Grasps side of beam	1
Hugs the beam and one limb falls down from the beam	2
Hugs the beam and two limbs fall down from the beam, or spins on beam (>60 s)	3
Attempts to balance on the beam but falls off (>40 s)	4
Attempts to balance on the beam but falls off (>20 s)	5
Falls off: No attempt to balance or hang on to the beam (<20 s)	6
Reflexes absent and abnormal movements	4
Pinna reflex (head shake when touching the auditory meatus)	1
Corneal reflex (eye blink when lightly touching the cornea with cotton)	1
Startle reflex (motor response to a brief noise from snapping a clipboard paper	1
Seizures, myoclonus, myodystony	1
Maximum points	18

Note: One point is awarded for the inability to perform the tasks or for the lack of a tested reflex. A score of 13-18 indicates severe injury; 7-12 indicates moderate injury; 1-6 indicates mild injury.

6.3.6.4. Ladder rung

The ladder rung test was used to assess skilled walking of both hindlimb and forelimb placing. The placing, stepping and limb coordination is measured (Schaar et al., 2010). The spacing of the ladder rungs was varied to prevent a compensatory reliance for impairments through learning the spacing and location of the rungs. Animals with motor system injury have been shown to display impairments with the ladder rung assessment (Schaar et al., 2010).

6.3.6.5. Statistical analysis

Descriptive stats were utilized expressed as mean ± SEM (standard error of the mean) and standard deviation of independent experiments. Experiments were repeated three times.

6.4. Results and discussion

6.4.1. Animal survival, recovery and qualitative behavioral observations and study duration

All animals survived the TBI and implantation of the novel 3-in-1 scaffold. No obvious differences were noted between the treatment groups during qualitative cage side observations of recovery, grooming, eating and ambulation behavior. The animals generally lost weight during the first 2 days post surgery and gained weight thereafter. While the rats had notable deficits involving the contralateral forelimb and hind limb after injury, the deficits improved over time as noted with behavioral assessments later in the chapter. It was noted that all of the animals survived the implantation and the scaffold. This established substantiates that the implantation of the scaffolds is technically feasible in the Sprague-rat model and is tolerated by the animals. Routine hematoxylin and eosin (H&E) staining was conducted for histomorphometric analysis and general histologic observation of the injury and effects of scaffold implantation (Figure 6.2.). Histological data obtained at each survival time (3, 14 and 28 days) were used to compare tissue loss and lesion volumes between the sham and intervention groups. The time-point in this study of 4 weeks was not long enough to track the entire response over a majority of the degradation for the scaffold. However, the time points chosen here reflected important time-points for comparison. Acute inflammation occurs within the first week. Macrophages infiltrate brain injury sites within the first week (Hazy et al., 2020; Wong et al., 2007). Thereafter, chronic inflammation sets in and remains constant. Intervention within the first week is required to aid in attenuating the immune response. Therefore we chose to sample at 3, 14 and 28 days as any differences in the tissue response elicited by the scaffold would have occurred in the first few days and be evident by the 28 day mark.

6.4.2. *In vivo* effect of acellular 3-in-1 hybrid scaffold intervention

6.4.2.1. *In vivo* implantation and decreased bleeding

It was observed during the surgeries that the implantation of the scaffolds (Figure 6.1) decreased bleeding. This effect is similar to the effect of applying a gauze or cotton during surgeries to stop initial bleeding. The added benefit herein with the scaffold is that while acting like a gauze, the scaffold is also an implant therefore does not require removal as a gauze/cotton required removal before closing the lesion.

One of the properties anticipated in surgical scenarios with the scaffold insertion is compression. The scaffold exhibited translational potential in a practical surgical setting. The scaffolds deformable network and shape memory property enabled it to undergo recoverable deformation during surgical transfer into the lesion cavity. This shape-memory property, previously confirmed by the hysteresis curve (compression testing) is important from a translational surgical application perspective. Moreover, the scaffold may in future be explored for delivery in a less invasive injection route due to its observed deformable network and shape memory property.

The experimental design, surgical procedures and technique, coupled with the anesthetics, analgesics and choice of interventions outlined in the methods enabled the successful induction in all animals and resulted in 100% recovery of all animals induced with TBI. All the animals were awake and active within 20minutes post-surgery. This traumatic brain injury model surgical technique and study design may be applied in future for future therapeutic intervention research in brain tissue engineering, repair and regeneration. The present study demonstrated that the TBI injury can be confined and localized while leaving the contralateral side of the brain structurally (Figure 6.2) and functionally intact (behavioral assessment observations).

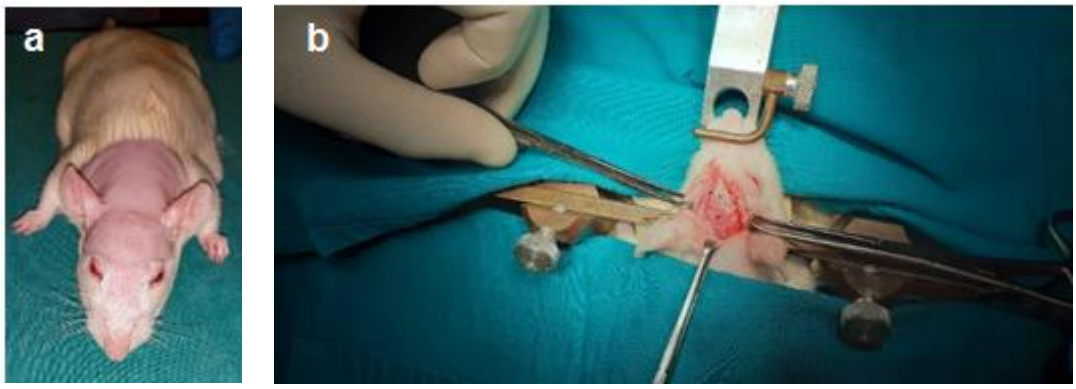

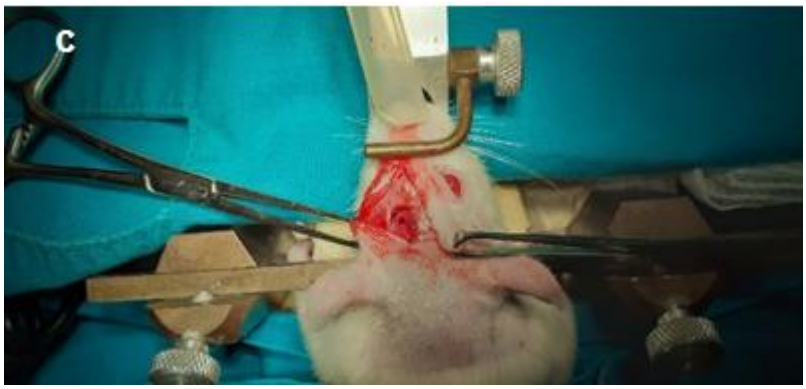







Figure 6.1. Surgical procedures with recovery. a) The head of the rat was shaved between the ears to expose the scalp followed by sterilization with 70% ethanol. b) craniectomy, the

coordinates were: coordinate A=+4,+1; coordinate B=−2,+1; and coordinate C=+4, +6. c) corticectomy. c) Corticectomy. d) Scaffold implantation. e) Scaffold in lesion cavity. f) injury site closure and post-surgical recovery.

6.4.2.2. Shape of brain with or without scaffold implantation

The brain in the sham group showed a distortion and shrinkage of the ipsilateral cerebral cortex, this is notable at days 14 and 28 (Figure 6.2. c, c*). The sham lesions appeared irregularly shaped. However, with the scaffold, remained in the same site for 28 days after implantation and remained almost intact in the brains of all rats (Figure 6.2). The plausible reason for the observed difference would be the fact the scaffold kept the walls of the defect from caving in whereas no structure in the sham group was available to keep the lesion walls from caving in, resulting in the observed tissue distortion.

6.4.2.3. Cell infiltration and tissue formation after scaffold implantation

Newly formed tissue was noted after scaffold implantation. Brain tissue encompassed the scaffold rather than shrinking away from it (Figure 6.2b,b*, d, d* f and f*). This alludes to tissue-scaffold contact. The scaffold remained intact within the lesions without sliding out. This observed tissue-scaffold contact is critical for access, migration and integration of surrounding cells (observed herein) and tissue structures into the scaffold for tissue continuity. The scaffold was well attached to the surrounding brain tissues and the marginal cavities of the scaffolds were progressively occupied by newly formed tissue. Initially at 3 days (Figure 6.2b*) the periphery of the scaffold is surrounded by scant lightly eosinophilic poorly staining serum-like material. This scant eosinophilic poorly staining serum-like material is an expected observation due in part to the breach of the blood-brain-barrier (BBB). The BBB is required for the homeostasis of the neural extracellular environment. The penetrating traumatic brain injury induced herein resulted in the disruption of the BBB causing vasogenic edema(Michinaga and Koyama, 2015; Rahaman and Del Bigio, 2018). Vasogenic edema is characterized by the extracellular accumulation of fluid resulting from the movement of serum/plasma proteins into the brain (Michinaga and Koyama, 2015). This is observed in histological slides as an acelluar esosinophilic material. When macroglia ingest plasma proteins they become engoged and uniformely esosinophilic (Rahaman and Del Bigio, 2018). This serum-like material evolved at 14 days (Figure 6.2d*) to a cellular space, a large number of intact and degenerate neutrophils infiltrated around the scaffold. By day 28 (Figure 6.2f*) fusiform to spindle-shaped mesenchymal/fibroblastic cells had infiltrated the scaffold periphery.

6.4.2.4. *In vivo* 3D structural support, architectural integrity and stability

Figure 6.2.e* shows the day 28 rat sham brain sample. A large elongated almost linear irregular defect consisting of central necrosis that appeared liquefactive was noted at the in the sham sample. Liquefactive necrosis is a type of necrosis that results in the transformation of tissue into a liquid viscous mass (Modo, 2019). This may be indicative of a loss of structural tissue support, cell debri and a disrupted ECM. Alternatively, the scaffold maintained its 3D architecture at the lesion site at day 28 Figure 6.2.f*), when the sham brain had liquefied at the lesion center. This shows the potential role of the scaffold as a viable 3D structural support at the lesion site - to temporarily play the role of the ECM toward augmenting cellular organization into 3D tissue formation.

The defect/lesion cavity is completely filled with the scaffold at day 28 (Figure 6.2 f*). This is indicative of the *in vivo* stability of the scaffold. The interconnected walls of the scaffold are clearly visible in all scaffold intervention groups (Figure 6.2b*, d*, f*). Small fragments of the scaffolding material are visible within the lesion area surrounded by epithelioid macrophages in moderate numbers. The brain is a highly hydrated tissue comprising ~80% water in composition(De Souza and Dobbing, 1971; Mahumane et al., 2018) and the cells contain a large amount of digestive enzymes (hydrolases) that cause the tissue to become soft and liquefy. The scaffold area not becoming liquid and scaffold material presence indicates the effectiveness of the 1,4-butanediol diglycidyl ether crosslinker in stabilizing the soluble scaffolding biomaterials (e.g. hyaluronic acid, gelatin) used in the fabrication of the scaffold. *In vivo* stability is important as this ensures adequate residence time for sturdy support at the lesion site for growing cells, and replacement of the native ECM by the cells.

6.4.2.5. Scaffold intervention on lesion cavity and surrounding tissue

The liquefactive debris will have neurotoxic effects if allowed to permeate to the pericavity space (Zbesko et al., 2018). The glial scar that is formed by reactive astrocyte and microglia to compartmentalize the area of liquefactive necrosis from the rest of the brain is ineffective. Zbesko and co-workers noted that molecules present in the area of liquefactive necrosis leak across the glial scar to the adjacent tissue (Zbesko et al., 2018). Liquefaction was observed more in the sham versus the scaffold intervention brain. The presence of the biomaterial scaffold may thus mitigated the effects of liquefactive damage. In addition, the presence of the scaffold may have played a role in decreasing tissue damage by leading those cells away from the border of the defect or preventing them from reaching the surrounding parenchyma from circulation by acting as a barrier and a trap for the infiltrating cells stemming from the BBB breach. It is possible that this passive prevention by the scaffolds presence at the lesion site may have been able to save some of the parenchyma from delayed death and to slow the

formation of a glial scar in Figure 6.2f* whereas the lesion appears sharply demarcated form the surrounding neuropil.

On day 28, the scaffold is filled with cells, scattered numbers of loose red blood cells and moderate numbers of degenerate neutrophils as well as proteinaceous globular structures. Peripherally, they are also infiltrated by fusiform spindle-shaped mesenchymal/fibroblastic cells. In contrast, the multifocal areas on the periphery of the necrotic region of the sham sample show expansive mineralization/calcification. The area is surrounded by moderate numbers of pigment laden or foamy macrophages compatible with gitter cells, and possibly mild glial cell proliferation. In the sham sample, the lesion is sharply demarcated from the surrounding neuropil and in surrounding grey matter, vacuolization of a mild degree is visible and single small areas of necrosis and calcification are visible. The observed (scaffold intervention, Figure 6.2f*) peripheral infiltration of the fusiform to spindle shaped mesenchymal/fibroblastic cells in the peripheral tissue is promising. *In vivo*, endogenous MSCs are likely activated after TBI and participate in neural recovery (Zhao et al., 2012). The cells can penetrate the BBB, migrate to the injury site, and secrete several factors (NGF, BDNF,GDNF and VEGF), modulate inflammation, regenerate BBB, neuronal and glial tissues (Willing et al., 2020). This observation is promising, a suggestion for the future however, a more accurate interpretation of gliosis, including the types of glial cells that are involved, would require further immunohistological staining and a longer study duration if it is expected to be of translational experimental significance.

6.4.2.6. Architectural vasculature: decreased bleeding, tissue integration potential

The scaffold was designed to be porous and permeable to allow the flow of nutrients, removal of waste products, ingrowth of vascular tissue and other tissue structures and to ensure the survival of cells within the scaffold. It was observed during the surgeries that the implantation of the scaffolds decreased bleeding. This effect is similar to the effect of applying a gauze or cotton during surgeries to stop initial bleeding. The added benefit herein with the scaffold is that while acting like a gauze, the scaffold is also an implant therefore does not require removal as a gauze/cotton required removal before closing the lesion. This is the added benefit of its porosity and permeable network.

The degree of occupation of the scaffold pores is from day 3 to 14 to 28 is progressively increasing (Figure6.2 b*, d*, f*). The pore size distribution of a scaffold should respect the average size of the cellular and tissue components. Figure 6.2 b* (scaffold at 3 days) indicated that the scaffold comprised of loose red blood cells and multifocal small to moderate numbers of neutrophils as well. At day 28, scaffold was filled with cells, scattered numbers of loose red

blood cells and moderate numbers of degenerate neutrophils as well as globular structures (Figure 6.2 f*). This is indicative of integrative property of the scaffold. Cells can migrate into the integrative interconnected porous scaffold and localize inside the scaffold). The novel 3-in1 scaffolds herein had average pore size ranging 59-286µm microns. This pore size distribution accommodates small pores (<80 um), medium pores (80-120um) and large pores (>120um) (Jurga et al., 2011). These small, medium and large pores are optimal for stem cell niche formation, neural network growth and medium and gas exchange respectively (Jurga et al., 2011). The scaffold porosity herein respects the size of an average adult human cell (~20um), pluripotent stem cells (3-5um) and mesenchymal stem cell (30-50um) (Habich et al., 2006; Jurga et al., 2011; Kucia et al., 2007; McGuckin et al., 2005).

The larger pores may have contributed to cell viability (flow of oxygen, nutrients and debri at the site). The scaffolds had a red color that was consistent in all samples, all the way to day 28 (Figure 6.2f*) post intervention. This may be a reflection of the internal vascular connectivity within the sponges, also verified by SEM characterization of the internal microstructure of the scaffold allowing blood to be perfused thoroughly in the scaffold.

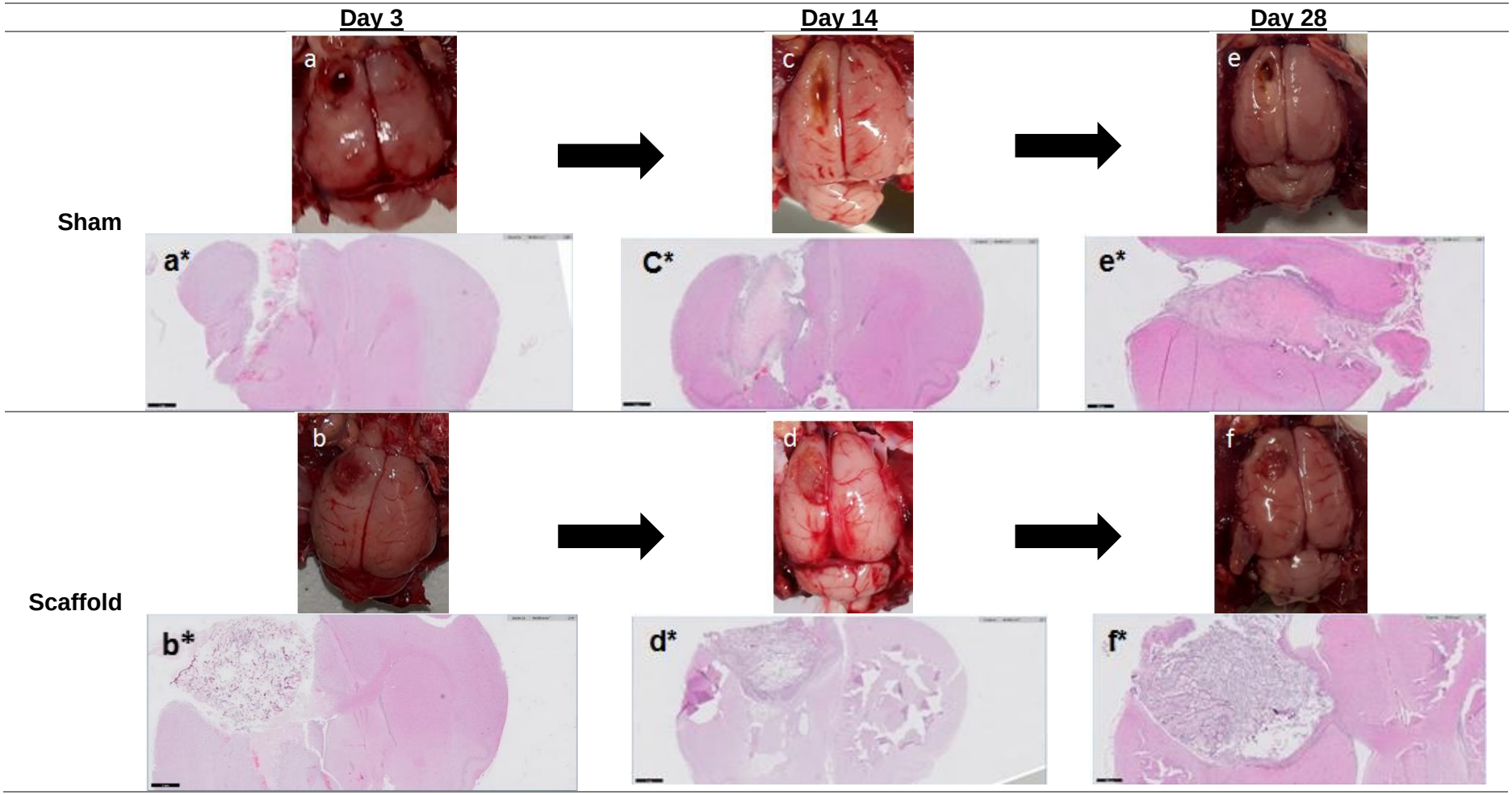

Figure 6.2. (a-f) Gross brain images before preservation in formalin and sectioning illustrating the visual difference at 3, 14 and 28 days post-TBI. (a*- f*) Hematoxylin and eosin (H&E)-stained sections of brain tissue without (a*, c* and e*) and with scaffolds (b*, d* and f*) implants at 3, 14 and 28 days post-TBI. Sham brain sections postoperative 3 days Scale bar: 1mm. b) Scaffold intervention brain sections postoperative 3 days Scale bar: 1mm. c) Sham brain sections postoperative 14 days Scale bar: 1mm. d) Scaffold intervention brain sections postoperative 14 days Scale bar: 1mm. e) Sham brain sections postoperative 28 days Scale bar: 500µm.

6.4.3. Recovery and behavioral analysis

The outcomes of TBI are determined using the Glasgow Outcome Scale using neurobehavioural ranges of recovery: (a) dead; (b) vegetative state; (c) severe disability; (d) moderate disability; (e) good recovery (Jennett and Bond, 1975). Therefore, according to the Glasgow Outcome Scale, the TBI induced herein resulted in good recovery. The rats were able to resume normal life (feeding, grooming walking etc.) despite the minor hind and forelimb deficit. The sensory, reflex, balance and motor performances of the animals were evaluated pre- and post-operatively using the cylinder test, adhesive removal test, mNSS and ladder rung tests. The reproducibility of motor weakness following the induction of TBI injury and the improvement thereafter in the rat models were the main interest.

6.4.3.1. Cylinder test

Figure 6.3 depicts limb use asymmetry. Pre-operative and normal (uninjured) rats prefer to use both limbs equally, whereas rats subjected to TBI favoured use of ipsilateral forelimb post-injury. It has been noted in literature that uninjured animals will often not use their contralateral limbs to balance while rearing along the walls of the cylinder (Gold et al., 2013; Woodlee et al., 2005). Unilateral injury to the brain results in contralateral neurological deficits and compensatory reliance on the less impaired side of the body (ipsilateral to injury) (Schaar et al., 2010). The difference in scores between the control (un-injured) rats and TBI induced rats (Sham and scaffold) was present up to three weeks (day 22 post surgery, Figure 6.3). A similar duration of 3 weeks was noted by Lee and co-workers(Lee et al., 2009). Gradual disappearance of limb preference was noted after 3 weeks (Figure 6.3) for both the sham and intervention group. After 3 weeks of surgery there was no noteworthy difference in limb preference the control and TBI (sham and scaffold) groups. The results herein (Figure 6.3) support the concept of functional behavioral recovery following TBI as described by previous researchers (Gonzalez et al., 2004; Lee et al., 2009).

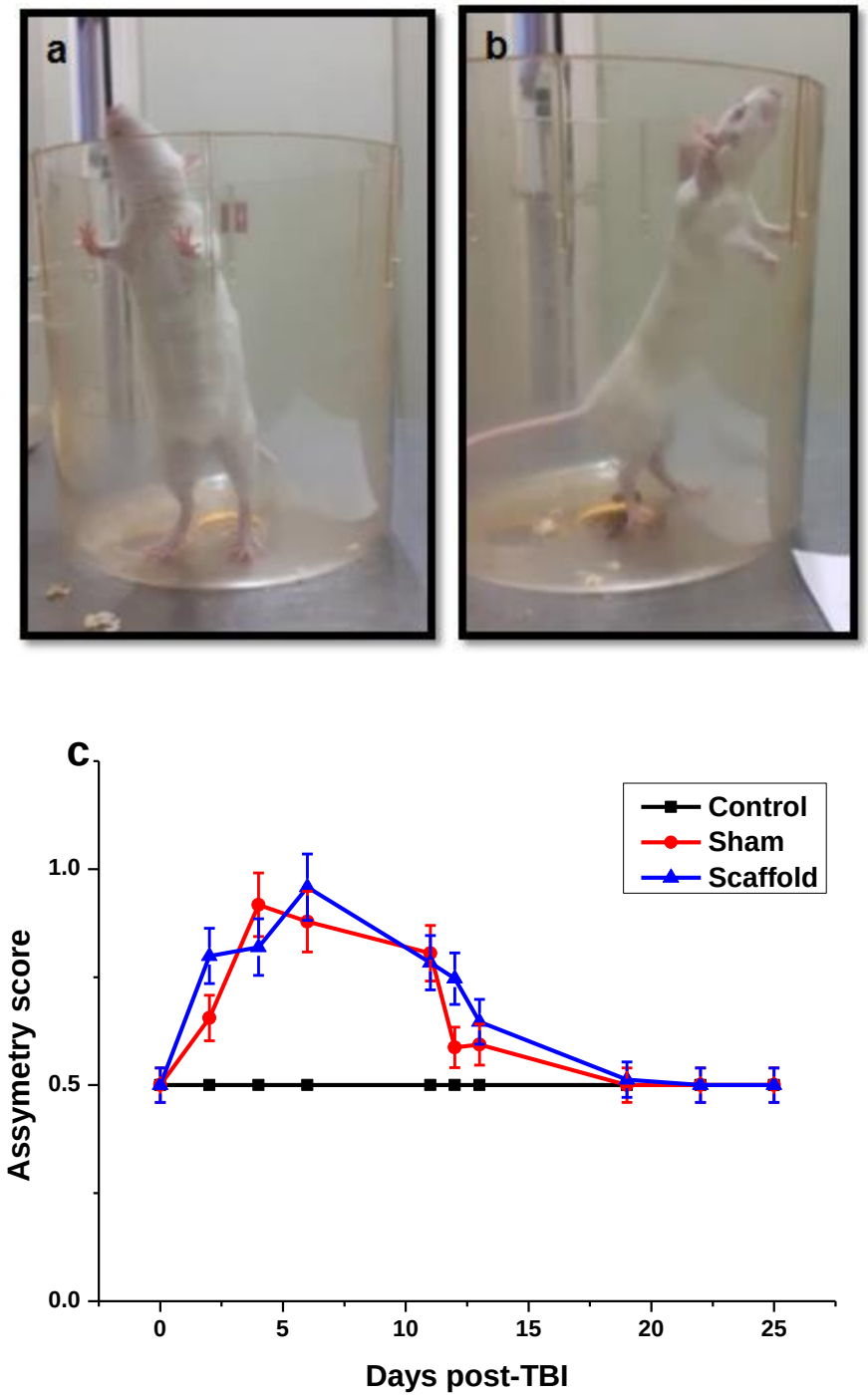

Figure 6.3. Cylinder test (Limb-use asymmetry), a) Uninjured rats spontaneously use both forelimbs, while b) post TBI (sham and scaffold groups) rat's exhibit reliance on the ispilatelateral forelimb. c) Asymmetries in forelimb use in the "cylinder" task assessment. Scores above 0.5 indicate a greater reliance on the unimpaired forelimb (ipsilateral).

6.4.3.2. Adhesive removal

The adhesive-removal test was conducted to evaluate sensorimotor deficits of the Sprague-Dawley rats before, and 3 to 25 days after TBI induction and scaffold intervention. As depicted

by Figure 6.4, the highest impaired function (increased time to detect and remove) was noted after TBI, 3 days, Figure 6.4. There was no significant difference in the sensorimotor activity (faster removal of the sticky dot) between the sham and intervention (scaffold) group. With time, both sham and intervention groups exhibited gradual improvement in sensorimotor activity (removal time was significantly shorter post 7 days after TBI).

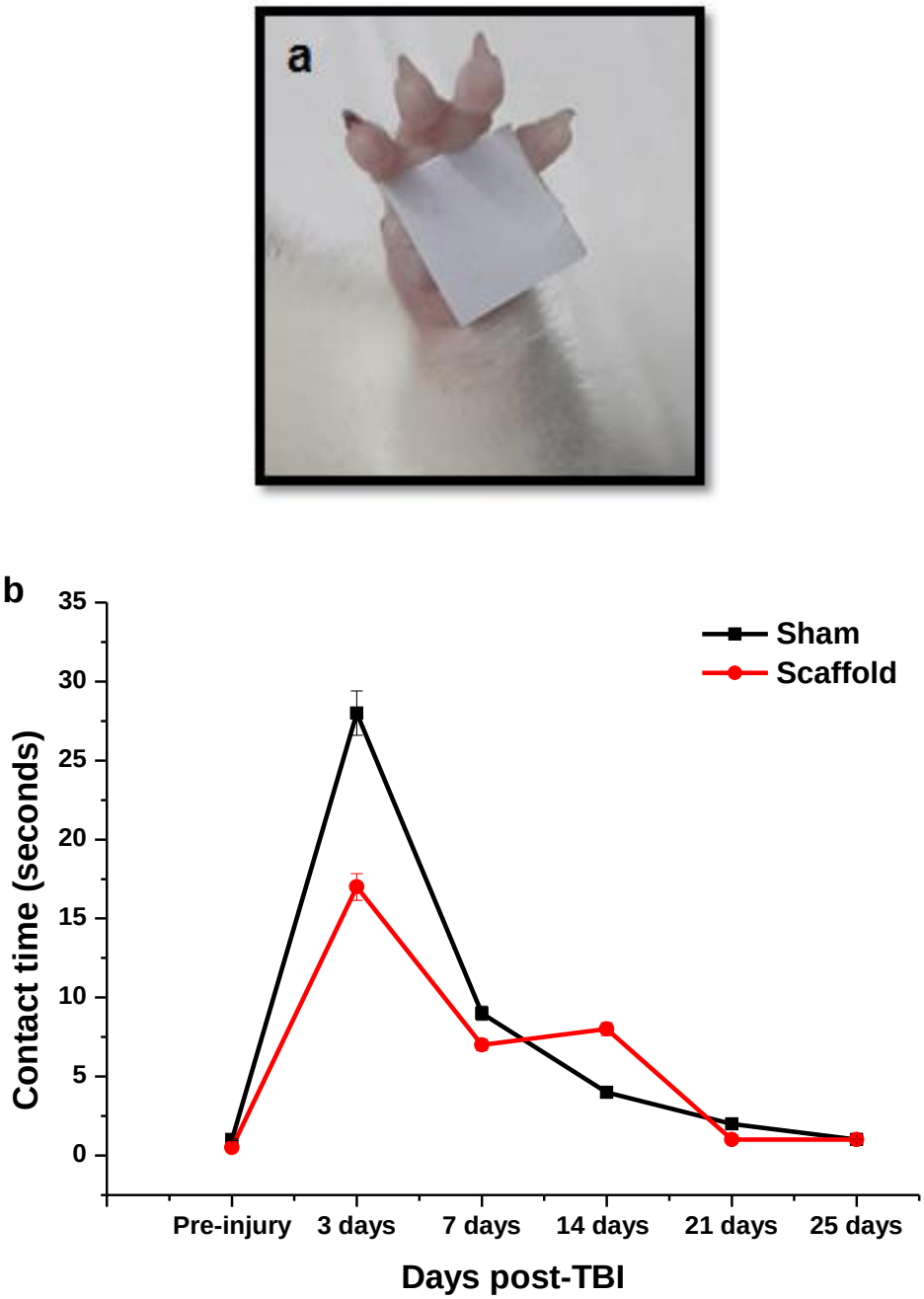

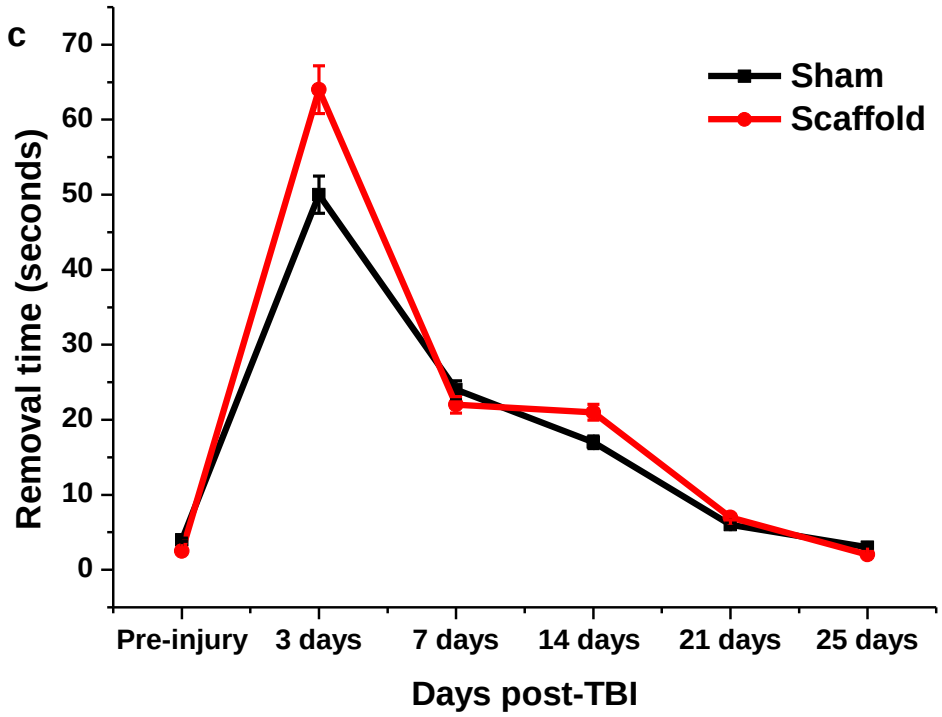

Figure 6.4. Effect of sensory experience on the recovery of tactile sensitivity. a) Adhesive tape plied on the rat paw. b) Tactile abilities post-TBI were assessed using the adhesive removal test in sham versus intervention group.

6.4.3.3. Modified Neurological severity score (mNSS) and ladder rung

Points were awarded for the inability to perform the tasks or for the lack of a tested reflex (normal score 1, maximal deficit score 18). Functional improvement by mNSS evaluation showed similar improvement in sham and intervention groups (Figure 6.5). A modified Neurological severity score (mNSS) test is a composite of motor, balance, sensory and reflex tests, which enables the assessment of injury severity graded on a scale of 0-18 (Table 6.1)(Wen et al., 2017) (Morris et al., 2017). The scores ranged 7.5 – 3.0 and 7.3 – 4.0 for the sham and scaffold intervention groups. This similarity in the ranges indicates to an extent the reproducibility of the surgery technique in producing similar motor, balance, sensory and reflex behaviour in all models and both groups fell within the range of mild to slightly moderate injury.

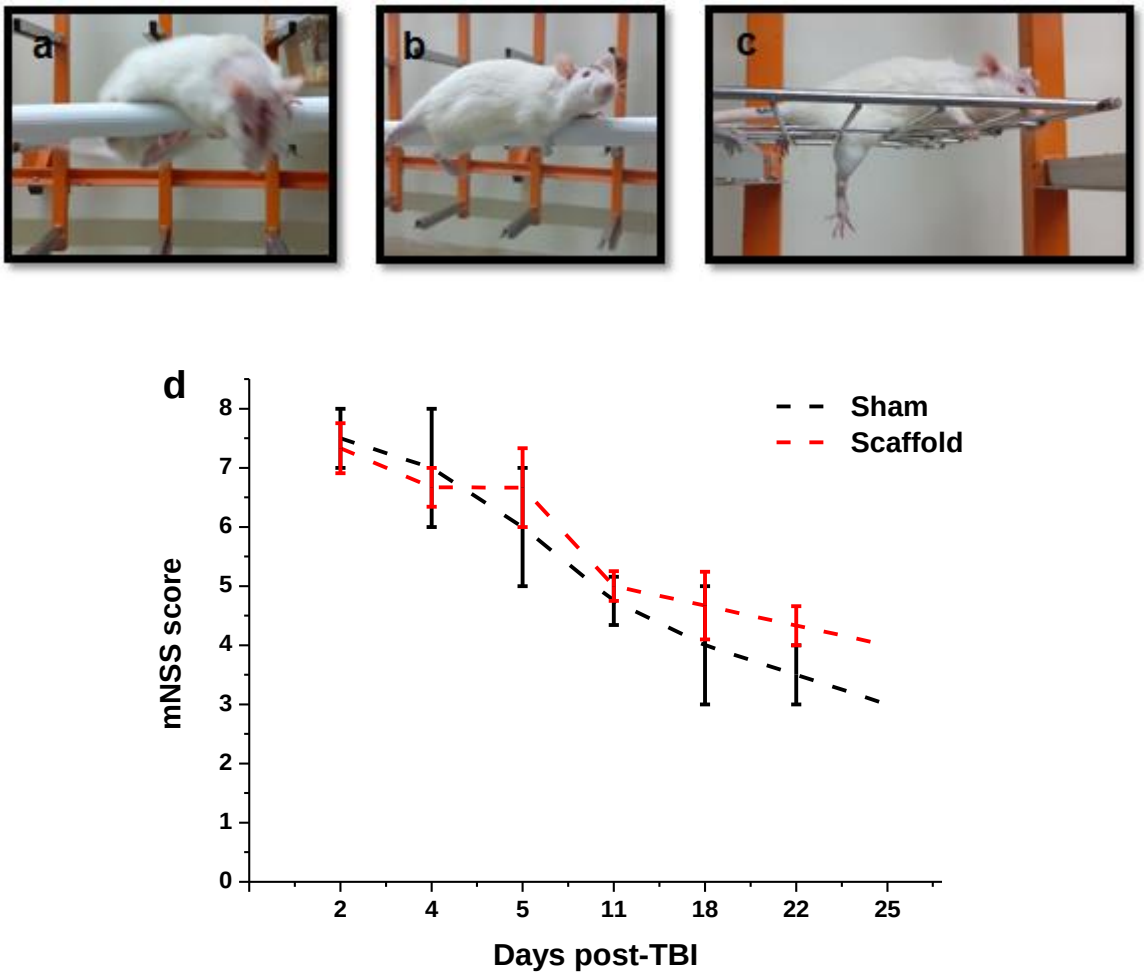

Figure 6.5. Modified Neurological Severity Score (mNSS) observations and results. a) Progression of improvement on beam balance test, initially animals attempted to balance hugging the beam with tow limbs but failed resulting in spinning and falling off, b) progressing to hugging the bean with both limbs but the contralateral limbs slide off the beam due to weakness. c) Photograph indicating a total miss in the contralateral hind limb in the ladder rung task. Total miss (d) Modified Neurological Severity Scores.

6.4.4. Chapter six summary

The present modified traumatic brain injury model is safe (no animals lost) and resulted in selective tissue damage, localized reproducible injury and significant observable reproducible sensory-motor weakness which may be useful for future application in the detection of neurological deficits and therapeutic research in brain tissue engineering, repair and regeneration.

The objective of trying to fill the lesion cavity was achieved successfully with the scaffold implanting procedure used in this study. The approach of hydrating the scaffold prior to implantation appeared to be advantageous due to the favorable alteration of the scaffold properties (softening from swelling). As noted in Chapter five, hydrating the scaffold results in

an increase in scaffold volume, this opening up the pores of the scaffold and increases the compliance of the scaffold network. It was important to hydrate the scaffold prior as practically, the implantation window during surgery is small.

While the scaffold achieved the desired results in some aspects, there remain areas of potential for improvement. For instance, we observed that even though the scaffold was able to fill the lesion cavity, the scaffold lesions were considerably larger that the lesions without scaffold. Additional injury could have occurred during implantation, subsequent expansion *in vivo*, the scaffolds may have been too large or even though the mechanical properties where theoretically similar (Chapter five), the mechanical properties may not have been precise enough to that of the native tissue. With regard to scaffold size, a smaller scaffold in reference to the lesion cavity may have reduced the injury, however, it would have not filled the cavity. We suggest that our choice to use a scaffold the same size as the lesion aided in the ability of the scaffold to fill the lesion cavity for tissue continuity potential and facilitated tissue-scaffold contact.

The novel 3-in1 hybrid scaffold implanted into the lesion remained at the lesion site over a period of up to 28 days, kept its integrity and the integrity of the brain shape and attached well to the surrounding brain tissues. The scaffold internal architecture could be observed i.e. the walls and interconnected pores. Taking into account that the scaffold did not appear to degrade significantly over the period up to 28 days, it is possible the at the novel 3-in1 scaffold could remain *in vivo* for a significantly longer period of time. The time points chosen here were chosen specifically for comparison, the time course of inflammation is as follows, macrophages invade within the first week after which chronic inflammation sets in and continues with consistency (Wong et al., 2007). Therefore scaffold was designed as an intervention in this acute phase. Therefore any differences elicited by the scaffolds will be elicited in the first week. Longer periods of studies would be required in future to determine whether the duration of the scaffold *in vivo* would be harmful or not. This is because macrophages noted at the lesion site have a complex role. On one hand they benefit the brain tissue post-BI by separating the healthy surrounding tissues to minimize further damage, removing tissue debri, promoting angiogenesis, reduce inflammation and promote axon regeneration (Cui et al., 2009; Hunt et al., 1984; Kigerl et al., 2009; Kumar and Loane, 2012; Neumann et al., 2009). On the other hand, macrophages can cause an upregulation of several pro-inflammatory cytokines, increased production of neurotoxic molecules and free radicals contributing to neurotoxicity (Kigerl et al., 2009; Schimmel et al., 2017). Peripheral tissue around the scaffold at day 28 was infiltrated by fusiform spindle-shaped mesenchymal/fibroblastic cells. The capability of MSCs to facilitate motor function recovery

out to 1 month after injury has been noted (Addington et al., 2015). Although mechanisms are not fully understood, the molecules secreted by MSCs could be contributing towards the neuroplasticity of the tissue, aiding to the functional recovery observed. In addition, the present scaffold materials are biodegradable, to allow for the tissues at the lesion site to replace the scaffold at the lesion site. Consistent with all tests was the gradual improvement in motor function. Further in-depth immunohistological studies over longer periods are required to observe the cell types involved and their role in the sustained improvement in motor function over time. The formalin-fixed tissues were fixed in wax for long term preservation in order to conduct future immunohistological analysis should resources be available.

Motor function recovery post brain injury is not well understood. The brain is a highly organized functional responsive network. Mechanisms such as neuroplasticity and vicariation are documented. Neuroplasticity is the ability of the nervous system to change is activity by reorganizing its connections, whereas vicariation is the ability of the one part of the brain to substitute for the function of another (Nishibe et al., 2010; Puderbaugh and Emmady, 2020). Observations may be impacted by behavioral compensation as observed with the shift in dominance of the ipsilateral limb or the concepts of variation and endogenous neuronal plasticity.

6.4.5. References

Addington, C.P., Roussas, A., Dutta, D., Stabenfeldt, S.E., 2015. Endogenous Repair Signaling after Brain Injury and Complementary Bioengineering Approaches to Enhance Neural Regeneration. Biomark Insights 10, 43–60. https://doi.org/10.4137/BMI.S20062

Chen Jieli, Li Yi, Wang Lei, Zhang Zhenggang, Lu Dunyue, Lu Mei, Chopp Michael, 2001. Therapeutic Benefit of Intravenous Administration of Bone Marrow Stromal Cells After Cerebral Ischemia in Rats. Stroke 32, 1005–1011. https://doi.org/10.1161/01.STR.32.4.1005

Cui, Q., Yin, Y., BENOWITZ, L.I., 2009. The role of macrophages in optic nerve regeneration. Neuroscience 158, 1039–1048. https://doi.org/10.1016/j.neuroscience.2008.07.036

De Souza, S.W., Dobbing, J., 1971. Cerebral edema in developing brain: I. Normal water and cation content in developing rat brain and postmortem changes. Experimental Neurology 32, 431–438. https://doi.org/10.1016/0014-4886(71)90009-4

Flecknell, P.A., Mitchell, M., 1984. Midazolam and fentanyl-fluanisone: assessment of anaesthetic effects in laboratory rodents and rabbits. Laboratory Animals 18, 143–146. https://doi.org/10.1258/002367784780891406

Gold, E.M., Su, D., López-Velázquez, L., Haus, D.L., Perez, H., Lacuesta, G.A., Anderson, A.J., Cummings, B.J., 2013. Functional assessment of long-term deficits in rodent models of traumatic brain injury. Regenerative Medicine 8, 483–516. https://doi.org/10.2217/rme.13.41

Gonzalez, C.L.R., Gharbawie, O.A., Williams, P.T., Kleim, J.A., Kolb, B., Whishaw, I.Q., 2004. Evidence for bilateral control of skilled movements: ipsilateral skilled forelimb reaching deficits and functional recovery in rats follow motor cortex and lateral frontal cortex lesions. European Journal of Neuroscience 20, 3442–3452. https://doi.org/10.1111/j.1460-9568.2004.03751.x

Guan, J., Zhang, B., Zhang, J., Ding, W., Xiao, Z., Zhu, Z., Han, Q., Wu, C., Sun, Y., Tong, W., Dai, J., Wang, R., 2014. Nerve Regeneration and Functional Recovery by Collagen-Binding Brain-Derived Neurotrophic Factor in an Intracerebral Hemorrhage Model. Tissue Engineering Part A 21, 62–74. https://doi.org/10.1089/ten.tea.2014.0139

Habich, A., Jurga, M., Markiewicz, I., Lukomska, B., Bany-Laszewicz, U., Domanska-Janik, K., 2006. Early appearance of stem/progenitor cells with neural-like characteristics in human cord blood mononuclear fraction cultured in vitro. Experimental Hematology 34, 914–925. https://doi.org/10.1016/j.exphem.2006.03.010

Hazy, A., Kowalski, E., Groot, N., Theus, M., 2020. Peripheral Immune Response following Traumatic Brain Injury. Advancement and New Understanding in Brain Injury. https://doi.org/10.5772/intechopen.93597

Hunt, T.K., Knighton, D.R., Thakral, K.K., Goodson, W.H., Andrews, W.S., 1984. Studies on inflammation and wound healing: angiogenesis and collagen synthesis stimulated in vivo by resident and activated wound macrophages. Surgery 96, 48–54.

Hwang, D.W., Jin, Y., Lee, D.H., Kim, H.Y., Cho, H.N., Chung, H.J., Park, Y., Youn, H., Lee, S.J., Lee, H.J., Kim, S.U., Wang, K.-C., Lee, D.S., 2014. In vivo bioluminescence imaging for prolonged survival of transplanted human neural stem cells using 3D biocompatible scaffold in corticectomized rat model. PLoS ONE 9, e105129–e105129. https://doi.org/10.1371/journal.pone.0105129

Jennett, B., Bond, M., 1975. Assessment of outcome after severe brain damage. Lancet 1, 480–484. https://doi.org/10.1016/s0140-6736(75)92830-5

Johnson, V.E., Meaney, D.F., Cullen, D.K., Smith, D.H., 2015. Animal models of traumatic brain injury. Handbook of clinical neurology 127, 115–28. https://doi.org/10.1016/B978-0-444-52892-6.00008-8

Jurga, M., Dainiak, M.B., Sarnowska, A., Jablonska, A., Tripathi, A., Plieva, F.M., Savina, I.N., Strojek, L., Jungvid, H., Kumar, A., Lukomska, B., Domanska-Janik, K., Forraz, N., McGuckin, C.P., 2011. The performance of laminin-containing cryogel scaffolds in neural tissue regeneration. Biomaterials 32, 3423–3434. https://doi.org/10.1016/j.biomaterials.2011.01.049

Keyvani, K., Reinecke, S., Abts, H.F., Paulus, W., Witte, O.W., 2000. Suppression of proteasome C2 contralateral to ischemic lesions in rat brain. Brain research 858, 386–92.

Kigerl, K.A., Gensel, J.C., Ankeny, D.P., Alexander, J.K., Donnelly, D.J., Popovich, P.G., 2009. Identification of Two Distinct Macrophage Subsets with Divergent Effects Causing either Neurotoxicity or Regeneration in the Injured Mouse Spinal Cord. J Neurosci 29, 13435–13444. https://doi.org/10.1523/JNEUROSCI.3257-09.2009

Kucia, M., Halasa, M., Wysoczynski, M., Baskiewicz-Masiuk, M., Moldenhawer, S., Zuba-Surma, E., Czajka, R., Wojakowski, W., Machalinski, B., Ratajczak, M.Z., 2007. Morphological and molecular characterization of novel population of CXCR4+ SSEA-4+ Oct-4+ very small embryonic-like cells purified from human cord blood: preliminary report. Leukemia 21, 297–303. https://doi.org/10.1038/sj.leu.2404470

Kumar, A., Loane, D.J., 2012. Neuroinflammation after traumatic brain injury: opportunities for therapeutic intervention. Brain Behav Immun 26, 1191–1201. https://doi.org/10.1016/j.bbi.2012.06.008

Lee, D.-H., Hong, S.H., Kim, S.-K., Lee, C.-S., Phi, J.H., Cho, B.-K., Wang, K.-C., 2009. Reproducible and persistent weakness in adult rats after surgical resection of motor cortex: evaluation with limb placement test. Childs Nerv Syst 25, 1547–1553. https://doi.org/10.1007/s00381-009-0973-9

Lee, D.-H., Lee, J.Y., Oh, B.-M., Phi, J.H., Kim, S.-K., Bang, M.S., Kim, S.U., Wang, K.-C., 2013. Functional recovery after injury of motor cortex in rats: effects of rehabilitation and stem cell transplantation in a traumatic brain injury model of cortical resection. Child's Nervous System: ChNS: Official Journal of the International Society for Pediatric Neurosurgery 29, 403–411. https://doi.org/10.1007/s00381-012-1969-4

Mahumane, G.D., Kumar, P., Du Toit, L.C., Choonara, Y.E., Pillay, V., 2018. 3D scaffolds for brain tissue regeneration: Architectural challenges. Biomaterials Science 6, 2812–2837. https://doi.org/10.1039/c8bm00422f

Marklund, N., 2016. Rodent Models of Traumatic Brain Injury: Methods and Challenges. Methods Mol. Biol. 1462, 29–46. https://doi.org/10.1007/978-1-4939-3816-2_3

McEarlane, S., 2016. NSAID Analgesia for adult rodents SOP meloxicam (metacam). UBC animal care guidelines SOP: Tech 19 - UBC ACC Metacam SOP [WWW Document]. URL https://animalcare.ubc.ca/sites/default/files/documents/TECH%2019%20-%20UBC%20ACC%20Metacam%20SOP%20%282016%29.pdf

McGuckin, C.P., Forraz, N., Baradez, M.-O., Navran, S., Zhao, J., Urban, R., Tilton, R., Denner, L., 2005. Production of stem cells with embryonic characteristics from human umbilical cord blood. Cell Proliferation 38, 245–255. https://doi.org/10.1111/j.1365-2184.2005.00346.x

Meng, Y., Chopp, M., Zhang, Y., Liu, Z., An, A., Mahmood, A., Xiong, Y., 2014. Subacute Intranasal Administration of Tissue Plasminogen Activator Promotes Neuroplasticity and Improves Functional Recovery following Traumatic Brain Injury in Rats. PLoS ONE 9, e106238–e106238. https://doi.org/10.1371/journal.pone.0106238

Michinaga, S., Koyama, Y., 2015. Pathogenesis of Brain Edema and Investigation into Anti-Edema Drugs. Int J Mol Sci 16, 9949–9975. https://doi.org/10.3390/ijms16059949

Modo, M., 2019. Bioscaffold-Induced Brain Tissue Regeneration. Front Neurosci 13. https://doi.org/10.3389/fnins.2019.01156

Morris, D.C., Lee Cheung, W., Loi, R., Zhang, T., Lu, M., Zhang, Z.G., Chopp, M., 2017. Thymosin β4 for the Treatment of Acute Stroke in Aged Rats. Neurosci Lett 659, 7–13. https://doi.org/10.1016/j.neulet.2017.08.064

Neumann, H., Kotter, M.R., Franklin, R.J.M., 2009. Debris clearance by microglia: an essential link between degeneration and regeneration. Brain 132, 288–295. https://doi.org/10.1093/brain/awn109

Nishibe, M., Barbay, S., Guggenmos, D., Nudo, R.J., 2010. Reorganization of motor cortex after controlled cortical impact in rats and implications for functional recovery. Journal of Neurotrauma 27, 2221–2232. https://doi.org/10.1089/neu.2010.1456

Nyanzu, M., Siaw-Debrah, F., Ni, H., Xu, Z., Wang, H., Lin, X., Zhuge, Q., Huang, L., 2017. Improving on Laboratory Traumatic Brain Injury Models to Achieve Better Results. Int J Med Sci 14, 494–505. https://doi.org/10.7150/ijms.18075

Puderbaugh, M., Emmady, P.D., 2020. Neuroplasticity, in: StatPearls. StatPearls Publishing, Treasure Island (FL).

Rahaman, P., Del Bigio, M.R., 2018. Histology of Brain Trauma and Hypoxia-Ischemia. Acad Forensic Pathol 8, 539–554. https://doi.org/10.1177/1925362118797728

Schaar, K.L., Brenneman, M.M., Savitz, S.I., 2010. Functional assessments in the rodent stroke model. Experimental & Translational Stroke Medicine 2, 13. https://doi.org/10.1186/2040-7378-2-13

Schimmel, S.J., Acosta, S., Lozano, D., 2017. Neuroinflammation in traumatic brain injury: A chronic response to an acute injury. Brain Circ 3, 135–142. https://doi.org/10.4103/bc.bc_18_17

Sotocinal, S.G., Sorge, R.E., Zaloum, A., Tuttle, A.H., Martin, L.J., Wieskopf, J.S., Mapplebeck, J.C.S., Wei, P., Zhan, S., Zhang, S., McDougall, J.J., King, O.D., Mogil, J.S., 2011. The Rat Grimace Scale: a partially automated method for quantifying pain in the laboratory rat via facial expressions. Mol Pain 7, 55. https://doi.org/10.1186/1744-8069-7-55

Wen, Z., Xu, Xiaomeng, Xu, L., Yang, L., Xu, Xiaohui, Zhu, J., Wu, L., Jiang, Y., Liu, X., 2017. Optimization of behavioural tests for the prediction of outcomes in mouse models of focal middle cerebral artery occlusion. Brain Research 1665, 88–94. https://doi.org/10.1016/j.brainres.2017.04.001

Willing, A.E., Das, M., Howell, M., Mohapatra, S.S., Mohapatra, S., 2020. Potential of mesenchymal stem cells alone, or in combination, to treat traumatic brain injury. CNS Neuroscience & Therapeutics 26, 616–627. https://doi.org/10.1111/cns.13300

Wong, D.Y., Hollister, S.J., Krebsbach, P.H., Nosrat, C., 2007. Poly(epsilon-caprolactone) and poly (L-lactic-co-glycolic acid) degradable polymer sponges attenuate astrocyte response and lesion growth in acute traumatic brain injury. Tissue Engineering 13, 2515–2523. https://doi.org/10.1089/ten.2006.0440

Woodlee, M.T., Asseo-García, A.M., Zhao, X., Liu, S.-J., Jones, T.A., Schallert, T., 2005. Testing forelimb placing “across the midline” reveals distinct, lesion-dependent patterns of recovery in rats. Experimental Neurology 191, 310–317. https://doi.org/10.1016/j.expneurol.2004.09.005

Xiong, Y., Mahmood, A., Chopp, M., 2013. Animal models of traumatic brain injury. Nature Reviews Neuroscience 14, 128–142. https://doi.org/10.1038/nrn3407

Yao, H., Gao, M., Ma, J., Zhang, M., Li, S., Wu, B., Nie, X., Jiao, J., Zhao, H., Wang, S., Yang, Y., Zhang, Y., Sun, Y., Wicha, M.S., Chang, A.E., Gao, S., Li, Q., Xu, R., 2015. Transdifferentiation-Induced Neural Stem Cells Promote Recovery of Middle Cerebral Artery Stroke Rats. PLOS ONE 10, e0137211–e0137211. https://doi.org/10.1371/journal.pone.0137211

Zbesko, J.C., Nguyen, T.-V.V., Yang, T., Frye, J.B., Hussain, O., Hayes, M., Chung, A., Day, W.A., Stepanovic, K., Krumberger, M., Mona, J., Longo, F.M., Doyle, K.P., 2018. Glial scars are permeable to the neurotoxic environment of chronic stroke infarcts. Neurobiology of Disease 112, 63–78. https://doi.org/10.1016/j.nbd.2018.01.007

Zhao, J., Chen, N., Shen, N., Zhao, H., Wang, D., Shi, J., Wang, Y., Cui, X., Yan, Z., Xue, H., 2012. Transplantation of human umbilical cord blood mesenchymal stem cells to treat a rat model of traumatic brain injury. Neural Regen Res 7, 741–748. https://doi.org/10.3969/j.issn.1673-5374.2012.10.004

CHAPTER SEVEN

STUDY CONCLUSION, RECOMMENDATIONS AND FUTURE OUTLOOK

7.1. Conclusions

Traumatic brain injury is a complex neuro-degenerative disease. Therefore, strategies to design a successful scaffold or any intervention for TBI requires careful planning and evaluation. While the current preliminary knowledge (e.g. secondary injury mechanisms, neural cell line responses to biomaterials) may provide reasonable targets for the development of interventions, the limited global understanding of TBI pathology may be too simplistic to develop an approach that is based on a very limited number of targets. To date, there are no therapies for TBI of clinical standard. Although a decellularized brain tissue matrix would be the best choice for a neural tissue engineering scaffold, the limitation of brain tissue as an accessible resource is a great obstacle for the practical application of this type of scaffold (decellularised native tissue matrix). Mimic the architecture of the ECM as close as possible is one potentially viable alternative.

Cavitary defects the brain tissue stemming from injury (e.g. removal of tumours) may require novel interventions that offer a tissue-mimetic pro-regenerative platformative bridging functions while delivering therapeutics to enhance tissue repair and tissue discontinuity.
Tissue engineered scaffolds have shown various degrees of experimental success and potential. Therefore, the aim of this study was to fabricate a neuromimetic scaffold for potential tissue engineering application. A scaffold was designed to mimic the 'tissue building requirement needs'. When referring to 'tissue building requirement need' we refer to the extracellular matrix. A noteworthy feature of ECM's is that the ECM is unique in architecture and composition to the particular organ and its functions. The brain ECM has been previously described as 'resembling foam', a porous fluid-saturated solid' and 'fluid-bathed multiphase material' with interconnected channels of irregular size and shape (Mahumane et al., 2018). Or the more descriptive "intricate interwoven fiber meshwork of collagen and elastic fibers embedded in a highly hydrated gel-like material of glycosaminoglycans, proteoglycans, and glycoproteins (Lee et al., 2008). With this imagery, we endeavoured to design a neuromimetic scaffold; a scaffold that mimics the brain tissue extracellular matrix architecture. We therefore proposed a 3-in-1 system wherein nanofibers were "in-process" embedded into a cryogel scaffold followed by filling of the macro-microporous architecture with an ECM-mimicking

hydrogel. The polymers used herein were FDA-approved and most importantly they were specifically selected based on processibility and their ability to enable us to mimic the composition of the native brain ECM. For example, hyaluronic acid is the main structural backbone of the native brain ECM. The proteins, polylysine, gelatin, and elastin to facilitate cell attachment. N-acetylcysteine incorporated was used for its antioxidant properties and to show therapeutic drug delivery potential. Poly(lactic-co-glycolic acid) PLGA has shown neural tissue application potential. The crosslinker, BDDE was added to improve the aqueous stability as most of these materials are water soluble and the brain is estimated 80% water.

Individual systems were successfully fabricated in the form of hydrogels, nanofibers, cryogels via chemical crosslinking, electrospinning and the cryogelation method respectively. The ease of the fabrication process parameters (e.g. polymerization temperature, flow rate, polymer ratios) enabled tunability of scaffold properties (e.g. porosity, nanofiber diameter). The fabrication process was inexpensive, simple and reproducible. Independently, the systems showed desirable scaffolding properties. Neuronal cell lines PC12 and A172 exhibited viability and proliferation (NAC-loaded nanofibers) with all three individual systems.

Using a brain ECM-based hybrid multicomposite system design approach enabled us to mimic the complex hierarchical hybrid 3D nano-micro-macroporous architecture of the native brain tissue to a significant degree. The use of BDDE is reported herein for neural application and proved to be an effective crosslinker as shown by the *in vivo* stability of the otherwise water soluble biomaterials (e.g. hyaluronic acid, gelatin). The BDDE crosslinked 3-in-1 composite scaffold not only combined the advantages of processing conditions (electrospinning, cryogelation), biomaterials (gelatin, HA, PLGA, NAC) and components (hydrogel, nanofibers and cryogel), but exhibited new features, for example glass transition temperature, architecture, swelling ratio, cytotoxicity which arose from new interactions occurring between scaffold components. Scanning electron microscopy revealed a 3D nanoreinforced structure with interconnected pores, this indicates that the scaffold structure is simultaneously supportive and integrative. The scaffold further showed potential for cell culture, *in vivo* and drug delivery applications. The research presented is our way of contributing data to the progression of research efforts for traumatic brain injury therapies.

In this study we highlighted BDDE as a scaffolding crosslinker from *in vitro* assays on neuronal A172 and PC12 adherent cells and a follow-up *in vivo* study on Sprague-Dawley rats. The neural cell viability and *in vivo* stability of the BDDE crosslinked scaffolds highlights BDDE as a potential viable crosslinker for neural (brain) tissue application. Future work evaluating the safety of BDDE as a crosslinker for neural tissue would add value to its application potential

as 1,4-Butanediol diglycidyl ether crosslinked hyaluronic acid products have already been approved by the US Food and Drug Administration (FDA) as a soft tissue filler with stability, biodegradability and a long safety record has spanning over 15 years (Yang et al., 2016).

In vivo experiments showed that the scaffold was integrative, infiltration of brain tissue material, and cells was noted within the scaffold due to its interconnected porous design. The scaffold was integrative. This study has demonstrated that brain lesion cavities in the Sprague-Dawley rat brain were successfully filled with the novel 3-in-1 scaffold biomaterial system. Brain tissue material (red blood cells, neutrophils, proteinaceous globular structures, and other cells were noted to have crossed the interface between the scaffold and the native brain tissue to infiltrate the scaffold pores. The density of non-scaffolding tissue derived material significantly increased within the scaffold pores from 3 days to 28 days.

While not indicative of a regenerative response, the results suggest that the novel 3-in1 scaffold system has properties of an implantable scaffold to fill the lesion cavity. By filling the cavity, the potential exists for repopulation of tissue at the lesion site with exogenous or endogenous cells to facilitate tissue repair.

7.2. Recommendations

Although we cannot clinically use this novel 3-in-1 scaffold at the present moment, further studies may make this scaffold a novel tool for tissue engineering application. These further studies in particular refer to immunohistology and longer *in vivo* experiments. Immunohistological staining is recommended for future work to derive a more accurate interpretation of gliosis, including the cells types that are involved in the newly forming tissue. This would substantially improve the interpretation of the events at the lesion site, inside the scaffold and the tissue surrounding the lesion site for future work to derive experimental significance towards clinical translation potential. Moreover, this is recommended not only for the novel 3-in-1 scaffold, but also for the individual component systems (nanofibers, hydrogel, cryogel). This recommendation is informed by the observed differences in the *in vitro* influence on PC12 and A172 neural cell line viability of the components. The recommended staining is for: bromodeoxyuridine (BrdU), glial fibrillary acidic protein (GFAP), ionized calcium adapter molecule-1 (Iba1) and neuron-specific nuclear protein (NeuN), these are markers to identify newly produced cells (newly synthesised DNA), differentiating astroglial, microglial and neuronal cells respectively. Further in-depth immunohistological studies over longer periods are required to observe the cell types involved and their role in the sustained improvement in motor function over time. It is for this reason that the formalin-fixed tissues were fixed in wax

for long term preservation to allow for future immunohistological analysis should resources be available.

The scaffold was designed as an acute phase intervention. Acute inflammation occurs within the first week after which chronic inflammation sets it (Wong et al., 2007). Therefore, interventions to prevent subsequent injury are needed during the acute phase. We were able to successfully apply the scaffold as an acute intervention due to its easy of handling and implantation during the surgical procedure. The scaffold showed a deformable network with shape-memory behaviour. It is recommended therefore that future work would benefit from further exploring the injectability of the scaffold. If applied via injection, this would minimise implantation associated trauma and potential contamination of the scaffold between packaging and implantation.

The present modified traumatic brain injury model is safe (no animals lost) and resulted in selective tissue damage, localized reproducible injury and significant observable reproducible sensory-motor weakness which may be useful for future application in the detection of neurological deficits and therapeutic research in brain tissue engineering, repair and regeneration. Motor function recovery post brain injury is not well understood. The brain is a highly organized functional responsive network. Mechanisms such as neuroplasticity and vicariation are documented. Neuroplasticity is the ability of the nervous system to change is activity by reorganizing its connections, whereas vicariation is the ability of the one part of the brain to substitute for the function of another (Nishibe et al., 2010; Puderbaugh and Emmady, 2020). Observations may be impacted by behavioural compensation as observed with the shift in dominance of the ipsilateral limb or the concepts of variation and endogenous neuronal plasticity. A limitation of this study includes the length of experimental *in vivo* studies. Longer observations of animals is recommended for future work to determine the progressive effects of the scaffold at the lesion site and behavioural recovery. This may determine whether functional or scar tissue is formed. A longer time point will also be able to track the entire degradation response of the scaffold as it is being remodelled and replaced by new tissue at the lesion site. Such an observation would yield very insightful results on the ECM remodelling patterns and tissue formation (e.g. sequence in which ECM elements are laid down first, sequence of cell infiltration).

7.3. Future Outlook

The novel 3-in-1 scaffold design herein may serve as a prototype for future composites that will combine the benefits of multiple systems, hybridization for tissue engineering

applications targeting various soft tissues (e.g. pulmonary tissues, bold vessels, cardiac tissue).

Four specific scaffold systems were presented, namely nanofibers, cryogel, hydrogel and the novel 3-in-1 scaffold. All four systems showed neural cell application potential and PC12 and A172 neural cell line viability. This is a contributory step forward in the area of biomaterials for artificial tissue phantoms for surgical training. These scaffolds may offer surgeons the practical tactical experience required without limited restrictions to practice operations due to the ease of production of the scaffolds and there are not ethical issues
To achieve a therapeutic breakthrough in TBI interventions, future work would benefit from multifaceted approach. This would require combining information and data from multiple sources. Subia and co-workers initiated a step toward the organization of data integration to aid biologist and material scientists towards optimizing data and informing standards (Subia et al., 2012). A large amount of data has been generated over the years in the field of biomaterials sciences seeking to created tissue-mimetic pro-regenerative implant for tissue repair and regeneration. This means there is a great amount of data on various scaffold systems, fabrication methods, biomaterials, innovations and discoveries to inform designs and future research work in the area. All these scaffolds show “experimental success” or “potential” with no scaffold of consummate results of clinical standard to date. The scientific community would benefit greatly from an appropriate biomaterial database, to not only prevent duplication of research efforts but also gain information about recent developments, progress, biomaterial combinations, outcomes and most importantly, have an informed database when initiating research to accelerate and optimise research investment, funding and resources towards the progression of TBI therapies. This would require an unlikely collaboration between academics and programmers. A continuous critical assessment in this field and dialogue among the academics and programmers will contribute immensely in knowledge sharing, establishing standards for assessments (*in vitro, in vivo*), sharing resources, assessments and thus accelerate scientific advancement towards bridging the gap between ‘experimental success’ and ‘clinical translational success’ of the scaffolds (Subia et al., 2012). The data stemming from this research (e.g. biomaterial ratios, combinations, fabrication parameters) can be utilized to feed into the proposed database. And highlighted recommendations suggested herein and missed analysis (such as crosslinking density and porosity relationships) can be used to inform the research gaps that need attention. With the rise of artifical intelligence and technologies like 3D printing, these technologies should be evaluated for application as an expedient tools to create a database of scaffold variables and various tissue-specific ECM algorithims and computer aided design templates and to enable the extraction of usable, translatable data from the scattered patterns of experimental lab “potential”, developing a

platform to marry structure-biological-response pattern reference base to propel current tissue engineering efforts beyond “scaffolds for potential application”. To ensure the sustainability and affordability of national healthcare systems and programs, healthcare expenditure needs to be strategic. The creation of databases can aid in sourcing funding for research of this type through the speedy production of prototypes and more predictable information. It is therefore imperative to prioritize high quality research to build capacity (human resource, research centres, industry and therapies) in order to best utilize current research knowledge in many institutions to inform infrastructure development and ultimate industrialization.

In conclusion, the research and resulting developed novel 3-in-1 scaffold documented in this thesis holds potential not limited to neural tissue regeneration but extends to the domain of other tissue-engineering and regenerative medicine applications requiring the combination of cell culture, advanced drug delivery techniques. The scaffold exhibited neuromimetic properties, cell culture, drug delivery and implant application potential for brain tissue. The research presented is our way of contributing data to the progression of research efforts for traumatic brain injury therapies.

7.4. References

Lee, J., Cuddihy, M.J., Kotov, N.A., 2008. Three-Dimensional Cell Culture Matrices: State of the Art. Tissue Engineering Part B: Reviews 14, 61–86. https://doi.org/10.1089/teb.2007.0150

Mahumane, G.D., Kumar, P., Du Toit, L.C., Choonara, Y.E., Pillay, V., 2018. 3D scaffolds for brain tissue regeneration: Architectural challenges. Biomaterials Science 6, 2812–2837. https://doi.org/10.1039/c8bm00422f

Nishibe, M., Barbay, S., Guggenmos, D., Nudo, R.J., 2010. Reorganization of motor cortex after controlled cortical impact in rats and implications for functional recovery. Journal of Neurotrauma 27, 2221–2232. https://doi.org/10.1089/neu.2010.1456

Puderbaugh, M., Emmady, P.D., 2020. Neuroplasticity, in: StatPearls. StatPearls Publishing, Treasure Island (FL).

Subia, B., Mukherjee, S., Bahadur, R., Vitor, C., Reis, L., Sabarinathan, R., Sekar, K., Kundu, S., 2012. Biomat _dBase: A Database on Biomaterials. Tissue Engineering and Regenerative Medicine Journal 5, 59–67. https://doi.org/1875-0435/12

Wong, D.Y., Hollister, S.J., Krebsbach, P.H., Nosrat, C., 2007. Poly(epsilon-caprolactone) and poly (L-lactic-co-glycolic acid) degradable polymer sponges attenuate astrocyte response and lesion growth in acute traumatic brain injury. Tissue Engineering 13, 2515–2523. https://doi.org/10.1089/ten.2006.0440

Yang, R., Tan, L., Cen, L., Zhang, Z., 2016. An injectable scaffold based on crosslinked hyaluronic acid gel for tissue regeneration. RSC Advances 6, 16838–16850. https://doi.org/10.1039/c5ra27870h

APPENDIX A

ETHICS CLEARANCE CERTIFICATE

STRICTLY CONFIDENTIAL

ANIMAL ETHICS SCREENING COMMITTEE (AESC)

CLEARANCE CERTIFICATE NO. 2017/08/49/D

APPLICANT: Ms G Mahumane

SCHOOL: Pharmacy and Pharmacology
DEPARTMENT:
LOCATION:

PROJECT TITLE: Determination of the effect of an acellular scaffold implant in Sprague-Dawley rat model with traumatic brain injury

Number and Species

16X 6-8 week old 250g female Sprague-Dawley live rats and 8X 6-8 week old 250g female Sprague-Dawley cadaver rats

Approval was given for the use of animals for the project described above at an AESC meeting held on 2017/08/29. This approval remains valid until 2019/10/09.
Unreported changes to the application may invalidate the clearance given by the AESC
An annual progress report must be provided

The use of these animals is subject to AESC guidelines for the use and care of animals, is limited to the procedures described in the application form and is subject to any additional conditions listed below:

Signed: _____ Date: 11 October 2017
(Chairperson, AESC)

I am satisfied that the persons listed in this application are competent to perform the procedures therein, in terms of Section 23 (1) (c) of the Veterinary and Para-Veterinary Professions Act (19 of 1982)

Signed: _____ Date: 11/10/2017
(Registered Veterinarian)

cc: Supervisor: Professor V Pillay, Professor Y Choonara and Dr P Kumar
Director: CAS

Works 2000/lain0015/AESCCert.wps

APPENDIX B

CONFERENCE PROCEEDING: 5TH BRICS YOUNG SCIENTIST FORUM (2020)

Bioarchitecture-mimicking medical materials: A hybrid NAC-loaded biomaterial scaffolding system for potential biomedical applications

G.D. Mahumane, P. Kumar, Y. E. Choonara and V. Pillay

Wits Advanced Drug Delivery Platform Research Unit, Department of Pharmacy and Pharmacology, School of Therapeutic Science, Faculty of Health Sciences, University of the Witwatersrand, Johannesburg, 7 York Road, Parktown, 2193, South Africa.

Abstract

Introduction/objectives: Traumatic brain injury (TBI) is the greatest contributor to global death and disability among all trauma related injuries. It is a silent global epidemic and interventions for TBI are sorely lacking (therapies, funding, dedicated research centers, and human resource). While tissue engineered biomaterial scaffolds have shown various degrees of experimental success, there is yet to be a 3D scaffold that exhibits consummate results of an effective clinical standard to date.

Discussion: A novel neuro-mimetic scaffold was fabricated through the design of a 3-in-1 system wherein NAC-loaded nanofibers were “in-process” embedded into a cryogel scaffold followed by filling of the macro-microporous architecture with a hydrogel. The hybrid scaffold presented with an interconnected nano-micro-macro-porous architecture. The scaffold had tunable structural and hydrophilic properties; a compressive moduli of 0.12kPa and 1.45kPa for the hydrated and dry state, fast swelling rate and low equilibrium swelling ratio of 15 within 24hours, potentially capable of quickly filling the lesion cavity without compressing the surrounding tissue following surgical implantation. N-acetylcysteine was released in a biphasic pattern, an initial burst release stage (13,9%) followed by sustained release. In vitro neural cytocompatibility of the 1,4-butanediol diglycidyl ether (BDDE) cross-linked scaffold to both PC12 and A172 neural cell lines was evidenced by 84% and 81% cell viability values respectively.

Recommendation: Incorporating artificial intelligence as an expedient tool to create a database of tissue engineering variables and data mining, thus extracting usable, translatable data for evidence-based designs and formulations.

Conclusions: The research presented contributes data to the design and fabrication of a tailor-made hybrid nano-micro-macro scaffolding system with tunable properties that retains and exhibits sustained release of NAC while maintaining PC12 and A172 cell viability for potential neural tissue engineering application. Further evaluation with *in vivo* analysis will be conducted to determine the extent of the potential.

APPENDIX C

CONFERENCE PROCEEDINGS: South African Medical Research Council (2019)

Synthesis and characterization of N-Acetylcysteine-loaded PLGA nanofibers as a neuro-scaffold

G.D. Mahumane, Y.E. Choonara, P. Kumar and V. Pillay

Wits Advanced Drug Delivery Platform Research Unit, Department of Pharmacy and Pharmacology, School of Therapeutic Science, Faculty of Health Sciences, University of the Witwatersrand, 7 York Road, Parktown, Johannesburg, South Africa.

Abstract

Background: Traumatic brain injury often results in irreversible damage to the patient. To date, there are no therapies that have translated to clinical practice for traumatic brain injury (TBI). N-Acetylcysteine (NAC) has potential as an antioxidant and neuroprotective pharmacological candidate. However, the drug suffers low bioavailability. Nanofibers have the potential as scaffolding and drug delivery systems for soft tissue application. This research seeks to fabricate and characterise NAC-loaded PLGA nanofibers for the potential as a stable drug-eluting scaffolding system.

Methods: The nanofibers were prepared using the via blend electrospinning technique. The fibres were characterised by scanning electron microscopy, XRD, DSC, TGA, FTIR, water contact angle measurement and tensile testing. The drug entrapment, loading, and release were characterised with the aid of UV/Vis spectroscopy.

Results: Interconnected porous nanostructures with nanofiber diameters ranged from 90-370 nm. The T_g of the NAC/PLGA nanofibers was above the physiological temperature of 37°C. DSC and XRD suggest that the drug is in a disordered crystalline phase of dispersion throughout the PLGA polymer matrix. Drug entrapment efficacy was obtained at 84%, and drug loading was obtained at 28%. A biphasic drug release profile with an initial 13.9% cumulative percentage release was achieved within the first eight hours.

Conclusion: This work focused on the approach that can be used in fabricating nanofibers capable of delivering antioxidant drug NAC to the brain. Morphology, physicochemical and physico-mechanical characterisation of the nanofibers attest to their stability and ability to mimic nanoscale extracellular matrix feature. The biphasic release profile of the drug was observed as a result of the efficient encapsulation of the drug. Thus, the drug will be present for a prolonged period to induce effect even at a later stage where conventional treatments are limited to induce a therapeutic effect.

APPENDIX D

CONFERENCE PROCEEDINGS: South African Medical Research Council (2018)

Synthesis and characterization of a nanoengineered biomedicated (NAC-eluting) PLGA nanofibrous scaffold

Gillian Dumsile Mahumane, Pradeep Kumar, Yahya Essop Choonara and Viness Pillay

Wits Advanced Drug Delivery Platform Research Unit, Department of Pharmacy and Pharmacology, School of Therapeutic Science, Faculty of Health Sciences, University of the Witwatersrand, 7 York Road, Parktown, Johannesburg, South Africa

Abstract

Background: Traumatic brain injury often results in irreversible damage to the patient. To date, there are no therapies that have translated to clinical practice for traumatic brain injury (TBI). N-Acetylcysteine (NAC) has potential as an antioxidant and neuroprotective pharmacological candidate, however the drug suffers low bioavailability. Nanofibers have potential as both scaffolding and drug delivery systems for soft tissue application. This research seeks to fabricate and characterise NAC-loaded PLGA nanofibers for potential as a stable drug eluting scaffolding system.

Methods: The nanofibers were prepared using the via blend electrospinning technique. The fibres were characterized by scanning electron microscopy (SEM), XRD, DSC, TGA, FTIR, water contact angle measurement and tensile testing. The drug entrapment, loading, and release was characterised with the aid of UV/Vis spectroscopy.

Results: Interconnected porous nanostructures with nanofiber diameters ranging 90-370nm. The Tg pf the NAC/PLGA nanofibers was above the physiological temperature of 37°C. DSC and XRD suggest that the drug is in a disordered crystalline phase of a dispersion throughout the PLGA polymer matrix. Drug entrapment efficacy was obtained at 84% and drug loading was obtained at 28%. A biphasic drug release profile was with an initial 13.9% cumulative percentage release within the first 8 hours. Concluding observations: This work focused on

the approach that can be used in fabricating nanofibers capable of delivering antioxidant drug NAC to the brain. Morphology, physicochemical and physico-mechanical characterisation of the nanofibers attest to their stability and ability to mimic nanoscale extracellular matrix feature. The biphasic release profile of the drug was observed due to the efficient encapsulation of the drug. This means the drug will be present for a prolonged period to induce effect even at a later stage where conventional treatments are limited induce therapeutic effect.

APPENDIX E

CONFERENCE PROCEEDINGS: South African Medical Research Council (2017)

Fabrication and characterization of a 3D, hybrid scaffold for neural tissue engineering

G.D. Mahumane, P. Kumar, Y. Choonara, V. Pillay

Wits Advanced Drug Delivery Platform (WADDP), Department of Pharmacy and Pharmacology, University of the Witwatersrand, Johannesburg, Gauteng, South Africa

Abstract

Background: Traumatic brain injury (TBI) often results in irreversible, costly and debilitating damage, in part, because of the lack of effective therapies. Through the provision of physical and chemical cues to augment repair, scaffolds in the field neural tissue engineering show great application potential. Unfortunately, current scaffolds have proven limited in functional repair and efficacy, suffering from poor design, poor mechanical properties and fast degradation.

Objective: To fabricate and characterize the properties of a 3D hybrid scaffold comprising nanofibers embedded in a squeezable, highly porous cryogel matrix which exhibit fast, extensive swelling behaviour, mechanical stability for neural tissue repair post-TBI.

Methods: Conducting poly (lactic-co-glycolic acid) (PLGA) nanofibers were prepared by electrospinning followed by coating with a conducting polymer (polypyrrole) via admicellar polymerization. Thereafter, these fibers were dispersed in a gel comprising hyaluronic acid with BDDE as a crosslinker. This nanofiber/gel solution was then subjected to cryogelation at sub-zero temperatures to produce a nano-reinforced cryogel matrix.

Results: Scanning electron microscopy and surface conductivity tests were used to determine optimal conditions for polymerization. Cryogelation conditions such as pH, freezing temperature, polymerization time/degree of crosslinking, and composition of gel solution were varied to determine their influence on gel properties. Characterization was completed by

obtaining FTIR, TGA, DCSC, NMR, swelling ratio, texture analysis and scanning electron microscopy imaging.

Conclusion: Material properties of this 3D hybrid scaffold will elucidate conditions for the fabrication of a suitable pro-regenerative platform with sufficient contact guidance cues migratory cues to augment neural regeneration post implantation.

APPENDIX F

CONFERENCE PROCEEDINGS: South African Medical Research Council (2016)

Nano-reinforced hydro-filled cryogel scaffold for neural tissue regeneration

G. Mahumane, Y. Choonara, P. Kumar and V. Pillay

University of the Witwatersrand, Wits Advanced Drug Delivery Platform Research Unit, Department of Pharmacy and Pharmacology, Faculty of Health Sciences, Johannesburg, South Africa

Abstract

Background: Traumatic brain injury (TBI) often results in irreversible damage due to the limited regenerative ability of the Central Nervous System (CNS) and the lack of effective therapies to aid in the regeneration of neurons following injury. Recent investigational approaches have shown promise for neural regeneration through the development of 3D biomimetic tissue engineered scaffolds.

Objective: The purpose of this study is to synthesize a novel brain tissue-mimicking scaffold for application in neural tissue regeneration. The aim of this research is to design a 3-in-1 system wherein nanofibers will be “in-process” embedded into a cryogel scaffold followed by filling of the macro-microporous architecture with an ECM-mimicking hydrogel for neural tissue engineering.

Methods: The scaffold system will be fabricated using modified methods such as electrospinning, self-assembly techniques and functionalized with bioactive molecules to deliver both structural and bioactive cues. Thereafter, the scaffold will be subjected to chemical, physical, and mechanical characterization (pore volume, porosity, density, swelling ratio, X-ray diffraction, thermal analysis, Fourier transform infrared, rheological analysis, and degree of in vitro degradation). The biocompatibility of the scaffold will be investigated by *in vitro* and *in vivo* experimentation with stem cell and animal models respectively.

Results: The clinical potential of the implant will be determined following *in vivo* testing in animal models.

Conclusion: This novel 3-in-1 scaffold system will be designed for application as a surrogate implant with pro-regenerative properties to aid in neural tissue regeneration following TBI. This system may also be applied to significantly advance clinical translation of current neural tissue regeneration strategies such as stem cell and drug delivery.

APPENDIX G

RESEARCH PAPER PUBLICATION:

doi.org/10.3390/pharmaceutics12100934

pharmaceutics

MDPI

Article

Repositioning *N*-Acetylcysteine (NAC): NAC-Loaded Electrospun Drug Delivery Scaffolding for Potential Neural Tissue Engineering Application

Gillian D. Mahumane, Pradeep Kumar, Viness Pillay and Yahya E. Choonara *

Wits Advanced Drug Delivery Platform Research Unit, Department of Pharmacy and Pharmacology, School of Therapeutic Science, Faculty of Health Sciences, University of the Witwatersrand, 7 York Road, Parktown, Johannesburg 2193, South Africa; gillian.mahumane@wits.ac.za (G.D.M.); pradeep.kumar@wits.ac.za (P.K.); viness.pillay@wits.ac.za (V.P.)

* Correspondence: yahya.choonara@wits.ac.za; Tel.: +27-11-717-72052

Received: 15 September 2020; Accepted: 27 September 2020; Published: 30 September 2020

check for updates

Abstract: Traumatic brain injury (TBI) presents a serious challenge for modern medicine due to the poor regenerative capabilities of the brain, complex pathophysiology, and lack of effective treatment for TBI to date. Tissue-engineered scaffolds have shown some experimental success in vivo; unfortunately, none have yielded consummate results of clinical efficacy. N-acetylcysteine has shown neuroprotective potential. To this end, we developed a N-acetylcysteine (NAC)-loaded poly(lactic-co-glycolic acid) (PLGA) electrospun system for potential neural tissue application for TBI. Scanning electron microscopy showed nanofiber diameters ranging 72–542 nm and 124–592 nm for NAC-free and NAC-loaded PLGA nanofibers, respectively. NAC loading was obtained at 28%, and drug entrapment efficacy was obtained at 84%. A biphasic NAC release pattern that featured an initial burst release (13.9%) stage and a later sustained release stage was noted, thus enabling the prolonged replenishing of NAC and drastically improving cell viability and proliferation. This was evidenced by a significantly higher cell viability and proliferation on NAC-loaded nanofibers for rat pheochromocytoma (PC12) and human glioblastoma multiform (A172) cell lines in comparison to PLGA-only nanofibers. The increased cell viability and cell proliferation on NAC-loaded nanofiber substantiates for the repositioning of NAC as a pharmacological agent in neural tissue regeneration applications.

Keywords: nanofibers; electrospinning; drug delivery; N-acetylcysteine; scaffold; drug release; Poly(D,L-lactide-co-glycolide (PLGA)

APPENDIX H

LITERATURE REVIEW PUBLICATION: doi.org/10.1039/c8bm00422f

Biomaterials Science

REVIEW

View Article Online
View Journal | View Issue

Check for updates

Cite this: *Biomater. Sci.*, 2018, **6**, 2812

3D scaffolds for brain tissue regeneration: architectural challenges

Gillian Dumsile Mahumane, Pradeep Kumar, Lisa Claire du Toit, Yahya Essop Choonara and Viness Pillay *

Received 18th April 2018,
Accepted 18th September 2018

DOI: 10.1039/c8bm00422f

rsc.li/biomaterials-science

Biomaterials are being utilized to engender biomimetic, pro-regenerative constructs in the form of 3D scaffolds to augment functional neural tissue (brain tissue) repair and regeneration. Tissue engineered three-dimensional (3D) scaffolds have shown various degrees of experimental success, indicating great potential for development as treatment options. However, there is yet to be a 3D scaffold that exhibits consummate results of an effective clinical standard. Critical assessment of the performance of current 3D scaffolds could provide insightful feedback for tailoring future 3D scaffolds towards more promising results. This review provides a critical analysis of current 3D scaffolds for neural tissue engineering. Architectural properties, such as porosity, swelling, and architectural influences, such as design approach and polymeric material choice, were scrutinized for suitability for the desired tissue target properties. Success and shortcomings of various 3D scaffolds were evaluated through the analysis of tissue integration of the 3D scaffold *in vivo*. Investigations focused on in this review included those: (1) reporting at an *in vivo* experimental level in animal models, (2) involving polymer-based (natural/synthetic) scaffolds described as possessing a '3D' architecture, (3) targeting brain tissue regeneration (4) published from 2011 onward.

APPENDIX I

DETAILS OF DRUG RELEASE FOR CHAPTER 3

Construction of a calibration curve for UV spectroscopic determination of NAC, determination of drug loading, entrapment efficiency (DEE), and release

A calibration curve for NAC was conducted in PBS (pH 7.4; 37°C) by analysing a known series of concentrations of NAC (0-0.13mg/ml) in PBS on a UV spectrophotometer (Lambda 25, UV/VIS Spectrometer, PerkinElmer®, Waltham, MA, USA) at a wavelength of 224nm. A linear curve was generated with the observed absorbance plotted on the y-axis and the corresponding concentrations (mg/mL) on the x-axis. With the intercept set at 0, the curve presented an R^2 value of 0.9909, demonstrating good linearity, and the equation determined as y=3.7171x (Figure 8).The DEE of nanofibers was calculated by first accurately weighing samples of NAC-loaded nanofibers and dissolving them in formic acid. The actual drug quantity (D_a) was analyzed by UV spectrophotometry (Lambda 25, UV/VIS Spectrometer, PerkinElmer®, Waltham, MA, USA) and computed from a standard linear curve of the drug at a λmax of 224nm. The D_a was compared with the amount of drug that was loaded during the electrospinning process (D_t). All tests were performed in triplicate (n=3) and presence of the polymer was taken into account. Equation 8.1 was used to compute the DEE, where the theoretical drug (mg) in the formulation was determined as a function of the fibre weight.

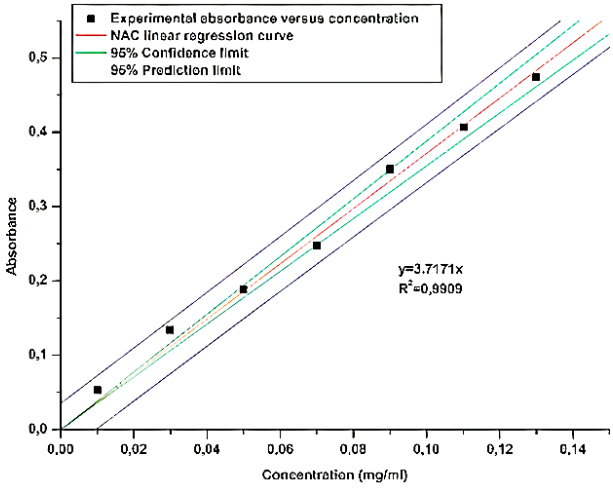

Figure 8. The calibration curve obtained for NAC.

Equation 8.1. %DEE = (Da/Dt) x 100

where %DEE = Percentage of drug entrapped; Da = Actual drug quantity (mg) measured by UV spectrophotometry and Dt = Theoretical drug (mg) added to the formulation.

The drug release of NAC/PLGA nanofibers were measured in order to determine the release profile of the system. Samples of NAC/PLGA nanofibers were immersed in 100mL of PBS (pH 7.4) and the release studies were carried out at 37 °C, 30rpm in a thermostatic shaking incubator. Measurements were taken at intervals of 10minutes, 1hour, 2hours, 4hours, and 24 hours. At each specific time point, 3mL of sample was withdrawn, and the same amount was replaced with fresh PBS to satisfy the perfect sink-conditions and keeping the volume constant. The concentration of NAC was determined based on a calibration curve using a UV Vis spectrometry, with UV detection at a wavelength of 224 nm. The accumulative weight and relative percentage of the released NAC were then calculated using the calibration curve of the drug in PBS (pH 7.4). This experiment was conducted for the drug loaded nanofibers. The release experiments for each sample were performed in triplicate and the average values have been reported.

The cumulative percentage of released NAC is calculated using the given formulae (equations 2-5)[20]

Equation 2.

$$Concentration\ of\ drug\ \left(\frac{mg}{ml}\right) = (slope\ \times absorbance) \pm intercept$$

Equation 3.

$$Amount\ of\ drug\ released\ mg/ml\ = Concentration\ \times dissolution\ bath\ volume\ \times dilution\ factor\ released$$

Equation 4.

$$Percentage\ drug\ released\ (\%) = (actual\ drug\ (mg)\ \div theoratical\ drug\ (mg))\ \times\ 100$$

Equation 5.

$$Cumulative\ percentage\ drug\ released\ (\%) = (volume\ of\ sample\ withdrawn\ \div bath\ volume) \times p(t-1) + pt$$

Where Pt = Percentage release at time t

Where P (t – 1) = Percentage release previous to ‘t’.